



**HAL**  
open science

# Interactions électroniques en physique mésoscopique, microscopie à effet de grille local et interférométrie sur un contact ponctuel quantique

Boris Brun

► **To cite this version:**

Boris Brun. Interactions électroniques en physique mésoscopique, microscopie à effet de grille local et interférométrie sur un contact ponctuel quantique. Autre [cond-mat.other]. Université de Grenoble, 2014. Français. NNT : 2014GRENY049 . tel-01137642

**HAL Id: tel-01137642**

**<https://theses.hal.science/tel-01137642>**

Submitted on 31 Mar 2015

**HAL** is a multi-disciplinary open access archive for the deposit and dissemination of scientific research documents, whether they are published or not. The documents may come from teaching and research institutions in France or abroad, or from public or private research centers.

L'archive ouverte pluridisciplinaire **HAL**, est destinée au dépôt et à la diffusion de documents scientifiques de niveau recherche, publiés ou non, émanant des établissements d'enseignement et de recherche français ou étrangers, des laboratoires publics ou privés.

## THÈSE

Pour obtenir le grade de

### DOCTEUR DE L'UNIVERSITÉ DE GRENOBLE

Spécialité : **Physique de la matière condensé et du rayonnement**

Arrêté ministériel : 7 août 2006

Présentée par

**Boris BRUN**

Thèse dirigée par **Marc SANQUER**  
et codirigée par **Hermann SELLIER**

préparée au sein l'Institut Néel, CNRS, Grenoble  
et de l'Ecole doctorale de physique de Grenoble

# Electron interactions in mesoscopic physics: scanning gate microscopy and interferometry at a quantum point contact

Thèse soutenue publiquement le **17 Octobre 2014**,  
devant le jury composé de :

**Patrice ROCHE**

CEA SPEC, Saclay, Rapporteur

**Francesco GIAZOTTO**

Scuola Normale Superiore, Pisa, Rapporteur

**Harold BARANGER**

Duke University, North Carolina, Examineur

**Julia MEYER**

CEA INAC / UJF, Grenoble, Examineur

**Dietmar WEINMANN**

CNRS IPCMS, Strasbourg, Examineur

**Marc SANQUER**

CEA INAC, Grenoble, Directeur de thèse

**Hermann SELLIER**

CNRS NEEL / UJF, Grenoble, Co-Directeur de thèse



---

# Abstract

In this thesis, we studied the effect of electron electron interactions in quantum point contacts (QPCs). Quantum point contacts are small quasi-one dimensional channels, designed on a high mobility two-dimensional electron gas (2DEG). A negative voltage applied on a pair of metallic split gates above the sample surface allows to open or close the QPC. As a QPC opens, more and more electronic modes are allowed to cross the QPC, and its conductance increases by discrete steps, separated by a conductance quantum  $2e^2/h$ . This can be understood from a single-particle picture in one-dimensional transport, as each transverse mode carries a conductance quantum.

But from their first realization 25 years ago, quantum point contacts have shown deviations from this picture, attributed to electron electron interactions. The most well known are a shoulder below the first plateau, around  $0.7 \times 2e^2/h$ , called the "0.7 anomaly", and a peak in the differential conductance that arises at low temperature: the zero bias anomaly (ZBA).

The tool we used to study these interaction effects is a scanning gate microscope (SGM). It consists by changing locally the device's potential with the polarized tip of an atomic force microscope (AFM), and record the changes in conductance as a function of the tip position. By performing this technique at very low temperature, we showed that we can modulate the conductance anomalies of QPCs. We interpret our result as the signature of a small electrons crystal forming spontaneously at low density in the QPC due to the Coulomb repulsion: a Wigner crystal. We can modify the number of crystallized electrons by approaching the tip, and obtain signatures of the parity of the localized electrons number in transport features. Depending on this parity, the Wigner crystal has a different spin state, and screening of this spin by the surrounding electrons through the so-called Kondo effect leads alternatively to a single peak or a split ZBA. This discovery brings a significant advance in this field, that has attracted research efforts of many important groups in the world over the past 15 years.

We then performed interferometric measurements thanks to the scanning gate microscope by creating in-situ interferometers in the 2DEG. We obtained signatures of an additional phase shift accumulated by the electrons in the ZBA regime. We attribute this effect to the universal phase shift that electrons accumulate when crossing a Kondo singlet, reinforcing that the debated origin of the ZBA lies in Kondo physics.

Finally, we adapted the SGM technique to the study of thermoelectric transport in QPCs, and for the first time imaged interferences of electrons driven by a temperature difference.

---

# Résumé en français

Au cours de cette thèse nous avons étudié les effets des interactions entre électrons dans les contacts ponctuels quantiques (QPCs). Les contacts ponctuels quantiques sont des petits canaux quasi-unidimensionnels, définis à partir de gaz électroniques bidimensionnels de haute mobilité (2DEG). Une tension négative appliquée sur des grilles métalliques au dessus de la surface permet d'ouvrir ou fermer le QPC. Lorsqu'un QPC s'ouvre, de plus en plus de modes électroniques peuvent traverser le QPC, et sa conductance augmente par pas discrets, séparés par un quantum de conductance  $2e^2/h$ . On peut le comprendre par le transport unidimensionnel d'une seule particule, car chaque mode transverse contribue pour un quantum de conductance.

Mais depuis leurs premières réalisations, les QPCs ont montré des déviations par rapport à ce modèle à une particule. Les plus connues sont un épaulement sous le premier plateau, autour de  $0.7 \times 2e^2/h$ , appelé "l'anomalie 0.7", et un pic dans la conductance différentielle qui apparaît à basse température: l'anomalie à zéro polarisation (ZBA).

L'instrument que nous avons utilisé pour étudier ces effets d'interactions est un microscope à effet de grille local (SGM). Cette technique consiste à modifier localement le potentiel d'un dispositif à l'aide d'une pointe de microscope à force atomique (AFM) chargée négativement, et enregistrer les modifications de la conductance en fonction de la position de la pointe. En utilisant cette technique à très basse température, nous avons montré que nous pouvons moduler les anomalies de conductance du QPC. Nous avons interprété nos résultats comme la signature d'un cristal d'électrons se formant spontanément à basse densité dans le QPC à cause de la répulsion Coulombienne: un cristal de Wigner. On peut modifier le nombre d'électrons cristallisés en approchant la pointe, et obtenir des signatures de la parité du nombre d'électrons localisés dans le transport électronique. En fonction de cette parité, le cristal de Wigner présente un état de spin différent, et l'écrantage de ce spin par les électrons de conduction au travers d'un mécanisme appelé effet Kondo donne une anomalie à zéro polarisation formant alternativement un simple pic ou un double pic. Cette découverte apporte une avancée significative à ce domaine, qui a concentré les efforts de plusieurs groupes importants ces 15 dernières années.

Nous avons ensuite réalisé des mesures interférométriques à l'aide du microscope SGM, en créant in situ des interféromètres dans le gaz 2D. Nous avons obtenu les signatures d'un déphasage supplémentaire dans le régime de la ZBA. Nous attribuons cet effet au déphasage universel accumulé par les électrons à la traversée d'un singulet Kondo, ce qui renforce le fait que la ZBA trouve son origine dans les phénomènes Kondo.

Enfin, nous avons adapté la technique SGM au transport thermoélectrique dans les QPCs, et avons imagé pour la première fois les interférences d'électrons se déplaçant sous l'effet d'une différence de température.

---

# Acknowledgments

The time to acknowledge people who helped me all along this thesis comes at the very end, though I could never have achieved a tenth of this work without the help of numerous people.

Of course I would first like to thank Hermann for having written and directed the scientific project, and chosen me as the PhD student in charge of this work. He always guided me with patience, spent time to follow my investigations and the experimental results, and encouraged me in creating new collaborations that proved to be essential in this work. Aside physics, I really enjoyed to spend time with him during these three years. Looking around, I understood that a passioning research subject is not the first requirement for a satisfying thesis. It comes in second position, the first one being a friendly and understanding supervisor, and I enjoyed these three years particularly because Hermann definitely has these essential human skills. Marc has also been a wise director, helped me to follow the right directions, and suggested me essential collaborations. I also thank him for the time he spent to gather all the electronics spread in the C1 building each time I needed to measure devices in the LATEQS team.

Fruitful collaborations have been the key for me to achieve this work. I first would like to acknowledge Vincent Bayot. If he had not invited me to visit Belgium, my thesis would have been completely different, and would probably not contain its principle results. It is definitely in Louvain-La-Neuve that started the most fruitful and passioning collaboration. I have a special thanks for Benoit Hackens, and I apologize for having dried out his Helium fundings during my stays in his team! None of this would have been possible without the essential help of Frederico Martins. Thanks Fred for your contagious love of experimental physics, your determination, and all those good moments spent on the fridge sofa discussing about life till the end of the night to keep on measuring. It was a pleasure to work with Sebastien Faniel, and his fine knowledge of all the fridge's whims! I also thank Damien Cabossart, and his promising work on graphene rings. Finally I have a thought for the whole team, including Sadia and Jean-Michel, and I'm afraid to misspell Handra and Nhan's names to thank them... See you soon, I'll try to come back!

I also thank many people from the near field team at Neel Institute, Aurelien for his every-day craziness, Guillaume for his calm enthusiasm, his Comsol simulations and a magic paraglide flight together, the irreplaceable Mr. Jean-Francois Motte, Serge for his great supervision of this team, and finally Jochen, Sven, Katrin, Joanna, Anna, Olivier, Arnaud, Pierre, Jean-Yves, Jean-Baptiste, Sayanti, Hervé, Benjamin for team lunches in a joyful mood!

---

On the other side of the border, in CEA, I also wish to thank many people, I hope not to forget too much of them!

First in the LATEQS' great experimentalists team, thanks to Benoit Voisin for his teachings in low-temperature nano-electronics and all those years spent at school together, but also away from the labs in everyday's life. Benoit Roche for his smart Labview programming and his grateful help, Charlene and her love for travels and the nice time spent in Poland at EP2DS, sharing a small students' room with Benoit to pay for three in one week what others paid alone for one night, Claude for his justified grouching against the research system nowadays, and also Xavier, Francois, Alex, Max, Jean-Eude Paul, Silvano, Eduardo, Julien, and of course Eva!

In CEA I also spent time in the scaring theorist's building where I always felt home thanks to a welcoming atmosphere and really kind persons. Xavier Waintal has provided me the opportunity to familiarize with his wonderful program: Kwant. By first writing a program to model the devices I studied, he opened me a door I could not have guessed at the beginning. Thank you for this time spent to explain me the basics of tight binding models. Kwant would not have been brought to (open-access) life without Christoph Groth. I also owe him my familiarization with this incredible tool and the basics of parallel computation. Thank you both for this experimentalists' friendly tool, it often guided my intuition. I'll try to evangelize experimentalists as I can! Julia and Manuel's wise advices and great discussions were always a pleasure, but not as much as skiing in Aussois between two talks! Thank you also Caro for these moments spent in summer schools and "vaconferences", scuba diving, mountain-biking, paragliding, skiing and hiking is a common ground easier to share than Green functions! Thanks also to Driss, Tatiana and Roman.

Away from these three "home-labs", I would like to thank people from Strasbourg: Dietmar Weinmann and Rodolpho Jalabert for their research interest in SGM, and Cosimo Gorini for the long discussions in Aussois drinking beers. Ciao mista, we'll meet again! Pascal Simon also welcomed me in Paris, I hope we will keep working together in the future, that's a pleasure. I just hope not to suffer once more in a summer school your way of "teaching bozonization in five minutes", even with adapted material...

Thanks finally to Jean-Louis Pichard and Adel About for their creative ideas that gave rise to this project and inspired me, and Genevieve Fleury for continuing this promising work.

Finally, discussions with Klaus Ensslin, Thomas Ihn, Clemens Rössler and Nikola Pascher during conferences have been really interesting, as well as the advices of Alex Hamilton.

During a PhD in nanoelectronics, an essential starting point is to have good sample to measure. For this I thank the LPN team for their wonderful job! I was first mad to struggle one year to observe the first conductance plateaus, measuring samples full of switching noise or leaky gates. But after all, it taught me that it is not obvious to build a clean two-dimensional electron gas, nor to design a clean lithographic pattern on the surface. So I congratulate them because the samples I measured during the second part of my thesis were perfect! Many thanks to Ulf Gennser for having grown the layer and communicating with us, and thank you Dominique for having spent some public holidays to

---

realize the lithography, despite your new time-consuming position at the head of the LPN.

I of course acknowledge the jury members, first Francesco Giazotto and Patrice Roche for having accepted the task to read this manuscript, Harold Baranger for having suffered my approximative English, Dietmar Weinmann for his encouragements, and Julia Meyer for presiding this jury.

Finally, I would like to thank all my friends out of the lab's life because research is impossible without daily enriching experiences. I thank my house-mates Raoul, Flop and Max for having bravely left town to settle in Bellecombe, these were two passioning years in the countryside. Thank you for these experiences lived together, culminating with Chap-à-Chap, what an experience!! Of course my most lovely thoughts go to Amandine, who left her life in North to join me in Grenoble, diving into a new challenging experience.

A last thought goes to my family to close these acknowledgements, with a special one for my mother, who always encouraged me on this way of symbiosis with science, keeping open eyes on the surrounding world. I also thank my sister Fanny for having always been a model for me, and having always overcome my achievements, to follow her so promising way. Keep on this way, now it is your turn to start a PhD!

---

# Contents

<b>1</b>	<b>Transport in Quantum Point Contacts</b>	<b>17</b>
1.1	Quantum point contacts	18
1.1.1	GaAs/AlGaAs heterostructures	18
1.1.2	Linear conductance	20
1.1.3	The saddle-point model	21
1.1.4	Non-linear conductance	23
1.2	Characterization of our quantum point contacts	24
1.2.1	The samples	24
1.2.2	Measuring quantum transport	27
1.2.3	Linear conductance traces	28
1.2.4	Non-linear conductance traces	31
1.2.5	Numerical model: introducing Kwant	32
1.2.6	Disorder in quantum point contacts	34
1.3	Conclusion	37
<b>2</b>	<b>Interactions effects in quantum point contacts</b>	<b>39</b>
2.1	The 0.7 anomaly	40
2.1.1	Temperature and magnetic field dependence	40
2.1.2	Bias dependence	41
2.1.3	Other experimental observations	43
2.2	The zero bias anomaly	44
2.2.1	First observation	44
2.2.2	Other experiments	45
2.2.3	Recent breakthrough	45
2.3	Theoretical models of localization	46
2.3.1	Mechanisms for conductance anomalies assuming localization	46
2.3.2	Spontaneous charge localization in numerical simulations	46
2.3.3	Perspectives : calculation of transport in presence of strong interactions	48
<b>3</b>	<b>Scanning Gate Microscopy</b>	<b>49</b>
3.1	Scanning gate microscopy	50
3.1.1	Introduction	50
3.1.2	Branches and interferences	51
3.1.3	Two types of interferences	53
3.2	Our scanning gate microscopes	54

3.2.1	Low temperature atomic force microscopy . . . . .	54
3.2.2	The microscopes . . . . .	54
3.2.3	The conductive tips . . . . .	55
3.2.4	Imaging quantum transport . . . . .	55
3.3	Interferences . . . . .	56
3.3.1	SGM images on the plateau . . . . .	56
3.3.2	Dependence on QPC opening . . . . .	58
3.3.3	Temperature dependence . . . . .	61
3.3.4	Non linear behavior . . . . .	63
3.4	Tip potential . . . . .	65
3.4.1	Estimating the shape of the tip tail . . . . .	65
3.4.2	What is the size of the depleted region? . . . . .	66
3.4.3	Electrostatic simulations . . . . .	67
3.5	Modeling scanning gate microscopy . . . . .	68
<b>4</b>	<b>Ballistic interferometers</b>	<b>73</b>
4.1	Sample and measurements . . . . .	74
4.1.1	The device geometry . . . . .	74
4.1.2	Generating interference . . . . .	75
4.1.3	Transconductance . . . . .	76
4.2	Influence of different parameters . . . . .	77
4.2.1	Dependence on QPC opening . . . . .	77
4.2.2	Dependence on temperature . . . . .	80
4.2.3	Dependence on magnetic field . . . . .	81
4.2.4	Polarization influence . . . . .	82
4.3	Numerical simulations . . . . .	83
4.3.1	Interference without disorder . . . . .	83
4.3.2	The role of disorder . . . . .	84
4.3.3	Modeling magnetic field . . . . .	85
4.4	Conclusion . . . . .	86
<b>5</b>	<b>Wigner and Kondo physics in quantum point contacts</b>	<b>89</b>
5.1	Kondo effect in quantum dots and quantum point contacts . . . . .	90
5.1.1	The Kondo effect in mesoscopic physics . . . . .	91
5.1.2	Non equilibrium Kondo effect . . . . .	93
5.1.3	Two-impurity Kondo effects . . . . .	94
5.1.4	Odd and even Kondo effect in QPCs . . . . .	95
5.2	Wigner crystallization revealed by scanning gate microscopy . . . . .	98
5.2.1	Conductance anomalies without tip . . . . .	98
5.2.2	Isotropic rings in SGM images . . . . .	99
5.2.3	Modulation of the 0.7 anomaly . . . . .	102
5.2.4	Modulation of the zero bias anomaly . . . . .	103
5.2.5	Interpretation in terms of Wigner crystallization . . . . .	105
5.2.6	Reproducibility in a second sample . . . . .	110
5.2.7	Higher conductance analogues . . . . .	113
5.3	Conclusion . . . . .	116

---

<b>6</b>	<b>Kondo phase shift revealed by scanning gate interferometry</b>	<b>119</b>
6.1	Introduction . . . . .	120
6.2	Kondo transmission and Kondo temperature in QPCs . . . . .	121
6.2.1	Universal scaling of the conductance . . . . .	121
6.2.2	Analysis of the Kondo peak in our QPCs . . . . .	123
6.2.3	Discussion . . . . .	126
6.3	Probing Kondo phase shift with a scanning gate microscope . . . . .	126
6.3.1	Description of the experiment . . . . .	126
6.3.2	Avoiding ZBA splittings . . . . .	129
6.3.3	Temperature dependence of the phase shift . . . . .	130
6.3.4	The energy window of the phase shift . . . . .	131
6.3.5	Value of the phase shift . . . . .	133
6.3.6	Phase shift versus QPC opening . . . . .	135
6.3.7	Interpretation . . . . .	135
6.4	Conclusion and perspectives . . . . .	137
<b>7</b>	<b>Imaging a coherent electron flow driven by a temperature difference</b>	<b>141</b>
7.1	Introduction . . . . .	142
7.2	The thermopower . . . . .	142
7.2.1	Definition . . . . .	142
7.2.2	Thermopower of a QPC . . . . .	144
7.2.3	The Mott's law . . . . .	145
7.2.4	First measurements on QPCs . . . . .	145
7.3	Thermopower measurements . . . . .	146
7.3.1	Experimental technique . . . . .	146
7.3.2	Differential conductance . . . . .	147
7.3.3	Thermopower . . . . .	147
7.3.4	Evaluating $\Delta T$ . . . . .	149
7.3.5	Influence of the heating current . . . . .	150
7.3.6	Deviations from the Mott's law . . . . .	152
7.4	Scanning gate microscopy of the thermopower . . . . .	152
7.4.1	Imaging thermally-induced coherent flow . . . . .	152
7.4.2	Validity of the Mott's law . . . . .	153
7.5	Conclusion . . . . .	155
<b>A</b>	<b>Kwant code example</b>	<b>161</b>
<b>B</b>	<b>Publication related to Chapter 5</b>	<b>167</b>
<b>C</b>	<b>French summary</b>	<b>177</b>
	<b>Bibliography</b>	<b>189</b>



# Introduction

## Physics in low dimensions

By reducing the dimensions of conductors and lowering the temperature, one can reach a scale where electronic transport exhibits quantum effects. The electrons coherence length becomes of the order of the system size, and their wave-like nature appears in transport properties. In particular, at this mesoscopic scale, interference effects have first been detected in universal conductance fluctuations of small wires [1] and Aharonov-Bohm experiments on metallic rings [2].

By reducing the dimensionality with the advent of two-dimensional electron gases (2DEG), quantum transport in condensed matter physics has turned to a new age. 2DEG made of Silicon MOSFET (Metal-oxide-semiconductor field-effect transistor), allowed the discovery of the integer quantum Hall effect [3], that quickly led to the Nobel prize of Klaus Von Klitzing (1985).

This discovery demonstrated the fact that reducing the dimensions of the systems allows a deeper investigation of quantum effects in condensed matter. By tuning the potential landscape of semiconductor 2DEG, a new type of devices have been developed, and allowed to study transport across a small electronic island (quantum dots), and quasi one dimensional channels that are the subject of this thesis: quantum point contacts[4, 5]. A few years after the discovery of the integer quantum hall effect, experimental signatures of fractional quantum Hall effect have been reported[6] in cleaner 2DEG made out of GaAs (that will be the system used in this thesis), and immediately explained as arising from electron electron interactions leading to fractionally charged excitations[7]. For this fundamental discovery in the field of many-body quantum physics, the authors were also awarded a Nobel prize (Tsui, St Örmer and Laughlin, 1998).

This discovery demonstrated that semiconductor 2DEG are not only a testbed for single particle quantum effects in condensed matter physics, but also allow an investigation of the many-body problems, opening a new field in experimental quantum mechanics.

## Electron interactions in one dimension

Electron electron interactions in one-dimensional devices are the subject of this thesis. In particular, we are interested in the effects of interactions in quantum point contacts (QPCs). A QPC is a small constriction defined in a 2DEG, that can be opened or closed by applying a negative voltage on metallic split gates above the 2DEG. First developed 25 years ago, these devices seem a perfect realization of single-particle one dimensional

transport. By opening the constriction, one can let one by one transverse electronic modes go through the QPC, and its conductance evolves by steps of the conductance quantum  $2e^2/h$  each time a new mode is opened. But from their very first realization, QPCs have shown deviations from this picture, attributed to electron electron interactions. The most well-known deviation is the 0.7 anomaly: an unexpected shoulder around  $0.7 \times 2e^2/h$ . The other famous deviation from the single-particle picture is a peak in the differential conductance of QPCs around zero bias, called the zero bias anomaly (ZBA).

These two anomalies have attracted research efforts of many groups in the world, but still remain an open problem nowadays. They are of interest on a technological point of view, because we need to fully understand the QPCs, that are the simplest device one can design in the field of quantum transport, before fully understanding more complex nanoelectronics devices. These anomalies are also a fascinating subject from the fundamental point of view, as they are supposed to arise from electron electron interactions, that often lead to the most complicated problems in quantum mechanics.

## Scanning gate microscopy

The tool chosen in this thesis to investigate interactions effects in QPCs is the scanning gate microscope (SGM). It is derived from atomic force microscopy (AFM), and consists in changing the devices' conductance at low temperature thanks to the polarized metallic AFM tip. By recording the device conductance as a function of tip position, one can image quantum transport phenomena in semiconductor nanostructures. But far more than producing beautiful images of the quantum world, a scanning gate microscope can be used as an additional transport parameter, and reveal rich physics when combined with transport measurements. We will see in particular how the polarized tip of a scanning gate microscope can be used to finely tune the potential landscape of a QPC and reveal crucial informations on the many-body effects involved in the conductance anomalies. We will also describe how the polarized tip can be used to create in situ electronic interferometers allowing to perform phase-sensitive experiments on QPCs.

## Organization of this thesis

This manuscript is organized as follows:

In Chapter 1, we present the basics of quantum transport in heterostructures, and the single-particle picture of QPCs. We discuss the role of disorder in QPCs and introduce a numerical tool that is used along this thesis to investigate single-particle phenomena: Kwant[8].

Chapter 2 introduces the conductance anomalies in QPCs and summarizes part of the long road that has been achieved on these subjects over the past two decades.

In Chapter 3, we introduce scanning gate microscopy and study the potential created by the tip. We also analyze the interference fringes observed in our SGM images and discuss their possible origin.

In Chapter 4, we present a new type of ballistic interferometers that we developed to mimic SGM experiments, on which a sharp gate is designed one micron away from the QPC,

acting as a local scatterer. We characterize the interferences obtained in these devices and compare them to the ones observed in SGM. In the light of numerical simulations, we also discuss the possible role of the disorder in the contrast of these interferences.

Chapter 5 presents the major result of this thesis. We show how the polarized tip of a scanning gate microscope can be used to tune in-situ the potential landscape of a quantum point contact, and how it changes the many-body state forming in the QPC channel. We will first describe the context, and discuss a recent experiment that shows the existence of several localized electrons in QPCs[9]. We will then show that we can also manipulate this many-body state by approaching the polarized tip of a SGM towards the QPC. Our observations confirm their interpretation and shines a new light on the mechanism involved in the localization of these electrons.

In Chapter 6, we present an interferometric study by forming a Fabry-Pérot cavity between the QPC and the tip-depleted region. By recording the spectroscopy of the interferences obtained in this configuration, we show that the zero-bias anomaly induces a phase shift of the interferences. We describe in detail the characteristics of this phase shift and propose an explanation based on Kondo physics.

Finally, Chapter 7 presents thermoelectric measurements of QPCs, and shows how we can successfully adapt the SGM technique to the imaging of thermoelectric transport.



# Chapter 1

## Transport in Quantum Point Contacts

### Contents

---

<b>1.1</b>	<b>Quantum point contacts</b>	<b>18</b>
1.1.1	GaAs/AlGaAs heterostructures	18
1.1.2	Linear conductance	20
1.1.3	The saddle-point model	21
1.1.4	Non-linear conductance	23
<b>1.2</b>	<b>Characterization of our quantum point contacts</b>	<b>24</b>
1.2.1	The samples	24
1.2.2	Measuring quantum transport	27
1.2.3	Linear conductance traces	28
1.2.4	Non-linear conductance traces	31
1.2.5	Numerical model: introducing Kwant	32
1.2.6	Disorder in quantum point contacts	34
<b>1.3</b>	<b>Conclusion</b>	<b>37</b>

---

## Introduction

The most simple object that one can imagine in the field of quantum transport is probably a quantum point contact (QPC). It is a small quasi one-dimensional channel connecting large two-dimensional reservoirs, that carries a definite number of transverse electronic modes. Its conductance is quantized in units of the conductance quantum  $2e^2/h$ , reflecting the number of perfectly transmitted transverse modes. In this sense, it beautifully illustrates the very fundamental principle of quantum transport, known as the Landauer-Büttiker formula.

On the other hand, closing a quantum point contact below the first plateau, letting less than a single transverse mode going through, leads to dramatically low electronic density. Counter-intuitively, reducing the electronic density results in increased electron-electron interactions, and this leads to rich physics dealing with the most complicated problems in quantum mechanics.

This makes of a quantum point contact an elegant device to illustrate the basics of quantum transport as well as a perfect platform to study fundamental many-body quantum physics.

In this chapter, we focus on the single-particle picture of quantum point contacts, interactions effects will be discussed in Chapter 2. In section 1.1.1, I will briefly introduce the properties of high mobility two-dimensional electron gases (2DEG) obtained with semiconductor heterostructures, then move to one dimension and describe the first experiments on QPCs, in the linear and non-linear regimes, and the theoretically expected behavior. In section 1.1.2, I present the basic properties of the QPCs investigated in the thesis, considering only the single-particle effects (not the interactions effects). For this purpose, I will describe the sample fabrication, the measurements set-up, show some experimental results and discuss the particular role of disorder. I will introduce a numerical code used all along this thesis to perform quantum transport simulations: Kwant.

## 1.1 Quantum point contacts

### 1.1.1 GaAs/AlGaAs heterostructures

Among the different possibilities to confine electrons in a single plane, one is based on III/V semiconductors alloys. In this field, the cleanest electron gases are obtained from heterostructures of GaAs and AlGaAs. These semiconductors can be grown in a very clean way by “molecular beam epitaxy” (MBE), leading to pure crystals with very few lattice defects. The band diagram in these semiconductor heterostructures can be adjusted in such a way that the conduction band drops below the Fermi energy in an extremely thin layer, leading to a single conduction plane. The electronic subbands in this plane are separated by a large energy, and only one subband is usually occupied at low temperature.

Even though different recipes are possible to realize high quality 2DEG, the one in Fig.1.1 presents the most frequently used structure. On a GaAs substrate is grown a layer of AlGaAs, in which a silicon doping layer is embedded. The silicon atoms give electrons that are “trapped” at the GaAs/AlGaAs interface, since the conduction band drops below the Fermi energy. The electrons trapped in this quantum well experience a

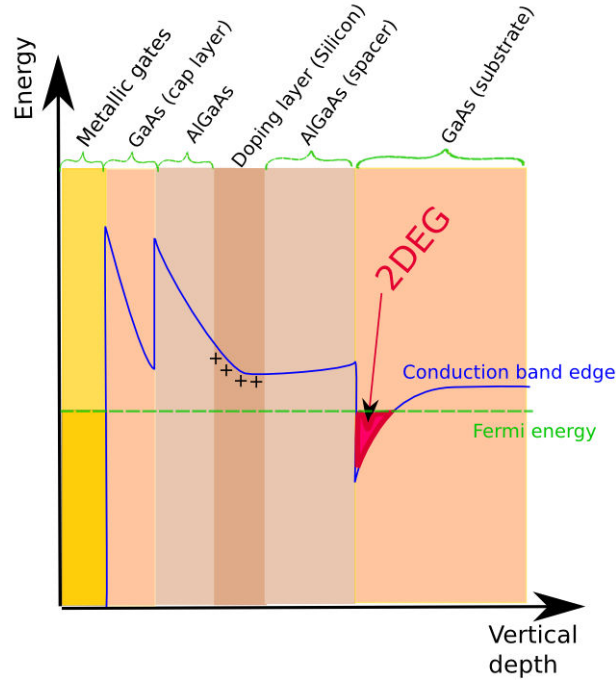


**Figure 1.1** *GaAs/AlGaAs heterostructure: typical composition and resulting conduction band edge of GaAs/AlGaAs heterostructure*

very high mobility, because the lattice is very clean due to the epitaxial growth process, and mainly because the ionized Si donors are really far away from the 2DEG, reducing scattering events. The 2DEG are typically buried from tens to hundreds nanometers below the sample surface.

Mobilities in these heterostructures reach usually  $10^6 \text{cm}^2/\text{V.s.}$  and the electronic density is of the order of  $10^{11} \text{e}^-/\text{cm}^2$ .

With such high mobilities, the mean free path goes up to several microns. This means that transport is quasi-ballistic on macroscopic scales, which offers a great platform for an interesting type of experiments: ballistic electronics.

The typical density of these 2DEG can be compared to three-dimensional metals, by putting it to the power  $3/2$ , which would give around  $10^{17} \text{e}^-/\text{cm}^3$ . This is far below usual metals, that contain around  $10^{23} \text{e}^-/\text{cm}^3$ . This particularly low densities corresponds to small kinetic energies which tends to increase the effect of electron interactions. These effects are central in this thesis and will be discussed all along this manuscript.

These low densities correspond to Fermi wavelengths of tens to hundred nanometers. This means that one can design structures of the order of the Fermi wavelength, offering an incredible range of quantum nano-electronic devices. Finally, this kind of density gives typical Fermi energy around 10 meV, and at reasonably low temperatures (for example 4.2K, in liquid  $^4\text{He}$  at atmospheric pressure), the electrons phase remains well defined on a few microns, leading to phase coherent ballistic electronics.

To measure transport in these structures, this 2DEG should be contacted electrically. This is usually achieved by depositing a multilayer metallic alloy on the surface (usually

Ni/Ge/Au/Ni/Au), and heat up the structure for AuGe to diffuse down to the 2DEG, defining ohmic contacts and enabling to measure the conductance of the 2DEG.

To enter the field of mesoscopic physics (phase coherence), the 2DEG has to be patterned into a micron-size device. This is achieved by depositing metallic gates in the sample surface. Applying a negative voltage on these gates repels the electrons in the 2DEG, and enables one to reshape the 2DEG potential landscape into quantum point contacts (1D confinement) or quantum dots (0D confinement).

### 1.1.2 Linear conductance

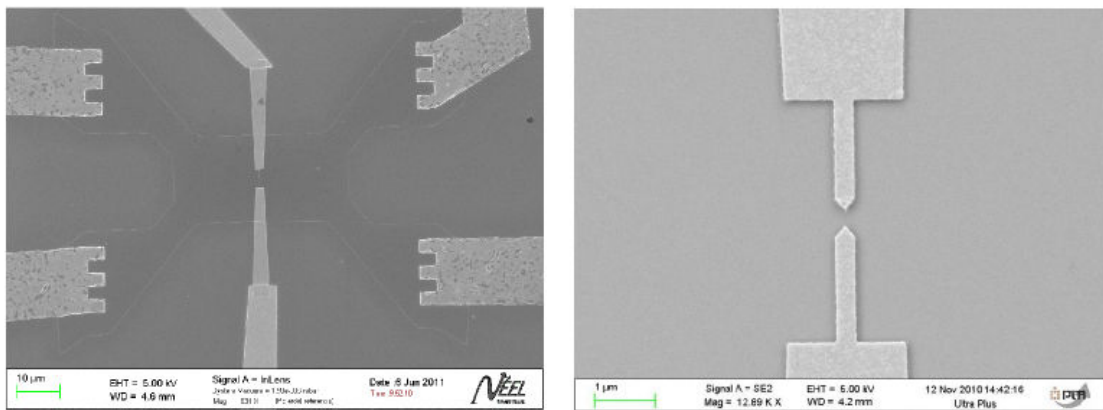


**Figure 1.2** *Typical scanning electron microscope (SEM) image of a QPC from this work: Metallic split gates are deposited to split the 2DEG in two parts. On the left (large field), one can see the shape of the conductive part, defined as the MESA. Four ohmic contacts are defined to contact the 2DEG and perform 4-point measurements. The ohmic contact have a different texture compared to the split gate.*

The simplest mesoscopic device that can be achieved out of a 2DEG is a quantum point contact. Thanks to electronic beam lithography technique, a pair of thin metallic split gates are deposited above the 2DEG, defining a small constriction (Fig.1.2). Applying a negative voltage on these split gates repels the electrons of the 2DEG below the gates, letting a finite electronic density only in the central part, through which current flows. By controlling the applied gate voltage, one can open or close the constriction. The first experimental realizations of this type of devices have been achieved in the late 80's, at the same time in two different groups [4, 5].

The first experimental traces of a QPC conductance vs. gate voltage from these works are shown in Fig.1.3.

The first experimental observation is that the conductance does not behave at all in a monotonic fashion, but exhibits striking quantization. As a QPC opens, its conductance is found to be quantized in units of the conductance quantum  $2e^2/h$ , with a good accuracy. This conductance quantization can be understood as follows: in a narrow 1D channel, the transverse wave-function is quantized and the propagation along the channel axis involves

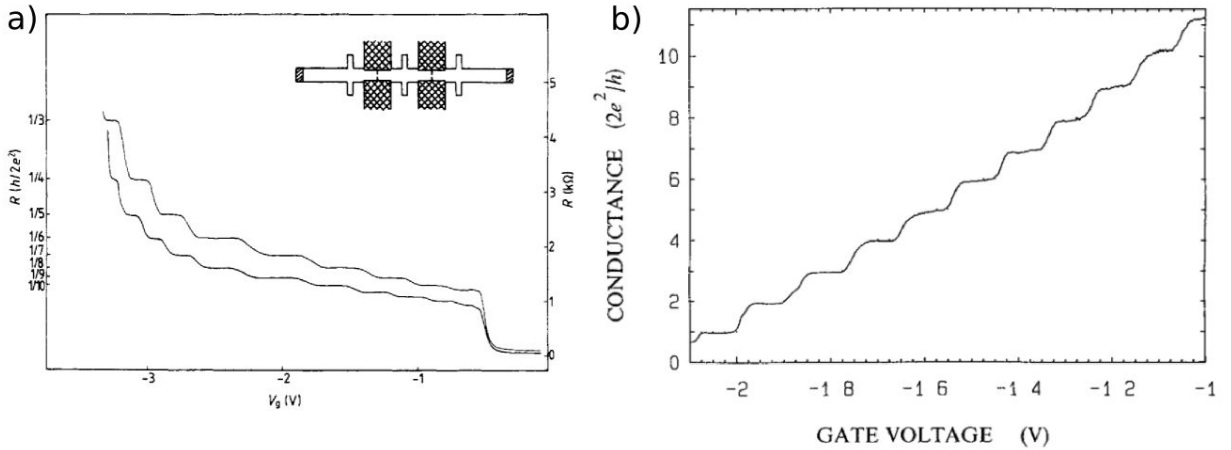


**Figure 1.3** *Two first experiments demonstrating conductance quantization in QPCs:* a) Resistance of a QPC as a function of gate voltage in units of  $h/2e^2$ . The trace exhibits steps corresponding to conductance quantization. Adapted from Ref.[5]. b) Conductance of a QPC as a function of gates voltage, in units of  $2e^2/h$ . Adapted from Ref.[4].

discrete modes, as in electromagnetic waveguides. When the QPC opens, more and more transverse electronic modes can go through the constriction. As each of these modes contributes to the total conductance for  $2e^2/h$ , the conductance evolves in steps, with one additional conductance quantum each time a new mode is allowed to cross the QPC.

### 1.1.3 The saddle-point model

To better understand this conductance quantization, a beautiful calculation [10] has been proposed soon after the first experimental demonstration. This model can be summarized as follows. The QPC defines a constriction separating infinite two-dimensional leads. In the 2DEG, the constriction is defined electrostatically a hundred nanometers below the metallic split gates, which tend to smooth most of the geometric details of the gates. A good approximation is then to consider that the very center of the QPC potential forms a saddle-point, with a positive curvature in the transverse axis (denoted as  $y$  in the following), and negative one along the transport axis (denoted as  $x$ ). This saddle potential can then be expressed as follows:

$$V(x, y) = V_0 + 1/2m^*\omega_y^2y^2 - 1/2m^*\omega_x^2x^2 \quad (1.1)$$

$\omega_y$  and  $\omega_x$  are parameters defining the curvatures in the longitudinal and transverse directions, I will discuss later how to evaluate them experimentally and numerically. This simple saddle-point approximation has the advantage to be solvable analytically[10]. The hamiltonian of the problem simply writes:

$$H = p^2/2m^* + V(x, y) \quad (1.2)$$

where  $p^2/2m^*$  is the kinetic energy,  $m^*$  being the effective mass of the electrons trapped in the GaAs quantum well.

The hamiltonian can be separated regarding  $x$  and  $y$ , and a well known problem of quantum mechanics appears in the transverse direction: an harmonic oscillator in a parabolic well, defined by  $V(y) = 1/2m^*\omega_y^2 y^2$ . The solution of this problem is that the allowed transverse wave-functions are the eigen-modes of the harmonic oscillator  $\psi_n$ , associated with discrete energy values  $E_n = (n + 1/2)\hbar\omega_y$ .

### 1.1.3.1 One-dimensional transport

To evaluate the current flowing through this quasi-1D channel, we can proceed as follows: it is the integral of the current density at all accessible energies, given that one side of the channel is biased by a voltage  $V_{sd}$  (at zero temperature for simplicity).

$$I = e \sum_{n=1}^N \int_{E_f}^{E_f + eV_{sd}} D_n(E) v_n(E) T_n(E) dE \quad (1.3)$$

where  $D_n(E)$  is the 1D density of state,  $v_n(E)$  is the group velocity of each transverse mode, and  $T_n(E)$  is the transmission probability of each mode. In 1D, the electronic density of states writes down  $D_n(E) = \frac{2}{2\pi\hbar} \sqrt{2m^*/(E - E_n)}$  (where the factor 2 stand for spin degeneracy). The group velocity is independent of the considered subband and can be expressed as  $v_n(E) = \partial E_n / \partial p_x = \sqrt{(E - E_n)/2m^*}$ .

Interestingly, these two quantities depend in an exact opposite way on the energy (and effective mass), therefore their product is independent of energy, and simply equals  $2/h$ . For small source-drain voltage (linear regime), the transmission is roughly constant in this energy window and can be replaced by  $T_n(E_f)$ .

Then the current simply writes:  $I = 2e/h * eV_{sd} \sum_n T_n(E_f)$ . As a consequence, the linear conductance  $I/V_{sd}$  of a 1D channel expresses as follows:

$$G = \frac{2e^2}{h} \sum_{n=1}^N T_n \quad (1.4)$$

,where the  $T_n$  are transmission probabilities of each mode at the Fermi level. This formula is known as the Landauer formula and traduces the fundamental law of mesoscopic transport: the conductance of a mesoscopic device is given by the number of perfectly transmitted modes times the conductance quantum  $2e^2/h$ .

### 1.1.3.2 Smooth plateaus in QPCs

In an infinitely long wire ( $\omega_x = 0$ ), the transmission coefficient is 0 for each subband lying above the Fermi energy and 1 for those of energy lower than  $E_f$ . In such a wire, as the split-gate voltage is lowered, less and less modes can be transmitted, and the conductance drops by integer values of  $2e^2/h$ , down to 0.

Then one can wonder why the conductance steps of QPCs are experimentally smooth, as this simple picture shall give infinitely sharp conductance steps. The thermal smearing of the Fermi distribution is not responsible for the smoothness of the transitions. As it will be discussed later, the 1D subband separation is of some meV, which corresponds to tens of Kelvins, whereas the electronic temperature in Fig1.3 is evaluated to be below 100mK,

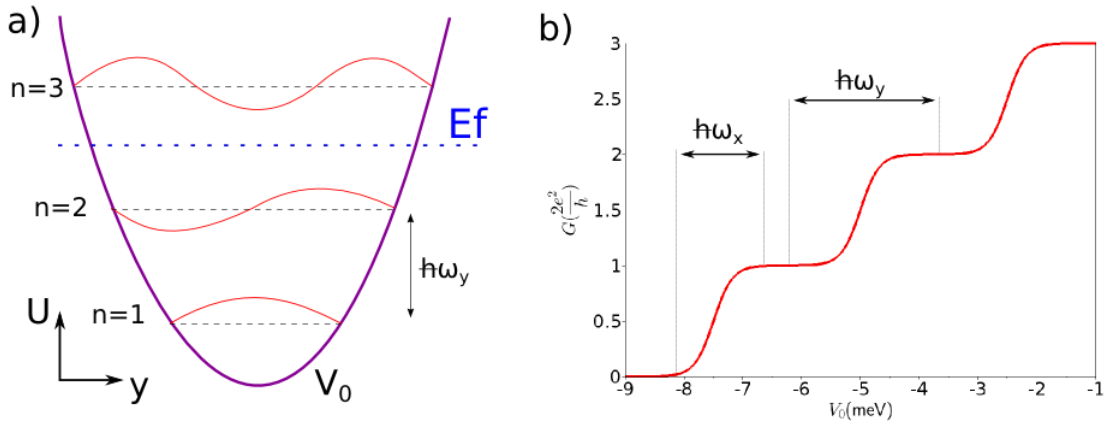


**Figure 1.4 Saddle-point model:** a) Schematics of the transverse harmonic potential and the authorized transverse wave-functions. Given the drawn scenario (corresponding to a particular  $V_0$ ), the two first modes ( $n=1$  and  $2$ ) are transmitted through the QPC, but the third one is reflected:  $G = 2*2e^2/h$ . b) Calculated conductance as a function of  $V_0$  for a  $E_f = 8\text{meV}$ , for  $\omega_x/\omega_y = 0.8$

which cannot account for the smooth transitions.

To understand these smooth transitions, one has to consider the finite length of the QPC and solve the entire problem of a transmission through a saddle point (i.e. take a finite longitudinal curvature  $\omega_x$ ). The solution [10] then gives a transmission for each subband:

$$T_n(E) = \frac{1}{1 + e^{-\pi\epsilon_n}} \quad \text{where} \quad \epsilon_n = 2(E - \hbar\omega_y(n + 1/2) - V_0)/\hbar\omega_x \quad (1.5)$$

This solution gives smooth transitions between plateaus, even for zero temperature, where the "smoothness" is governed by the ratio  $\omega_x/\omega_y$ . As sketched in Fig.1.4, a mode opens on an energy window of width  $\hbar\omega_x$ , and two modes are separated by  $\hbar\omega_y$ . A required condition to see plateaus in the conductance traces is then to have a potential in the constriction that respects  $\omega_x \leq 2\omega_y$ , otherwise plateaus are so smooth that they're almost invisible. An other required condition regarding experimental considerations is that the electronic temperature shall be smaller than the subband spacing and their natural width, i.e.  $k_B T \ll \hbar\omega_y, \hbar\omega_x$ .

### 1.1.4 Non-linear conductance

Up to this part, we considered a problem where source and drain are aligned at the same energy. The differential conductance  $G = \partial I/\partial V|_{V_{sd}=0}$  is then called the linear conductance. But the differential conductance can be measured in a situation where source and drain are misaligned, by applying a DC voltage between both, that can be higher than the 1D subbands energy spacing. The answer of the system is then called non-linear [11].

This non-linear response has early been predicted [14] to exhibit half-integer quantization (by odd values of  $e^2/h$ ), as soon as the DC bias would be of the order of the subbands energy spacing. This proposition has immediately been verified experimentally

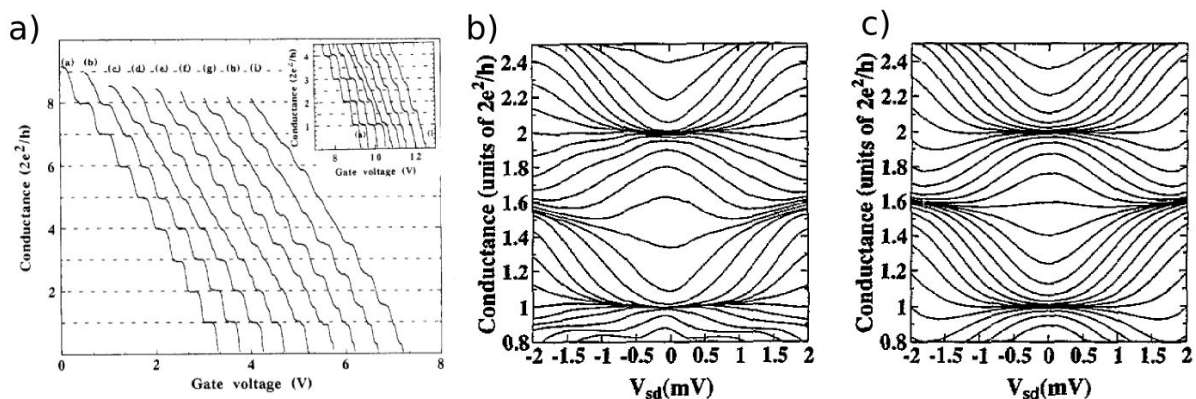


**Figure 1.5 Non linear conductance of QPCs:** a) Linear conductance for different source-drain DC bias, from 0 to 4 mV (left to right). Half-quantized plateaus are visible at high source-drain bias. Adapted from Ref.[12]. b) Cascade plot of conductance traces  $G(V_{sd})$  for different values of gate voltages, between the first and second plateau. Plateau appear as accumulation of traces. c) Simulation of the corresponding situation, assuming a linear drop of the potential along the QPC channel. Adapted from Ref.[13]

in the Cavendish group [12]. It has then been shown [13] that an accurate "odd quantization" is only obtained when the bias voltage drops symmetrically on both sides of the QPC.

This makes non-linear transport a powerful tool to investigate the energies involved in a QPC. The first measurement of a QPC non-linear response is presented in Fig.1.5a. Differential conductance traces are shown for different values of  $V_{sd}^{DC}$ . When  $V_{sd}^{DC} \sim 4\text{meV}$ , half quantized plateaus are clearly seen in the traces, and integer plateaus are not visible anymore.

The cascade plot Fig.1.5b presents several traces  $G(V_{sd}^{DC})$  for different gate voltages. The linear response  $G(V_g)$  corresponds to a vertical cross-section in the center of this cascade plot, for  $V_{sd}^{DC} = 0$ . In this type of plot, plateaus appear as an accumulation of traces, as the conductance on plateaus remain the same for different gate voltages. One can see that at sufficiently high source-drain bias, plateaus at odd values of  $e^2/h$  appear in the differential conductance. As explained in Ref. [13], this half-integer quantization correspond to a situation where for example the source chemical potential is aligned with one subband, and the drain is aligned with the next subband.

This type of plots therefore allow to directly measure the subbands energy separation, corresponding to the value of  $V_{sd}$  for which half plateaus appear.

## 1.2 Characterization of our quantum point contacts

### 1.2.1 The samples

#### 1.2.1.1 The heterostructure

All the data presented in this manuscript were recorded from samples designed on the same GaAs/AlGaAs heterostructure (08JN13). It was grown at LPN in Paris, by An-

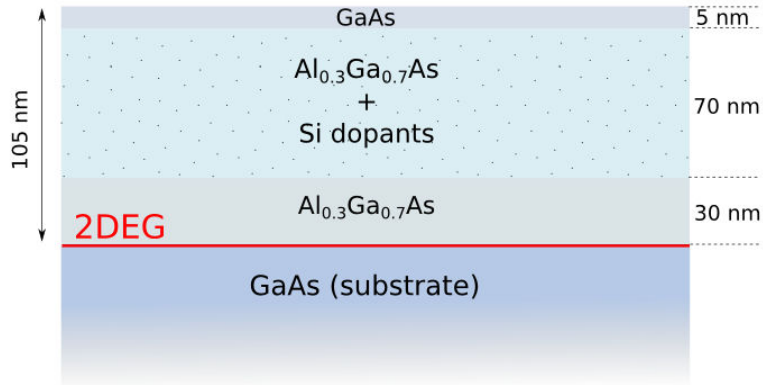


**Figure 1.6 Schematic of the 08JN13 heterostructure:** The growth process defines an heterostructure hosting a 2DEG 105 nm below the sample surface. The Si dopants are deposited in a "volumic doping layer", starting 30 nm above the 2DEG.

tonella Cavanna, Abdelkarim Ouerghi and Ulf Gennser, following the growth sequence presented in Fig.1.6.

A 30 nm thick layer of  $Al_{0.3}Ga_{0.7}As$  is grown on top of the GaAs substrate to separate the doping layer from the 2DEG, followed by a 70 nm thick  $Al_{0.3}Ga_{0.7}As$ , in which silicon dopants are embedded. This technique is called "volumic doping", and differs from the "delta-doping" often used in the growth of these structures with a single plane of silicon atoms. Finally, a last thin (5 nm) GaAs layer is grown on top, called the cap layer, to prevent AlGaAs from oxidation.

The Si atoms give their electrons, parts are trapped at the GaAs/AlGaAs interface and form the 2DEG, whereas other electrons go to the surface. The 2DEG hosted in this heterostructure has a mobility around  $10^6 cm^2/V.s.$  and the electronic density is about  $2.5 \cdot 10^{11} e^-/cm^2$ . It is buried 105 nm below the surface.

### 1.2.1.2 The lithographic gates

The samples are then fabricated on this heterostructure. The patterns were designed in Grenoble and the process was realized by Dominique Mailly and Christian Ulysse in Marcoussis.

First the ohmic contacts made of Ni/Ge/Au/Ni/Au are deposited by evaporation and lift-off. Then the sample is heated such that the AuGe diffuses down to the 2DEG. The MESA is then designed by chemical etching of the heterostructure everywhere except on a region where the 2DEG is preserved. Then metallic gates and markers are deposited on the surface, and are about 150 nm thick. The split gates of the QPC presented in this thesis define a 300 nm wide and 270 nm long constriction for samples A and B, and 270 nm wide and 300 nm long constriction for samples C and D. Though many different geometries have been designed and fabricated, only these two geometries could be investigated during the time of the thesis, but they revealed a rich and beautiful physics, overcoming our expectations. 5 different samples are presented in this manuscript, labeled A to E.

## 1.2. CHARACTERIZATION OF OUR QUANTUM POINT CONTACTS

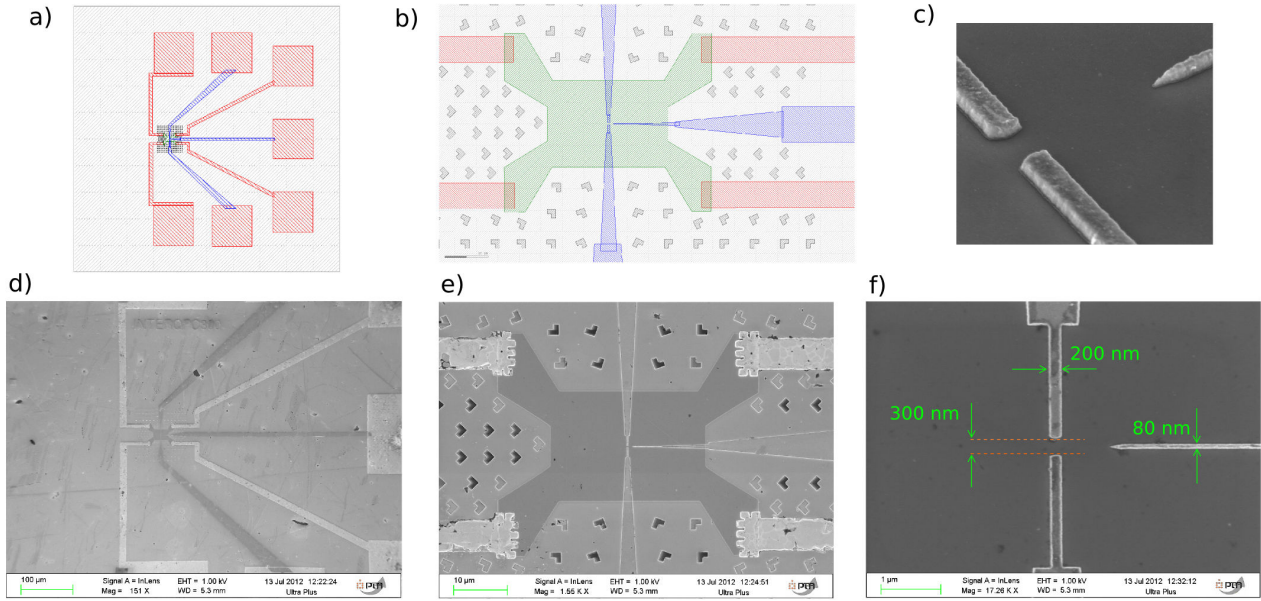


**Figure 1.7** *Lithographic process:* a) and b): design of the lithographic patterns with a layout editor. Gates are colored in blue, mesa in red, ohmic contacts in red and markers in black. d) and e): SEM images of an interferometer at different scales. c) and f): zoom on the central part of an interferometer, and dimensions of the gates.

They will be used all along this thesis in the different figures, that are summarized in this tabular.

Sample name	Length (nm)	Width (nm)	Figures
A	200	300	1.9a-b, 4.2 to 4.4
B	200	300	3.5c, 3.6, 3.11, 4.7, 5.7 to 5.14
C	300	270	1.9c-d; 3.9; 4.5; 5.15, 5.16, 5.18; 6.1 to 6.8
D	300	270	1.11; 7.5 to 7.10
E	?	?	1.10; 4.5

The other geometries should be studied in the future. On some samples, we designed a sharp gate (80 nm thin) in front of the QPC (see Fig.1.7). The distance between this sharp gate and the QPC was varied between 700 nm and 1800 nm. The aim of this sharp gate is to backscatter the electrons towards the QPC and generate interferences. The samples on which these gates are defined will therefore be called interferometers in the following, and their transport properties will be discussed in Chapter 4.

Note that for sample B, studied in Chapter 5 and used in the corresponding publication (see Appendix B), the length was thought to be 270 nm but a more recent analysis of some SEM images suggest a length of rather 200 nm. Therefore, the electrostatic simulations presented in the article consider a QPC a bit longer than the device (270 nm instead of 200 nm), but this small difference would not change significantly the results nor the interpretation.

## 1.2.2 Measuring quantum transport

### 1.2.2.1 Measurement principle

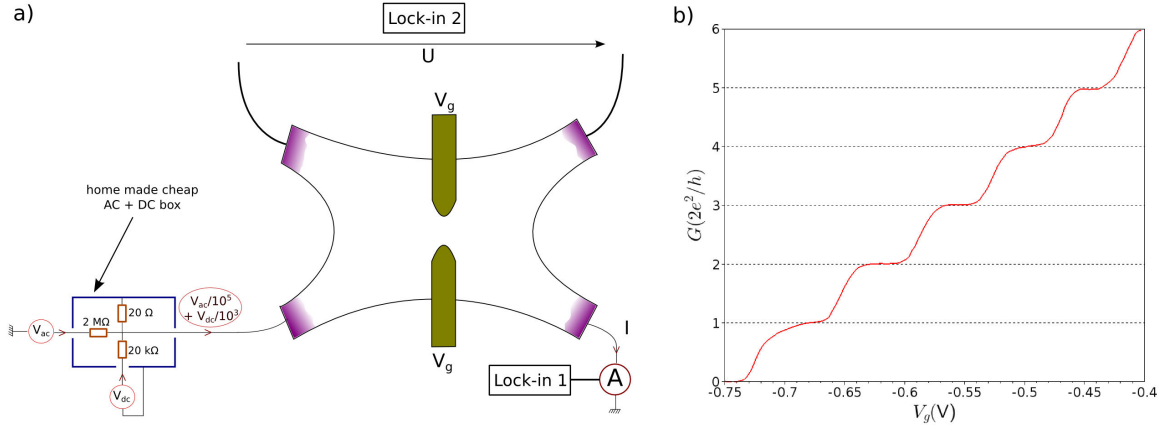


**Figure 1.8 Measurement setup:** a) Schematics of the measurement. A “DC + AC box“ is used to polarize the sample. The current and the applied voltage are simultaneously measured thanks to 2 lock-in. b) Conductance  $G(V_g)$  in units of  $2e^2/h$ , measured by lock-in technique in 4-point measurement, at a base temperature of 20 mK. A series resistance of  $600 \Omega$  is added to take into account the 2DEG resistance.

The conductance of a mesoscopic device is measured either with a voltage bias or with a current bias, depending on its impedance. High impedance devices are biased by controlling the potential difference between source and drain contacts, while low impedance devices are biased by controlling the current flowing through the device. The case of a QPC is special because its impedance varies from a few  $k\Omega$  when several modes are open to an infinity when the QPC is closed. It is then prevented to current bias a QPC, because its impedance is likely to become greater than the polarization impedance when it closes. The chosen method to measure the QPCs conductance all along this thesis is a third method called “4-points measurement“. It consists in polarizing the sample with a small AC voltage, measure the current flowing through the device and measure the voltage directly applied at the 2DEG level thanks to two additional ohmic contacts, as sketched Fig.1.8a. In this way, we can get rid of the voltage drop along the ohmic contacts (that typically have a  $500\Omega$  impedance at low frequency and zero magnetic field) and directly divide the measured current by the measured voltage. The applied bias is a low-frequency (typically 100 Hz) AC voltage, of amplitude around  $10\mu V$ . The current and voltage are measured using two lock-in operating at the excitation frequency.

Finally, despite the low resistance of the mesa (typically  $30 \Omega$  at low temperature), an undesirable voltage drop along 2DEG from the ohmic contacts to the QPC has to be taken into account to evaluate the conductance of the QPC itself. This access resistance is attributed to the squeezing of the current lines near the QPC region and is of the order of  $600 \Omega$  in the samples studied in this thesis. This resistance is evaluated such that the plateaus in the QPC conductance curve match integer values of  $2e^2/h$ .

To perform non linear conductance measurements discussed in section 1.1.4, an “AC + DC” box was often used, as schemed on Fig.1.8. This is a simple home-made system that

add a small AC voltage bias to a “large” DC one, using a floating DC source.

### 1.2.2.2 The cryostats

These measurements have to be performed at low temperature, and different cryostats were used during this thesis for scanning gate microscopy and magnetotransport experiments.

Two dilution fridges have been used at the CEA Grenoble in the LATEQS team. They answer to the nice nicknames of “Bigoudène, and ”La diluette“. Bigoudène is a powerful 20 year old cryostat, carrying a 3 Tesla superconducting magnet, typically working nowadays at a base mixing chamber temperature of 30 mK. La diluette is a small cryostat, aimed to measure tiny samples, operating at a base temperature of 50 mK. Despite the efficient cryogenic set up on these two machines, it appeared difficult to lower the electronic temperature of the measured QPCs down to some hundreds of mK. These fridges have been used for the studies of the interferometers discussed in chapter 4.

Scanning gate microscopy has first been tried in a liquid helium cryostat at 4.2 K at Institut Néel Grenoble. This thesis began with the design and fabrication of a new microscope assembly to reach better stability. However the temperature of this 4.2K cryostat turned out to be too high to observe conductance quantization in our QPC (see Fig.1.10a).

Scanning gate microscopy experiments reported in this manuscript have therefore been carried out in a dilution fridge at much lower temperature. The experiments were done during two long time stays at IMCN in Louvain-la-Neuve, Belgium, in the team of Benoit Hackens and Vincent Bayot. This really powerful machine, developed under the supervision of Vincent Bayot, is a 20 years old cryostat in which many important breakthrough have been performed in both solid state and mesoscopic physics. Since the arrival of Benoit Hackens in the team first as a post-doc and now as a permanent researcher, a low temperature scanning gate microscope is embedded in this fridge. Though all the wiring inherent to the microscope, that can eventually bring heat to the mixing chamber and deteriorate the fridge performances, this machine still operates at a base temperature of 20 mK, thanks to the clever wiring improvements of Sebastien Faniel. But the major asset of this machine is definitely the associated electronics. Whereas most recent set-up usually take advantage of fully numerical instrumentation, this machine is fitted with really powerful old fashion analogical electronics. Thanks to this clean instrumentation, the electronic temperature in this setup almost reaches the mixing chamber temperature, that will be discussed in Chapter 5.

### 1.2.3 Linear conductance traces

Typical measurements of QPC conductance versus gate voltage of some QPCs obtained using the different set-ups are presented Fig.1.9. Fig.1.9a and b were recorded on sample A in CEA at a mixing chamber temperature of 50 mK. As one of the ohmic contacts was not working, the conductance is calculated using the applied voltage, and taking into account

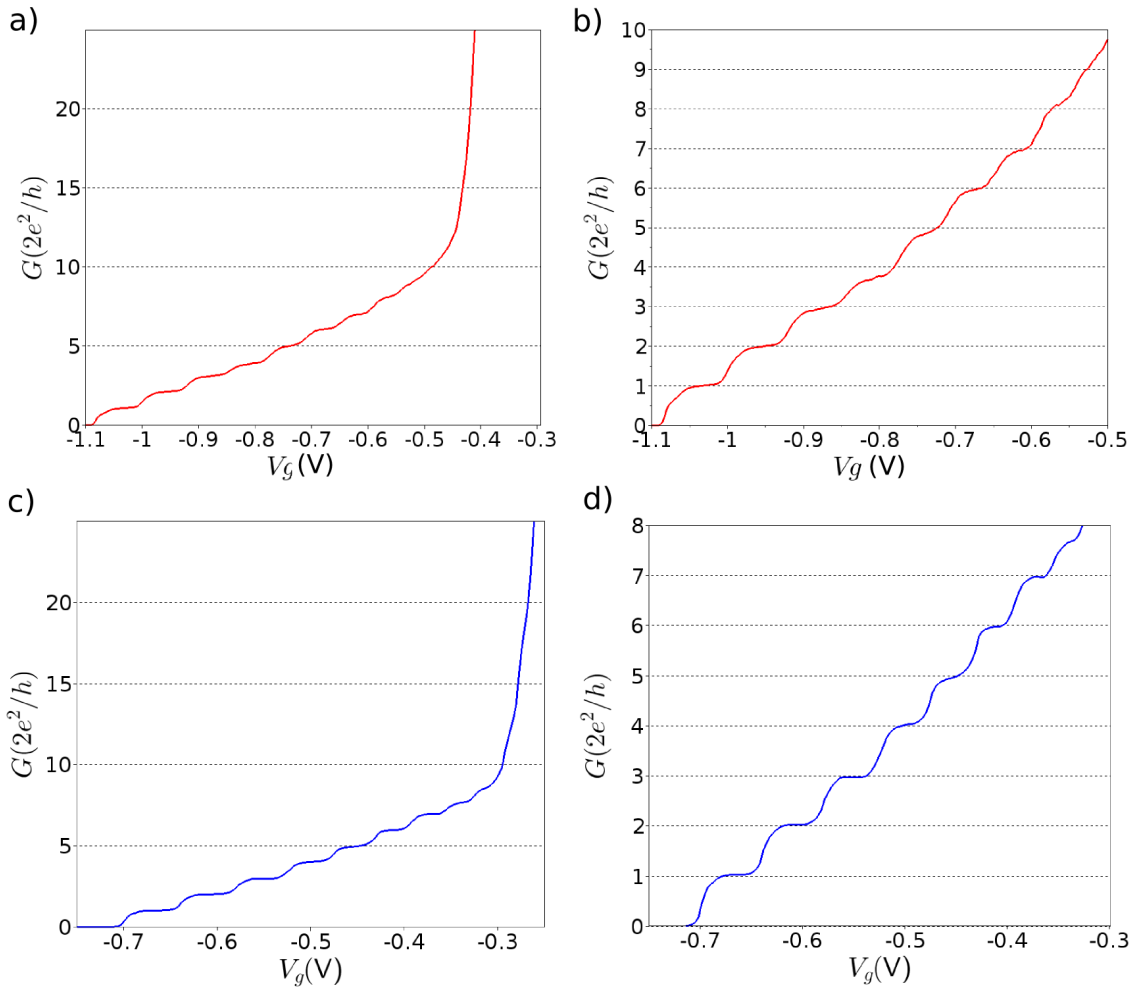


**Figure 1.9** *Different QPCs conductance traces: a) Linear conductance versus split gate voltage  $V_g$ , ranging from 0 to  $-1.2V$ , measure on sample A in CEA. The gate voltage required to disable tunneling below the gates is around  $-0.4V$ . b) Same QPC, the conductance curve is zoomed on the QPC regime. c) Linear conductance of sample C measured in LLN at its first cooldown. d) Zoom of c) on pinch-off.*

a  $2.4k\Omega$  series resistance corresponding to the filters impedance, the ohmic contacts and the access resistance. This series resistance is adapted such that the plateaus match integer values of  $2e^2/h$ . Fig.1.9c and d were recorded on sample C in Louvain-La-Neuve, in a 4-point measurement, at a mixing chamber temperature of 20 mK. The conductance is corrected by an access resistance of  $600\Omega$ .

The gate voltage required to reach depletion of the 2DEG below the gates can be read on Figs.1.9a and 1.9c, and correspond to  $\sim -0.45V$  for sample A and  $-0.3V$  for sample C. This difference can be explained by the gates geometry: gates of sample A are 200 nm wide whereas gates for sample they are 300 nm wide. For gate voltages above this values, the measured conductance is the one of the 2DEG, and tunneling of the conduction electrons occurs below the split gates. At the depletion threshold, the sample behaves as a field effect transistor, and the conductance experiences a fast drop. If the constriction is wide

## 1.2. CHARACTERIZATION OF OUR QUANTUM POINT CONTACTS

enough, a QPC is formed for gate voltages below this threshold value, in the center of the split gates. Then lowering  $V_g$  prevents one by one the transverse modes to flow through the QPC, and the conductance drops by steps of  $2e^2/h$  down to the pinch-off as shown in Figs.1.9b and 1.9d. Note that these pinch-off values are also different for these two samples, and the small geometrical difference can account for this difference. Indeed, QPC A is 300 nm wide and 200 nm long, whereas QPC C is 270 nm wide, and 300 nm long. Therefore a less negative voltage is required to completely close QPC C.

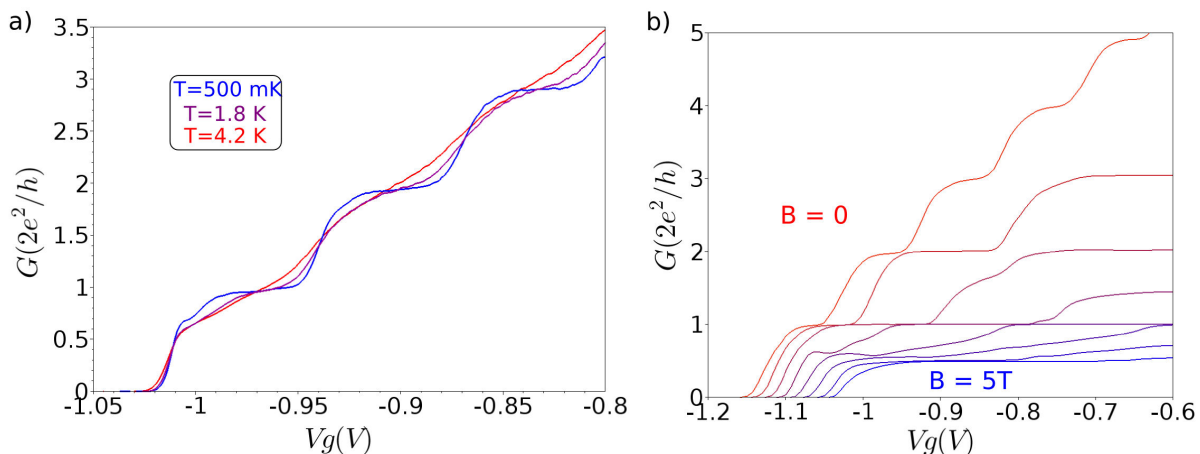


**Figure 1.10 Temperature and magnetic field dependence:** a) Traces of  $G(V_g)$  for different temperatures: 500 mK, 1.8 K and 4.2 K. recorded in CEA on QPC A. b)  $G(V_g)$  recorded at 20 mK in Louvain-La-Neuve on QPC E, at different perpendicular magnetic fields, ranging from 0 to 5T by steps of 0.7T.

The temperature dependence of the plateaus are presented Fig.1.10a. Increasing temperature tends to smooth the plateaus, that completely disappear around 4K. This is due to thermal averaging of the QPC modes when the electronic temperature is too high compared to the subbands spacing. This unfortunately prevented us to use the 4K set-up in Institut Néel during this thesis, as the energy scales of the phenomena studied in this thesis are even one order of magnitude lower than the subband spacing, as will be discussed later on. Note that the plateaus in curves  $G(V_g)$  do not evolve anymore with decreasing temperature below 1K (except the opening of the first mode that will be discussed later on and all along this manuscript). The shape of the steps is given by the longitudinal curvature  $\omega_x$ , hence does not depend on temperature if  $k_B T \ll \hbar\omega_x$ .

A parallel magnetic field would split the plateaus in half-integer plateaus spaced by  $e^2/h$ , because it lifts the spin degeneracy due to the Zeeman effect [5]. For technical reasons, this experiment has not been reproduced during this thesis. But we could apply a perpendicular magnetic field, that gives rise to interesting orbital effects. In the bulk 2DEG, the Landau levels start to form even at low magnetic field, giving rise to a more accurate quantization and flat plateaus in the QPC conductance traces (Fig.1.10b). The plateaus enlarge, the energy scale giving the typical plateaus length becomes the cyclotron pulsation  $\omega_c = eB/m^*$ , rather than the potential curvature  $\omega_x$  [10]. Together with the fact that a perpendicular magnetic field prevents most backscattering events, this leads

to long well-defined plateaus in the conductance traces, as presented (Fig.1.10b). The effect of a perpendicular magnetic field on a QPC, together with the role of disorder and interactions gives rise to incredibly rich physics, that have not been studied during this thesis. An interesting recent detailed study can be found in Ref.[15].

### 1.2.4 Non-linear conductance traces

As discussed in section 1.1.4, the non-linearity of a QPC can be measured by adding a DC voltage to the small AC voltage applied to measure the differential conductance. It is typically used to make the spectroscopy of the energy levels of a quantum device.

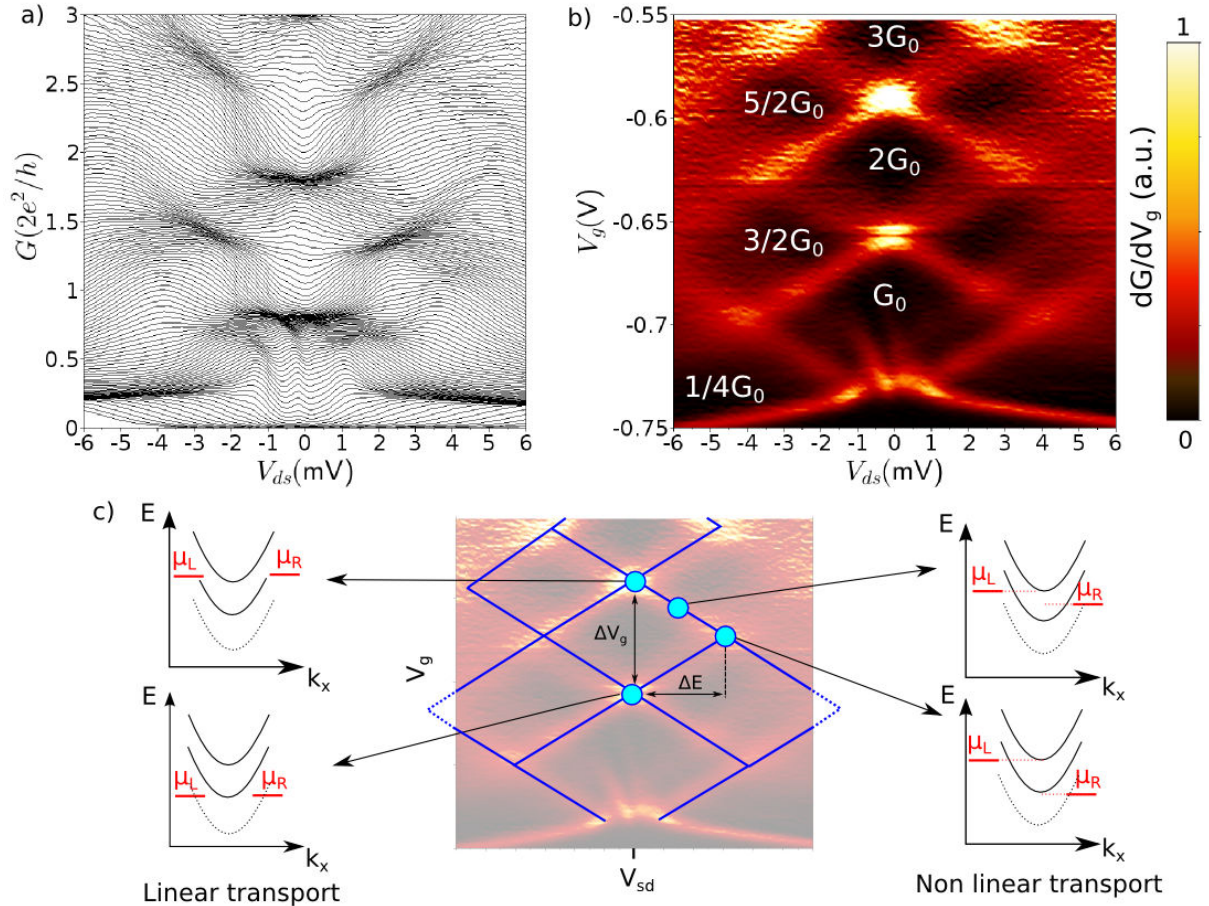


**Figure 1.11 Non-linear transport of quantum point contacts:** a) Traces  $G(V_{sd})$  for different  $V_g$ . Plateaus appear as accumulation of traces. b) Differential of  $G$  with respect to  $V_g$  as a function of  $V_g$  and  $V_{sd}$ . Plateaus appear as dark regions and transitions as bright lines. c) Subband 2 and 3 dispersion relation and chemical potentials of left and right lead ( $\mu_L$  and  $\mu_R$ ) for different  $V_{sd}$ . These data were recorded in Louvain on QPC D, at a base temperature of 20 mK

A typical measurement of a QPC non-linear response is presented in Fig.1.11. The cascade plot Fig.1.11a presents several traces  $G(V_{sd}^{DC})$  for different gate voltages. As explained in section 1.1.4 at sufficiently high source-drain bias, plateaus at odd values of  $e^2/h$  appear in the differential conductance. This half-integer quantization correspond to

a situation where for example the source chemical potential is aligned with one subband, and the drain is aligned with the next subband (schemes of the different situations are sketched Fig.1.11c).

Another way to look at these data is to plot the transconductance (i.e. the derivative of this cascade plot w.r.t.  $V_g$ , see Fig.1.11), as a function of source-drain bias and gate voltage. In this landscape, the plateaus appear as black regions (because changing the gate voltage doesn't change the device's conductance), and transitions between plateaus appear as bright spots, as  $V_g$  has a strong influence on the transmission. The bright transition lines correspond to a situation where the chemical potential of one of the leads is aligned with one of the subbands edge. This type of plots therefore allow to directly measure the subbands energy separation, corresponding to the value of  $V_{sd}$  for which the transition lines intersect. For example, from Fig.1.11b one can directly read that the second and third subbands are spaced by  $\Delta E = 4\text{meV}$ .

An other interesting information that can simply be extracted from these colorplots is the so-called "lever-arm parameter", which traduces how does the saddle-point rise (in energy) with the gate voltage. It just requires to extract the gate voltage required to go from one transition to another at zero source drain bias  $\Delta V_g$ . For example Fig.1.11c, the lever arm is given by  $\Delta E/\Delta V_g \sim 50 \text{ meV/V}$ .

These values for both the energy spacing and the lever-arm parameter are typical of all the QPCs studied in this thesis, as they were defined on the same heterostructure, and designed with similar geometries.

### 1.2.5 Numerical model: introducing Kwant

To go one step beyond single mode approximations or qualitative explanations, an interesting approach is to use numerical tools. The results presented in this section are obtained with an incredibly powerful tool that makes quantum transport simulations accessible: *Kwant* [8]. It is a free-access code that smartly takes advantage of several computation languages, such that a simple personal computer can solve complicated quantum transport problems. I used only a few percent of the extremely wide possibilities of Kwant, concentrating on transport in 2DEG devices.

Kwant offers a user-friendly way of solving the Schrödinger equation, using a discretized tight-binding hamiltonian, through a so-called "scattering region".

To solve the Schrödinger equation in the scattering region, one first has to give the potential landscape  $V(x, y)$ , which will be used in the hamiltonian. It is important to note that Kwant does not calculate the potential self-consistently, i.e. screening from the 2DEG is not taken into account. One therefore has to approximate the potential landscape using various methods. The particular case of a QPC requires the potential created by rectangular gates deposited on the sample surface. For this purpose, we use an exact electrostatic solution proposed in Ref.[16]. Assuming fixed potential on the surface ( $V_g$  on the gates and 0 elsewhere), the authors propose an elegant solution to analytically calculate the potential created by a rectangular gate at a distance  $d$  below the gate. The solution for a gate defined by  $L < x < R$  and  $B < y < T$ , at a distance  $d$  from the gas is the following:

$$\Phi(x, y, d) = V_g * [g(x - L, y - B) + g(x - L, T - y) + g(R - x, y - B) + g(R - x, T - y)] \quad (1.6)$$

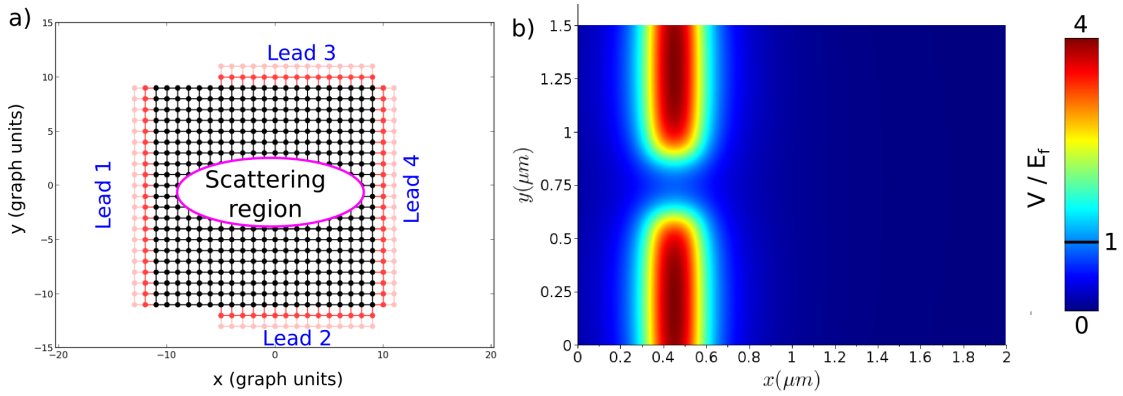


**Figure 1.12** *Ingredients required to run Kwant:* a) Example of a (small) scattering region. Dots are sites and links between them represent possible hoppings from one site to its neighbors. Red regions define the connection between the different leads and the scattering region. b) Potential  $V(x, y)$  in units of  $E_f$  generated following an analytic model [16] of two rectangular gates at the surface, 100nm above the 2DEG.

$$\text{where } g(u, v) = \frac{1}{2\pi} \text{atan}\left(\frac{uv}{d\sqrt{u^2+v^2+d^2}}\right)$$

The resulting potential for two 200 nm wide rectangular gates separated by 300 nm, on a 2DEG buried 100nm below the surface is plotted Fig.1.12. The scattering region is then connected to leads, and among the large output functions of Kwant, the most useful is the total transmission from one lead to an other. Depending on the chosen electronic density and the lead width, a given number of electronic modes can propagate in the lead, enter the scattering region, eventually suffer intermode scattering depending on the potential landscape and come out in other leads. All these modes contribute to the total conductance of the device, and the sum of all these contributions give the total conductance of the scattering region, thanks to the Landauer-Buttiker formula, as discussed previously.

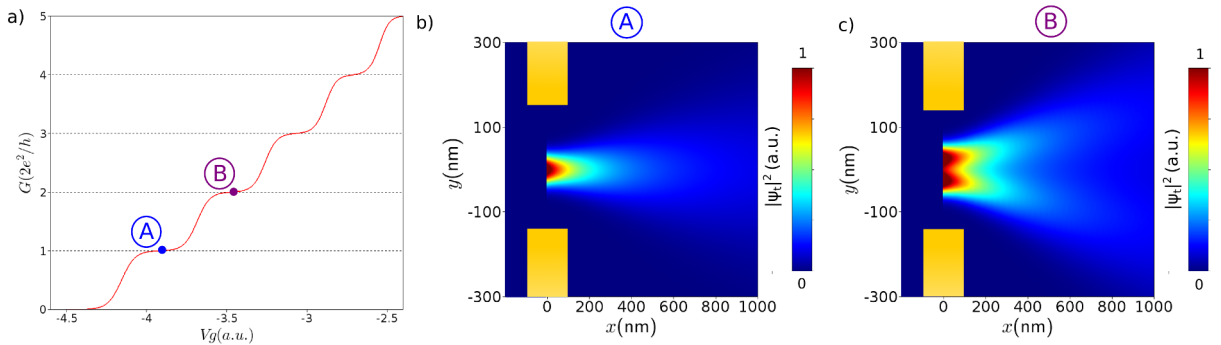


**Figure 1.13** *Typical useful outputs of Kwant:* a) Conductance  $G$  of the scattering region vs gate voltage b) Square modulus of the sum of all wave-functions coming out of lead 1 for a QPC open to the first (b) and second mode (c).

Using the potential sketched in Fig.1.12, with leads defined on both sides of the QPC

gates (containing about 60 modes each), one can then change the voltage applied on the gates  $V_g$  and compute the conductance through the scattering region (see Fig.1.13). Note that this simple picture already completely differs from the Büttiker model previously introduced, which assumed perfect adiabaticity (i.e. each incoming mode coming from infinity is an eigen-mode of the QPC). Here the situation is dramatically non-adiabatic, as about 60 different transverse modes coming from the left lead collapse into one or a few modes in the QPC. It is interesting to note that for example on the first plateau, all the 60 incoming modes contribute to the first QPC mode with different probabilities (they're "filtered" by the QPC), and the resulting single QPC mode carries exactly one quantum of conductance: this is the beauty of quantum mechanics, and is really close to what happens in the experiment. It is also really interesting to note that despite the dramatic non-adiabaticity of a QPC, the adiabatic model proposed by Büttiker [10] gives an excellent approximation, suggesting that the physics of a QPC is governed by the central part of the channel.

Another interesting output of Kwant I will refer to along this thesis is the square modulus of the total wave-function coming out of the QPC at the Fermi energy. In Kwant, the wave-functions of the modes coming out of a given lead are separated outputs. To get an idea of the transmitted electrons repartition, I will often compute the square modulus of the sum of all wave-functions coming out of one lead (the left one), and hide the left side of the QPC as most of the electrons are reflected by the gates and only a few are transmitted.

### 1.2.6 Disorder in quantum point contacts

Major deviations from the perfect case discussed above arise from two distinct phenomena: disorder and electron-electron interactions. These are two complicated problems, that can in some cases lead to similar signatures. It is therefore primordial to distinguish their fingerprints.

Fig.1.14 presents an example of some effects induced by disorder on QPCs conductance curves. It can lead to what is usually called "resonant structures", appearing as shoulders or dips in the QPC characteristic. A way to reveal the role of disorder in this type of resonant structures is to apply a different voltage on the two split gates, and sweep the average gate voltage. In this way, the position of the saddle-point displaces laterally, and the disorder experienced by the electrons is changed depending on the gate voltages difference. Therefore these resonances are changed depending on this difference, as seen Fig.1.14, unlike the intrinsic interaction-induced effects, as discussed in the next chapter.

To understand this problem, a microscopic origin of this disorder is required. The disorder in GaAs heterostructures is mainly attributed to the residual potential fluctuations due to the ionized donors above the 2DEG. As discussed before, these donors are pretty far away from the 2DEG. This prevents most "hard-scattering" events of electrons and provides them a really high mobility. Nevertheless, the electrons in the 2DEG still feel some potential fluctuations due to the random distribution of ionized dopants, that affect the electronic transport, especially when the density is reduced [17], which renders this

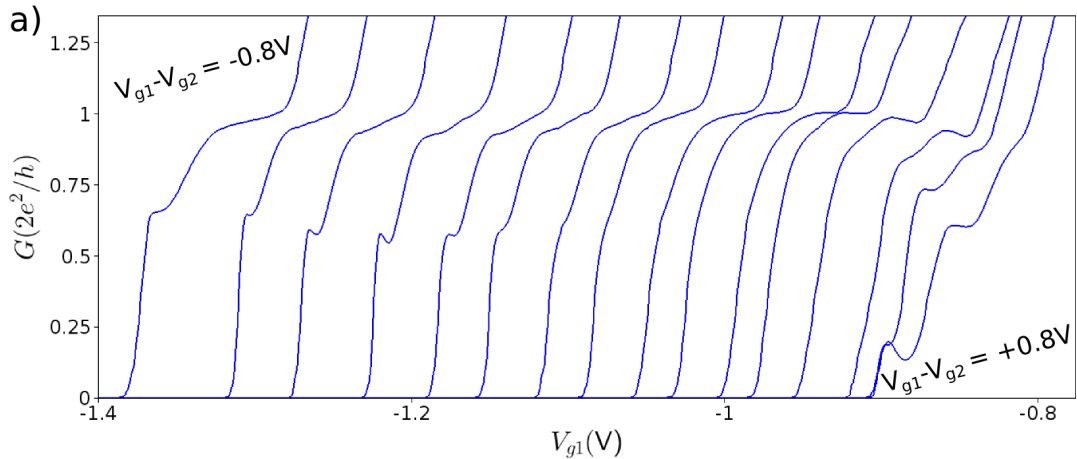


**Figure 1.14** *Experimental example of resonant structures due to disorder:* Measurement of QPC A conductance curve for a given cooldown different from Fig.1.9a, showing resonances. Different traces are presented as a function of  $V_{g1}$  (one of the gates voltages), for different values  $V_{g1} - V_{g2}$ .

problem fundamental in the study of QPCs as the density is really low when only a few modes are transmitted.

As this is a problem including random potential distributions and as it leads to nontrivial transport features such as intermode-scattering [18], numerical quantum transport appears as an appropriate tool to treat this problem.

Even in clean QPCs, the residual disorder can affect the conductance quantization. This problem has been extensively studied in the 90's [19, 20, 21, 22], and I will briefly discuss the main effects, illustrated with results obtained with Kwant. To model the residual random potential fluctuations, I use the method proposed in Ref.[17]. The ionized dopants are modeled by randomly distributed punctual charges at a distance  $d$  from the 2DEG and  $h$  from the sample surface (this technique assumes zero potential on the surface, which has the great advantage to give analytic solutions, even though it is not suitable to model every situations). This distribution gives a random potential in the 2DEG that is correlated on a typical length called  $\sigma_d$ . As soon as enough dopants are taken into account,  $\sigma_d$  is governed by the distance from the doping layer to the gas and not by the dopant density. Once this type of maps generated, the only parameter that remains to be scaled is the standard deviation of these fluctuations. I rescale the mean value of these fluctuations to be zero and the deviation to a given percentage of  $E_f$ .

An example of simulation is shown in Fig.1.15. First the disorder displaces the pinch-off towards more positive values of  $V_g$ , in a fashion that is dependent of the exact configuration, and precisely the sign of the local fluctuation at the very top of the saddle-point (a local negative fluctuation at this point shifts the pinch-off towards more negative values though no example is given there). Disorder landscapes correlated on small spatial scales  $\sigma_d$  tend to create resonances on the conductance steps (configuration A Fig.1.15c), strongly affecting the QPC conductance as soon as the deviation of the fluctuations reach a few

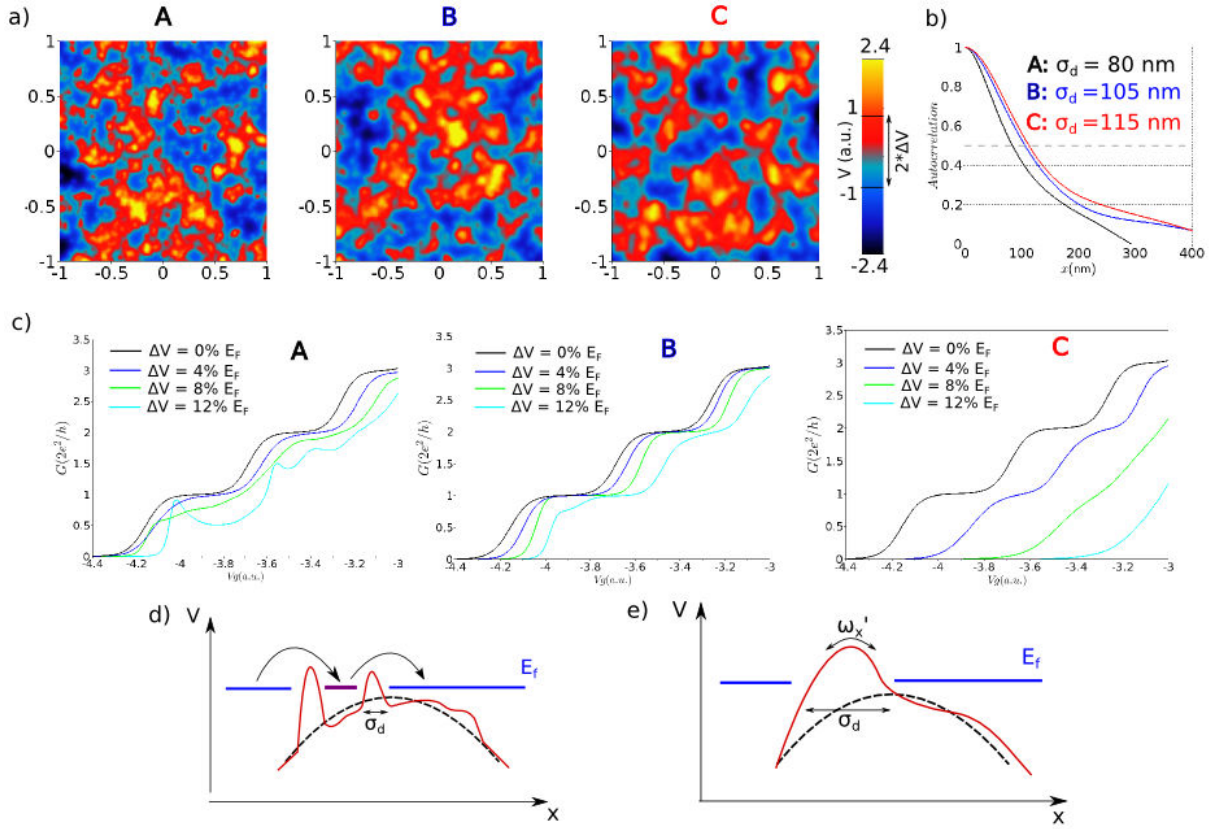


**Figure 1.15 Influence of disorder correlation length and FWHM:** a) 3 different types of disorder A, B and C corresponding to dopants respectively 30, 40 and 50 nm above the 2DEG. b) Autocorrelation function of these distributions, and corresponding correlation lengths  $\sigma_d$ . c) Effect of these different potential distributions on the QPC conductance for different FWHM ranging from 0 to 12% of  $E_f$ . d) Example of specific potential landscape along transport axis leading to resonant structures for small  $\sigma_d$ . e) Example of potential landscape for large  $\sigma_d$  leading to a change in  $\omega_x$ .

percent of  $E_f$ . A scheme of a possible corresponding mechanism is drawn on Fig.1.15d, where sharp barriers create Fabry-Pérot resonances at specific openings. This can also be seen as a shallow quantum dot forming in the channel.

Disorder correlated on larger length scales however tend to "smooth" the conductance steps, and this can be understood as follows: the typical length scale  $\sigma_d$  overcomes the curvature of the QPC saddle-point, changing  $\omega_x$  and smoothing the plateaus (configuration C Fig.1.15c, a corresponding scheme is drawn on Fig.1.15e). This is consistent with the extensive simulations presented in Ref.[21]. A global remark is that the disorder-induced deviations from the perfect case are configuration-dependent, and strongly depend on the exact potential fluctuations in the very center of the QPC, that governs its behavior. This study shows that a typical energy scale of 10% of  $E_f$  for the potential fluctuations already strongly affects the conductance steps. This is not surprising as this almost corresponds to 1 meV, which is comparable to the subbands spacing.

In the samples studied in this thesis, the effect of disorder was sometimes observed, but most QPCs showed rather clean conductance steps. Note that the same sample could

present really different curves from one cooldown to an other, and could exhibit clean conductance steps or some resonances. As an example, sample A is presented Fig.1.9b at a given cooldown, and shows smooth expected steps, and its characteristic after an other cooldown is shown Fig.1.14.

### 1.3 Conclusion

We have seen in this chapter the non-interacting picture of quantum point contacts. Designed out of high mobility 2DEG, QPCs exhibit conductance quantization. At low temperature, their conductance versus gate voltage shows quantized plateaus separated by smooth transitions. The smoothness on the transitions can be understood from the Buttiker adiabatic model, and arise from the finite length of QPCs. Non-adiabaticity can be studied thanks to numerical models but does not change much the characteristics. However, disorder due to the residual potential of ionized dopants can induce deviations from these clean models.

Before discussing the effect of interactions, that will also lead to deviations from the perfect case, we can summarize the effects of disorder.

First, as the way residual potential fluctuations affect the conductance are strongly dependent on the exact potential in the channel, resonances due to disorder are strongly affected by a displacement of the QPC in real space as presented Fig.1.14. These signatures can also change within the same sample for different cooldowns: the doping layer "freezes" below 120 K, giving a definite potential landscape at low temperature.

A second interesting point that is not shown here is that increasing temperature tends to smooth these resonances, as well as a small perpendicular magnetic field. This has been extensively studied experimentally [23] as well as theoretically [20], and we will see in the following how it differs from the fingerprints of the puzzling feature studied in this thesis: the 0.7 anomaly.

### 1.3. CONCLUSION

---

# Chapter 2

## Interactions effects in quantum point contacts

### Contents

---

<b>2.1</b>	<b>The 0.7 anomaly</b>	<b>40</b>
2.1.1	Temperature and magnetic field dependence	40
2.1.2	Bias dependence	41
2.1.3	Other experimental observations	43
<b>2.2</b>	<b>The zero bias anomaly</b>	<b>44</b>
2.2.1	First observation	44
2.2.2	Other experiments	45
2.2.3	Recent breakthrough	45
<b>2.3</b>	<b>Theoretical models of localization</b>	<b>46</b>
2.3.1	Mechanisms for conductance anomalies assuming localization	46
2.3.2	Spontaneous charge localization in numerical simulations	46
2.3.3	Perspectives : calculation of transport in presence of strong interactions	48

---

*There are a number of very interesting open problems even in the most simple case of a ballistic transport through a quantum point contact. 0.7 anomaly is a key word here.*

**Daniel Loss**

*This is [...] one of the stubbornest problems in mesoscopic physics: the phenomenology of a quantum point contact (QPC), which should be a simple ballistic channel but has long been found to show effects that appear to come from spin and many-body interactions.*

**Anonymous referee**

## Introduction

The previous section has shown that despite its apparent simplicity a real QPC exhibits complex features, even in a non-interacting picture. However, from the very first realizations of QPCs, additional features have been observed, that cannot be explained within a single-particle framework. The two main features assumed to arise from electron-electron interactions are a shoulder around  $0.7*2e^2/h$ , called the 0.7 anomaly, and a zero bias peak emerging at low temperature in the differential conductance: the zero bias anomaly (ZBA).

This Chapter briefly reviews part of the huge amount of experimental and theoretical works on these subjects, up to very recent results.

## 2.1 The 0.7 anomaly

### 2.1.1 Temperature and magnetic field dependence

The most famous deviation from the expected non-interacting behavior is the so-called “0.7 anomaly”, an additional plateau around  $0.7*2e^2/h$ .

Though it was first observed in pioneers experiments in 1988[4, 11, 23, 24], this structure has waited until 1996 to be systematically studied in the Cavendish laboratory (Cambridge) [25]. This very first study of the 0.7 structure already achieved some major breakthrough in this field, suggesting that it arises from electron-electron interactions, and that it is somehow related to spin physics.

The authors reported that this structure was observed in most QPCs they measured, and showed two main remarkable behaviors:

- This 0.7 “plateau“ continuously evolves down to  $0.5*2e^2/h$  in parallel magnetic field, which is the signature of Zeeman-split subbands. (Fig.2.1a)
- It is more pronounced as the temperature is *increased*, unlike disorder-induced resonant structures discussed in the previous chapter. (Fig.2.1b)

Under a strong parallel magnetic field, the QPC conductance curve  $G(V_g)$  exhibits half plateaus as well as integer ones, because the 1D subbands are no longer spin degenerate. This is due to a Zeeman term in the hamiltonian  $H_Z = g\mu_B\vec{B}\cdot\vec{S}/\hbar$ , that unbalances spin up and spin down subbands in energy. Here  $\mu_B$  is the Bohr magneton ( $\mu_B = e\hbar/2m^*$ ),  $g$  is the Landé factor (which equals 2 for free electrons, and -0.44 for bulk GaAs), and  $\vec{S}$  is the electron spin operator. The fact that the 0.7 anomaly evolves down to the half plateau  $e^2/h$  (Fig.2.1a) suggests that it is related to the electron spin, and the author even proposed this effect to be a signature of spontaneous spin polarization occurring in the QPC, even at zero magnetic field. In this study, they also reported that the effective  $g$  factor strongly increases for the lowest subbands, and attributed this effect to electron-electron interactions [26], that are stronger at low electronic density.

The second major experimental fact reported in this study is that the 0.7 anomaly is more prominent at *higher* temperatures, even being the last remaining feature when the quantized steps have vanished. Though the authors did not understand this surprising behavior

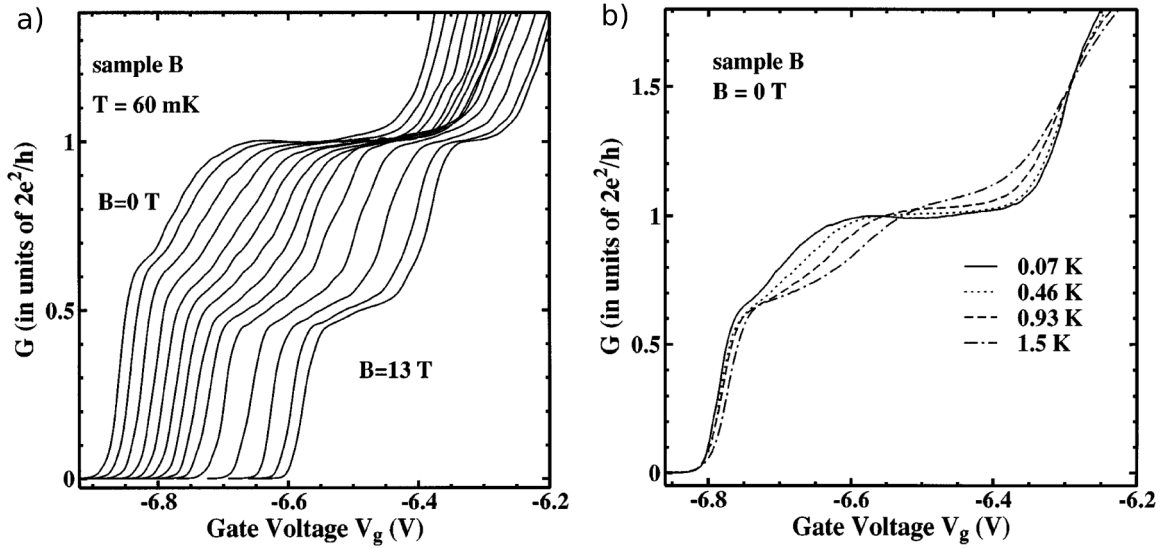


**Figure 2.1** *First systematic measurements on the 0.7 structure: a) Evolution of the 0.7 structure under a parallel magnetic field from 0 to 11T by steps of 1T. The measurement is performed at 60 mK. b) Evolution of the 0.7 structure for different temperatures (without magnetic field). Adapted from Ref.[25]*

at this point, they aptly presented this fact as ruling out possible impurities-induced effects, as this would lead to resonances that tend to disappear with increasing temperature. Another point that definitely discards disorder as responsible for this conductance anomaly is that this feature is insensitive to a lateral displacement of the QPC by playing on the voltage difference between the two gates [27]. In this way, the residual disordered potential in the channel is changed (see section 1.2.6), and the fact that the 0.7 anomaly is almost insensitive to these changes suggests an intrinsic effect.

### 2.1.2 Bias dependence

The response of the 0.7 anomaly to a DC source-drain bias is surprising, and gives additional information on the possible subbands structure that can lead to this non-integer plateau. A typical non linear behavior of a QPC below the first plateau is presented in Fig.2.2 taken from Ref.[28].

In this spectroscopy, one can see that under a small DC bias voltage, the 0.7 anomaly evolves to a much pronounced plateau around  $\sim 0.85 \times 2e^2/h$ . To explain the surprising bias dependence of the 0.7 anomaly, the authors proposed a phenomenological model including an anomalous subband, separated from the normal 1D ones by an energy gap  $\Delta$  that would vary with the QPC opening. They showed (Fig.2.2 c) that the conductance around the 0.7 anomaly grows exponentially with decreasing temperature, associated with a characteristic activation temperature  $T_a$ . According to their measurements and analysis,  $T_a$  strongly depends on the QPC opening, ranging from hundred mK to almost 15K when approaching the perfect transmission first mode (Fig.2.2 d). They repeated this analysis on 6 different samples, and found that the energy gap  $\Delta$  is simply connected to the activation temperature  $T_a$  by the simple relation  $\Delta = k_B T_a$ .

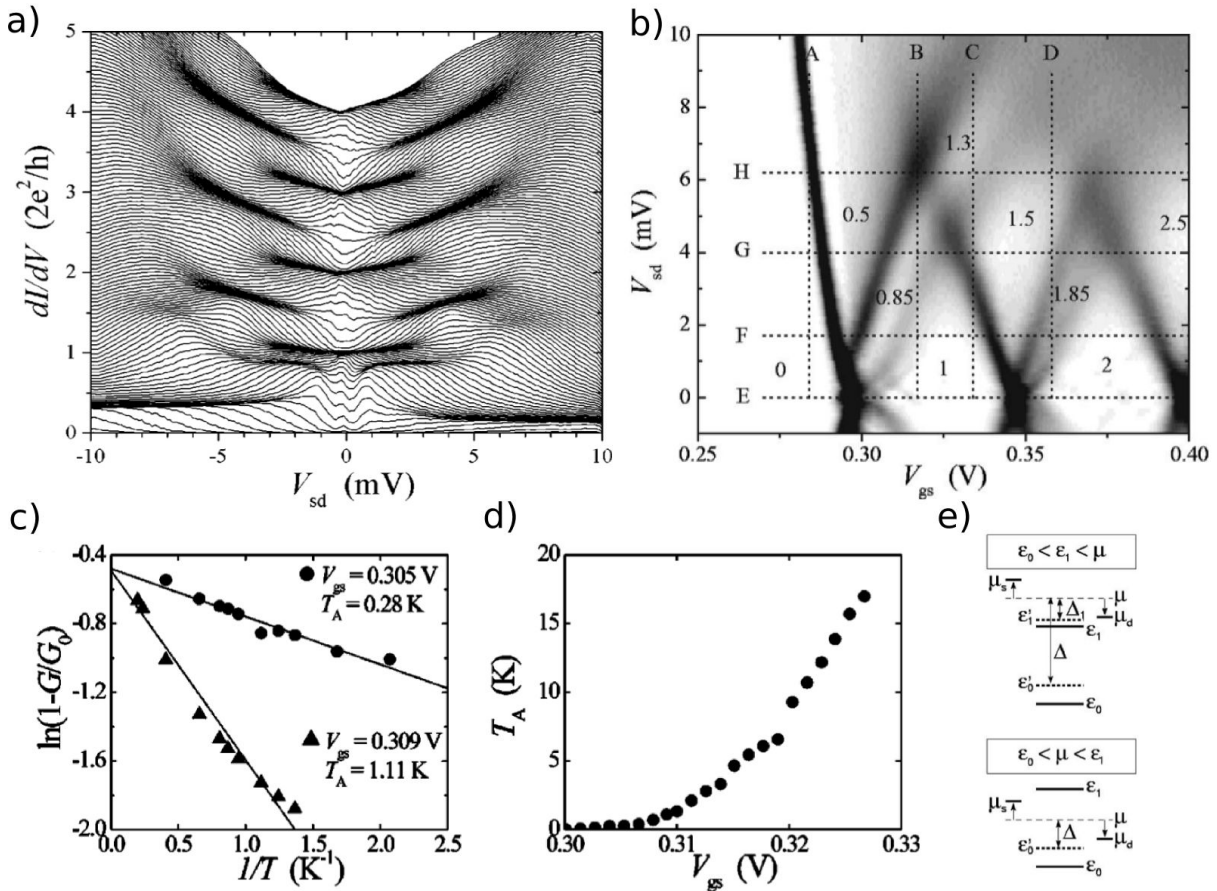


**Figure 2.2** *Bias and temperature dependence of the 0.7 anomaly:* a) Cascade plot  $G(V_{ds})$  for different  $V_g$  measured at 300 mK applying an AC voltage of 50  $\mu$ V. The 0.7 anomaly is more prominent with source-drain and evolves to around  $0.8*2e^2/h$ . b) Corresponding transconductance plot  $\partial G/\partial V_{ds}$  with labeled normal and anomalous plateaus. c) Temperature evolution of the conductance below the first plateau, for two different QPC openings. d) Activation temperature  $T_a$ , assuming an "Arrhenius" behavior, as a function of gate voltage below the first plateau. e) Scheme of the normal and anomalous subbands for two different openings. All these figures are extracted from [28]

A phenomenological model is detailed in [29], that accounts for several of these experimental observations. It suggests a spin unbalance due to electron-electron interactions effects, that lead to two different 1D subband for the two spin species, separated by a gap that would depend on the chemical potential ( $\mu$ ). Under a well chosen (phenomenological) evolution of this gap with  $\mu$ , experimental data regarding temperature, bias and magnetic field of the 0.7 anomaly could be reproduced. However, no microscopic description of the phenomenon leading to this spin gap was proposed. Note that this interpretation assumes partial spin polarization in the channel.

### 2.1.3 Other experimental observations

These conductance anomalies have been extensively studied over the last 20 years by different experimental approaches, and I will briefly cite a few results. An impressive and detailed review can be found in Ref.[30], that details a quasi-exhaustive list of the state-of-the-art on this subject until 2011.

#### 2.1.3.1 Shot noise

Two beautiful experiments have been performed to measure the shot noise at the 0.7 anomaly [31, 32]. The shot noise is a very powerful technique, that brings interesting information on the different transmission probabilities of electrons through different modes, and is really challenging to measure. Unlike the differential conductance that only brings information on the total transmission, it gives access to the statistics of the electrons crossing a mesoscopic device. These two experiments reported a reduction of the shot noise at the 0.7 anomaly, interpreted as an evidence for two different conduction channels contributing in this regime. This can therefore be interpreted as a support for the spin-gap model [29].

#### 2.1.3.2 Thermopower

Another experimentally accessible quantity is the thermopower of a mesoscopic device. This quantity, also called the Seebeck coefficient, traduces the way a (thermoelectric) voltage sets up across a device when source and drain are set to different temperatures. Under appropriate assumptions, the thermopower  $S$  of a mesoscopic device is simply related to its conductance by the Mott formula:  $S = \frac{\pi k_B^2 T}{3e} \frac{1}{G} \frac{\partial G}{\partial \mu}$ . One of these assumptions is to neglect the role of electron-electron interactions in the device conductance. The study of the thermopower at the 0.7 structure [33], revealed a breakdown of the Mott's law in this regime, reinforcing the crucial role of the interactions in this anomaly. The thermopower of QPCs is extensively discussed in Chapter 7, where our measurements are presented.

#### 2.1.3.3 Scanning gate microscopy

The main experimental tool that has been used in this thesis is a scanning gate microscope. It consists in a low temperature atomic force microscope (AFM), with a charged metallic tip used to affect transport in nanostructures thanks to an electrostatic effect. The conductance of the device is measured while this tip is used as a movable gate to affect transport. A full description and history of this extremely powerful technique is given in Chapter 3. Concerning the 0.7 anomaly, this technique has allowed partial control of this feature, and revealed the appearance of an additional plateau at  $e^2/h$ , interpreted by the authors as a signature for spontaneous spin polarization occurring in the channel [34].

A more recent investigation of the 0.7 anomaly with this technique has confirmed that the 0.7 anomaly was an intrinsic phenomenon that happens even in very clean QPCs, independently of the disordered landscape [35].

## 2.2 The zero bias anomaly

### 2.2.1 First observation

At very low temperature, the 0.7 anomaly shades off and the linear conductance curve shows no more anomaly. This phenomenon was studied in detail in the (impressive) thesis of Sarah Cronenwett [36] in the Harvard group, under the supervision of Charlie Marcus and David Goldhaber-Gordon. The main result of her work concerning the 0.7 anomaly [37] is summarized in Fig.2.3. In this paper, a clear correspondence is made between the low-temperature fate of the 0.7 anomaly and the emergence of a zero bias peak in the non-linear source-drain characteristic of a QPC at low temperature (Fig.2.3a).

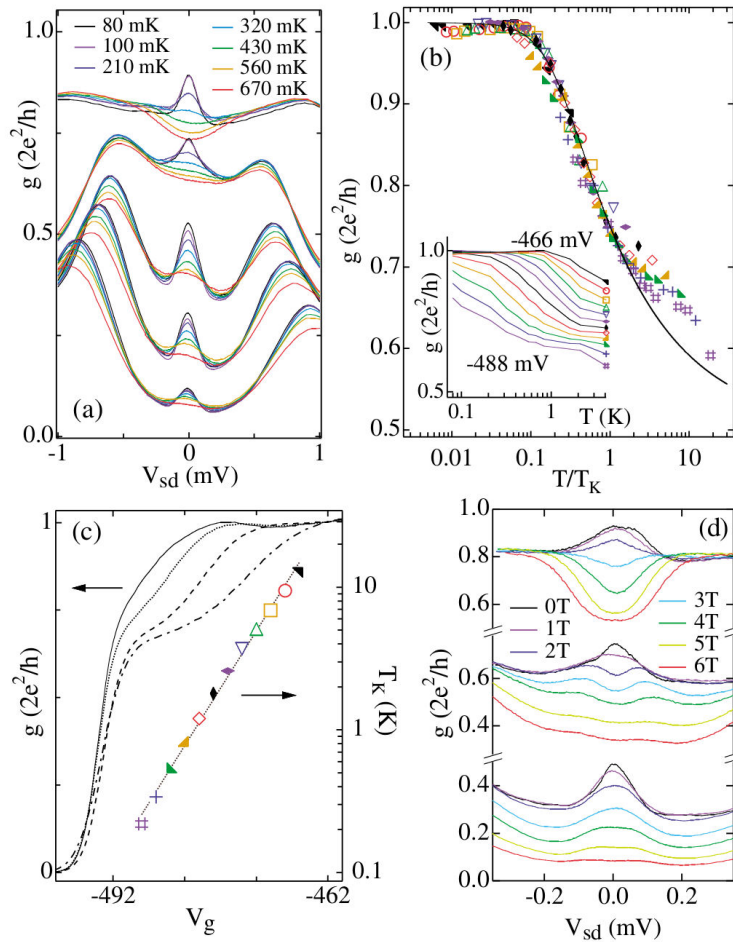


**Figure 2.3 Possible Kondo physics in QPCs:** a) Traces  $G(V_{ds})$  for different QPC openings below the first plateau, at different temperatures. b) Scaling of the conductance as a function of temperature for different gate voltages. All the curves fall down on a modified Kondo form (black line). c) Linear conductance curves  $G(V_g)$  at different temperatures and Kondo temperatures extracted from b) for different openings. d) Evolution of the ZBA with magnetic field at different openings. These plots are adapted from Ref.[37].

This peak has been shown to scale as a modified form of the Kondo effect, that emerges when a localized spin is screened by the surrounding conduction electrons at low enough

temperature. This somehow defines a starting point for a microscopic description of the low-density regime of QPCs, and redefines the activation temperature proposed in Ref.[28] as an effective Kondo temperature  $T_k$ . Detailed discussion of the Kondo effect and of the work by S.M.Cronenwett et al. is done in Chapters 5 and 6.

This beautiful experimental work gives an explanation for this zero bias anomaly (ZBA) based on the existence of a localized spin in the QPC channel.

## 2.2.2 Other experiments

Since the work of Cronenwett et al., some studies have revealed the existence of bound states in QPCs, and a few compared the zero bias anomaly in QPCs with the Kondo effect in quantum dots.

In Ref.[38], the authors built a sample with two nearby QPCs, one tuned below the first plateau and one used as a sensitive detector. Around the pinch-off of the first QPC, they observed a peak in the conductance of the second QPC, interpreted as a signature of the formation of a bound state in the first QPC, thereby supporting the interpretation of the ZBA as due to a localized state.

In Ref.[39], Sfigakis et al. analyzed and discussed the difference between the 0.7 and zero-bias anomalies. They showed that these two effects are not completely equivalent, but they did not claim that these two effects are independent phenomena. They also conclude that bound states are probably present in most quantum wires.

In Ref.[40] Sarkozy et al. investigated the evolution of the ZBA from  $2e^2/h$  down to very low conductance and observed a non-constant Zeeman splitting under magnetic field. Their measurements also reveal a different behavior of the ZBA above and below  $0.7 \times 2e^2/h$ , both for the height and the width of the peak. They interpreted their result as discarding spontaneous spin polarization in QPC and one-dimensional Kondo physics.

In Ref.[41], Ren et al. carried out a similar investigation of the ZBA at very low conductance. They reported that the zero bias peak height in the low conductance regime (down to  $10^{-4} \times 2e^2/h$ ) is proportional to the average conductance and proposed that at low conductance the localized state is split into two localized states separated by the central barrier.

Based on these studies, the Zero bias anomaly appears to be different from the Kondo effect known in quantum dots, though it shares some similar features. We will discuss in details these differences in Chapter 6.

## 2.2.3 Recent breakthrough

More recently, this zero bias peak was found to be split for some gate voltages[9]. This splitting was observed in many devices, and successive splittings have been reported while increasing the channel length in specific samples with several metallic gates. These split peaks (see Fig.5.4) have been shown to scale as non-equilibrium Kondo effect versus temperature and magnetic field, revealing that not only a single spin could localize in QPCs, but an odd or even number of electrons depending on the QPC geometry. This experiment and the comparison with our results are extensively discussed in Chapter 5.

Both their and our experiments strongly support the scenario of a spontaneous charge

localization in QPCs, as compared with earlier models involving spontaneous spin polarization of the subbands [29, 25] which are not compatible with the observed Kondo effects. Finally, as there is no system more open than a quantum point contact, localization in a QPC is not obvious (keeping in mind that disorder has been ruled out to explain the 0.7 anomaly and the ZBA), but has received extensive theoretical support that is discussed in the following section.

## 2.3 Theoretical models of localization

Over the past 20 years, many theoretical approaches have attempted to explain the 0.7 anomaly, but none has fully convinced the whole community yet. I will focus on those who predict a spontaneous localization channel, as they are the only ones that are compatible with the most recent experiments (I will therefore skip those based on other microscopic models like scattering by phonons [42] or plasmons [43]).

### 2.3.1 Mechanisms for conductance anomalies assuming localization

Several proposals attempted to explain conductance anomalies in QPCs relying on the possible existence of a localized state in the channel. Based on this assumption, Yigal Meir proposed a mechanism including a localized spin [44, 45], that would affect transport at high temperature and lead to Kondo effect at low temperature, accounting for the ZBA. The localization of this spin was justified by a numerical simulation discussed in the next section.

Some other proposals relied on the existence of a Wigner crystal [46, 47, 48], giving different explanations. Wigner crystallization is a dramatic effect that can occur in low density electronic systems, that lead electrons to form an ordered lattice when the Coulomb repulsion overcomes the kinetic energy [49]. It is extensively discussed in Chapter 5, and I just briefly discuss here some proposals assuming such a 1D Wigner crystal to form in QPCs. Whereas Ref.[48] proposed that ferromagnetic correlations exist in this electron chain giving a spin polarized state, Ref.[46] relies on the fact that in a 1D Wigner crystal, spin and charge excitations are decoupled. These two type of excitations are not affected in the same way by temperature, possibly explaining the strange behavior of the 0.7 anomaly with temperature. However, this picture does not account for the ZBA as far as the investigation has been pushed [50]. Finally, Ref.[47] proposed an explanation based on charge density waves, which are precursors of Wigner crystallization, and the author demonstrate that this leads to conductance anomalies below the first plateau similar to the 0.7 anomaly, though the temperature dependence was not discussed.

### 2.3.2 Spontaneous charge localization in numerical simulations

The way some electrons could localize in a QPC is highly debated regarding the fundamentally open character of these devices. In a pure 1D system, it is well accepted that electrons will tend to form a Wigner crystal as soon as the density is low enough, though the exact critical density to reach this crystallization is intensively debated and seems

to depend on the confining potential [51]. However the case of a QPC is tricky because it is not a pure 1D system. It continuously evolves from 2D reservoirs to a quasi-1D channel, making it difficult to treat theoretically and numerically. In addition, to reach such a dramatic effect of the interactions, they shall not be treated perturbatively, pushing further the challenge to compute this type of system.

Localization in inhomogeneous 1D wires has nevertheless been shown using different numerical methods. Though I do not fully understand the implications of all these different methods, I will try to briefly summarize the main results.

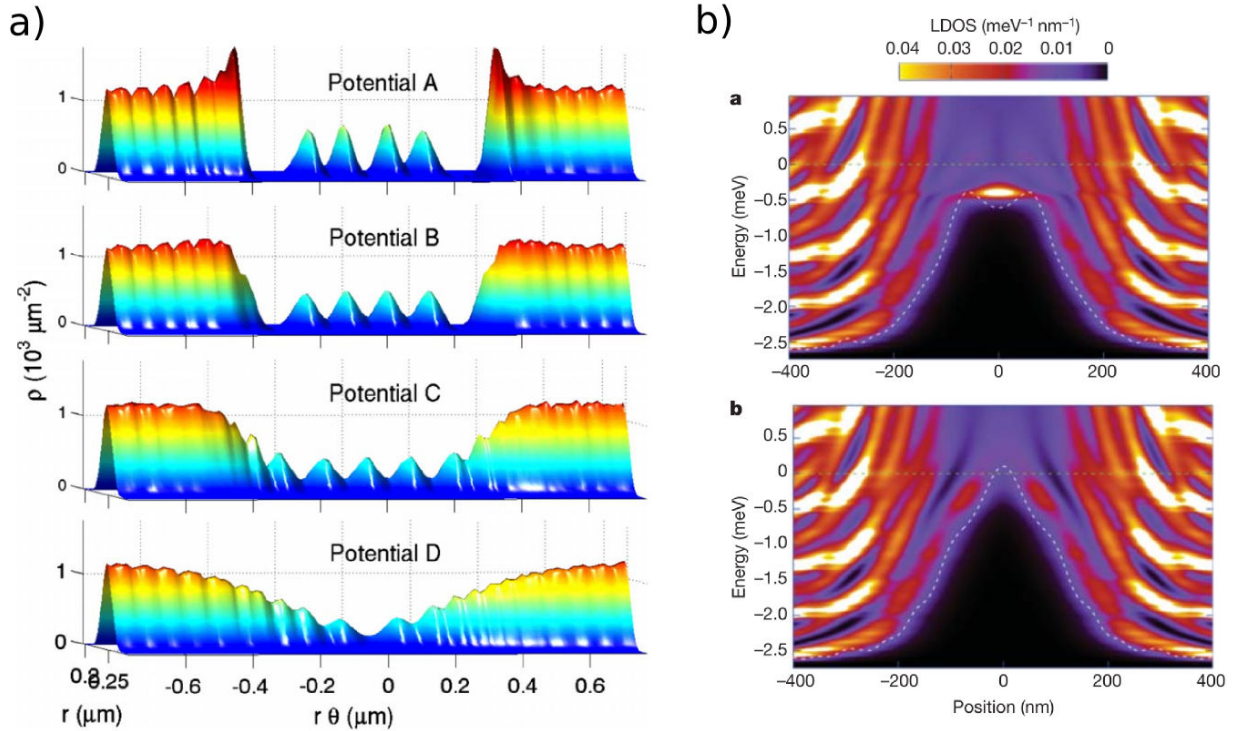


**Figure 2.4** *Two different calculations suggesting localization:* a) Result of Quantum Monte-Carlo simulations on a 1D ring containing a low-density region, for different shapes of the constriction potential. Adapted from Ref.[52]. b) Results of spin-density functional theory calculations, representing the local density of states (LDOS) along the wire for the two different spin species. Adapted from Ref.[45].

In Ref.[47], the author performed 1D Hartree-Fock calculations and showed that one or more charges could separate from the leads in the low-density region. This study has then been extended in Ref.[53] using two different Hartree-Fock approaches, confirming this result.

Yigal Meir performed spin-density functional theory (SDFT) and also found that 1 to 3 electrons could localize in a QPC due to electron interactions[44, 45] (see Fig.2.4b). This work has then been extended to show that up to 7 electrons can localize [9], adjacent electrons carrying opposite spins. The main criticism about these calculations (as far as I understand) is that SDFT is based on an artificial spin symmetry breaking, that unbalances the two spin species, and one has then to take the limit of no asymmetry. This is sometimes criticized as artificially favoring the localization of a single spin.

In Ref.[51], calculations based on Quantum Monte-Carlo simulations showed that in purely 1D wires localization occurs at low enough density, discussing the required critical density.

Quantum Monte-Carlo simulations were also performed in an inhomogeneous 1D wire [52], and suggest that a few electrons crystal can form in the low-density region (see Fig.2.4a). Electron spins in this chain have been shown to be coupled antiferromagnetically, which is consistent with the results of Ref.[45]. Finally, using a numerical density matrix renormalization group (DMRG) approach, the authors of Ref.[54] showed that there is a smooth transition towards Wigner crystallization in 1D, as the density is reduced.

All those different numerical methods suggest that spontaneous localization of electrons can occur in QPCs, even sometimes suggesting the formation of a small 1D Wigner crystal, when the interactions are dominant at low density. Many questions then remain. One can wonder first if this localization really occurs in the experiment, and if so which form it takes, how many charges and spins are localized, and how they are coupled to the leads. It is also possible that under given conditions this small electron chain exhibits a transition toward a zig-zag configuration, as suggested theoretically [55] and experimentally [56], where the ground state would become ferromagnetic. Beginning of answers to these questions are proposed in Chapter 5 of this thesis, but this does not answer the ultimate question of how electrons flow through this exotic configuration.

#### 2.3.3 Perspectives : calculation of transport in presence of strong interactions

It appears a tough problem to treat 1D electronic transport when interactions are taken into account. In one dimension under strong interactions, the usual Fermi liquid description of the excitations no longer holds, which complicates the problem of transport. The excitations of interacting 1D systems are no longer fermionic, and charge and spin excitations have to be considered as separate bosonic (collective) excitations. A step in the treatment of transport in interacting inhomogeneous 1D system has recently been made in Ref.[57], that pretends to explain *all* the experimental observations concerning the conductance anomalies in QPCs. The argument of the authors is based on the Van Hove singularity, a singularity in the 1D electronic density of states at the bottom of the 1D subbands. They used two impressively developed numerical methods to justify that this well known Van-Hove singularity could be responsible for the 0.7 anomaly, when interactions are taken into account. In this 1D model, the interactions are treated perturbatively and do not lead to dramatic localization in the QPC compared to some other studies discussed above. This study and the experimental one discussed above[9] supporting localization of a definite number of electrons in QPC were published back to back in the *Nature* journal, though they do not seem compatible with each other.

Our point of view on this work is that they reach a wrong conclusion because they could not push the interaction parameter high enough to obtain the regime of the conductance anomalies as they are observed in real experiments. Their conclusion on the absence of localization is therefore not justified. Note that the simulations presented in the previous section showing localization can not calculate transport properties. This question is therefore still an open problem.

# Chapter 3

## Scanning Gate Microscopy

### Contents

---

<b>3.1 Scanning gate microscopy</b> . . . . .	<b>50</b>
3.1.1 Introduction . . . . .	50
3.1.2 Branches and interferences . . . . .	51
3.1.3 Two types of interferences . . . . .	53
<b>3.2 Our scanning gate microscopes</b> . . . . .	<b>54</b>
3.2.1 Low temperature atomic force microscopy . . . . .	54
3.2.2 The microscopes . . . . .	54
3.2.3 The conductive tips . . . . .	55
3.2.4 Imaging quantum transport . . . . .	55
<b>3.3 Interferences</b> . . . . .	<b>56</b>
3.3.1 SGM images on the plateau . . . . .	56
3.3.2 Dependence on QPC opening . . . . .	58
3.3.3 Temperature dependence . . . . .	61
3.3.4 Non linear behavior . . . . .	63
<b>3.4 Tip potential</b> . . . . .	<b>65</b>
3.4.1 Estimating the shape of the tip tail . . . . .	65
3.4.2 What is the size of the depleted region? . . . . .	66
3.4.3 Electrostatic simulations . . . . .	67
<b>3.5 Modeling scanning gate microscopy</b> . . . . .	<b>68</b>

---

## Introduction

In this Chapter, we present the central technique used in this thesis: scanning gate microscopy (SGM). We will briefly review the history of its invention, and the fields in which this tool have proved to be really useful since. We then present in a second time results obtained on the ultra-low temperature SGM in Louvain-La-Neuve, Belgium, on our QPCs. We will concentrate in this chapter on the SGM images obtained on the first conductance plateau, and particularly on the interferences that we observe on these images. We also propose a method to characterize the potential created by the polarized tip of the microscope and present a numerical way of modeling SGM experiments using Kwant[8].

### 3.1 Scanning gate microscopy

#### 3.1.1 Introduction

Among the different methods used to investigate quantum transport, there is one called scanning gate microscopy (SGM), that is central in this thesis. It consists of disturbing electrostatically a device thanks to the polarized metallic tip of an atomic force microscope (AFM), and recording the changes in the device's conductance induced by the tip potential.

This technique has been developed in the middle of the 90's in Harvard, and a first step has been achieved in 1996, demonstrating a local answer by scanning a polarized tip above a quantum point contact [58](Fig.3.1a). After years of improvement in the same group, this technique has struck the community, demonstrating both the possibility to image in real space the wave-functions of electrons coming out of a QPC[59] (Fig.3.1b), as well as branched flow of electrons in a disordered potential decorated with electronic interferences[60](Fig.3.1c).

Since these first impressive breakthrough, many groups have developed this technique, and built low temperature AFM to perform SGM. Scanning gate microscopy has been applied to many different systems. It is particularly adapted to devices made out of 2DEG, because direct tunneling from the 2DEG to the tip is prevented by the insulating AlGaAs layer, forbidding for example scanning tunneling microscopy (STM). Various experiments have been realized on these heterostructures, including quantum point contacts in zero [61], small [62] and high [63] magnetic field, quantum dots containing a few [64, 65] or one electron [66], quantum rings [67, 68] and various interferometers [69, 70].

Concerning QPCs in zero magnetic field, a long road has already been achieved in the various groups using this technique. Initial works concerned mainly single-particle effects, such as imaging wave-functions of different modes [59], and investigating the role of disorder in the observed branched flow [71, 60] as well as in the interferences [70, 61]. A few theoretical investigations following these experiments, tried to understand what is measured using this technique, and investigating for example the formation of the interferences and the way they shall decrease with distance [72, 73], the role of temperature [74], the surprising stability of the observed branched flow [75], and non-linear effects [76]. Different experiments have more recently turned on many-body effects in QPCs, investi-

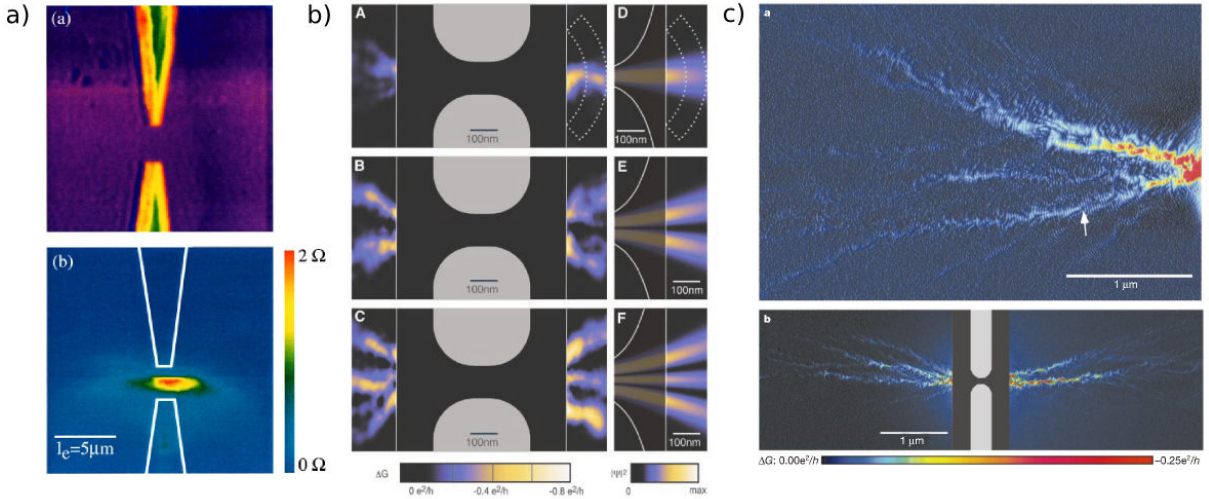


**Figure 3.1** *First scanning gate microscopy images:* a) Up: images of the gates recorded by electric force microscopy (EFM), down: QPC conductance with respect to tip position. A clear local answer is seen when the tip is above the constriction. Adapted from [58]. b) High resolution SGM images showing the wave functions of the electrons for the three first modes of a QPC. Left panel up to down: the QPC is tuned respectively to the 1st, 2nd and 3rd mode. The right panel shows simulations of the wave-function square modulus for these 3 situations. Adapted from [59]. c) SGM images of the branched electronic flow. Interference fringes spaced by  $\lambda_F/2$  are clearly seen on the branches. Adapted from [60].

gating electron-electron scattering in the leads [77], and the 0.7 anomaly [?, 35]. Different possibilities to explore many-body phenomenon by non-local effects using SGM have also been a matter of theoretical investigations [78, 79].

### 3.1.2 Branches and interferences

In the years following the invention of this technique, the Harvard's group carried out a detailed investigation of the main features observed in SGM images on a QPC. The thesis of Mark Topinka[80] and Brian Leroy[81], under the supervision of Robert Westervelt, revealed several interesting characteristics concerning mainly the branches of the electron flow and the interferences. In parallel with these experimental investigations, interesting numerical calculations have been performed also in Harvard, detailed in the thesis of Scot Shaw[82] in Heller's group, that brought some support to understand the precise role of disorder in both branches and interferences.

The main features of these work can be summarized as follows. It is first important to note that all these pioneer measurements were performed at temperatures of 1.7K and 4.2K. The first surprising observation was that fringes were observed up to a few microns away from the QPC. These fringes appear as parallel ripples, mainly in the branches of the electron flow and perpendicular to it. They are visible for sufficiently negative tip voltages, and when the tip is really close to the sample surface (a few tens of nanometers). As they are spaced by  $\lambda_F/2$ , they were attributed to electronic interferences.

The fact that these interferences were still visible microns away from the QPC was completely unexpected at these temperatures. Indeed, one would expect at these temperatures that a broad range of wavelength contribute to these interferences, blurring them on a few hundreds of nanometers as discussed in section 3.3.3.2. The interferences were therefore suggested to occur not directly between the tip-induced depletion region and the QPC but rather in small cavities between the tip and hard-scatterers due to disorder in the 2DEG. To support this statement, the Harvard group designed reflector gates in front of QPCs and showed that these interferences observed at high temperature were induced by hard scatterer in the 2DEG[70]. Here hard scatterer denotes local potential fluctuations important enough to backscatter the electrons, in contrast with background random potential fluctuations whose standard deviations is small compared to  $E_f$ .

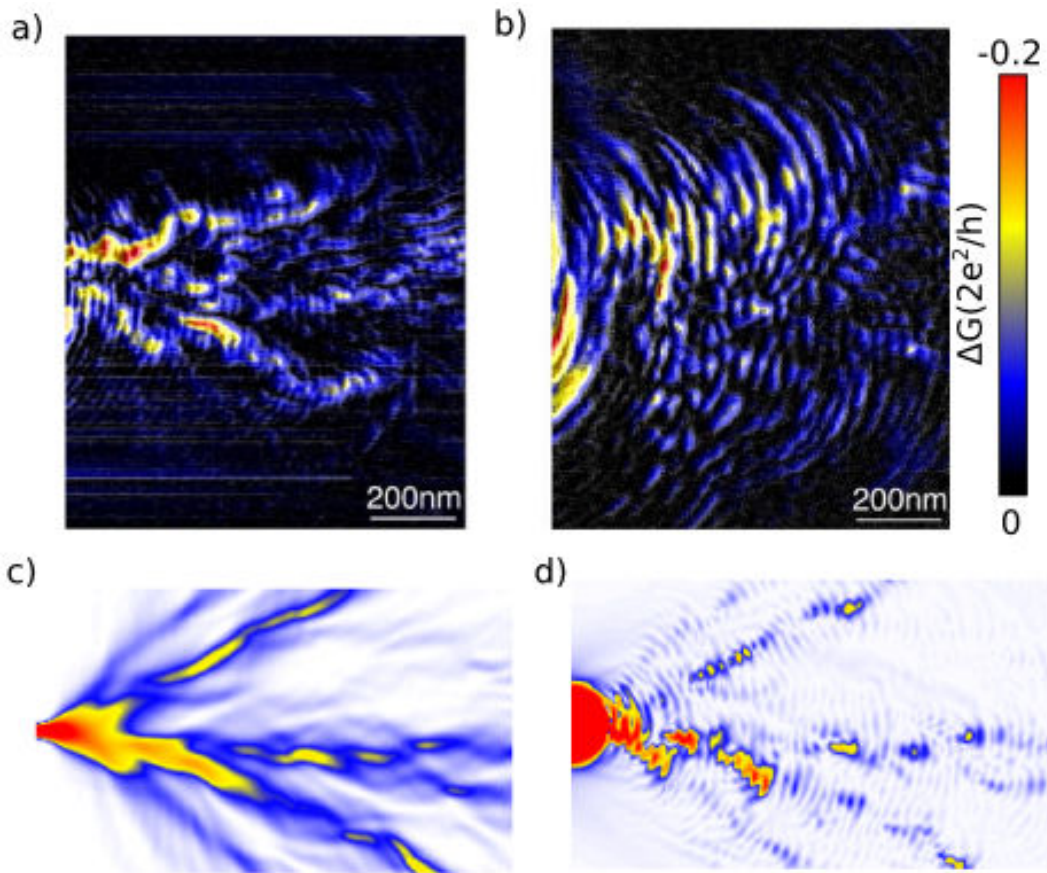


**Figure 3.2 Results from the Harvard group:** a) SGM image in front of a QPC (the QPC is on the left of the image) for a given electronic density. b) Same image for a lower density controlled by a backgate voltage. Adapted from [81] c) Simulated out of equilibrium local density of states in presence of a smooth disordered potential. d) Simulated conductance as a function of a scatterer position for the same disordered potential. Adapted from [82]

Moreover, by the means of a backgate used to control the bulk electronic density, the authors demonstrated that the interferences were spaced by half the bulk Fermi wavelength far away from the QPC (see Fig.3.2 and Ref.[81]). In parallel, numerical investi-

gation demonstrated that this hypothesis of interferences occurring between the tip and hard scatterers is reasonable and essentially explains the spatial repartition of this type of fringes and their temperature robustness[82]. This numerical investigation also revealed that the branches observed in the experiment were strongly correlated to the preferential electron trajectories flowing in the 2DEG reservoirs through the smooth disordered potential landscape in absence of the tip (see Fig.3.2c and d).

### 3.1.3 Two types of interferences

The SGM technique has then been developed in Stanford, under the supervision of David Goldhaber-Gordon, with the expertise of Mark Topinka. In this team, scanning gate microscopy on QPCs made out of GaAs 2DEG of different mobilities brought some new insights on the observed interferences. First, a study at 4.2K showed that the interferences disappear in layers of mobility greater than  $10^6 \text{cm}^2/\text{V.s}$ , and the electronic flow exhibits less branches[71]. This result therefore confirmed that the originally observed interferences were strongly assisted by disorder.

In the same group, after the development of a scanning gate microscope in a  $^3\text{He}$  system, it has been shown that a new type of interference fringes appear at lower temperatures (around 350mK) even in samples of mobility  $4.10^6 \text{cm}^2/\text{V.s}$ [83]. These fringes are not present at 1.7K and are attributed to a mechanism similar to a ‘‘Fabry-Pérot’’ interferometer occurring directly between the depleted regions below the tip and below the split-gate. (Fig.3.3).

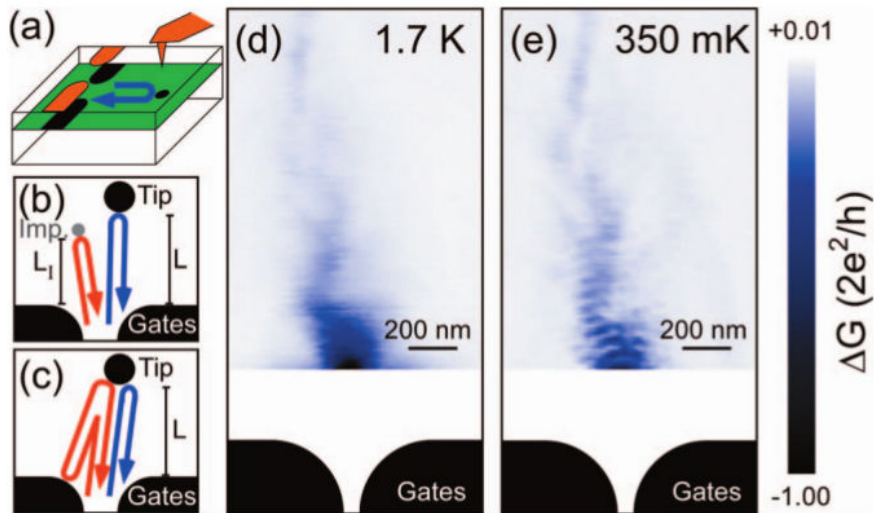


**Figure 3.3 Results from the Stanford group:** a) Schematics of the experiment. b) and c) Two possible mechanisms to explain this new type of interference fringes. d) and e) SGM images on a high mobility sample ( $4.10^6 \text{cm}^2/\text{V.s}$ ) at temperatures of 1.7 K and 350 mK. Adapted from Ref.[83].

Finally, the development of a scanning gate microscope in Cambridge in a dilution fridge operating at a base temperature of 150 mK, allowed the investigation of the many-body effects occurring below the first plateau thanks to this technique[?]. The authors

defined electrostatically a QPC by erasable electrostatic lithography (ELL)[84]. It consists in depositing negative charges on the sample surface thanks to the charged tip, to repel the electrons underneath. They defined in this way a QPC that could then be opened and closed at will by placing the tip above the defined constriction, and applying a variable negative voltage on it. The authors reported the appearance of an additional plateau at  $0.5 \times 2e^2/h$  as well as the 0.7 anomaly, and interpreted their results as a possible spontaneous spin polarization in the QPC.

## 3.2 Our scanning gate microscopes

### 3.2.1 Low temperature atomic force microscopy

The first challenge in the practical realization of SGM is the construction of a low temperature atomic force microscope (AFM). This has to be achieved in order to place the tip above the desired part of the sample. To do so, conventional AFMs are often based on the deflections of a cantilever, measured by a laser beam deflection. This detection technique is forbidden in the case of high mobility GaAs 2DEG because light creates lots of electron-hole pairs that strongly affect transport and sometimes even induce leakages from the gates to the 2DEG. The widely used technique to address this problem is to glue a tip at the end of a quartz tuning fork. The tuning fork is then excited at its resonance frequency which is tracked continuously by a phase lock loop (PLL). By the means of motors and a scanner, the tip is approached towards the surface. The tip approaches the sample step by step, in the following sequence: the Z-scanner is extended to its maximal range ( $4 \mu m$  at low temperature), retracted if the tip does not touch the sample, a Z-motor step (about  $1 \mu m$ ) is then made, and this operation is repeated until the tip touches the surface (this operation can take around one hour). When the tip interacts with the substrate, the tuning fork resonance is shifted because of the tip/sample interaction force. The PLL keeps the TF on resonance and measures the applied frequency shift. A feedback loop is then used to keep this frequency shift constant (some hundreds of mHz), by adjusting the height with the Z-scanner, while the tip is moved in the horizontal plane with the X- and Y-scanners to make a topographic image.

This allows to perform topography without the use of a laser beam. Measuring topography as well as SGM images is eased by the use of Nanonis commercial soft and hardwares, offering a user-friendly interface to perform various scanning probe microscopy techniques.

### 3.2.2 The microscopes

Two different scanning gate microscopes were used during this thesis. One based in Institut Néel, in Grenoble, operating at 4K in liquid Helium, and one in IMCN, in Louvain-la-Neuve (Belgium), embedded in a dilution fridge, at a base temperature of 20mK.

The setup in Grenoble has been redesigned at the beginning of this thesis, to reach a better stability during cooldowns. Indeed, the tip is aligned with the sample at room temperature, but the whole setup moves while cooling down. Unfortunately, the base temperature of 4.2 K in this setup appeared to be too high to study quantum point contacts, because thermal broadening does not allow to see conductance steps at this

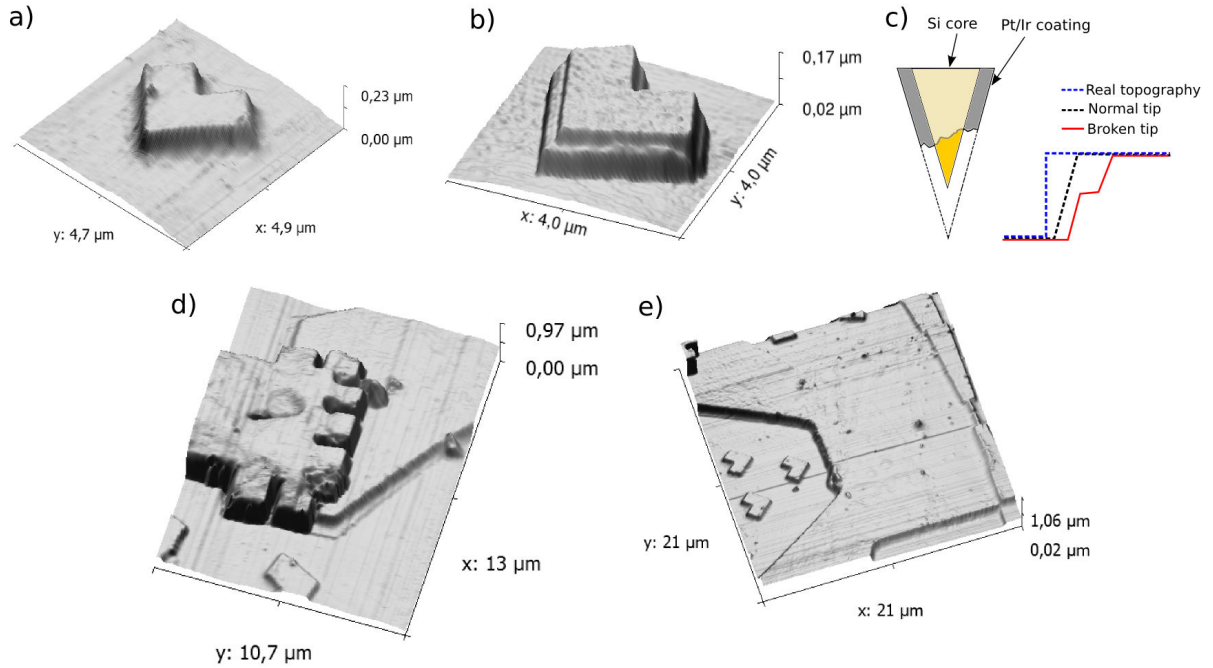


**Figure 3.4 Topography at low temperature:** a) Topography of a marker with a clean tip. b) with a partially broken tip. c) Schematics of a broken tip, where the coating has been broken, possibly leading to image b). The different apparent topographies of a step for a clean and a broken tip are shown. d) Topography of a ohmic contact. e) Topography of one side of a (dirty) sample. a, d) and e) were recorded at Grenoble in the 4K setup, and b) in Louvain-La-Neuve at 20mK, after an unfortunate tip breaking.

temperature (see Fig.1.10).

We therefore used the SGM of Benoit Hackens in Louvain-La-Neuve. This powerful machine is described in Chapter 1, and all the SGM data presented in this manuscript were obtained using this setup.

### 3.2.3 The conductive tips

The tip used during this thesis are sharp commercial AFM tips (from MikroMasch), placed at the end of a cantilever. The topography nonetheless allows to find the place of interest on the sample and is used to calibrate the scanner displacement for a given applied voltage on the piezo, since the size of the markers is well known. It also gives an idea of the tip shape. Indeed, the apparent topography recorded in AFM is in fact a convolution of the real landscape and the tip shape (schemed Fig.3.4c). For example Fig.3.4b is recorded with a tip whose conductive coating has probably been damaged, leading to artificial intermediate steps when probing a single sharp step.

### 3.2.4 Imaging quantum transport

Once the sample is found at low temperature thanks to the markers (extreme care should be taken during this operation in order to keep the tip sharp and clean), we can perform

scanning gate microscopy. To find the exact position of the QPC, we almost close the QPC thanks to the gate voltage and perform SGM at large tip height (typically  $1 \mu m$ ). A negative voltage of a few volts is applied to the conductive tip, and the QPC closes when the tip is above the constriction, leading to a spot of reduced conductance in the SGM maps. We avoid doing topography in the constriction at low temperature in order not to induce surface charges that would affect transport.

Finally, we place the tip in front of the QPC, about 30 nm above the surface, with a negative voltage of -6V applied on it, and record the conductance of the device. By moving the tip above the sample surface, we record the conductance of the device for every tip position. This defines images, namely conductance as a function of in-plane tip position, called SGM images. Note that the surface shall be kept extremely clean to perform this technique because the tip has to be moved 30 nm above the surface.

## 3.3 Interferences

### 3.3.1 SGM images on the plateau

We present here some typical SGM images recorded when QPCs are open on the first plateau. Fig.3.5 presents images recorded on samples B (3.5c) and D(3.5d) in Louvain. For both images, the QPC is open to the first plateau. The tip is scanned about 30 nm above the sample surface, with a negative voltage of -6V applied on it.

In the SGM maps, corresponding to the conductance of the device with respect to tip position, some main features can be observed when the first mode is fully open (see Fig.3.5). The conductance stays quantized to  $2e^2/h$  for most positions of the tip, where it doesn't seem to affect transport. However, for some specific tip positions, the conductance is strongly reduced, sometimes by 50 % . For these features to appear, the tip has to be sufficiently close to the surface (typically 30nm) and with a sufficiently negative voltage applied on it (typically -6V). The conditions on the tip voltage and height required to deplete the 2DEG are discussed in section 3.4.

The tip effect can be understood as follows: it creates a depletion region in the 2DEG, acting as a local scatterer that affects electron transport when placed on their trajectories. Electrons are then backscattered towards the QPC, consequently reducing the total conductance. The fact that these tip locations (with strong effect) draw branches suggests that electrons follow preferential paths in the leads, presumably attributed to the disordered potential [75], and that strongly depend on the 2DEG mobility [71].

An other remarkable feature is that the branches are decorated with interference fringes, spaced by roughly  $\lambda_F/2$ . They're attributed to electronic interferences due to different number of round trips between the depleted region and the QPC, possibly assisted by disorder, and are discussed in the following section.

These interference fringes have been a matter of intensive experimental studies[83, 77, 61, 71], but their deep origin still raises some questions. It is still nowadays unclear which mechanism gives rise to these fringes, and there might be several mechanisms at play. Though I cannot answer this complicated question, this section presents some interesting results that can rule out some possible mechanisms.

According to the standard interpretation, the fringe spacing corresponds to  $\lambda_F/2$ . In our

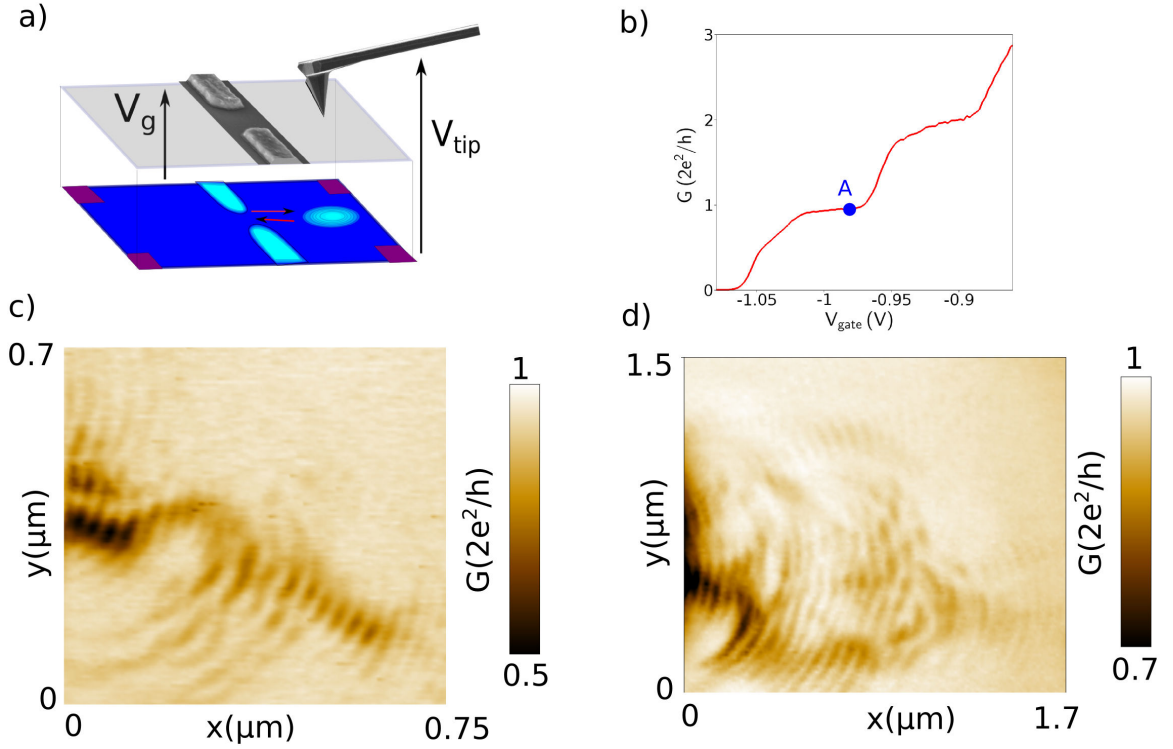


**Figure 3.5 SGM on the first plateau:** *a)* Schematics of the SGM principle, on a QPC. *b)*  $G(V_g)$  traces for sample B, at 20 mK. Blue point represents the gate voltage for which image c is recorded. *c)* and *d)*: SGM images obtained when the first mode of the QPC is open, for sample B (image c) and sample D (image d), at a base temperature of 20 mK. The QPCs are  $\sim 100$  nm on the left side of the images.

case, the bulk Fermi wavelength is 50 nm, hence  $\lambda_F/2 = 25$  nm ( $\lambda_F = \sqrt{2\pi/n}$  where  $n$  is the bulk density  $2.5 \cdot 10^{15} e^-/m^2$ ). In our SGM images, the fringe spacing is not constant, varying between 35 and 55 nm, which is much larger than the expected value of half the bulk Fermi wavelength. This would correspond to an average density of less than  $1 \cdot 10^{15} e^-/m^2$  in the region where these interferences form. This might be due to the global effect of the tip combined with the long-range effect of the gates voltage that tend to reduce in average the local electronic density between the tip and the QPC. This non-constant fringe spacing has also been reported [61], and the different proposed scenarios could not account for this behavior.

To analyze how these interferences depend on the QPC parameters, we have to sweep continuously one of these parameters while scanning the tip in space. Recording SGM images in two spatial dimensions is therefore not possible anymore. Instead, we choose a specific line (where the desired phenomenon is visible), scan the tip along this line, and vary the considered transport parameter between two successive lines.

### 3.3.2 Dependence on QPC opening

A first interesting question that can easily be answered experimentally is: how do these fringes depend on the QPC opening? To address this question, we choose a specific line where these fringes are visible, and record how does the contrast changes for different gate voltages. Some results are presented Fig.3.6, recorded on sample B.

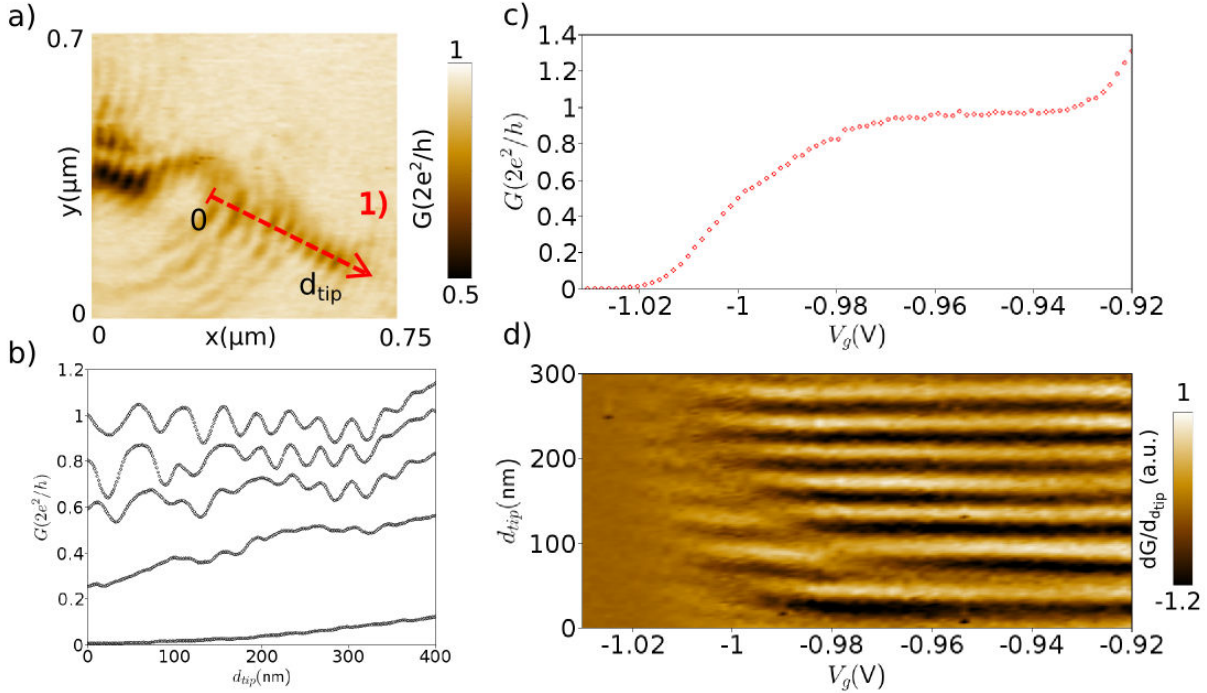


**Figure 3.6 Evolution of the interferences with QPC opening:** a) Same SGM image as in Fig.3.5c, sample B. The red dashed line is the one chosen to study the interferences. b) Conductance vs. tip position  $d_{tip}$  along red dashed line 1), for different values of  $V_g$ . c)  $G(V_g)$  when the tip is at the end of line 1) ( $d_{tip} = 400\text{nm}$ ). d)  $\partial G/\partial d_{tip}$  as a function of  $V_g$  and  $d_{tip}$ .

Fig.3.6a presents the SGM map obtained on the first plateau on sample B, i.e. when the first mode of the QPC is fully open. All the measurements presented here are recorded by applying a voltage of  $-6\text{V}$  on the tip, situated  $30\text{nm}$  above the sample surface. The conductance is measured in 4 points by a lock-in technique, applying an AC voltage of  $10\ \mu\text{V}$  on one contact, the mixing chamber temperature being  $20\ \text{mK}$ .

The line studied in this figure is the red dashed line labeled 1). An abscissa is defined along this line, labeled  $d_{tip}$ , the origin being taken on the QPC side. Looking at conductance with respect to tip position along this line exhibits interferences. Fig.3.6b presents these oscillations as a function of  $d_{tip}$ , for different QPC openings from the pinch-off to the first plateau. The interferences seem more contrasted on the plateau than near pinch-off. Another way to look at these data is to plot the conductance as a function of both  $d_{tip}$  and  $V_g$  and differentiate this plot with respect to  $d_{tip}$  to get rid of the average conductance that varies from  $0$  to  $2e^2/h$  along the first mode opening. In this fashion, the interferences are highlighted and their contrast as a function of the QPC opening can be directly observed (Fig.3.6d).

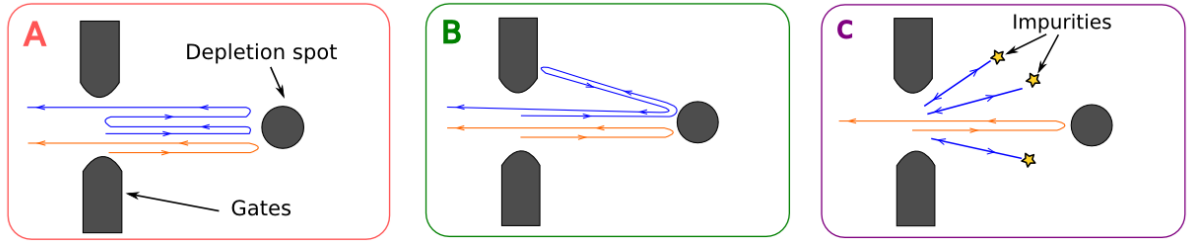


**Figure 3.7** *Possible simplified scenarios to explain the interferences:* A: The two mirrors of the Fabry-Pérot cavity are the tip-depleted region and the QPC. B: The two mirrors are the gate depleted region and the tip depleted region. C: Several contributions to the interferences come from trajectories that bounce on hard-scatterers.

In order to interpret the observed dependence on the QPC opening, we have to choose a model of interferometer and analyze how the contrast depends on the transmission of the "mirrors". Different mechanisms could explain interferences, some are sketched Fig.3.7. The simplest mechanism that could be involved corresponds to scenario A. After crossing the QPC, the electrons bounce once on the tip-induced depletion region, are backscattered towards the QPC, then cross it back. They can also be reflected by the QPC, bounce once more on the scattering region before crossing the QPC. Since electrons behave as fully coherent waves in quantum mechanics, they experience both paths that interfere either coherently or destructively, leading to oscillations in the total conductance. In this scenario, the two paths are dephased by exactly one wavelength when the scatterer is displaced towards the QPC by  $\lambda_F/2$ , leading to the same interference state. This forms a kind of electronic "Fabry-Pérot" cavity between two "mirrors", here the potential barrier of the QPC channel and the depletion region below the tip.

Though it is a well-known problem in optics, the main results of the Fabry-Pérot interferometer shall be reminded at this point. Fig.3.8 shows an example of a 1D cavity. The two mirrors are inequivalent, and respectively have transmission and reflexion coefficients  $t_1, r_1$  and  $t_2, r_2$ . We calculate the total transmission  $T$  through the cavity (from which the reflexion of interest in our case can be deduced by  $R = 1 - T$ ). The figure presents the transmission as a function of cavity length for different transmission of the first mirror  $t_1$  (modeling the QPC), divided by  $t_2$  ( $1/2$  in this example). Fig.3.8b shows the case of only two bounces in the cavity, whereas Fig.3.8c represents the fully developed formula in which an infinite number of bounces are taken into account, leading to sharp resonance peaks where the transmission reaches  $t_2$ .

This presents some similarities with the experiment of Fig.3.6, where the interference are observed for different values of transmission for the first mirror (the QPC), assuming a constant reflexion coefficient at the scattering region. Regarding this, as the interferences observed experimentally are looking like sinusoids rather than sharp peaks, one can guess that electrons contributing to these interferences may have crossed the cavity no more than two or three times.

An other interesting remark is that in the simple Fabry-Pérot model, there is no contrast as soon as mirror 1 (or 2) is perfectly transmitting (red curves). This is quite intuitive

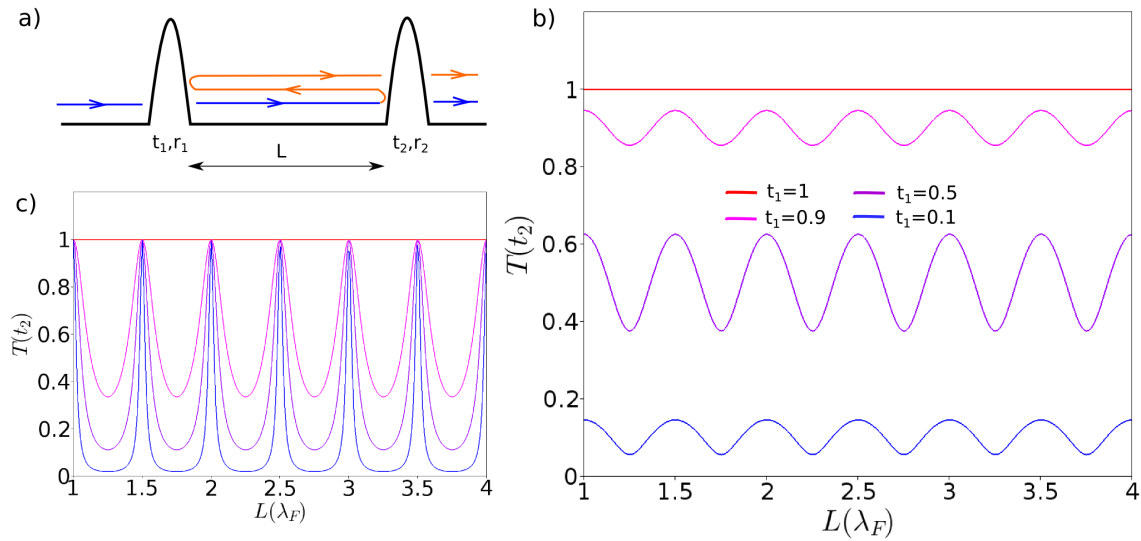


**Figure 3.8 1D Fabry-Pérot cavity:** a) Scheme of an optical Fabry-Pérot cavity. b) Total transmission as a function of cavity length  $L$  in units of the wavelength  $\lambda_F$ , for different values of  $t_1$ , considering only two bounces. c) Total transmission for different values of  $t_1$  taking into account an infinite number of bounces.

but is worth being reminded for the following. This suggests that the simple scenario A sketched in Fig.3.7 cannot explain the observed interferences, as they are more contrasted when the first mode of the QPC is fully open. Other models have to be considered that will be discussed regarding different experimental results. Scenario B offers an interesting alternative, where of the mirrors of the cavity would be the depleted region below the gates, as proposed in Ref.[83]. Hence there would be some contrast of the interferences even when the first mode of the QPC is fully transmitted. However, in this scenario, the mirror formed by the gates would move away from the tip as the gate voltage is brought to more positive values. Hence the interferences should accumulate phase monotonically with gate voltage, that we do not observe in the experiment (Fig.3.6d). Scenario C has been proposed to explain the interferences that survive at temperature up to 4.2K, in samples of mobility around  $2.10^5 \text{cm}^2/\text{V.s}$ [71], far away from the QPC. In our case, the interferences disappear for temperatures above 1K (see section 3.3.3) and the mobility is around  $10^6 \text{cm}^2/\text{V.s}$ , which suggests a different origin.

Several criticisms can be addressed to these simple models that do not seem to account for the gate voltage dependence of the interferences. First the system is not purely 1D, but 2D. Then the electrons can escape from the cavity not only by crossing the mirror formed by the tip. Indeed, as the 2DEG is depleted below the tip, the electrons cannot cross this region, but can escape from the cavity by simple geometric spreading of the wave-function, or by being scattered on potential fluctuations, or directly forward-scattered by the depletion spot. This can be modeled by taking a finite small reflexion coefficient  $r_2$  and considering only two bounces in the cavity, but it shall be kept in mind that the electrons do not cross the depletion spot.

An other difference is that the system does not contain only one mode. Even if a single

mode comes out of the QPC, the cavity can contain several modes and inter-mode scattering is likely to occur because of disorder. This important effect, that could be the key to understand contrast of the interferences on plateaus is extensively discussed in Chapter 4 and supported by numerical simulations.

Finally, we should say a few words on the phase shift visible below the first conductance plateau, in the region of the 0.7 anomaly (see Fig.3.6d). The shift is about  $\pi$  and occurs in a range of gate voltage that depends on tip distance. The same phase shift will be presented in Chapter 4, as it is also visible not only in SGM experiments, but also in transport properties of the interferometers (see Fig.4.4). As will be explained in chapter 5 and 6, this phase shift results from the localized state induced by electron interactions and controlled by the tip position.

### 3.3.3 Temperature dependence

#### 3.3.3.1 Measurements

The temperature dependence of these fringes also gives interesting informations. The data presented in Fig.3.9 summarize a measurement done on sample D, the QPC being just below the first plateau and shows that the interference fringes disappear with increasing temperature.

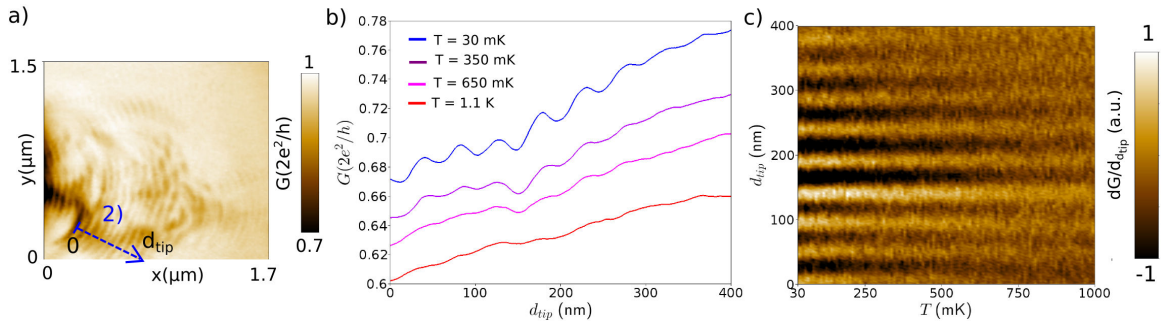


**Figure 3.9 Influence of temperature:** a) Same SGM image as in Fig.3.6d, recorded on the first plateau. b) Behavior of the interferences along blue dashed line 2), for different temperature. The interferences disappear around 1K. Curves are not shifted, the decreasing of the average conductance with increasing temperature is presumably due to the disappearance of the ZBA. c) Colorplot of the derivative  $\partial G/\partial d_{tip}$  as a function of  $T$  and  $d_{tip}$ .

This lost of contrast as the temperature is increased can be understood as follows: with increasing temperature, electrons with more and more different energies will contribute to these interferences, in a window  $E_F \pm k_B T$ . They will therefore have a spreading in wavelength  $\lambda_F \pm \Delta\lambda$ . These different contributions tend to blur the contrast, as in optics experiments with a non-monochromatic source.

It is important to note that the temperature given in those plots is the mixing chamber temperature. It does not automatically match the electronic temperature, that is difficult to lower down to the lattice temperature due to imperfect noise filtering of the electrical

### 3.3. INTERFERENCES

wiring, or due to current-induced electron heating in the sample itself. Another parameter limiting the contrast of the interferences is the applied AC voltage used to measure the conductance, here for example we apply a  $10 \mu\text{V}$  excitation, that corresponds to an electronic temperature of about  $100\text{mK}$ .

The global decreasing of the average conductance as the temperature increases is simply due to the disappearance of the zero bias anomaly discussed in Chapter 2, as this measurement was performed below the first plateau (around  $0.8 \cdot 2e^2/h$ ). For a given temperature, the average decreasing of the conductance when the tip is approached towards the QPC is due to the gating effect of the tip, discussed in section 3.4.

#### 3.3.3.2 (Very) simple model

To analyze this temperature dependence, I consider the simple model that follows. Let's assume that the interferences arise from a "Fabry-Pérot" like cavity, whatever the exact location of the reflections. For demonstration, I take reflexion coefficients of the two mirrors to be  $1/2$ .

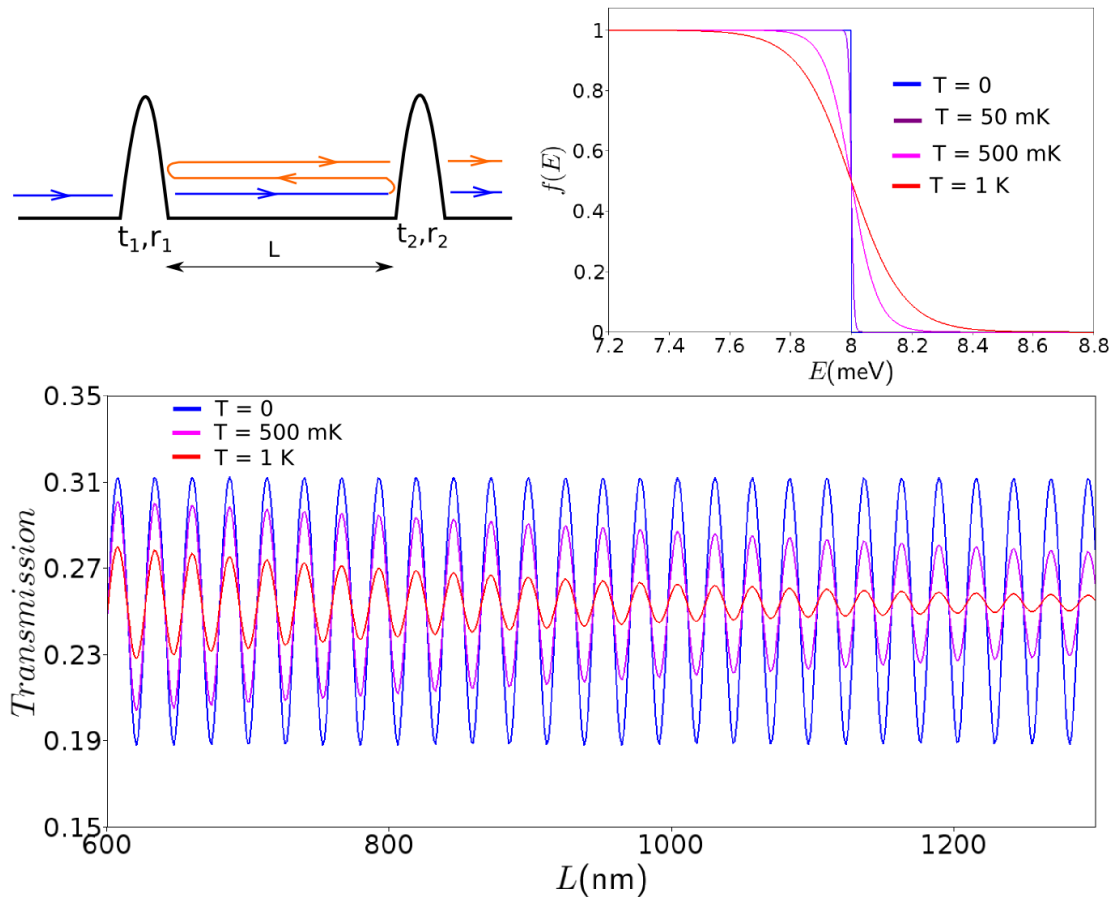


**Figure 3.10 Basic model:** a) Fabry-Pérot cavity, considering only two bounces,  $r_1$  and  $r_2$  are set to  $1/2$ . b) Fermi distributions around  $E_f$  for temperatures ranging from 0 to  $1\text{K}$ . c) Oscillations of the total transmission as a function of the cavity length for different temperatures.

To compute the finite temperature transmission of such a model system, one can take the finite temperature Landauer formula, assuming  $eV \ll k_B T$ :

$$G = \frac{2e^2}{h} \sum_n \int_0^\infty \tau_n(E) \frac{\partial f}{\partial E} dE \quad (3.1)$$

where  $f(E)$  is the Fermi distribution function at finite temperature and  $\tau_n(E)$  is the transmission of the  $n^{\text{th}}$  mode at energy  $E$ . This distribution for different temperature (in our case  $E_f = 8\text{meV}$ ) is presented Fig.3.10b. In this simple Fabry-Pérot model, I consider only trajectories of electrons crossing twice the cavity, and a single mode with a transmission  $\tau$  given by:

$$\tau(E, L) = ||t_1 t_2 e^{ik(E)L} + t_1 r_2 r_1 t_2 e^{3ik(E)L}|| \quad \text{where} \quad k(E) = \frac{\sqrt{2m^*E}}{\hbar} \quad (3.2)$$

Then the integral in equation 3.1 can be simply computed. The resulting transmission of the cavity as a function of its length is plotted on Fig.3.10c. At zero temperature, the oscillations due to the interferences do not decrease with distance. At finite temperature however, different wavelengths contribute to the interferences and the contrast decreases with increasing the cavity length. At 1K, we clearly see that when the cavity length is of the order of  $1 \mu\text{m}$ , the contrast has been suppressed by a factor 10 compared to zero temperature.

Though the decreasing contrast with distance at finite temperature is not completely clear from the experimental data Fig.3.9, the fact that the fringes disappear around 1K suggests that the cavity length in which these interference fringes form is of the order of a micron.

Even if this basic model does not take into account several aspects of the real system, in particular the inter-mode scattering in the QPC and the angular divergence in the 2DEG plane, it gives nonetheless an interesting information on the interferences.

### 3.3.4 Non linear behavior

The spectroscopy of these interferences also give interesting results, a bit more difficult to interpret. This can be done by scanning the tip along a specific line as before, and vary the source-drain DC voltage at fixed gate voltage. For example, Fig.3.11a shows how the interferences evolve when a DC bias is applied to the QPC. The QPC is the one presented in Fig.3.6a, the chosen line is the red dashed line 1), and the QPC is open to the first plateau.

A first experimental observation is that the interference fringes are visible up to 2 mV bias, and then disappear at larger biases (not shown here). A blurring of the interferences for energies above 2 meV cannot be explained by the contribution of higher QPC modes since the subband spacing is 4 meV. It might thus be related to an electron-electron inelastic scattering process at finite energies above the Fermi level, as suggested in [77] where similar energy scales are found. Note that the DC bias voltage should not be translated here into an effective temperature (that would smear out the interferences), since measuring the differential conductance probes only the electrons at the Fermi level of the reservoirs, in the narrow energy window given by the AC voltage ( $10 \mu\text{V}$ ).

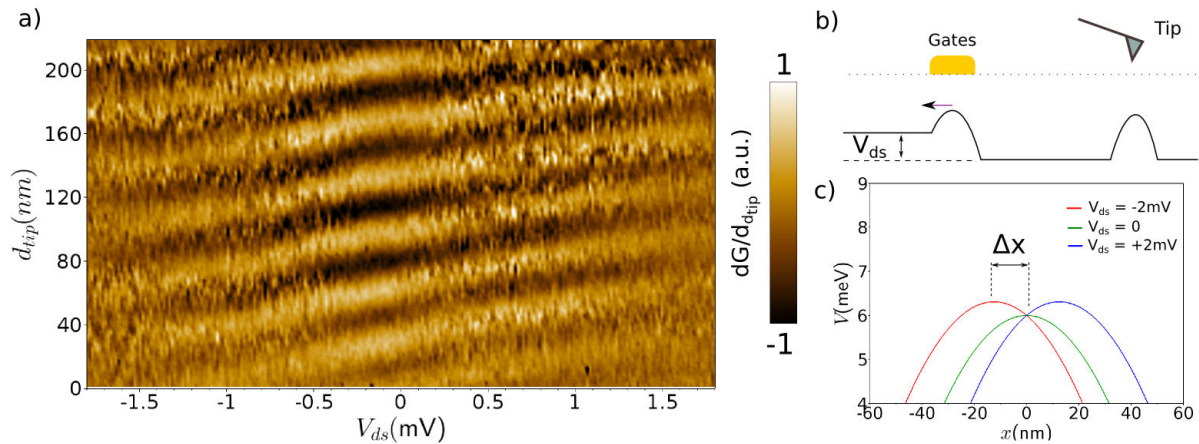


**Figure 3.11** *Fringes evolution with source-drain bias:* a) Evolution of the interferences with source-drain voltage. Data are recorded by scanning the tip along the red line 1) Fig.3.6a, the QPC being on the first plateau. Data are differentiated with respect to  $d_{tip}$  to highlight details. b) Schematics of a Fabry-Pérot cavity when the QPC is in the non-linear regime. c) Plot of the saddle-point potential top along transport axis, with  $\hbar\omega_x = 1.5$  meV, for different source-drain biases, assuming that the voltage drops linearly along the QPC, on a scale of 50 nm.

The second striking fact is that these interferences fringes are shifted to larger tip distances for more positive source-drain biases (the bias voltage is applied on the contact located on the side opposite to the SGM tip). This shift can result from the change in the electron wavelength with energy. It could also result from a change in the cavity length due to a shift of the QPC saddle-point along transport axis under finite bias. Both effects contribute additively and create a positive slope in the graph Fig.3.11a. The first effect is to shift the fringes by one period when the electron energy is increased by  $\Delta E/E_f = \lambda_F/L$ , i.e.  $\Delta E = 0.4$  meV if we consider that the cavity is about 1 micron long. Since the observed fringes shift by one period for an applied bias of 2 mV, the second effect may also be involved.

To quantify this second effect, the shape of the saddle-point under a DC bias voltage should be first investigated. This is an interesting question, and the answer is far from being obvious [85]. We can first rely on the saddle-point model [10] presented in Chapter 1. It is often assumed that the voltage bias drops linearly along transport axis [86]. To model this, I then chose to take a Büttiker's saddle-point model [10] presented in chapter 1, with a transverse confinement of curvature  $\hbar\omega_y = 4$  meV and along transport axis  $\hbar\omega_x = 1.5$  meV. Then the bias voltage is included as a potential that linearly depends on longitudinal coordinate  $x$ , and drops on a length  $L_{drop}$  that can be adjusted. The potential landscape is then given by  $V(x) = (1/2)m^*\omega_x^2 x^2 + \Delta V/L_{drop}x$ . The resulting potential around the saddle-point is drawn on Fig.3.11c, where  $L_{drop}$  is assumed to be 50 nm, for different voltage bias  $\Delta V$ . One can see that applying a DC voltage displaces the saddle-point in real space, in a way that depends on  $\omega_x$ . The maximum is obtained for  $\partial V/\partial x = 0$ , hence the abscissa of the saddle-point  $x_{sp}$  is given by  $x_{sp} = -\Delta V/L_{drop}m^*\omega_x^2$ . Assuming that  $L_{drop} = 50$  nm gives a saddle-point displacement of 20 nm for a voltage bias of 2 mV. Note that this effect is extremely sensitive to both the longitudinal curvature

of the saddle potential and the assumed length on which the voltage drop occurs, that are two quantities difficult to evaluate.

These two orders of magnitude are consistent with the observed phase shift of the interferences with source-drain voltage. As we apply source-drain bias, the QPC displaces in real space and the wavelength of the electrons enlarge, such that the tip has to be moved towards the QPC to keep the same interference state (i.e. the same cavity length). Following a specific interference fringe on Fig.3.11a requires to move the tip by 40nm when the source-drain voltage is changed by 2 mV. The two phenomena described above probably both play a role in this phase shift, but as they depend on quantities difficult to precisely evaluate, it is difficult to say whether one clearly dominates. Note that this is also consistent with a recent more precise theoretical investigation of this problem (i.e. how do interferences evolve with source-drain bias) [76]. An ingredient that is not taken into account and could also play a role in this phase shift is the way electrons are backscattered by the tip and by the QPC, that could depend on their energy.

## 3.4 Tip potential

One of the challenges in understanding the signal obtained in scanning gate microscopy is to model the tip-induced potential. Pioneers of this technique have already proposed some interesting analytic [58] and experimental [80] methods to evaluate how the local electronic density is affected below the tip. It seems that the tip creates a long-range potential, decreasing with distance on a typical scale that roughly matches the tip/2DEG distance.

In Ref.[80], the experimental method chosen was to measure the conductance of a QPC with a large AC bias of 5mV, such that the conductance with respect to the gate voltage is linear. Then the QPC is closed near pinch-off, and the tip is scanned above the channel. In this fashion, the SGM maps represent the tip-induced potential in 2D.

In this section, I present alternative methods to measure both the very tail of the tip-induced potential at the QPC center, and the size of the depletion region induced by the tip.

### 3.4.1 Estimating the shape of the tip tail

To measure the long-range effect of the tip, a method is to evaluate the cross-talk effect, i.e. how does the tip changes the potential at the very center of the QPC.

By approaching the tip toward the QPC, the saddle-point potential rises up, hence the gate voltage required to close the QPC moves towards more positive values. To evaluate this, we use the same data as in Fig.3.6. For clarity, these data are presented in Fig.3.12 but the conductance is differentiated w.r.t.  $V_g$ . In this way, the pinch-off is more visible, as the gate voltage strongly affects the conductance at this point. On this graph, we can directly visualize the way the pinch-off voltage moves when the tip is approached (the red thick curve). This curve somehow directly represents the shape of the tip tail.

A last step to put real energy scales of this potential tail is to convert the change in gate voltage induced by the tip to a change in energy of the saddle-point. This is done

### 3.4. TIP POTENTIAL

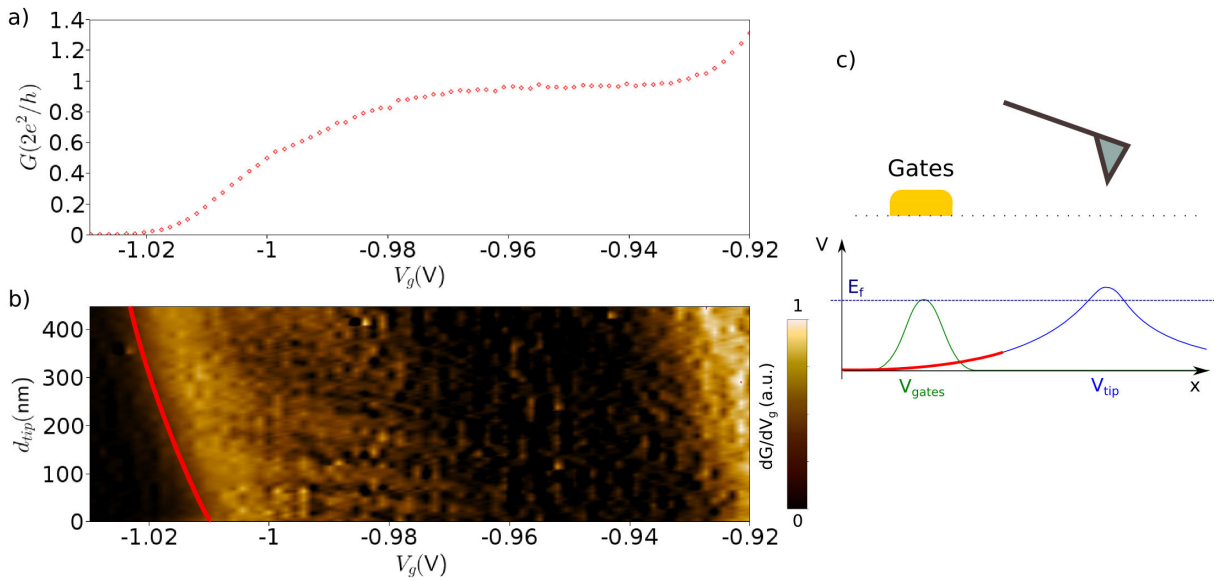


**Figure 3.12** *Characterization of the tip potential tail:* a) and b) Same data as in Fig.3.6 but the colorplot represents the derivative of the conductance with respect to gate voltage (instead of  $d_{tip}$ ). The way the pinch-off is affected by the tip is highlighted in red. c) Schematics of the potential landscape, contributions of the tip and the gates are separated for clarity.

with the lever arm parameter of the gates discussed in Chapter 1. Using this lever arm (50 meV/V), we find that in the situation presented here, the tip raises in average the saddle-point by  $500\mu\text{eV}$  when approaching the tip by 500nm. Of course this cross-talk is not constant (the curve is not linear) and depends on the absolute tip-to QPC distance.

#### 3.4.2 What is the size of the depleted region?

Interestingly, the interferences can bring useful informations on the tip-induced depleted region, as this is one of the mirrors of the Fabry-Pérot cavity. The first experiment that can be done is to look at how the interferences depend on the tip-to-surface distance. This can be done by scanning the tip above a line where the interferences are seen and vary the tip height. This measurement is shown in Fig.3.13a. The tip is scanned above the red line 1 shown Fig.3.6, the QPC being on the first plateau. A negative voltage of -6V is applied to the tip. The data are differentiated w.r.t. horizontal tip distance  $d_{tip}$  to highlight details, but the same informations can be extracted from raw data. The interferences clearly disappear when the tip is more than 50 nm above the sample surface. This corresponds to the depletion threshold. For an applied voltage of -6V, the tip has to be brought lower than 50nm towards the sample surface to create a depletion region and generate interferences. From this observation, we already know that the diameter of the depleted region is zero for the tip height of 50nm.

Another information can be extracted from this plot, based on the fact that the phase of the interferences changes with tip height. This can be understood as follows: as the tip is brought closer to the surface, the depletion region enlarges. As a consequence, to keep

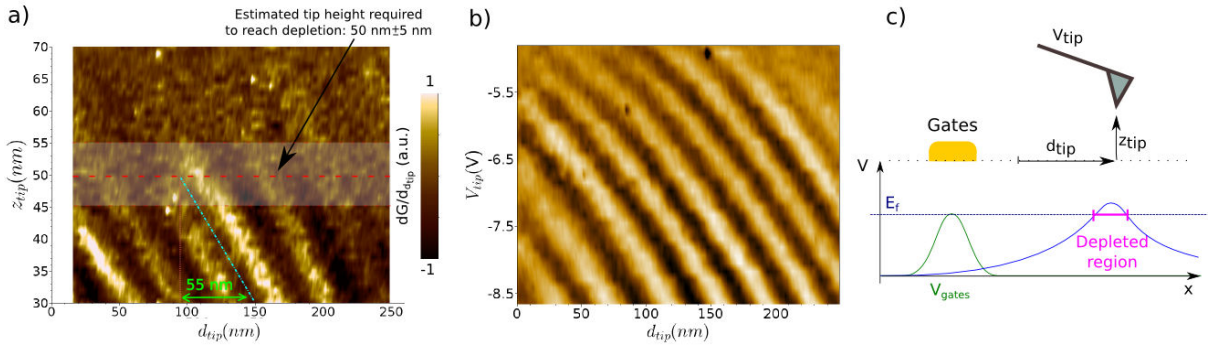


**Figure 3.13** *Characterization of the depletion threshold and depleted region size: a) Evolution of the interferences with tip height  $z_{tip}$ . The chosen line is the red line 1 from Fig.3.6, the QPC is on the first plateau. The voltage applied on the tip is  $-6V$ . b) For a tip/surface distance of  $30nm$ , evolution of the interference fringes with tip Voltage  $V_{tip}$ . c) Schematics of the experiment and resulting potential landscape at the 2DEG level created by the tip (blue curve) and by the gates (green curve).*

a constant interference state in the Fabry-Pérot cavity, the tip has to be brought *away* from the QPC. For example, to keep the same interference state, the tip has to be moved by  $55 \pm 5nm$  in the horizontal plane when it is lowered by  $20nm$  in the vertical direction from the depletion threshold ( $z_{tip} = 50nm$ ) to the working distance ( $z_{tip} \sim 30nm$ ). The depletion region has therefore enlarged by  $\sim 110nm$  ( $2 \times 55nm$ ), hence the diameter of the depletion spot is about  $110 \pm 10nm$ .

Another interesting information is how does the depletion spot enlarge with tip voltage  $V_{tip}$ . This can be done in the same fashion, by scanning the tip along the same line at fixed tip height  $z_{tip} = 30nm$  and vary  $V_{tip}$ . Fig.3.13b shows how the interferences evolve with  $V_{tip}$ , between  $-5$  and  $-8.5V$ . A clear change in phase can be observed as the tip voltage is lowered. Following the same interpretation as previously, the depletion region enlarges as the tip voltage is lowered (towards negative values), hence the tip has to be moved away from the QPC to keep the same interference state. Though the data were not recorded for less negative  $V_{tip}$ , the depletion threshold seems to be around  $-5V$ . Then lowering  $V_{tip}$  to the typical working voltage in this chapter of  $-6V$  enlarges the depletion spot by  $\sim 60nm$ , which is consistent with the previous estimation.

### 3.4.3 Electrostatic simulations

A different approach to evaluate the tip-induced potential consists in simulating the associated electrostatic problem. This has to be done taking into account screening by the 2DEG and the metallic gates. At this point, I would like to acknowledge Guillaume Bachelier who kindly took from his precious time to perform these simulations thanks to the Comsol software. It consists in finite elements calculations of the electromagnetic field in a region of space where metallic parts, dielectric (GaAs layer), the doping layer and the 2DEG are defined. Then the Poisson equation is solved by successive iterations and provides the local potential as well as local electronic density in the 2DEG.

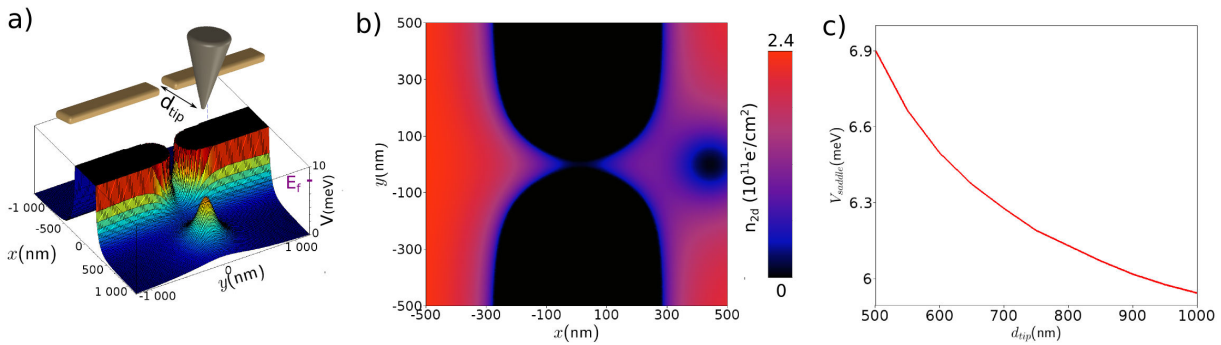


**Figure 3.14** *Classical electrostatic simulations:* a) Geometry of the gates and tip, over a typical potential map at the 2DEG level. b) Local electronic density when the tip is 400 nm away from the QPC center, 30nm above the sample surface, with a negative voltage of -6V on it, and -1V on the gates. c) Saddle-point potential with respect to absolute tip to QPC distance.

The system is modeled as follows: the metallic gates are 120 nm thick and define a 270 nm wide and 300 nm long constriction, corresponding to our sample geometry. The tip is modeled by a cone with a rounded apex of curvature radius 25 nm (Fig.3.14a). The 2DEG plane is located 105 nm below the surface according to our heterostructure and we take a dielectric constant  $\epsilon_r = 12.9$  between the 2DEG and the surface to model GaAs. We model the doping layer by a constant and uniform charged plane (in the 2DEG plane for stability reasons) of density  $2.5 \times 10^{11} \text{ cm}^{-2}$ , insensitive to local potential (modeling ionized dopants). When no voltage is applied neither on gates nor on the tip, the electron density in the 2DEG is  $2.5 \times 10^{11} e^-/\text{cm}^2$ . The local density is computed self-consistently depending on the local potential by successive iterations. This therefore includes screening from the 2DEG.

From the Potential map Fig.3.14b, the size of the depleted region is found to be of the order of 100nm, which is consistent with the value estimated above from the experiment. A second result is that the global density is in average really reduced between the tip and the QPC, which might explain why the observed interferences in the experiment are spaced by more than half the bulk Fermi wavelength.

To simulate the way the tip affects the saddle-point, this simulation has been realized for several tip positions along the longitudinal QPC axis. Fig.3.14c shows the potential at the saddle-point when the QPC is close to pinch-off, for different tip positions (here the tip distance is labeled from the center of the QPC). One can see that approaching the tip by 500 nm rises the saddle-point by almost 1 meV, which is consistent with what is measured from Fig.3.12.

## 3.5 Modeling scanning gate microscopy

To analyze the origin of the interferences, we simulate the transport through the QPC in presence of the tip using Kwant. As explained in chapter 1, the QPC is modeled

thanks to an electrostatic model proposed by Davies *et al* [16] to compute the potential induced by the gates. Possibly, disorder can be included following a method proposed in Ref.[17]. Then the tip potential has to be modeled. To do so, the method used for the gates[16] cannot help as it assumes fixed zero potential on the surface, and the tip is above the surface. The method we choose to include the tip in this potential landscape is the following: we therefore assume that the tip potential behaves as a screened impurity and hence can be described by the expression:

$$V(x, y) = V_t \times \frac{L_{tip}^3}{[L_{tip}^2 + (x - x_c)^2 + (y - y_c)^2]^{3/2}} \quad (3.3)$$

Where  $x_c$  and  $y_c$  are the tip coordinates in the 2DEG plane,  $V_t$  is the potential energy at the very top of the tip potential (that has to be larger than  $E_f$  to have a finite depleted region), and  $L_{tip}$  is the typical decay length of the tip potential whose order of magnitude is given by the vertical distance between the tip and the 2DEG. We used the experimental characterization proposed in 3.4 to evaluate reasonable values concerning  $V_t$  ( $1.5 * E_f$ ) and  $L_{tip}$  (100 nm). Note that the exact expression chosen for the tip potential does not really matter as soon as the tip tail and the depletion spot match the experimentally characterized values. A lorentzian or a Gaussian would essentially give the same transport simulation considering reasonable values for their maximum and decay length.

To understand how does the tip change the potential landscape, the total transmission and the wave-functions, we first take a look at transport without tip. The disorder has to be taken into account, and in this section a specific random background is chosen, corresponding to a random distribution of ionized dopants in the doping layer of the structure (see Fig.3.15a). The way this residual disorder affects the transmitted wave-functions is computed Fig.3.15c (clean case) and 3.15d (disordered). The total transmission of the QPC is shown 3.15b for different values of random fluctuations amplitude  $\Delta V$ . As discussed in Chapter 1, including this disordered potential landscape shifts the curves in  $V_g$  depending on the exact fluctuation sign at the center of the channel. Increasing the disorder amplitude  $\Delta V$  tends to create resonances in the curve  $G(V_g)$  for  $\Delta V > 0.1E_f$ .

With this unperturbed picture in mind, we now add the tip potential to this landscape and compute transport through the entire system including the QPC, the tip and the disorder potential, choosing an amplitude of  $0.1E_f$ . In particular, we calculate the total transmission for many positions of the tip, hence recreate what we measure in scanning gate experiments.

At this point, I would like to open a parenthesis and acknowledge once more Christoph Groth and Xavier Waintal, not only for the development of kwant and their grateful help in modeling our system, but for having initiated me to the black art of parallel computation, and given me unrestricted access to their thousand's cores cluster. This is really useful because instead of computing transport for different tip positions by doing loops on a single computer, one can use hundreds of computers at the same time, each one calculating transport for a specific tip position. Then a high resolution SGM map is simulated in a few hours, whereas it would take some days to a simple computer to perform such a calculation (including a complex random potential), despite the impressive efficiency of kwant.

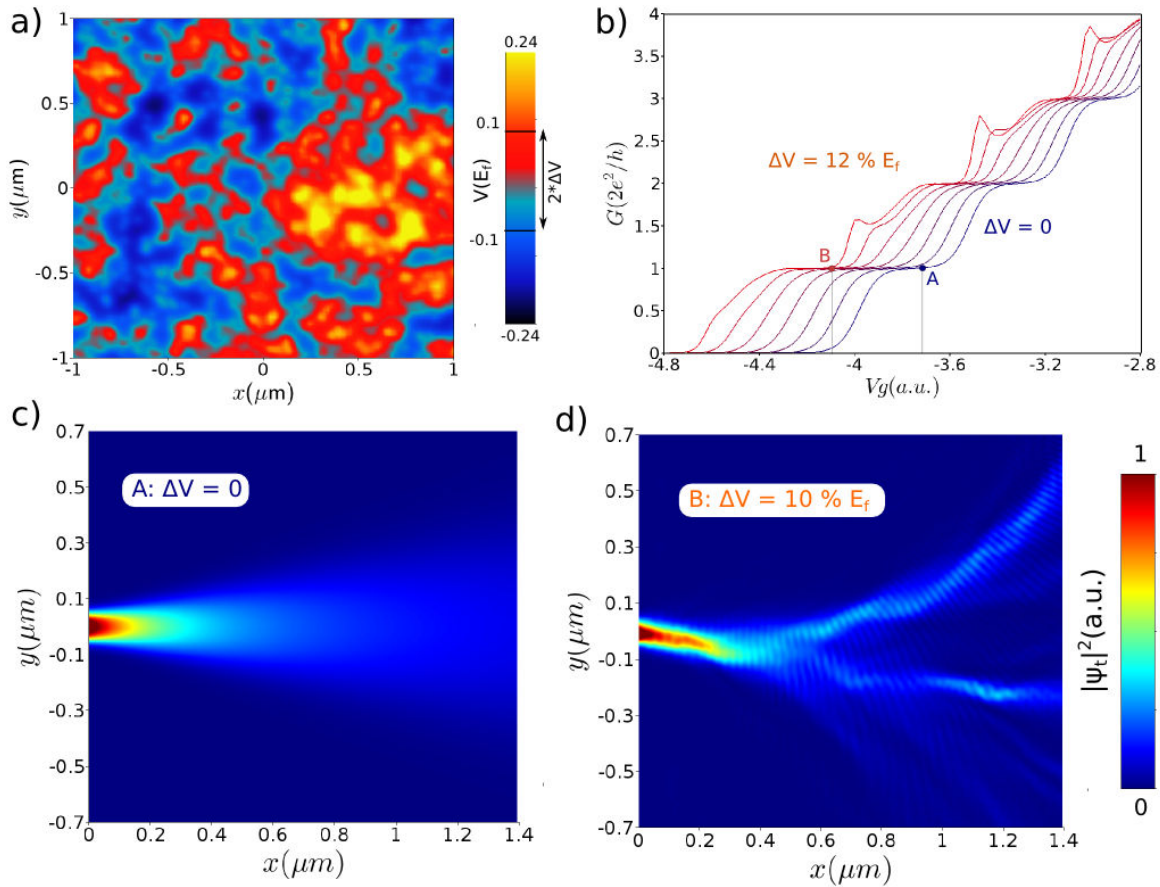


**Figure 3.15 Quantum transport simulations:** a) disordered potential used in this section. b) Conductance curve of the QPC  $G(V_g)$  for different values of the typical potential fluctuations  $\Delta V$ , ranging from 0 to  $0.12E_f$  by steps of  $0.02E_f$ . c) Transmitted wave-function square modulus on the first plateau without disorder (situation A). d) Transmitted wave-function square modulus with a disorder of amplitude  $0.1E_f$ , on the plateau (situation B).

The results of the SGM maps on the first plateau are presented Fig.3.16e for the clean case, and Fig.3.16g in presence of disorder ( $\Delta V = 0.1E_f$ ). It is clear that including disorder results in a branched flow, decorated with interferences, as observed experimentally. Interestingly in the disordered case, the branches in the SGM maps reflect the unperturbed transmitted wave-function, as seen by directly comparing the simulated SGM map and the electronic wave-function square modulus Fig.3.16f and g.

It is still an ongoing research to understand what is measured in the scanning gate microscopy of a quantum point contact [72, 73]. Though it is not a detailed theoretical investigation, our simple calculation including a random potential brings two informations:

- When disorder is taken into account in a realistic way, a branched flow and some contrasted interferences decorating the branches are visible even when the QPC is on a plateau
- The branches more or less reflect the wave-function square modulus of the electrons coming out of the QPC in absence of the tip, as discussed in Ref.[82].

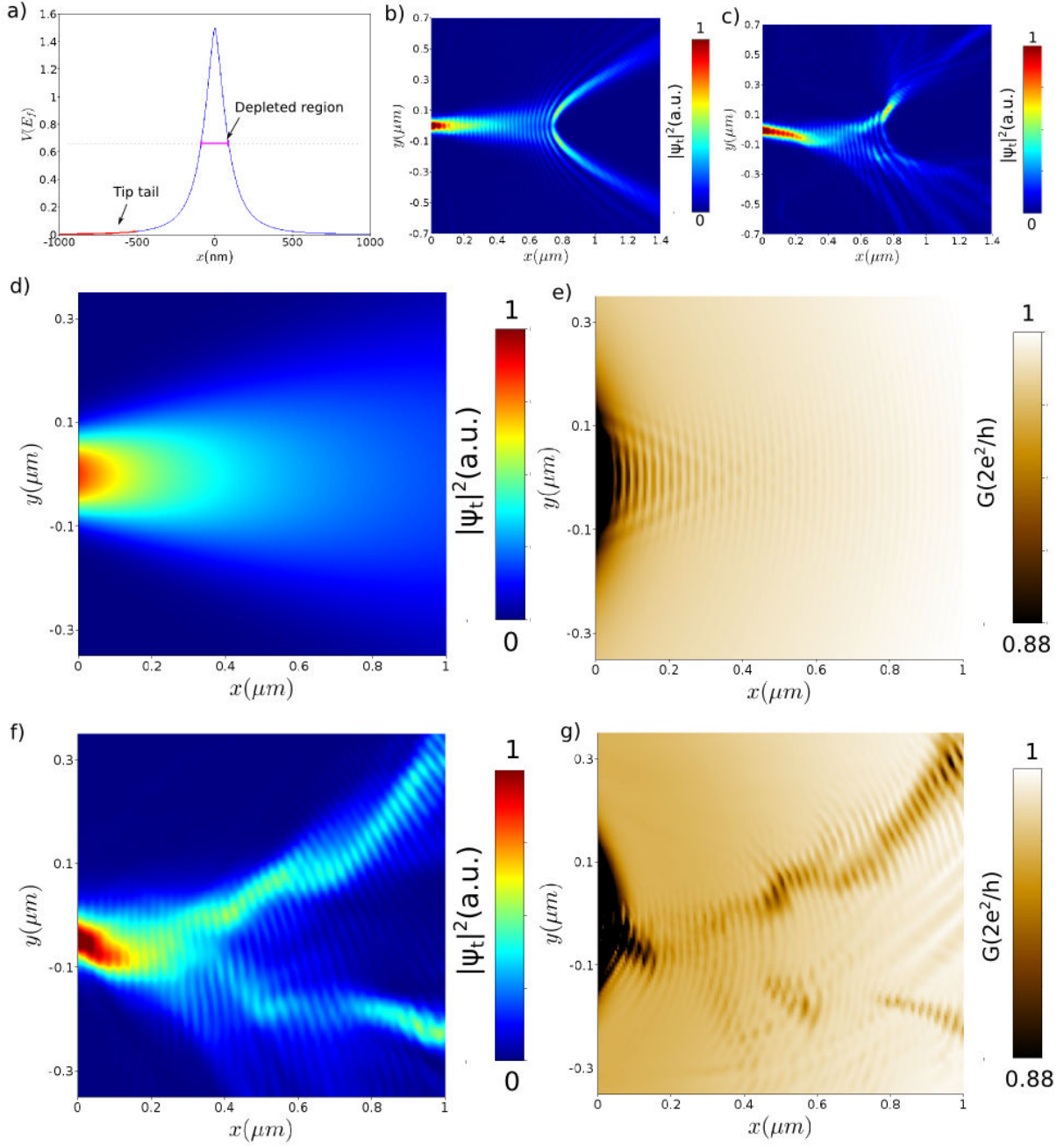


**Figure 3.16 Scanning gate microscopy simulations:** a) Profile of the tip potential along one axis.  $V_t$  and  $L_{tip}$  are adjusted such that the depletion spot is about 100 nm and the tip tail is about 1meV on 500 nm. b) and c) transmitted wavefunction square modulus for perfect and disordered leads, when the tip is in front of the QPC, 1 micron away from the channel center. d) to g) Unperturbed wave-function square modulus and simulation of SGM maps in the cases of clean leads (d-e) and disordered (f-g) with  $\Delta V = 0.1E_f$ . In both situations the QPC is on the first plateau.



# Chapter 4

## Ballistic interferometers

### Contents

---

<b>4.1</b>	<b>Sample and measurements</b>	<b>74</b>
4.1.1	The device geometry	74
4.1.2	Generating interference	75
4.1.3	Transconductance	76
<b>4.2</b>	<b>Influence of different parameters</b>	<b>77</b>
4.2.1	Dependence on QPC opening	77
4.2.2	Dependence on temperature	80
4.2.3	Dependence on magnetic field	81
4.2.4	Polarization influence	82
<b>4.3</b>	<b>Numerical simulations</b>	<b>83</b>
4.3.1	Interference without disorder	83
4.3.2	The role of disorder	84
4.3.3	Modeling magnetic field	85
<b>4.4</b>	<b>Conclusion</b>	<b>86</b>

---

## 4.1 Sample and measurements

### 4.1.1 The device geometry

One objective of my thesis was the design and study of a new interferometer type, based on an original idea of Jean-Louis Pichard and Axel Freyn. They proposed that a distant scatterer could perturb a QPC in a non-local way, to detect electron-electron interactions in the QPC [78, 87].

The theoretical proposal states that electron interactions inside the QPC could lead to enhanced interference amplitude, and could change the way the interference decays as a function of the scatterer to QPC distance.

To realize the proposed experiment, we choose to design a distant scatterer by depositing a metallic 80 nm thin gate, at distances from the QPC center ranging from 0.7 to 1.8  $\mu\text{m}$ . The devices made by our collaborators at LPN (see section 1.2.1) are in fact the same as those used for SGM experiments (the tip was on the opposite side and no voltage was applied to the third gate).

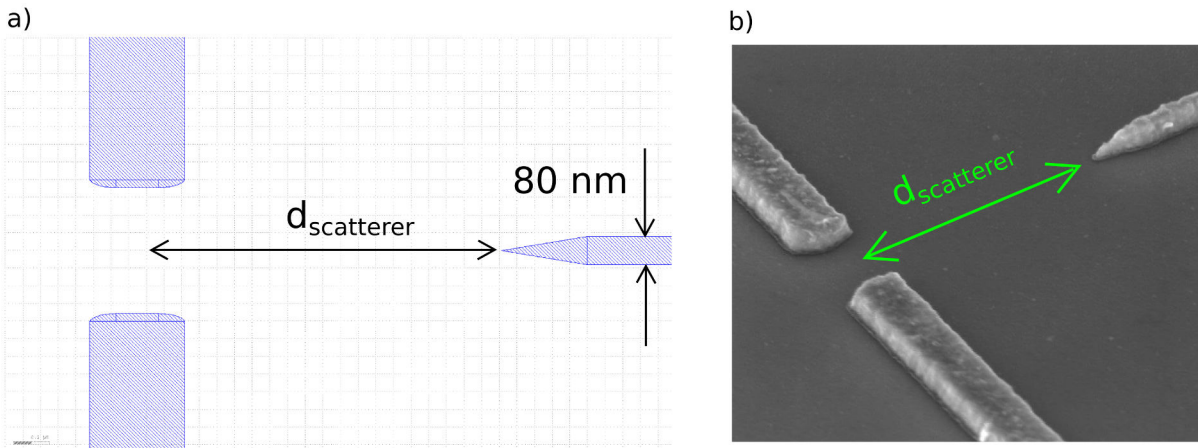


**Figure 4.1** *Design of the interferometers: a) Example of the typical lithographic pattern designed with a layout editor. b) SEM image of one of the interferometers provided by Dominique Mailly after the process.*

It is not the first time that one designs a reflector gate in front of a QPC. Soon after the development of scanning gate microscopy, the pioneers of this technique designed large reflector gates in front of QPCs and extensively studied this system during the impressive thesis of Brian LeRoy [81]. Their idea was to investigate the influence of disorder on the formation of the interference fringes observed in SGM experiments. They performed SGM on these samples, using the tip as a scatterer to generate interference, and checked how these interference fringes evolved with the voltage applied on the reflector [70].

The idea in our study is to directly use the reflector gate to generate interference, without the use of the SGM tip, and to compare the obtained interference with the ones observed in scanning gate experiments.

### 4.1.2 Generating interference

During this thesis, various interferometers of this type have been measured in Grenoble and in Louvain. Similar behaviors have been observed in every sample, but I will concentrate on two of them, sample A and sample B, and give an example of samples E and C. Samples A and B have been measured in CEA (LATEQS team, in Grenoble), in the cryostats presented in Chapter 1. Sample A was measured in “La diluette”, and sample B in “Bigoudène”.

Fig.4.2a shows the conductance curve versus split-gate voltage of sample A, with quantized plateaus and the 0.7 anomaly. Fig.4.2b presents the main effect of a negative voltage  $V_{g3}$  applied on the third gate, when the QPC is on the first plateau, and Fig.4.2c presents the effect of negative  $V_{g3}$  for different QPC openings.

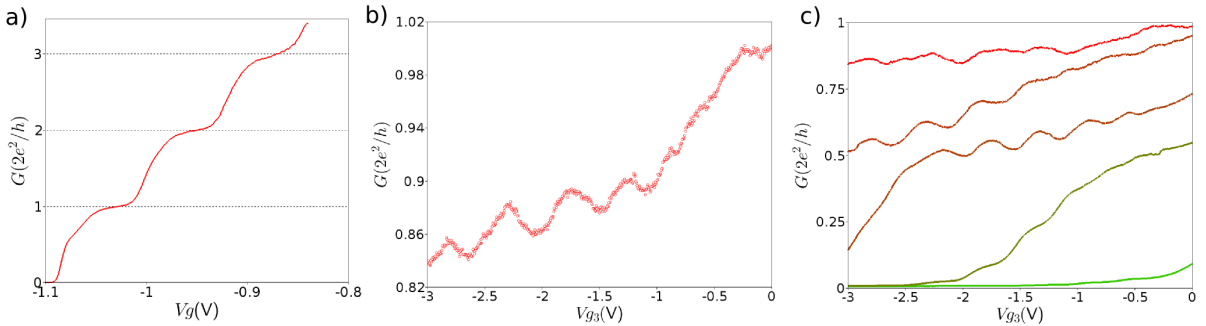


**Figure 4.2** *Generating interference with the third gate:* a) Conductance curve of QPC A  $G(V_g)$  at a base mixing chamber of 50 mK. b) Effect of a negative voltage applied on the third gate on the QPC conductance, on the plateau. c) Effect of the third gate for different QPC openings from the pinch-off to the plateau.

Below a threshold voltage of -0.5 V, the conductance drops due to two main contributions :

- 1) The third gate closes the QPC by direct electrostatic coupling (cross-talk) though though this scatterer is typically  $1\mu m$  away from the QPC. This “cross-talk” effect will be characterized in section 4.2.1.
- 2) The depleted region below the third gate increases the series resistance of the reservoirs and therefore lowers the overall conductance even on a quantized plateau.

The most striking feature is that the conductance oscillates as a function of  $V_{g3}$ . This non-monotonic behavior is similar to the interference observed in SGM experiments as a function of tip position discussed in the previous chapter. It can be understood as follows: as soon as a sufficiently negative voltage is applied on the third gate (about -0.5 V), it depletes the 2DEG underneath and creates a hard scatterer for the electrons coming from the QPC that backscatter them through the QPC, leading to a reduced conductance.

As  $V_{g3}$  is lowered, the depletion region is brought closer to the QPC, and a Fabry-Pérot cavity forms between the QPC and the third gate. Therefore the conductance exhibits oscillations as a function of  $V_{g3}$  depending on the electronic interference state in this cavity.

### 4.1.3 Transconductance

To get rid of the average effect of  $V_{g_3}$  on the conductance, we use a measurement trick often called the transconductance. It consists in differentiating the conductance with respect to the third gate voltage  $V_{g_3}$ . Though it can be done numerically, we choose an analog method to measure directly the quantity  $\partial G/\partial V_{g_3}$ .

To do so, we apply a small AC voltage (typically 10 mV) on the third gate, in addition to the large DC voltage, at a typical frequency  $f_t$  of 130 Hz. The sample is polarized with a small DC voltage bias (typically  $100\mu\text{V}$ ), and the modulation of the current flowing through the QPC at  $f_t$  is detected by a lock-in technique. The measured quantity is therefore  $\partial G/\partial V_{g_3}$ . A scheme of the measurement technique is presented Fig.4.3a.

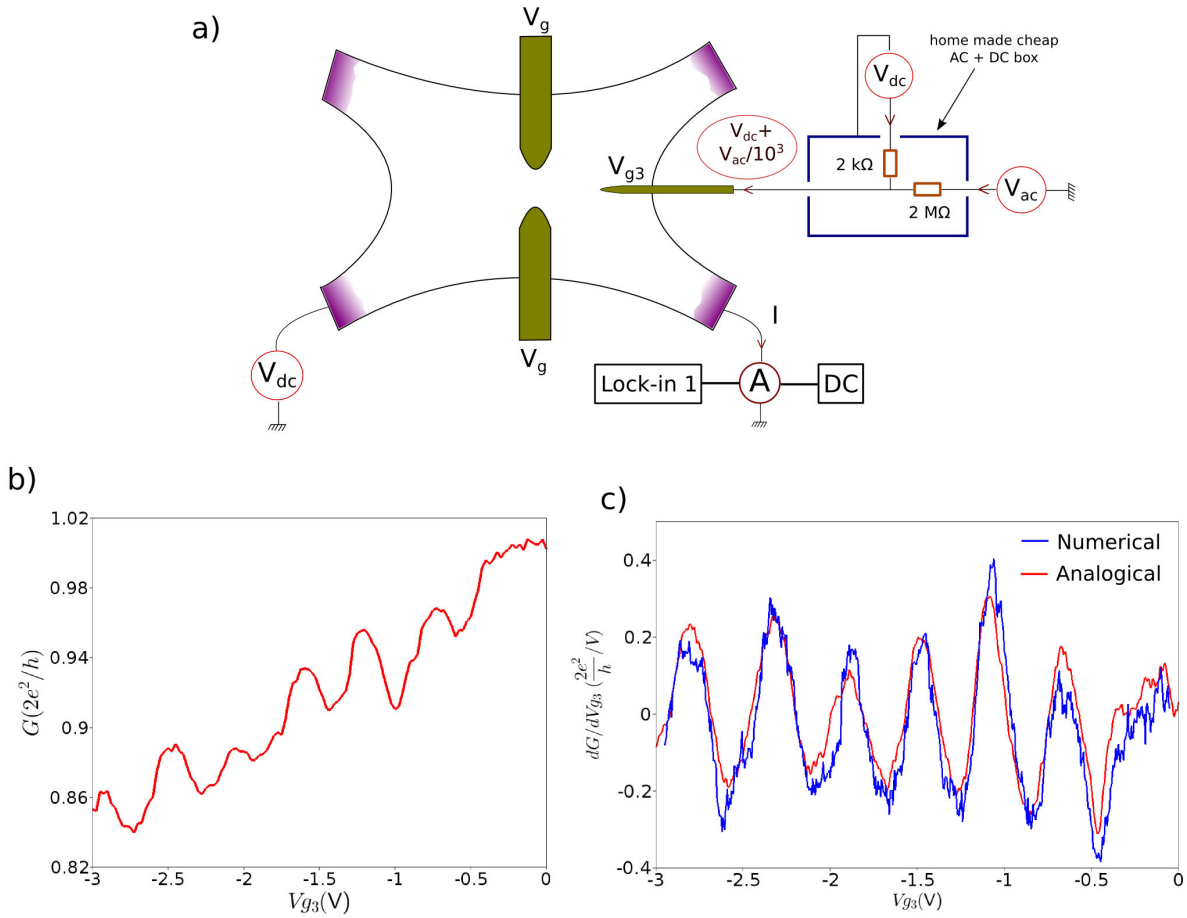


**Figure 4.3 Transconductance measurement:** a) Schematics of the measurement. An AC voltage is applied on the third gate additionally to the DC voltage and a small DC voltage is used to polarize the QPC. b) DC conductance as a function of  $V_{g_3}$  on the first plateau. c) Analogical transconductance  $\partial G/\partial V_{g_3}$  as a function of  $V_{g_3}$  measured by lock-in technique (red curve) and numerical derivative of the DC current with respect to  $V_{g_3}$  (blue curve).

A typical trace of the obtained signal  $\partial G/\partial V_{g_3}$  is presented Fig.4.3c, as a function of  $V_{g_3}$ . This presents the advantage to hide the global decrease in conductance due to the cross-talk effect, and hence highlights only the interference. For comparison, we always record at the same time the raw DC current by the means of a DC voltmeter reading the

output of the current amplifier. The numerical derivative of the DC current is plotted on the same graph (blue curve). Though the numerical derivative is less clean, the two signals exhibit the same variations. The amplitude of the lock-in signal has to be increased by 25% to match the numerical derivative because the lock-in had a non-zero phase reference during this experiment. A constant value has also to be subtracted, presumably due to a capacitive coupling between the measurement wires that bring some signal at the third gate voltage modulation frequency (127 Hz) to the current amplifier.

In the following, I will then plot the transconductance corrected in this way.

## 4.2 Influence of different parameters

As we did in scanning gate experiments, we can vary different transport parameters and see how the interference evolve.

### 4.2.1 Dependence on QPC opening

The first parameter that can easily be addressed experimentally is the evolution of these interference fringes with QPC opening. To investigate this effect, we sweep the scatterer voltage  $V_{g_3}$  and record these traces for several values of  $V_g$ . We then plot the transconductance as a function of both  $V_g$  and  $V_{g_3}$ . The resulting color-plot is presented Fig.4.4b.

A trace of the conductance curve  $G(V_g)$  with no voltage applied on the third gate is presented at the same time Fig.4.4a.

Several informations can be extracted from this graph, that are listed below.

- **Cross-talk:** A negative voltage applied on the third gate tends to move the pinch-off toward more positive values of  $V_g$ , due to a “cross-talk” effect, as discussed for the polarized SGM tip in the previous chapter. From the displacement of the pinch-off line with  $V_{g_3}$  (bright line on the left of Fig.4.4b), we can extract the lever arm parameter of the third gate, i.e. how does a negative voltage applied on the third gate rises the saddle-point energy at the QPC center. We can see that applying -3V on the third gate displaces the pinch-off gate voltage by 0.02V. The lever arm of the split gates, extracted following the method presented in Chapter1, Fig.1.11, is about 50meV/V, hence the lever arm of the third gate is about 0.35meV/V.

- **Depletion threshold:** A clear horizontal line is visible around  $V_{g_3} = -0.45V$ , which correspond to the voltage required to completely deplete the 2DEG below the third gate. The interference fringes are not visible for third gate voltages below this value, reinforcing the fact that a hard scatterer is required to generate these fringes.

- **Periodicity:** Two identical interference states in the cavity forming between the QPC and the third gate are expected each time the depletion threshold below the third gate is approached by  $\lambda_F/2(\sim 28nm)$  towards the QPC. The periodicity of this interference in  $V_{g_3}$  is about 0.5V, meaning that the depletion threshold moves by approximately 56 nm/V. It is important to note that this fringe spacing is found to vary between different samples and even presented an hysteretic behavior in the same sample. For example, applying a negative voltage as low as -5V on the third gate can irreversibly enlarge the

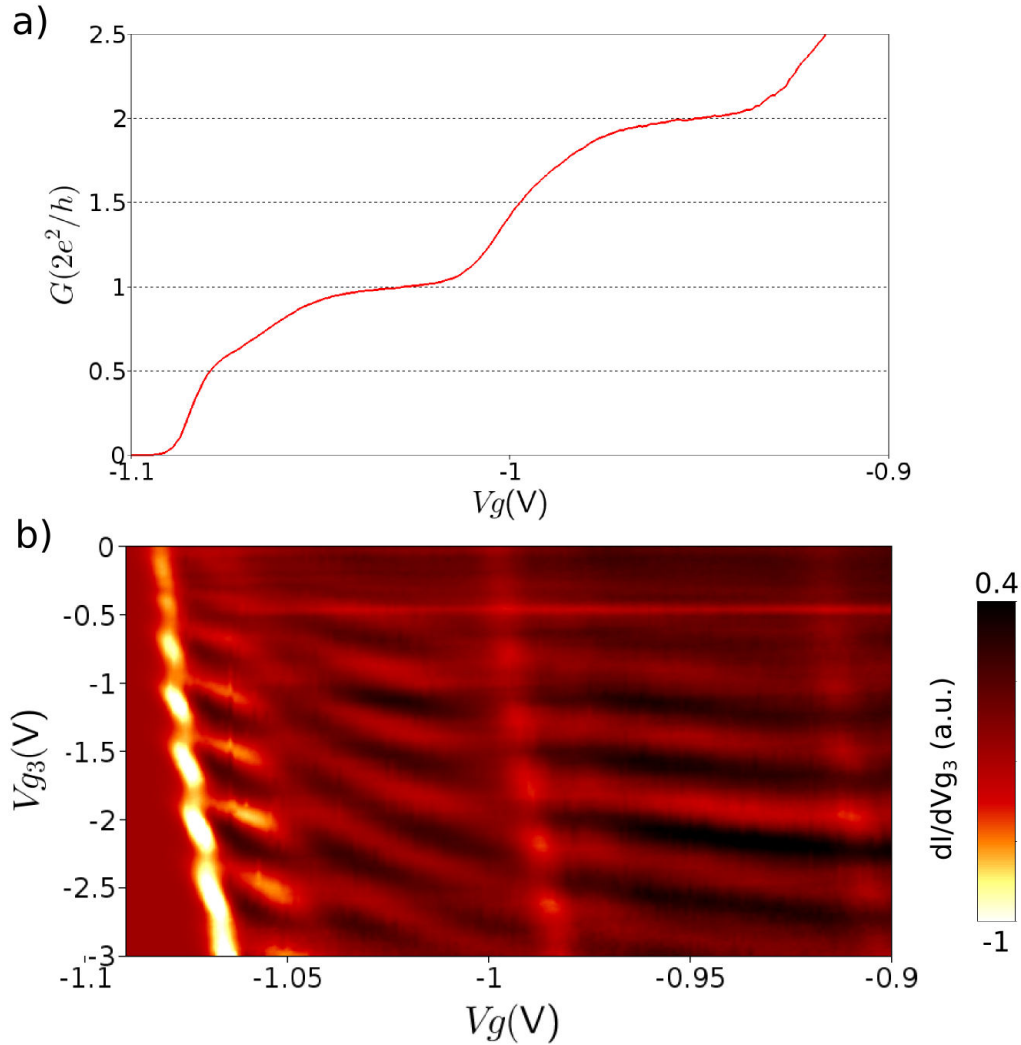


**Figure 4.4 Interference vs QPC opening:** a)  $G(V_g)$  at 50 mK, recorded by applying an AC voltage of  $50 \mu\text{V}$  on sample A. No voltage is applied on the third gate. As the data are recorded with only two ohmic contacts, the total conductance is corrected by a series resistance of  $2.5 \text{ k}\Omega$  to take into account the filters and the ohmic contacts. b) Colorplot of the analogical transconductance as a function of  $V_g$  and  $V_{g_3}$ , allowing to follow the evolution of the interference fringes with the QPC opening.

periodicity of the fringes, that can be reset by heating the sample above 150 mK. This is not surprising, as applying some volts on a gate situated directly on the sample surface can induce irreversible charge deposition in the heterostructure. This contrasts with the SGM experiments where the tip is never in contact with the sample surface.

- **Contrast:** A striking feature that can be directly observed on Fig.4.4b is that the interference are as contrasted on plateaus as in the transition in contradiction with theoretical predictions [73]. The same observation was done in the SGM experiments presented in the previous chapter. This effect could be the result of the disordered potential landscape in the 2DEG as will be discussed in section 4.3. One shall also note that in Ref.[73], the calculation is done in the perturbation regime, when the tip is very weak and does not

fully deplete the 2DEG as in this experiment.

- **Unexpected phase shift:** Interestingly, these interference fringes are even more contrasted at the 0.7 anomaly, and they present a surprising phase shift of  $\pi$  between the 0.7 anomaly and the first plateau. This effect may be related to Kondo physics at play below the first plateau, and will be extensively discussed in Chapter 6.

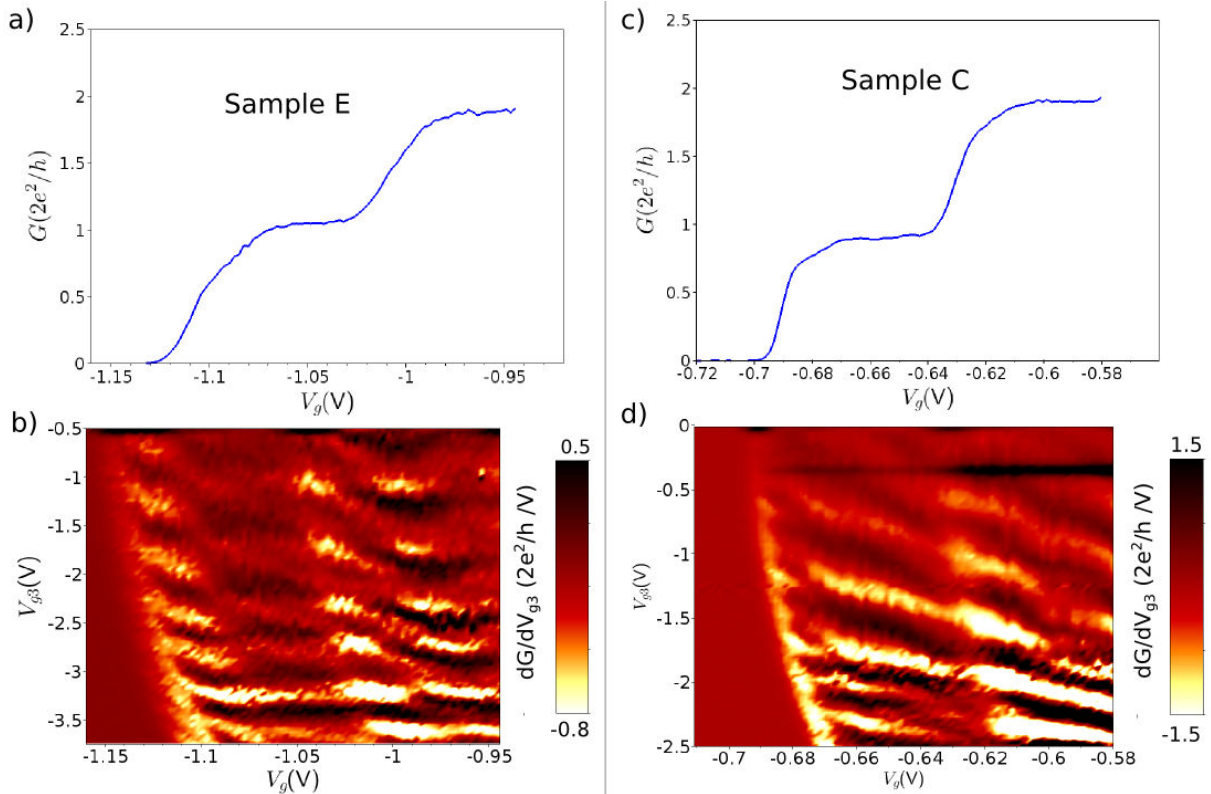


**Figure 4.5** *Dependence on QPC opening for two different samples: a) Sample E:  $G(V_g)$  recorded in 4 points by applying an AC voltage of  $10\mu V$ , at a base temperature of  $20\text{ mK}$ , for no voltage applied on the third gate. b) Numerical transconductance as a function of  $V_g$  and  $V_{g3}$ , allowing to follow the interference with the QPC opening, on sample E. c)  $G(V_g)$  for sample C recorded in the same conditions. d) Numerical transconductance for sample C as a function of  $V_g$  and  $V_{g3}$ . All these data were recorded in Louvain-La-Neuve.*

This analysis has been realized on several samples, an example is given for two different samples (E and C) Fig.4.5. These experiments were done in Louvain-La-Neuve, and the conductance is recorded using a 4-points technique, with an applied AC voltage of  $10\mu V$ . The transconductance plotted Fig.4.5b and d is therefore calculated numerically. The same main features as in Fig.4.4 are visible. Interestingly, the phase shift of  $\pi$  between the 0.7 regime and the first plateau is visible in both plots, though it is less pronounced for sample C.

### 4.2.2 Dependence on temperature

The temperature dependence brings additional information on these interference fringes. Traces of the transconductance as a function of the third gate voltage are presented Fig.4.6a. A complete characterization of the interference as a function of the QPC opening are presented Fig.4.6b to d, at temperatures of 500mK, 1K and 4K, with the same colorscale. It clearly appears that at a temperature of 1K, the interference fringes are already weaker than at low temperatures, and they completely disappear at 4K.

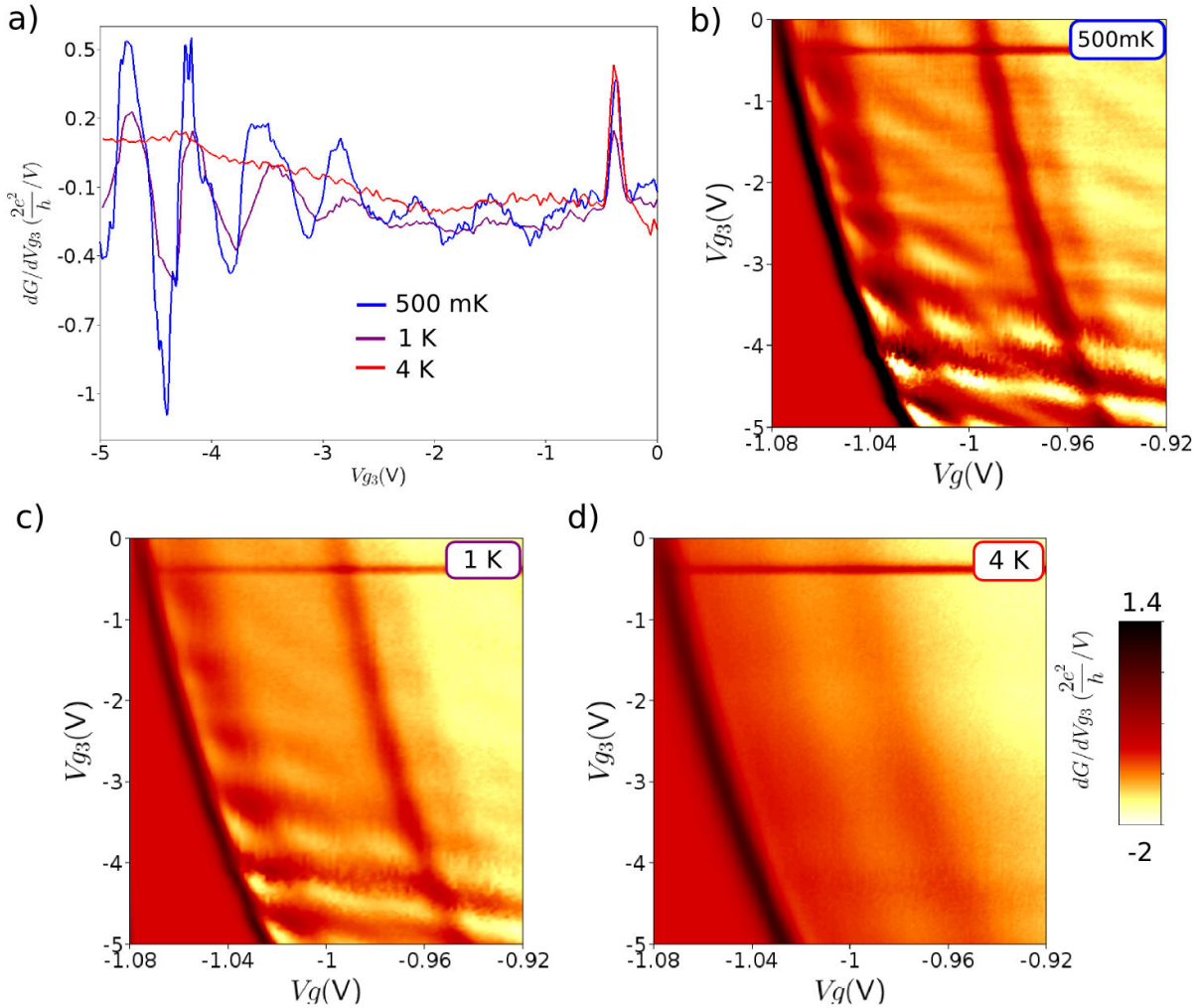


**Figure 4.6** *Temperature dependence of the interference:* a) Traces  $\partial G/\partial V_{g3}$  for a split gate voltage  $V_g = -1$  V, at temperatures of 500 mK, 1K and 4K on sample A. b) Complete characterization  $\partial G/\partial V_{g3}$  as a function of  $V_g$  and  $V_{g3}$ , at 500 mK. c) Same measurement at 1K. d) Same measurement at 4K, interference is not visible anymore.

Though these measurements were recorded on the same sample as the one presented Fig.4.4 (sample A), the signal is more messy because of an unfortunate electrostatic shock applied to the sample. The interference spacing is larger (as a function of  $V_{g3}$ ), and the dependence on the QPC opening is less clear, suggesting that these interferometers are highly sensitive to their environment and the history of the sample.

The fact that the interference disappears between 1 and 4K suggests that the Fabry-Pérot in which they form is about  $1 \mu\text{m}$  long, as discussed in the previous chapter. It also reveals that they may be similar to the ones observed in scanning gate experiment, as they present roughly the same temperature dependence.

### 4.2.3 Dependence on magnetic field

The effect of a magnetic field applied perpendicularly to the 2DEG brings interesting informations on the interference. A colorplot of the transconductance as a function of both  $V_{g3}$  and magnetic field is plotted Fig.4.7a, recorded on QPC B open to the first plateau.

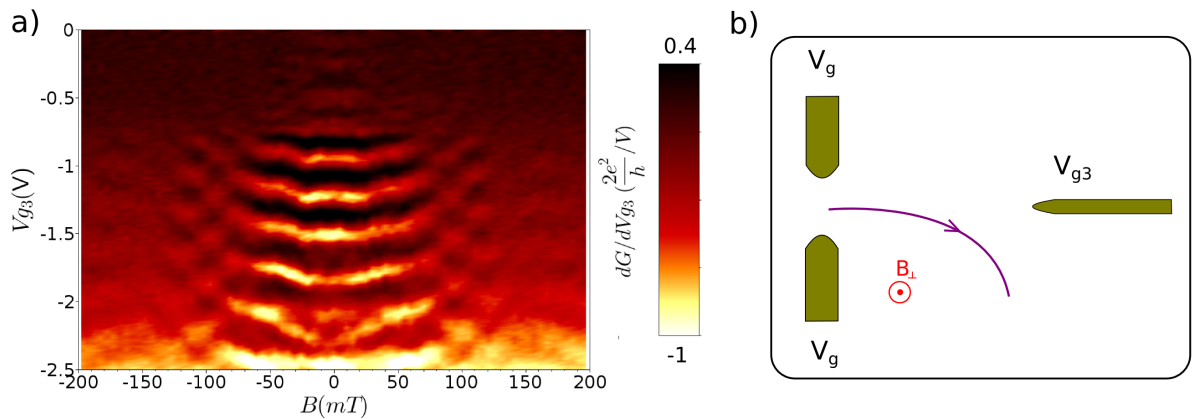


**Figure 4.7** *Effect of a perpendicular magnetic field: a) Transconductance as a function of  $V_{g3}$  and perpendicular magnetic field strength, the QPC being on the first plateau. This data were recorded in Grenoble on QPC B, at a base temperature of 50 mK. b) Schematics of the experiment under magnetic field, the electron trajectories drawn in purple are bent by the Lorentz force.*

On this plot, a striking feature is that the interference disappears for magnetic field of about 100 mT. This can be understood by the effect of a perpendicular magnetic field which is to bend the electron trajectories coming out of the QPC. The typical curvature radius of the trajectories is the cyclotron radius  $r_c = m^*v_F/eB$ . When this radius becomes of the order of the Fabry-Pérot cavity size in which this interference occurs, the interference is expected to disappear, as the electron trajectories are too much bent to allow several round-trips in the cavity. The field at which the interference disappears ( $\sim 100\text{mT}$ ) corresponds to a cyclotron radius of 900 nm. This therefore suggests that the interference directly occurs between the QPC and the third gate, situated  $1.2 \mu\text{m}$  away from the QPC in this specific sample. In case of interference induced by reflections on the disorder potential and the tip, there would always be some closed paths to interfere even with strongly curved trajectories.

Some remaining weak interference fringes are visible at higher fields, up to 200 mT, that might be due to trajectories assisted by disorder in the leads, though a deep understanding of this effect has not been achieved despite the extensive simulations presented in the following section.

#### 4.2.4 Polarization influence

The evolution of the interference with DC source-drain bias is surprising. An example is given Fig.4.8, when the QPC is open just below the first plateau. The signal is recorded analogically by applying a 30 mV AC excitation on the third gate and recording the current flowing through the QPC at this frequency by a lock-in technique. A first noticeable effect is that the average signal of the transconductance is proportional to the applied DC bias (see Fig.4.8a). It is not really surprising as the current flowing through the contact is proportional to this bias, so are its modulations by the third gate. To get rid of this effect, we subtract the average value of the signal for each value of  $V_{sd}$ . The obtained signal is plotted Fig.4.8b.

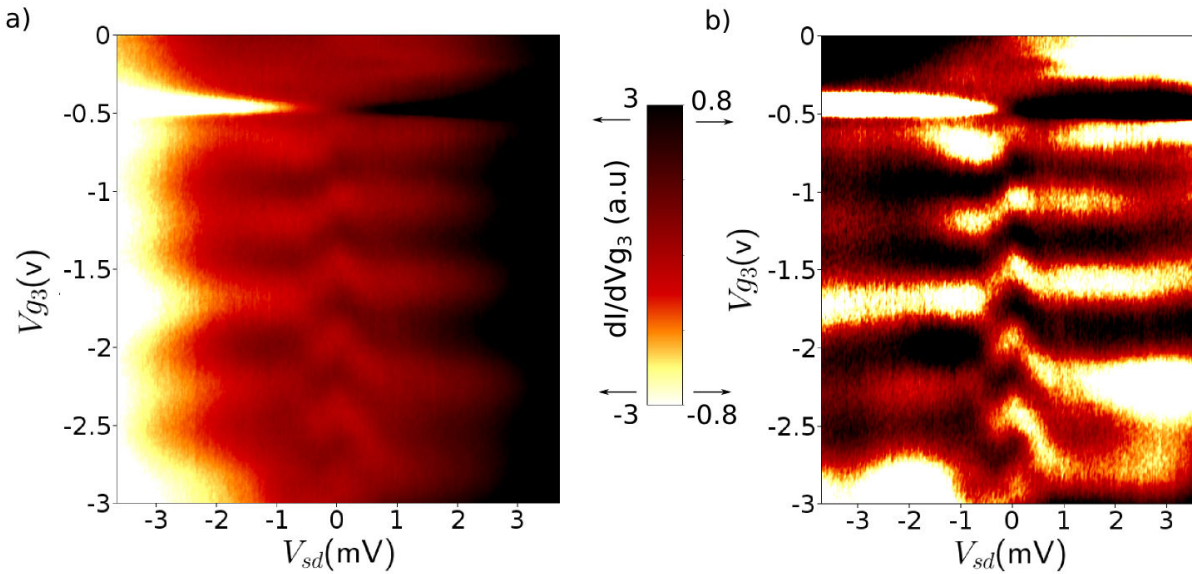


**Figure 4.8** *Effect of a DC source-drain bias: a) Analogical transconductance for sample B, just below the first plateau ( $V_g = -1.3V$ ), as a function of  $V_{g_3}$  and DC source-drain bias  $V_{sd}$ . b) Same data but the average signal over the different  $V_{g_3}$  has been subtracted to each vertical line at given  $V_{sd}$  to get rid of the background signal proportional to  $V_{sd}$ .*

The interference survive up to more than 3 mV of source-drain bias. As for the ones observed in SGM experiments and discussed in Chapter 3 (see Fig.3.11), this corresponds to energies comparable to the QPC 1D subbands spacing, and it is surprising to see that interference still survive up to such high biases.

The interference slightly accumulate phase with increasing source-drain bias, but in a different way that what was observed in SGM experiments. Indeed, the interference changes by half a period within a 7 mV of polarization difference. This contrasts with the displacement of the SGM fringes discussed in section 3.3.4, that moved by one period for a 2mV applied bias. An explanation might lie in the fact that during the experiment presented Fig.4.8, the bias voltage is applied on the contact located on the other side as the third gate. Then the two effects discussed in section 3.3.4 (the displacement of the QPC along transport axis with source-drain and the increasing wavelength that has to be compensated) have opposite effects. Unfortunately, we do not have data for an excitation on the side of the scatterer, which would allow to clearly elucidate this point.

A last feature visible in Fig.4.8 is a phase shift of the interference fringes at zero bias. This phase shift is related to the one visible Fig.4.4 as a function of gate voltage and will be extensively discussed in the light of more detailed SGM experiments in Chapter 6.

## 4.3 Numerical simulations

### 4.3.1 Interference without disorder

To complement the experiments, we use Kwant to investigate theoretically these interferometers. The device is modeled with two gates for the QPC and an additional one to model the scattering gate in front of the QPC. We choose to model the scattering gate by the analytic expression described in Ref.[16], using several rectangles to define a sharp apex.

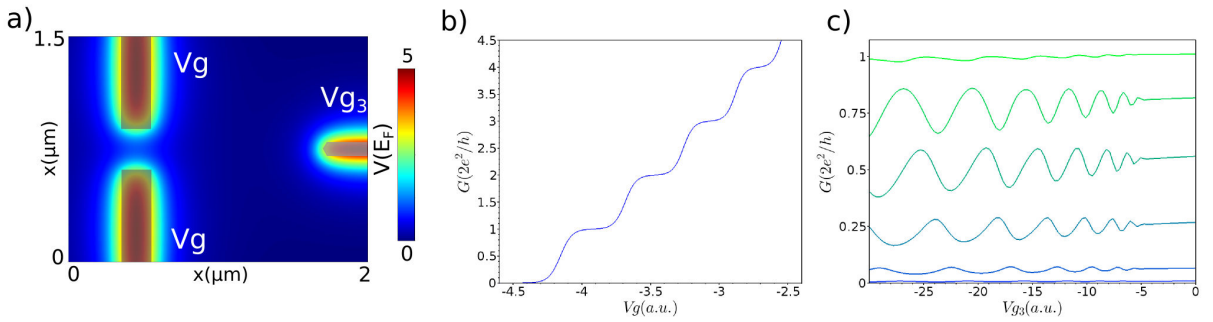


**Figure 4.9 Modeling the interferometer:** a) Potential map generated following the Davies' method [16] scaled to  $E_f$ . The corresponding gates shape are represented as gray polygons. b) Conductance as a function of the split gate voltage  $V_g$ . c) Conductance as a function of the third gate voltage  $V_{g_3}$  for different openings from the pinch-off to the first plateau.

(Fig. 4.6a). The conductance curve versus split-gate voltage is shown in Fig.4.9 in absence of disorder in the 2DEG. Applying a negative voltage  $V_{g_3}$  on the third gate indeed generates interference in the total conductance (Fig.4.9c). In this figure, traces of the total conductance as a function of  $V_{g_3}$  are shown for different QPC openings. As in the experiment, a sufficiently negative gate voltage (-5 arbitrary units) is required to generate interference, that corresponds to the depletion threshold of the 2DEG below the third gate. Then interference is clearly seen as a function of  $V_{g_3}$  for lower gate voltages. The first difference with the experiment is that the fringes spacing is not constant in  $V_{g_3}$ , but tend to enlarge as  $V_{g_3}$  is lowered. Though this effect is also present in the experiment, it is much less important. In the different interferometers, the fringe spacing in  $V_{g_3}$  was found to vary by roughly 30% depending on the sample and the hysteretic effect discussed above, whereas in this simulation it varies by 100%. This could be attributed to the way the effect of a gate voltage in the 2DEG is modeled. The way the depletion region enlarges with  $V_{g_3}$  is the key point to understand the periodicity of these fringes, as this governs the displacement of one mirror of the Fabry-Pérot cavity. As this mirror is the interface between a completely depleted region and the remaining part of the 2DEG, a correct calculation should take the 2DEG into account. Therefore, modeling the electrostatics

with the method proposed in Ref.[16] cannot accurately estimate this effect, which could explain this difference with the experiment.

A second important difference is that the contrast of the interference when the first mode is fully opened is really low compared to the case of half transmission. As discussed in the previous chapter and sketched Fig.3.8, this is what is expected from a simple single-mode Fabry-Pérot cavity since a perfect mirror does not form any cavity. The 2D quantum simulations show that it is also the case for the real device geometry, when mode-mixing between the QPC and the 2DEG and angular divergence of electron waves in the 2DEG are taken into account. We discuss in the following section how residual disorder could bring more contrast on the plateaus, as it is observed experimentally.

### 4.3.2 The role of disorder

The disorder in the 2DEG is now taken into account, following the method explained in Chapter 1 and Chapter 3 section3.5.

Including disorder in the numerical model reveals that contrasted fringes now appear also on the plateaus. An example for a specific disorder configuration is presented Fig.4.10. The disorder tends to increase the contrast of the interference on the plateau, and this effect is retrieved for a large range of disordered potential landscapes, though a few specific configurations lead to an opposite effect or strange interference patterns (not shown here). Fig.4.10b compares the interference for clean and disordered leads (different colors), in the case of half-transmitted and fully transmitted first mode. It appears clear that in the disordered case some high contrast is recovered even when the first mode is fully transmitted, although it remains larger in the transition.

Comparison of Fig.4.10c and 4.10d shows that the interference fringes are visible only in the transitions in absence of disorder, but everywhere in presence of disorder. Note that the second mode does not show any interference in absence of disorder due to the node of the wave function along the horizontal axis where the third gate is located, but that contrast is recovered in presence of disorder.

We now discuss the phase of the fringes versus split-gate voltage which gives information on the cavity size. The tilted fringes indicate that the interference accumulates phase as the QPC opens, in a way that seems overestimated compared to the experiment. A negative voltage applied on the split-gates affects the interference, and one of the reason could be that the electrons wavelength enlarges as they approach the QPC, in a way that depend on the QPC opening. Hence changing the gate voltage  $V_g$  can affect the interference state in the Fabry-Pérot cavity and so the phase of the interference. This effect tends to be overestimated if one does not take into account screening of the gate voltage by the 2DEG, which could reasonably explain the difference between the experiment and the model (see Fig.4.4b).

Another important difference is the dramatic effect that takes place below the first plateau in the experiment. The dephasing of  $\pi$  of the interference fringes at the 0.7 anomaly visible Fig.4.4b and Fig.4.5 is not reproduced in the model. The 0.7 anomaly indeed results from electron-electron interactions, which are not included in the simulations. The  $\pi$  phase shift observed at the 0.7 anomaly could be attributed to the Kondo effect at play below the first plateau as discussed in chapter 6.

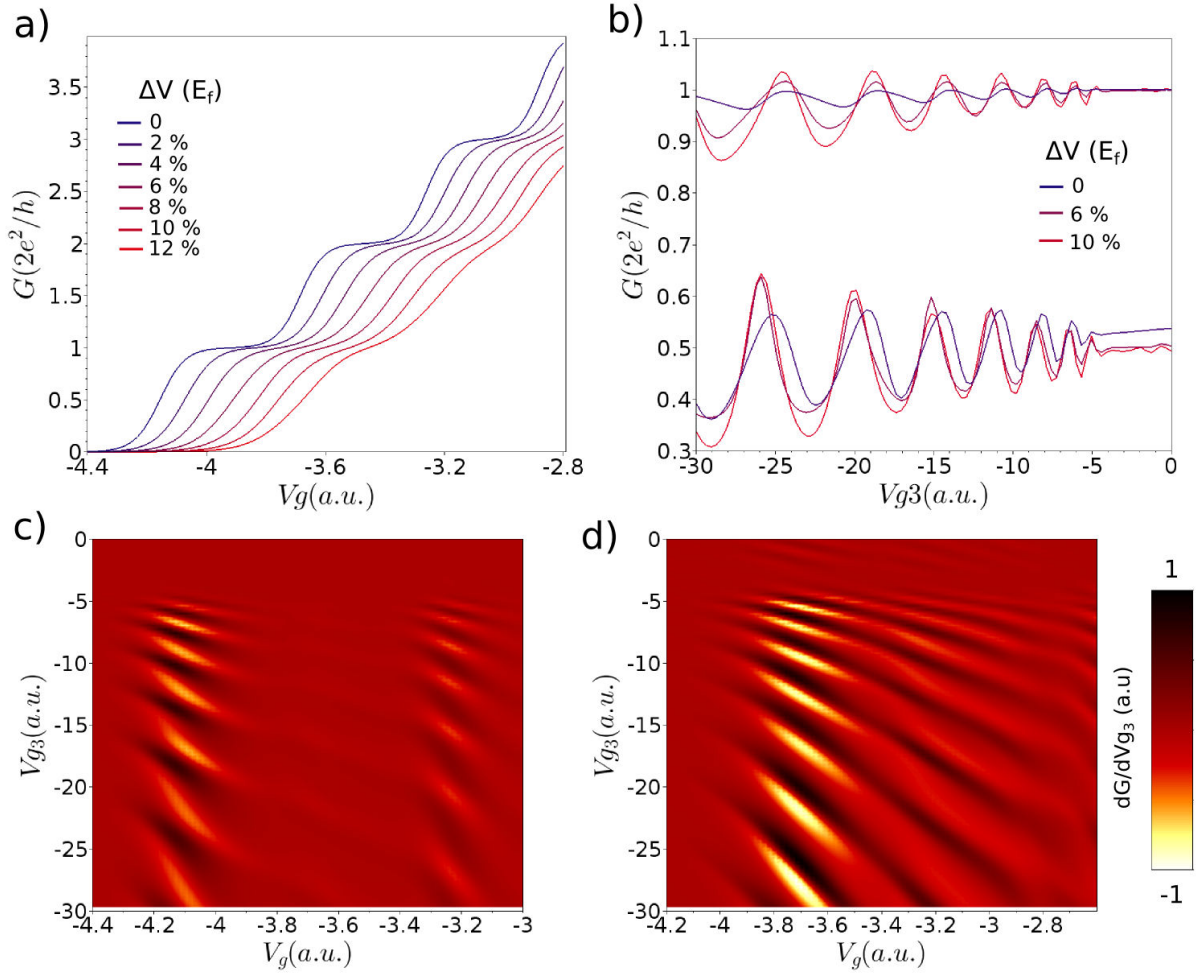


**Figure 4.10** *The role of disorder:* a)  $G(V_g)$  for different potential fluctuations FWHM  $\Delta V$  from 0 to 12% of  $E_f$ , for the chosen disorder landscape in this example. b) Conductance as a function of  $V_{g3}$  at half and full transmission of the first mode, for different disorder amplitudes. c) Full characterization of  $\partial G/\partial V_{g3}$  as a function of  $V_g$  and  $V_{g3}$  in the case of a perfect 2DEG. d) Same characterization for a disorder of fluctuations amplitude FWHM 10% of  $E_f$ .

### 4.3.3 Modeling magnetic field

Kwant also enables us to simulate the effect of an external magnetic field, applied perpendicularly to the 2DEG by adding a phase in the hopping term between two adjacent sites. We use this possibility to investigate the effect of a perpendicular magnetic field in these interferometers. The main results are summarized in Fig.4.11 for a given disordered potential landscape.

The main effect of a perpendicular magnetic field is to destroy the interference as soon as the corresponding cyclotron radius overcomes the distance between the QPC and the scatterer. The corresponding wave-functions coming out of the QPC under different magnetic field are presented Fig.4.11c. With increasing magnetic field, the amplitude of the density modulation in the Fabry-Pérot cavity become weaker, and eventually disappear when the electronic trajectories are too much bent to reach the scatterer.

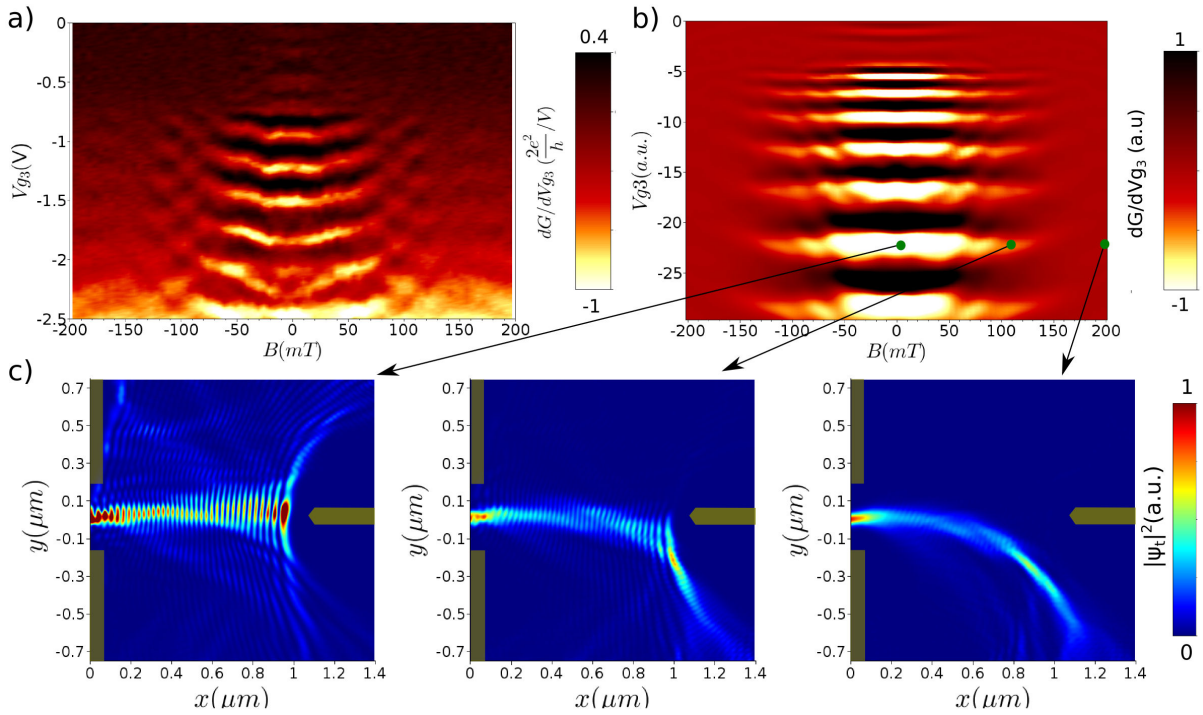


**Figure 4.11** *Simulations of magnetic field:* a) Experimental trace of the measured transconductance  $dG/dV_{g_3}$  as a function of  $V_{g_3}$  and magnetic field (same as Fig.4.7a). b) Simulation of  $dG/dV_{g_3}$  as a function of  $V_{g_3}$  and  $B$ . c) Transmitted wave functions corresponding to different specific magnetic field. From left to right: 0, 120 and 200 mT.

A computation of the transconductance  $\partial G/\partial V_{g_3}$  is presented Fig.4.11b, and is strikingly similar to the experimental result reminded Fig.4.11a. In particular, these interference fringes disappear around the same value of about 100 mT.

Another similarity with the experiment is the weakening of the interference with increasing field that does not occur smoothly but with oscillations. That is not the case when the system is modeled without including disorder (not shown here). These oscillations depend on the exact disorder configuration, but a more detailed investigation would be required to really understand their origin. In particular, it could be interesting to understand whether it can be connected to the disorder correlation length. The fact that these oscillations are not present when the system is modeled without including disorder indicates that the real devices also contain some disorder. However, the coincidence of the characteristic field (100 mT) in both theory and experiment shows that the interference results essentially from electron trajectories between the QPC and the tip.

## 4.4 Conclusion

In this Chapter, we have presented a new type of ballistic interferometers formed with a quantum point contact and a distant scatterer typically one micron away, realized by a thin metallic gate. Applying a negative voltage on this gate enlarges the depletion region below this gate and backscatters the electrons coming from the QPC. This creates

constructive or destructive interference depending on the distance between the depletion region and the QPC.

Temperature and magnetic field dependence support the fact that this interference probably take place in the Farby-Pérot cavity formed between the QPC and the sharp gate. Including a disordered landscape in a numerical model indicates that disorder could be responsible for the observed contrast on the plateau, that a simple single mode Fabry-model or a disorder-free numerical model cannot account for.

Striking similarities between these interference fringes and the ones observed in SGM experiments Fig.3.6 suggest that they share a common origin, namely the modulation of density of states in the cavity formed between the QPC and the distant scatterer.

Finally, a surprising sharp phase shift of the interference occurs between the 0.7 regime and the first plateau is always observed, that cannot be reproduced within extensive single-particle simulations, and will be clarified in Chapter 6.

#### 4.4. CONCLUSION

---

# Chapter 5

## Wigner and Kondo physics in quantum point contacts

### Contents

---

<b>5.1</b>	<b>Kondo effect in quantum dots and quantum point contacts</b>	<b>90</b>
5.1.1	The Kondo effect in mesoscopic physics	91
5.1.2	Non equilibrium Kondo effect	93
5.1.3	Two-impurity Kondo effects	94
5.1.4	Odd and even Kondo effect in QPCs	95
<b>5.2</b>	<b>Wigner crystallization revealed by scanning gate microscopy</b>	<b>98</b>
5.2.1	Conductance anomalies without tip	98
5.2.2	Isotropic rings in SGM images	99
5.2.3	Modulation of the 0.7 anomaly	102
5.2.4	Modulation of the zero bias anomaly	103
5.2.5	Interpretation in terms of Wigner crystallization	105
5.2.6	Reproducibility in a second sample	110
5.2.7	Higher conductance analogues	113
<b>5.3</b>	<b>Conclusion</b>	<b>116</b>

---

*The simplicities of natural laws arise through the complexities of the language we use for their expression.*

Eugene Wigner

## Introduction

This chapter presents the major result of this thesis. We will see how the polarized tip of a scanning gate microscope can be used to finely tune the potential of a quantum point contact, and how it can affect the many-body state forming in the low density regime. Thanks to this subtle manipulation of the many-body effects at play in this regime, we can get crucial informations on some mechanisms involved in both the 0.7 anomaly and the zero bias anomaly.

Since the Kondo effect is central in the analysis of the experimental results, We will start by a presentation of the various situations where Kondo-enhanced conductance peaks can be observed. We will then describe a recent experiment that shares strong similarities with our results. The group of Caspar van der Wal (Gröningen, Netherlands), during the thesis of Muhammad Javaid Iqbal [88], demonstrated that a definite number of electrons can localize in QPCs despite the fact that these devices are by essence open systems. We will first describe their experiments and before turning to our SGM results.

We will then see how approaching the polarized tip to the QPC modulates both the zero bias anomaly and the 0.7 anomaly, revealing alternating single or split peaks in the differential conductance, together with an alternating visibility of the 0.7 anomaly. We will discuss some possible scenarios and finally interpret these alternations as arising from a Wigner crystal forming in the channel, containing alternatively an odd or even number of charges, that can be controlled by the tip position. Depending on this parity, a resulting odd or even Kondo effect leads to a single ZBA or a split ZBA in the differential conductance curves.

Simple models and electrostatic simulations have been done to show that the 1D electron density is low enough to indeed produce Wigner crystallization in the channel.

To confirm our experimental results, we show the reproducibility of these observations on a second sample. Finally we discuss the fact that this Wigner crystal could survive up to several open modes in the QPC, possibly explaining the “0.7 analogues” above the first plateau.

## 5.1 Kondo effect in quantum dots and quantum point contacts

Last year, the open problem of conductance anomalies in QPCs has regained interest thanks to a major result in this field. As stressed in a recent review on these conductance anomalies[30], a clear experimental investigation of how the exact shape of a QPC potential does affect the conductance anomalies was still lacking at this time.

In the van der Wal group, an interesting study of how QPC’s geometry influences the conductance anomalies has been performed, as detailed in Iqbal’s thesis [88]. They first studied QPCs defined by two finger-gates, and designed several devices in which they varied the lithographic width and length of the constriction. This study was not conclusive, and no systematic influence of the geometry on neither the ZBA nor the 0.7 anomaly could be deduced, though these features were found to vary from sample to sample. Interestingly, the authors observed in several devices that the zero bias anomaly was not a single peak centered at zero bias, but found to be a split peak (a pair of peaks at finite

and opposite biases), for different ranges of QPC openings within the first transition. The authors stipulate that this split peak was the signature of an interesting out of equilibrium many-body phenomenon, namely “even Kondo effect”, that we briefly explain in the following.

### 5.1.1 The Kondo effect in mesoscopic physics

At this point, it should be clarified what is the Kondo effect. In simple words, it results from the screening of a magnetic impurity by the surrounding conduction electrons. In that sense, it is by essence a many-body effect. It was first proposed by Kondo to explain the anomalous increase in resistivity of metals at low temperature, when they contain dilute magnetic impurities. This problem has been studied in the 30’s, revealing that unlike usual metals, gold exhibits a strange behavior at low enough temperature[89] (Fig.5.1a).

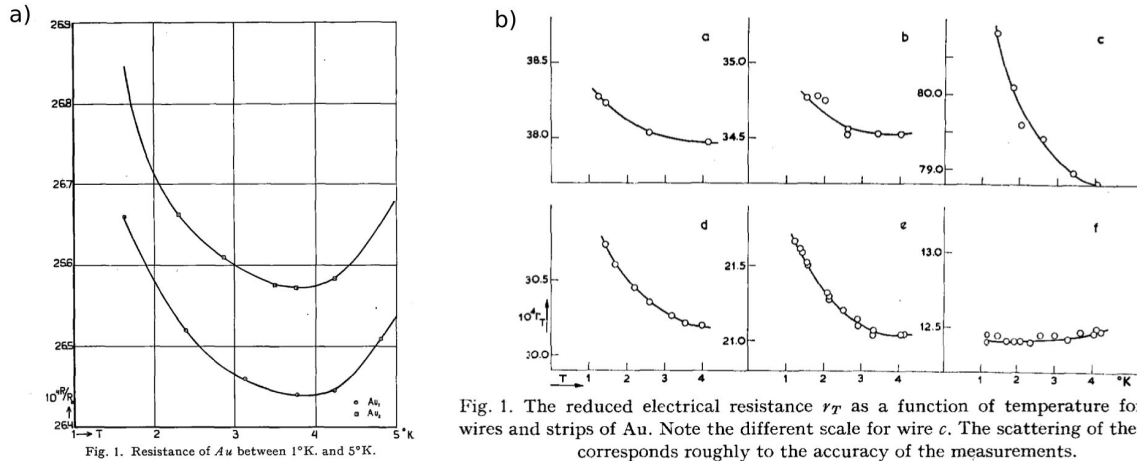


Fig. 1. The reduced electrical resistance  $r_T$  as a function of temperature for some wires and strips of Au. Note the different scale for wire  $c$ . The scattering of the points corresponds roughly to the accuracy of the measurements.

**Figure 5.1 Existence of a resistance minimum for metals:** a) First experimental evidence that gold resistance re-increases at low enough temperature. Adapted from [89]. b) Resistance of gold as a function of temperature for different magnetic impurity concentrations. Adapted from [90]

In metals, a dominant mechanism that limits the conductivity of the electrons is their scattering by the lattice vibrations (phonons). This mechanism tends to decrease with lowering temperature, so does the metals resistivity. However, in gold containing magnetic impurities, the resistivity was found to re-increase with lowering temperature below a given threshold. This anomaly has waited 30 years to be clearly attributed to magnetic impurities and the temperature dependence of the resistivity to be systematically studied depending on the impurities concentration [90](Fig.5.1b). At the same period, this apparently anomalous effect has been theoretically explained by Jun Kondo [91], who calculated the scattering rate of conduction electrons on magnetic impurities, and its temperature dependence. Thanks to the very good agreement with experiment and the beauty of the exact calculation, this example has then become the paradigm of solvable many-body quantum problems.

## 5.1. KONDO EFFECT IN QUANTUM DOTS AND QUANTUM POINT CONTACTS

This interesting mechanism has recently regained interest with the advent of nanoelectronics and the ability to study transport *through* a site containing a single magnetic impurity. The possibility to observe the Kondo-effect at the single-site level in mesoscopic physics has first been proposed theoretically, predicting an increased conductance when the Fermi levels of source and drain of reservoirs connected through a single magnetic impurity are aligned[14, 92]. This phenomenon, attributed to a resonant transmission through the impurity eased by collective spin phenomenon was predicted to be observable for temperatures below the so-called Kondo temperature  $T_K$ , that exponentially depends on the tunneling rate between the impurity and the leads.

A suitable system in which this effect can be observed and controlled is a quantum dot, a small electronic island isolated from the leads by tunnel barriers. The number of localized electrons is tunable at will with a gate, and one can choose to have an odd number of electrons in the dot. While sweeping the gate voltage, each electron added to the quantum dot occupies a new accessible level. If we assume that these levels are spin-degenerate, each first added electrons on a new level has for example a spin up, and the next one carries a spin down. In the case of an odd number of electrons in the dot, a single spin remains unpaired. In this configuration, the resulting island carries a single spin  $1/2$ . For this single localized spin to be screened by the surrounding electrons from the leads, some conditions are required. On one hand, the tunnel barriers have to be high enough such that the number of electrons remains well defined, and on the other hand the tunnel barriers have to be small enough for the Kondo effect to develop on a large enough energy scale compared to the experimentally accessible temperature range. This makes the Kondo effect on such a system challenging to observe experimentally.

This effect has been observed a decade after its proposal, on weakly confined GaAs/AlGaAs quantum dots[93, 94, 95].

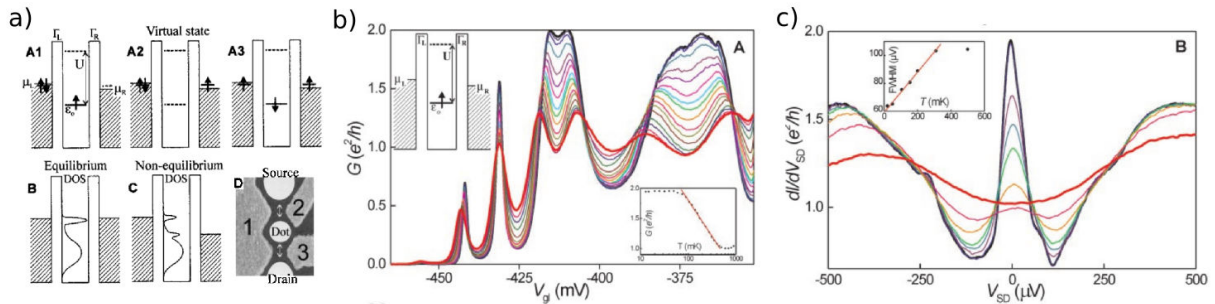


**Figure 5.2 Kondo effect in quantum dots:** a) Schematics of one of the first experiments on tunable Kondo effect through a quantum dot. The density of states in the quantum dot containing an even number of electrons is presented on B (at equilibrium) and C (out of equilibrium). Adapted from [94]. b) Kondo effect in the unitary limit. The conductance as a function of plunger gate voltage in the linear regime is presented for different temperatures between 15mK (blue curve) and 800mK (red curve). In the ranges of gate voltage where an odd number of electrons are localized, the conductance increases with lowering temperature to reach the conductance quantum. c) Non-equilibrium spectroscopy of the Kondo resonance centered at zero bias for different temperatures. Adapted from [95]

By the means of the plunger gate voltage, the number of electrons in the quantum dot can be tuned. Each time the number of electrons is changed by one, the conductance

exhibits a peak, known as a Coulomb blockade peak. It corresponds to a situation where the source and drain Fermi levels are aligned with an energy level of the dot, leading to an enhanced conductance. This effect can be dramatic in the case of strongly confined electrons (i.e. high tunnel barriers), leading to zero conductance between these peaks, whose width are given by the inverse of the tunneling rate in the zero temperature limit. However, in the experiments presented Fig.5.2, the confinement is voluntary weak to get an important Kondo effect, hence the Coulomb blockade peaks appear as smooth oscillations in the conductance. These peaks separate situations in which successively odd or even number of electrons are localized in the dot. With lowering temperature, the conductance between two successive valleys either decreases with lowering temperature, or rise to reach the conductance quantum  $2e^2/h$ . The explanation lies in the Kondo processes. In the valleys containing an odd number of electrons, the quantum dot contains a net spin  $1/2$ , making Kondo screening of this impurity by the leads possible, and leading to an increased conductance. However, in the valleys with even occupations the total spin is zero, hence no Kondo effect is possible, and the conductance decreases with temperature as expected for simple Coulomb blockade.

In the valleys with an odd occupancy, the Kondo effect can be seen as an enhanced density of states (DOS) in the dot, at the Fermi level of the reservoirs. When the source and drain are aligned (see Fig.5.2a situation B), this peak in the density of states leads to an increased conductance through the dot.

The finite bias situation is presented Fig.5.2c. By adding a DC source-drain voltage, the source and drain levels are misaligned, destroying the Kondo resonance in the transmission. However, each lead still screens the quantum dot spin, that gives rise to two peaks in the density of states at the Fermi energy of each lead.[96]. But as these two resonances do not overlap, this effect does not ease transport through the dot. The corresponding situation is schemed Fig.5.2a, situation B. At finite bias, dissipative processes occur when the electrons cross from one chemical potential to the other which tend to minimize the height of these two peaks[97].

### 5.1.2 Non equilibrium Kondo effect

When a magnetic field is applied on a quantum dot with an unpaired electron (odd occupancy), the spin degeneracy is lifted by the Zeeman energy  $g^* \mu_B B$ , where  $g^*$  is the Landé factor that depends on the material,  $\mu_B$  is the Bohr magneton and  $B$  is the magnetic field. In order to screen this polarized spin, conduction electrons from the leads now need a finite energy to tunnel in the excited state and flip the spin. This process is only possible in a non-equilibrium situation with different chemical potential in the two leads  $\Delta\mu = g^* \mu_B B$ . The resulting Kondo effect is an enhanced inelastic cotunneling process that screens the spin of the dot.

An equivalent description of this effect can be done by considering the DOS of the dot. When an external magnetic field is applied to a Kondo system, it unbalances the two possible spin states. As a consequence it splits each peak of the DOS associated with the two leads Fermi energy by  $g^* \mu_B B$ , as schemed Fig.5.3 . At equilibrium, there is no more increase of the conductance at low temperature because the peak in the DOS is split [98]. By unbalancing the two chemical potentials, 4 peaks appear in the DOS (Fig.5.3b). Two situations allow to recover the conductance enhancement due to the Kondo process, when

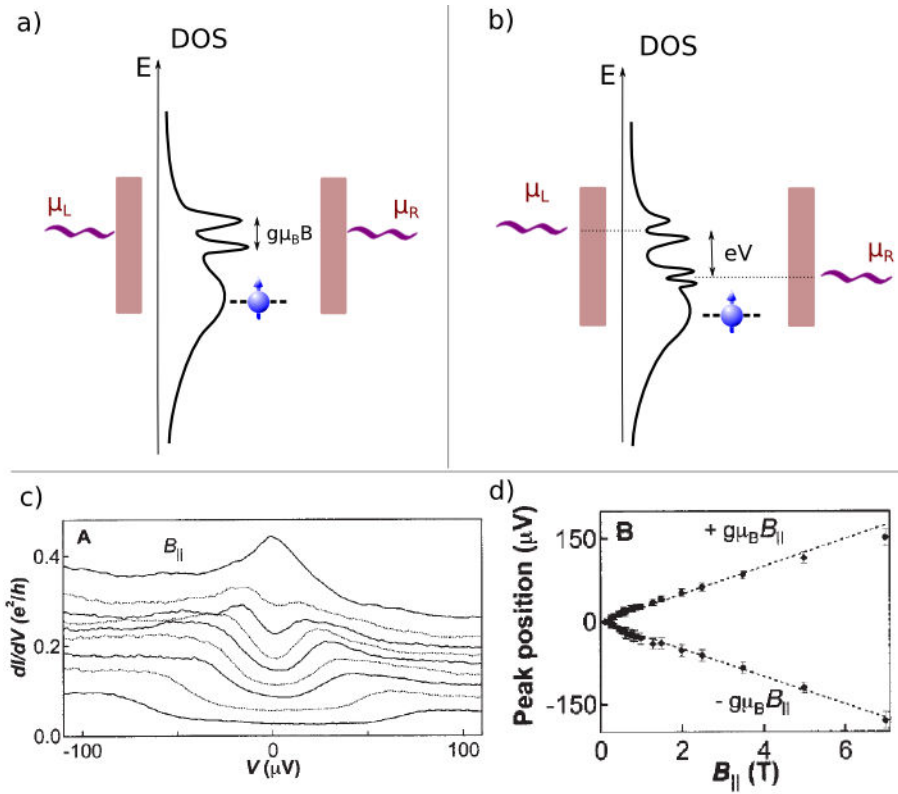


**Figure 5.3 Kondo effect under magnetic field:** a) DOS in an oddly occupied dot under magnetic field, when the source and drain are aligned. DOS when source and drain are misaligned. Each peak in the DOS associated with one lead splits into two peaks, resulting into 4 peaks in the DOS. c) Splitting of the Kondo peak in a quantum dot under magnetic field from 100 mT (upper curve) to 3.49T (lower curve). d) Spacing of the side peaks as a function of magnetic field. c) and d) are adapted from[94]

the upper peak (in energy) associated with one lead matches the lower peak associated with the other lead, and vice versa. These two situations produce peaks in the differential conductance at positive and negative bias, separated by  $2g^*\mu_B B$ . A good agreement with this prediction is found in experiments[94, 93] and shown Fig.5.3c and d.

### 5.1.3 Two-impurity Kondo effects

Interesting theoretical proposals followed these pioneer experimental results: the possibility to explore a "two-impurity Kondo effect" in coupled quantum dots [99, 100]. These works suggested that in well coupled series quantum dots, richer Kondo physics could be observed, with the possibility of observing a non-equilibrium Kondo resonance at finite bias at zero magnetic fields. This situation corresponds to two separate quantum dots, containing each a net spin 1/2. The total state of these two dots can therefore be a singlet or a triplet, depending on the tunnel and exchange couplings between these two spins. This therefore resembles to the situation of a single electron under magnetic field, with two different spin states having a different energy. Using a specific gate in the middle, the coupling between these two dots can be tuned independently from their occupation

and respective couplings to the leads. In a situation where the mutual coupling is greater than the two couplings to the leads, split peaks are expected for two coupled dots in a singlet state  $S=0$  due to non-equilibrium Kondo effect on the triplet state  $S=1$ . This is indeed observed experimentally by realizing this situation[101].

Finally, the non-equilibrium Kondo effect can also be observed in a single quantum dot containing an even number of electrons[102]. In this situation, the ground state is a singlet state that carries no net spin, but a non-equilibrium Kondo effect can arise, as the excited triplet state carries a net spin 1. This specific situation leads to enhanced conductance when the misalignment of the source and drain Fermi levels exactly matches the energy separation of the ground and excited state, leading to two peaks at opposite finite biases in the conductance. Since then, this "even Kondo effect" has then been observed in different systems, including for example molecular junctions [103] (a single molecule quantum dot), or carbon nanotubes[104]. Note that a singlet-triplet transition of the ground state can occur for certain quantum dot parameters and appears as a crossover between finite bias peaks (singlet) and a zero bias peak (triplet).

#### 5.1.4 Odd and even Kondo effect in QPCs

As mentioned in the introduction of the chapter, these two types of Kondo phenomena have been recently observed in quantum point contacts [9], using tunable-in-length devices.

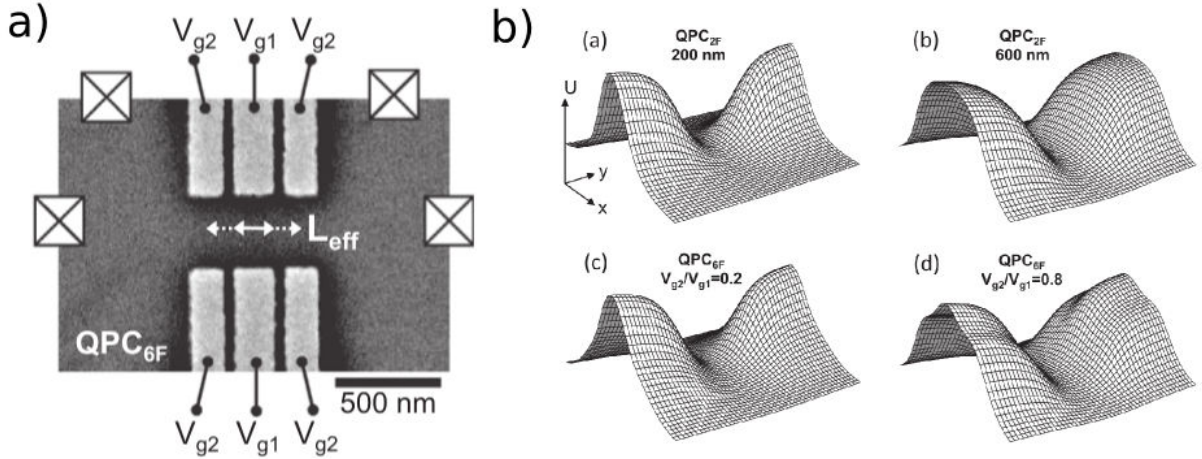


**Figure 5.4** *Tunable in length quantum point contacts:* a) Lithographic pattern of the tunable-in length devices. b) Electrostatic potential created by simple split-gates QPCs ( $QPC_{2f}$ ) and the tunable devices with 6 gates ( $QPC_{6f}$ ). Adapted from [105].

These devices were aimed to study the influence of the QPC geometry on the 0.7 anomaly. A first experimental characterization of these devices in the framework of single-particle transport has been carefully realized, and reported in ref.[105]. The samples are presented Fig.5.4a. By playing on the voltage difference between the central finger-gates and the lateral ones, the effective length of the channel formed electrostatically in the

## 5.1. KONDO EFFECT IN QUANTUM DOTS AND QUANTUM POINT CONTACTS

2DEG can be tuned. To evaluate the resulting geometry, the author used the method presented in Ref.[16], and performed simulations presented Fig.5.4b.

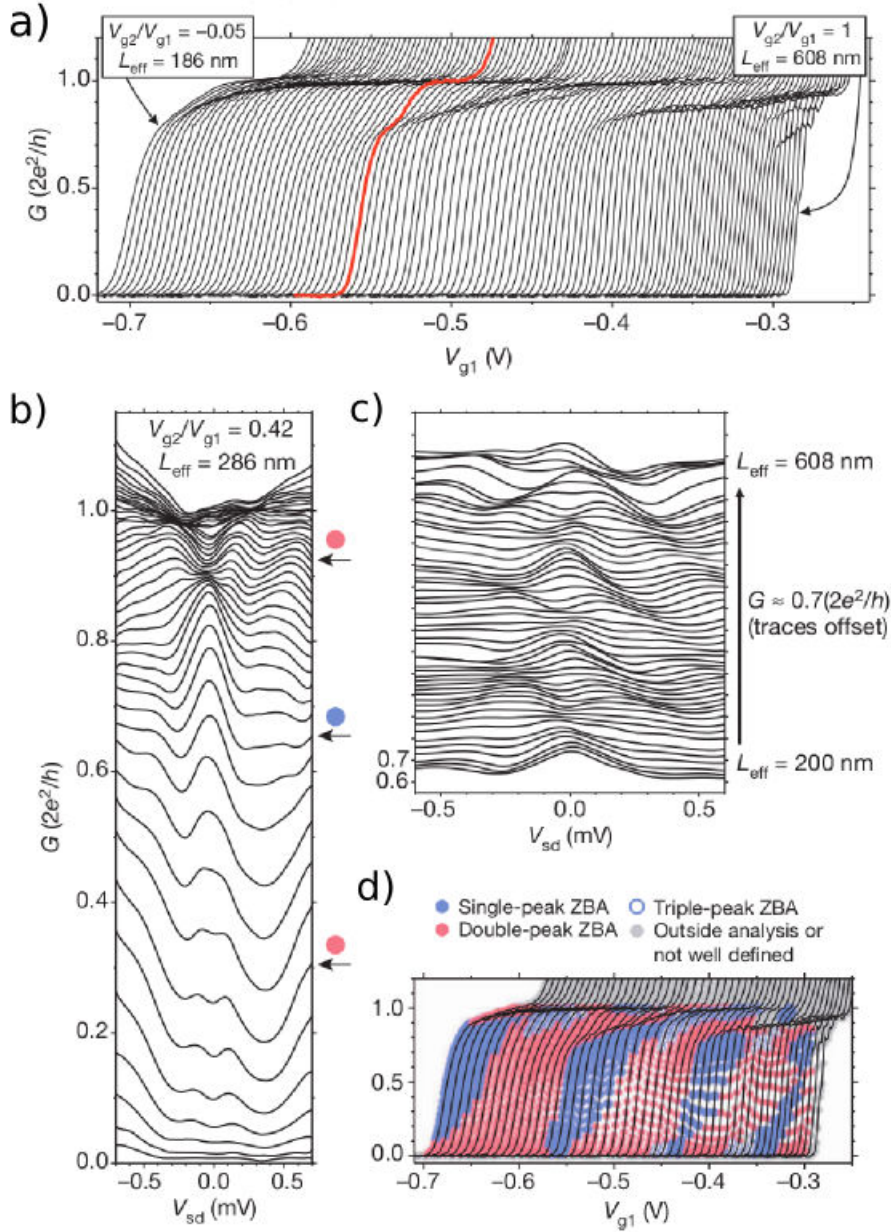


**Figure 5.5 Many-body effects tuned by effective channel length:** a) Traces of linear conductance  $G(V_{g1})$  for different channel lengths controlled by the ratio  $V_{g1}/V_{g2}$ . b) Spectroscopy of the QPC for a given  $L_{eff}$ , the ZBA appearing alternatively as a single peak and split peaks as the QPC opens. c) Linear conductance traces as a function of source-drain bias for a given QPC opening and different channel lengths. d) Complete analysis of the ranges in which the ZBA is found to be a split or a single peaks for different QPC openings (below the first plateau), and different  $L_{eff}$ . Adapted from [9].

They also performed an intensive exploration on the transport regimes obtained with these devices, depending on the gate voltage ratio  $V_{g1}/V_{g2}$ . They found that for values

of  $V_{g1}$  lower than  $V_{g2}$ , the devices essentially behave as usual quantum point contacts, whereas for values of  $V_{g2}$  lower than  $V_{g1}$ , quantum dots were formed.

They then investigated the behavior of these devices in the QPC regime, changing the effective length  $L_{eff}$  by playing on the gate voltage ratio  $V_{g1}/V_{g2}$ , and made a really important observation. As the QPC channel is made longer, at low temperature (80mK), the 0.7 anomaly is found to successively appear and shade off, up to three times in the accessible range of experimental parameters. (Fig.5.5a)

Interestingly, these successive modulations of the 0.7 anomaly correspond to simultaneous modulations of the ZBA character. For a given QPC opening, the ZBA is found to be alternatively a single peak or split peaks as  $L_{eff}$  is changed (Fig.5.5b).

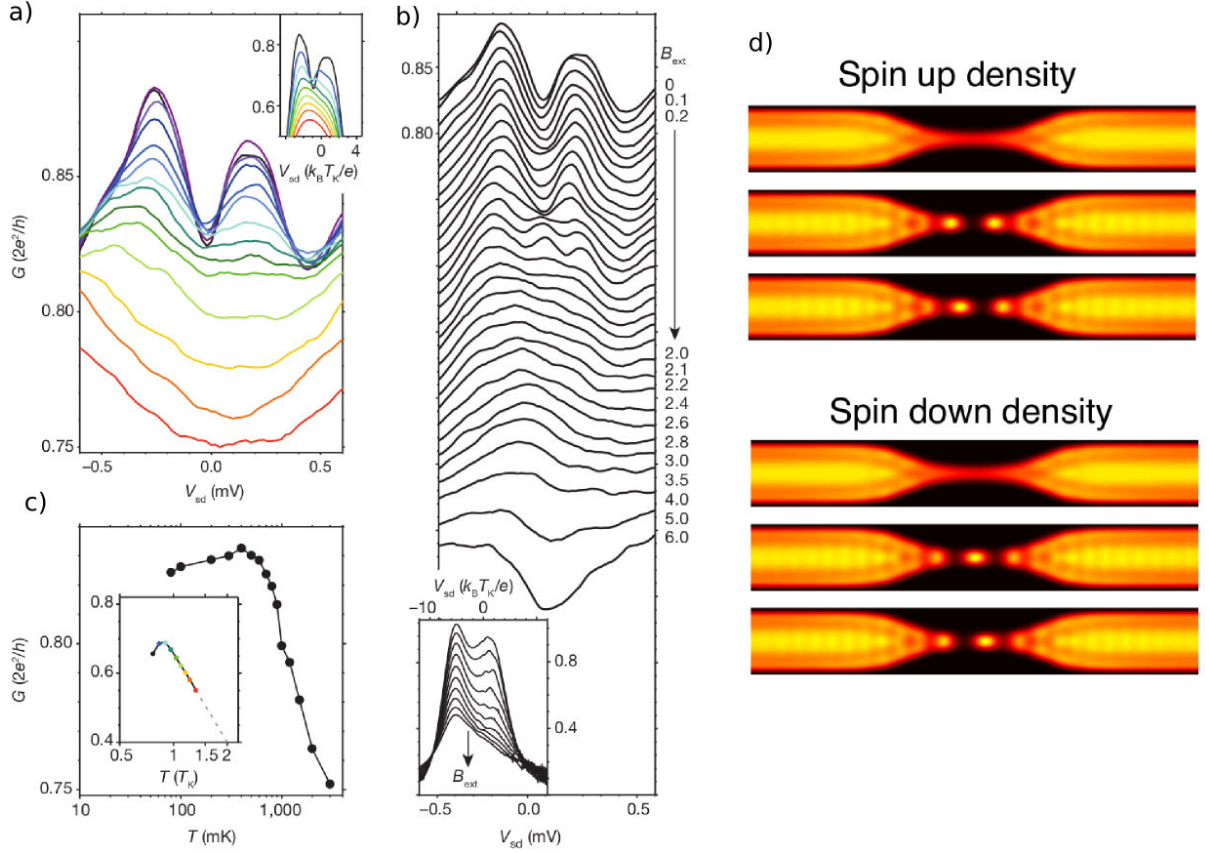


**Figure 5.6 Two-impurity Kondo effect:** a) Evolution of double-peak ZBA with temperature, between 3K (red curve) and 80mK (blue curve). b) Evolution of the double-peak with in-plane magnetic field. c) Evolution of the split ZBA conductance with temperature and comparison with a two-impurity Anderson model scaling (inset). d) Electronic density (from 0 to  $2.10^{14}m^{-2}$ ) obtained by SDFIT for the spin up and spin down species for the unpolarized solution and spatially symmetric and antisymmetric polarized solutions. Adapted from [9] and its supplementary informations.

The authors give an interpretation of this phenomenon in terms of a localized state, containing an odd or even number of electrons that can be controlled by changing the channel length. When an odd number of electrons is localized, it gives rise to a single-impurity Kondo effect, and a zero bias peak in the differential conductance, as described

and analyzed in Ref.[37]. However, when an even number of electrons is localized, simple Kondo effect cannot be observed as the ground state carries no net spin, but the triplet excited state can be probed in the spectroscopy, leading to non-equilibrium Kondo effect as in quantum dots. They performed numerical renormalization group calculations on a "two-impurity Anderson model" to justify the scaling of these split peaks with temperature and magnetic field, in good agreement with the experimental observations (Fig.5.6a-c). The fact that a finite number of electrons can localize in a QPC is not obvious, neither the fact that their number can be changed by the channel length.

To justify this interpretation, the authors performed spin-density functional theory to compute the realistic electronic density in a QPC including spin and coulomb interactions. The main result is presented Fig.5.6d), where a colorplot of the computed spin-up and spin-down densities is plotted. These simulations indicate that small islands containing one electron charge and one electron spin form in the channel, leading to a "chain" of adjacent opposite spins.

However, the parameter proposed to control the number of localized spins in this experiment is the effective length of the channel, which is defined based on a simple unscreened electrostatic model and choosing an arbitrary aspect ratio [105]. Though the signatures are really clear and the data and analysis pretty convincing, an underlying mechanism governing this localization is lacking, and we will see in the following that the analysis of our scanning gate microscopy experiment shines a new light on this point.

## 5.2 Wigner crystallization revealed by scanning gate microscopy

### 5.2.1 Conductance anomalies without tip

In the previous chapter, we discussed the scanning gate experiment in the vicinity of the fully transmitted first mode. In this section, we will extend our investigations below the first plateau, where signatures of electron electron interactions are visible in transport experiments (the 0.7 and zero bias anomalies). The results discussed in the first part of this chapter (except in section 5.2.6) were obtained on sample B.

Before looking at how SGM can affect many-body effects in the QPC, let's take a look at the transport features in the linear and non-linear regime in this sample, in absence of the tip. Fig.5.7b shows the linear conductance as a function of gate voltage, and one can see that the 0.7 anomaly is still visible, despite the fact that this measurement is recorded at a base temperature of 20mK, and an electronic temperature evaluated to be below 80mK. This contrasts with some studies (see for example Fig.2.3), in which the 0.7 anomaly completely vanishes at low enough temperature. Looking at non-linear transport Fig.5.7c, one can see the ZBA: a peak of increased differential conductance around zero bias. This peak disappears above 1K and its detailed temperature dependence is discussed on another sample in Chapter 6, section 6.2.2.1 . In Fig.5.7, the ZBA forms a single peak for conductances from 0 to roughly  $0.6 * 2e^2/h$  and splits into two peaks centered at  $\pm 250\mu V$  above. For clarity, a red curve (single ZBA) and a blue one (split peaks) have been highlighted. It will be clarified along this chapter that this splitting is responsible for the visible 0.7 anomaly at low temperature.

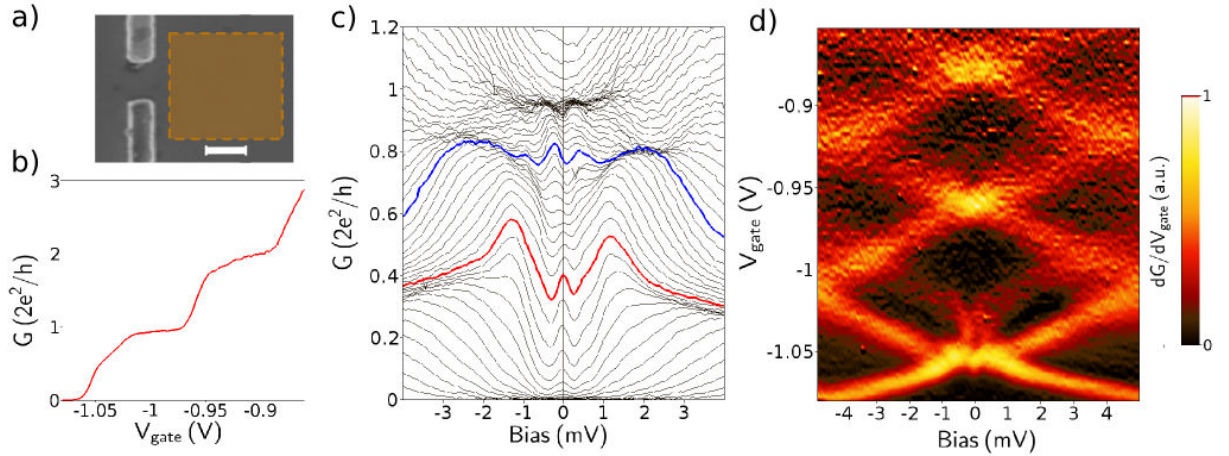


**Figure 5.7** *Transport measurements at 20 mK.* a) Electron micrograph of the QPC gates and position of the scanning area used in Fig.5.8 (dashed box). The scale bar is 300 nm. b) Differential conductance  $G$  at zero bias versus split-gates voltage  $V_{gate}$ : the 0.7 anomaly is visible below the first plateau. c) Differential conductance  $G$  versus source-drain bias for different gate voltage  $V_{gate}$  from  $-1.08$  V to  $-0.96$  V: the zero-bias peak in the red curve splits into finite-bias peaks in the blue curve. d) Numerical derivative of the differential conductance  $\partial G/\partial V_{gate}$  versus bias and gate voltage: yellow lines highlight transitions between conductance plateaus.

It shall be stressed at this point that this spontaneous splitting as the QPC opens is not an isolated fact found in this specific sample but rather a generic feature, that seems to occur particularly often in short QPCs. As stressed above, the Gröningen group studied about 80 different samples made of two-finger gates (QPC2f), and found that the ZBA was split into two peaks in roughly half of the samples, at different openings[88]. Other examples can be found in the literature, on different wafers and different geometries. For example, in the thesis of Sarah Cronenwett [36] fig 6-18 and 6-19, clear split peaks and triple peaks can be observed on two different samples, below the first plateau for "QPC2" and between the second and third plateau for "QPC1" (see Fig.5.17).

This type of splitting has also been observed and extensively studied in Ref.[106] in a QPC made in a 2D hole gas. In this work, this splitting has also been explained in terms of two-impurity Kondo effect, though one of the localized spins was claimed to be due to an impurity in the channel induced by disorder.

## 5.2.2 Isotropic rings in SGM images

In our case, Maps recorded for different QPC openings are presented Fig.5.8. As in Chapter 3, these maps are recorded with the tip situated 40 nm above the surface, and a negative voltage of  $-6$ V applied on it. The QPC conductance is measured with a 4-point technique, an AC voltage of about  $10 \mu\text{V}$  is applied at a frequency of 123Hz on one contact, and a current amplifier is connected to another contact on the opposite side of the QPC, read by a lock-in technique. The voltage across the QPC is measured between the two remaining contacts and demodulated thanks to a second lock-in. The SGM maps presented Fig.5.8(1-5) are plotted by dividing the measured current by the measured voltage,

## 5.2. WIGNER CRYSTALLIZATION REVEALED BY SCANNING GATE MICROSCOPY

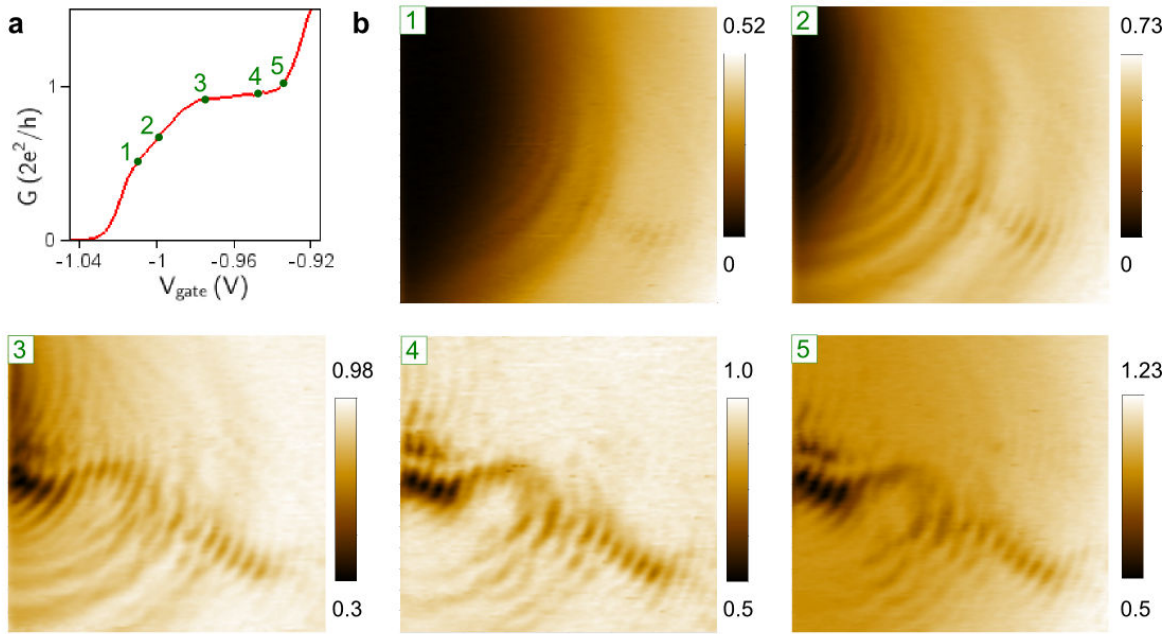


**Figure 5.8** *Scanning gate microscopy images for different QPC openings: a) Characteristic of the sample  $G(V_g)$ , the tip being several microns away, and points corresponding to average conductance in the following images. b) SGM images for different QPC openings, from the pinch-off to above the first plateau.*

and subtracting a resistance of  $600 \Omega$  to take into account the 2DEG resistance between the voltage probes and the QPC.

The tip parameters have been chosen to locally deplete the 2DEG, hence interferences are visible on the first plateau and below in specific branches (Fig.5.8), as extensively discussed in Chapters 3 and 4). These interferences are not of interest in this chapter and will be put aside to concentrate on a different phenomenon visible below the first plateau. In Fig.5.8(1-3), a new feature is clearly visible on the SGM images: concentric rings centered on the QPC channel (situated some hundreds of nanometers on the left of the images), whose spacing increases with the tip to QPC distance. It is first important to discriminate these rings from interference effects. For this purpose, the SGM tip can be scanned in a vertical plane above specific lines, where either these rings or interferences are visible.

Fig.5.9 presents the behavior of these rings and a comparison with interference fringes when scanning the tip in a vertical plane. Two lines are chosen to study the evolution of these phenomena with tip height: purple line 1 to study the rings, and green line 2 to study the interferences. The disappearance of the interferences when the tip is lifted more than 50 nm away from the surface as been discussed in Chapter 3, Fig.3.13: they vanish as soon as the tip is too far from the 2DEG to create a depletion region required to backscatter the electrons and produce interferences. From Fig.5.9, it is clear that the ring structure behaves in a completely different fashion. The rings indeed survive up to

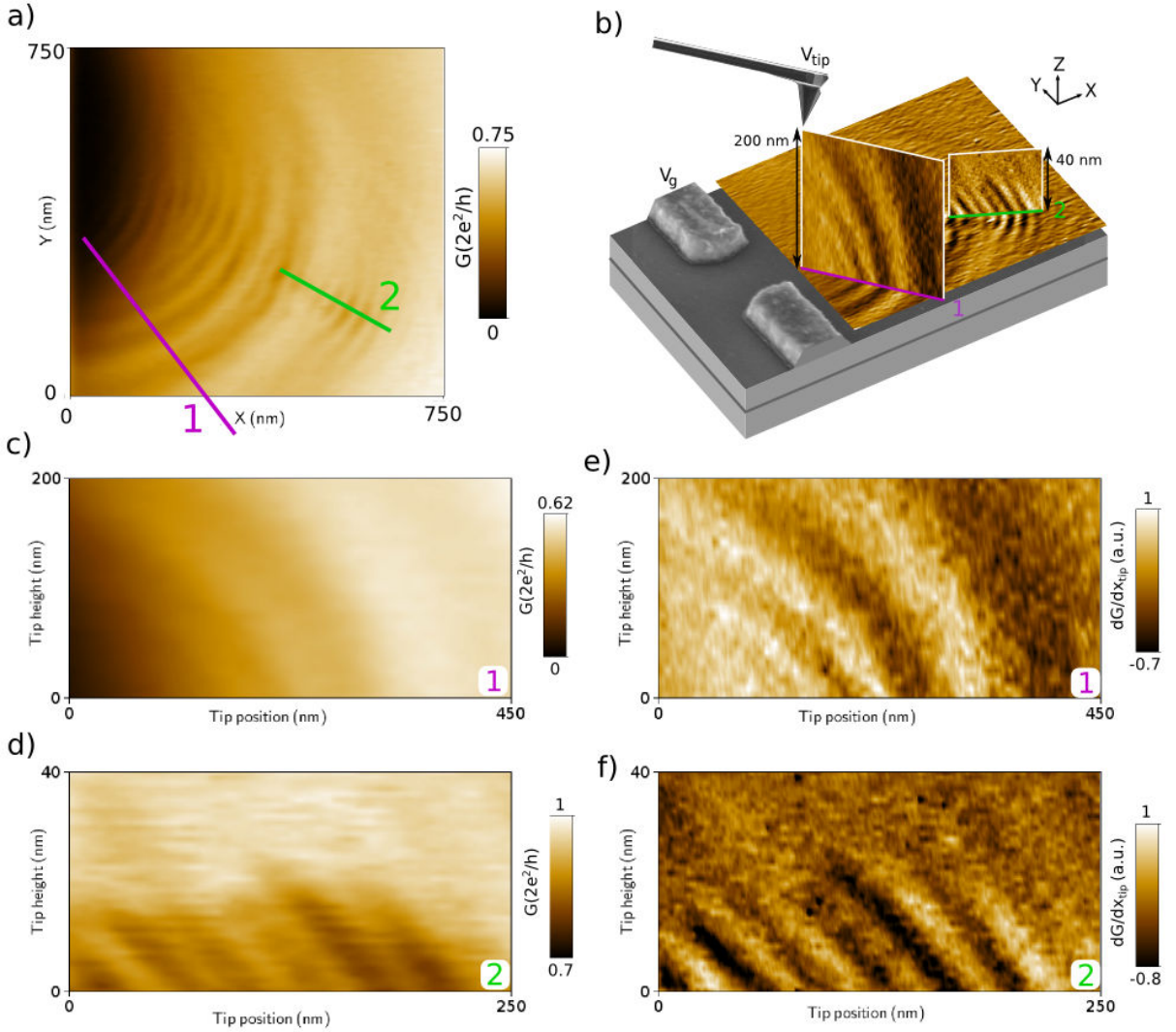


**Figure 5.9** *Three-dimensional SGM images: a) Horizontal SGM image, the QPC recorded below the first plateau (same as Fig. 5.8(2)). b) Reconstitution of vertical and horizontal SGM images differentiated w.r.t. horizontal axis for highlighting details. c) and d) Vertical images recorded by scanning the tip in a vertical plane above purple line 1 and green line 2, at gate voltage corresponding to Fig. 5.8b-2 and 4, respectively. Note the different vertical scales. e) and f) Same images as c) and d) but the signal has been differentiated along the respective tip position axis to highlight details.*

tip heights of 200 nm and bend towards the QPC, unveiling spheres centered on the QPC channel. This isotropic extension of the ring structure, in all the three dimensions of space contrasts with the interference fringes, appearing only in the branches of the electronic flow.

We therefore conclude that the new rings are not interferences but result from a direct tuning of the electrostatic potential in the QPC. The larger ring spacing at larger distances results from the smaller potential changes induced by the tip. It reminds the concentric features that are observed in scanning gate microscopy of quantum dots [64, 65, 66], or charge traps, that also extend in the three dimensions of space [107].

## 5.2.3 Modulation of the 0.7 anomaly

To understand the origin of these rings, the three dimensions of space represent too many parameters and shall be left aside, to keep only one dimension, and vary another parameter. For example, to investigate how do rings and interference fringes evolve with the QPC opening, we choose to scan the tip along the specific lines drawn Fig.5.10a, and vary the split gate voltage, as presented in Chapter 3.

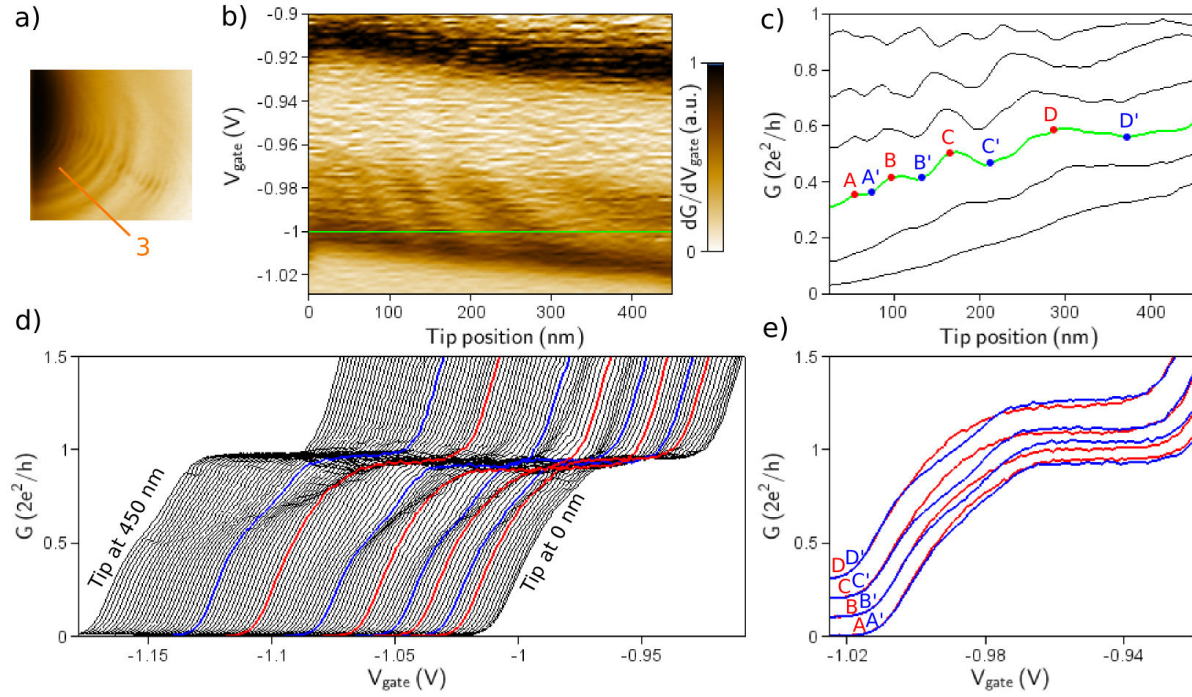


**Figure 5.10 Modulation of the 0.7 anomaly.** The figure analyses the zero-bias conductance oscillations when the tip is scanned along the orange line 3 indicated in (a) with the origin on the QPC side. (b) Trans-conductance  $dG/dV_{gate}$  versus tip position and gate voltage: black regions correspond to transitions between plateaus and oscillations are visible just below the first plateau. (c) Conductance  $G$  versus tip position for gate voltages  $V_{gate} = -0.964$  V,  $-0.983$  V,  $-0.992$  V,  $-1.000$  V,  $-1.006$  V,  $-1.012$  V (from top to bottom). Conductance extrema at  $V_{gate} = -1$  V (green curve) are labelled A to D (maxima) and A' to D' (minima). The global slope corresponds to the rise of the saddle-point potential when the tip approaches the QPC. (d) Conductance  $G$  versus gate voltage for different tip positions from 0 to 450 nm (successive curves are shifted to the left). (e) Same as in (d) for tip positions A to D (red curves, shifted vertically) and A' to D' (blue curves, shifted also horizontally to be compared with red curves): red and blue curves show no shoulder and a 0.7 anomaly, respectively. Small differences between plateaus values come from residual interference fringes.

Fig.5.10b shows that the ring-related conductance oscillations are only visible for gate voltages in the transition below the first plateau, just where the ZBA and 0.7 anomaly are observed. Fig.5.10c shows how the conductance oscillations evolve when the average conductance goes from 0 to  $G_0$  while changing the gate voltage. The oscillations are clearly visible above  $0.4 G_0$  and are blurred when approaching  $G_0$  because some interference fringes come into play. The increasing distance between conductance extrema (labeled A

to D for maxima and A' to D' for minima) is consistent with an oscillatory phenomenon in the QPC governed by an electrostatic coupling between the SGM tip and the QPC decreasing with distance. Plotting the conductance versus gate voltage (Fig.5.10c) reveals the oscillatory behaviour of the 0.7 anomaly. The amplitude of this modulation can be read from Fig.5.10e where curves at positions X and X' are compared two-by-two by shifting them horizontally to have the same pinch off voltage (as this value changes with tip position due to cross-talk effect: at first order, approaching the tip is equivalent to lowering the split-gate voltage). Curves at positions A to D are smooth with no shoulder, i.e. no anomaly, whereas curves at positions A' to D' present a reduced conductance above  $0.5 G_0$ , i.e. 0.7 anomalies. The concentric rings observed in SGM images (Fig.5.9a) therefore correspond to an alternating modulation of the 0.7 anomaly when the tip approaches the QPC.

### 5.2.4 Modulation of the zero bias anomaly

We now analyse the behaviour of the ZBA when the 0.7 anomaly repeatedly appears and disappears, and show that both anomalies are linked. Fig.5.11a shows the differential conductance versus source-drain bias for different tip positions (same scan line as in Fig.5.10a). Curves at positions A to D have a peak centred at zero bias (ZBA), whereas curves at positions A' to D' have a dip at zero bias and local maxima at  $\pm 250 \mu\text{V}$  bias (splitting of the ZBA), on top of the same V-shape background. Scanning the SGM tip therefore produces a repetitive splitting of the ZBA, that draws a checkerboard pattern in a color-plot of the spectroscopy versus tip position (Fig.5.11b). Note that a spontaneous (without tip) splitting of the ZBA of about  $250 \mu\text{V}$  also occurs while sweeping the gate voltage (Fig.5.7c, already discussed): we show later that these splittings have the same origin.

To summarize the properties of the concentric rings (Fig.5.9a), tip positions leading to conductance maxima correspond to a simple staircase in the conductance curve and a ZBA in the spectroscopy, whereas tip positions leading to conductance minima correspond to a 0.7 anomaly and a splitting of the ZBA. This demonstrates the fact that the ZBA restores at low temperature the shoulder created by the 0.7 anomaly [37] only if the zero-bias peak is not split. The two set of data taken along the same orange line 3 Fig.5.11a and changing either the gate voltage or the source-drain bias are plotted together Fig.5.12. It appears clearly that when the ZBA is split, the conductance versus gate voltage exhibits a 0.7 shoulder analogue to the higher temperature feature. Interestingly, the conductance modulations are only present above  $0.5 \times 2e^2/h$  in our sample. It therefore gives 0.7 anomalies. It could have been that the modulations extend from 0 to  $G_0$ , as the ZBA modulations reported in the work of Iqbal et al. (we don't have ZBA measurement below 0.5 in our case). There is therefore something special above  $0.5 \times 2e^2/h$  which is not yet understood and makes the 0.7 anomaly linked but not equivalent to the ZBA.

It shall be emphasized at this point that the modulation of both linear  $G(V_g)$  and non-linear  $G(V_{sd})$  curves with tip position are strikingly similar to the features reported in Ref.[9] by changing the channel length (Fig.5.5a and c).

## 5.2. WIGNER CRYSTALLIZATION REVEALED BY SCANNING GATE MICROSCOPY

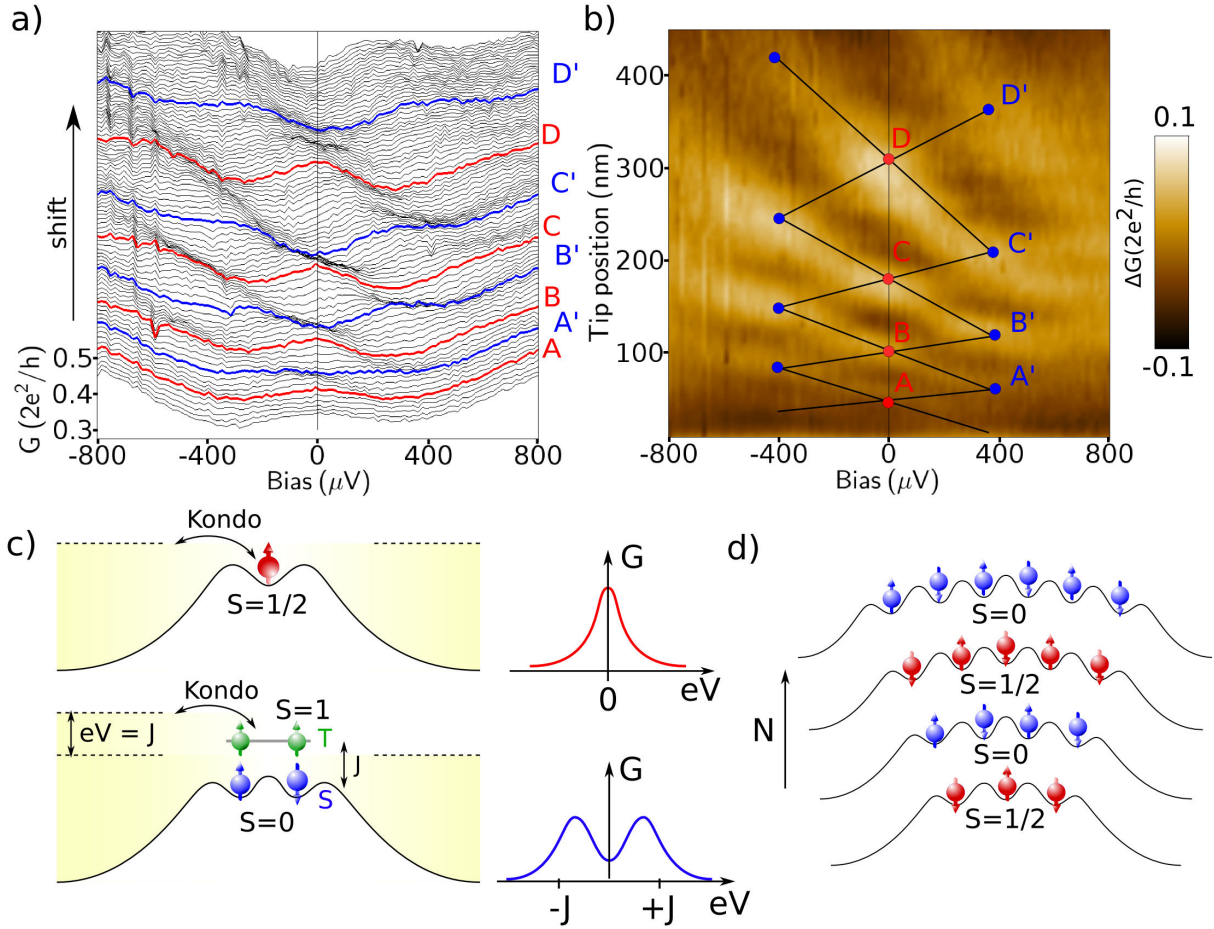


**Figure 5.11 Successive splittings of the ZBA with tip position.** The figure analyses the low bias source-drain spectroscopy when the tip is scanned along the orange line 3 indicated in Fig. 5.10a. (a) Differential conductance  $G$  versus source-drain bias at a fixed gate voltage  $V_{\text{gate}} = -1$  V for different tip positions from 0 to 450 nm (successive curves are shifted upwards by  $0.0075 2e^2/h$ ). (b) Color plot of the same data as in (a) but a linear fit of  $G(d_{\text{tip}})$  is subtracted to each vertical line to subtract the average cross-talk effect when the tip is approached towards the QPC. Peaks positions are indicated by dots: the successive ZBA splittings give a checkerboard pattern (the tilted pattern is due to a bias-induced change of the QPC position). (c) Schematic of the QPC potential with one (top) and two (bottom) localized electrons, corresponding respectively to a  $S = 1/2$  ground state with a zero-bias Kondo peak and to a  $S = 0$  ground state with finite-bias Kondo peaks involving the excited state  $S = 1$  with Singlet-Triplet energy splitting  $J$ . Right: conductance  $G$  versus bias  $V$  expected for each state. (d) Schematic of the QPC potential with an increasing number of electrons localized by Coulomb interactions. The antiferromagnetic spin coupling in this small 1D Wigner crystal gives either a  $S = 1/2$  ground state (ZBA) or a  $S = 0$  ground state (splitting of the ZBA), depending on the parity (respectively odd or even).

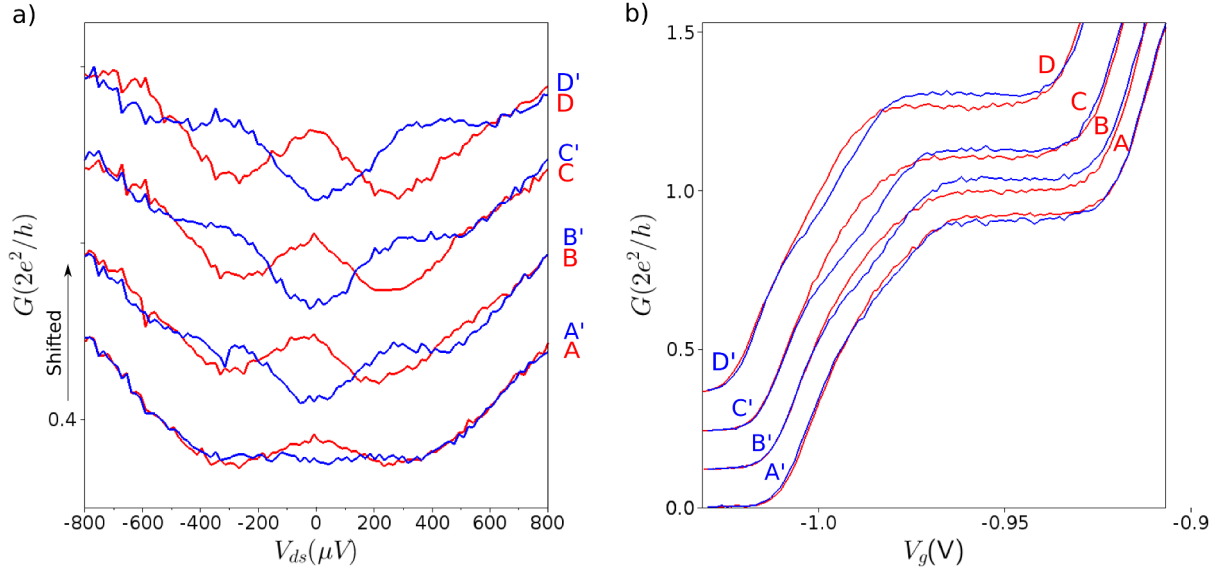


**Figure 5.12** *Comparison between 0.7 anomaly and ZBA modulations* a) Splittings of the ZBA for different tip positions, corresponding to conductance minima and maxima in the SGM maps, for fixed gate voltage  $V_{gate} = -1$  V. Different traces are offset for a clear comparison. b) Conductance  $G(V_g)$  for the same tip positions, shifted horizontally to have the same pinch-off voltage and vertically by step of  $0.1 * e^2/h$  for clarity.

## 5.2.5 Interpretation in terms of Wigner crystallization

### 5.2.5.1 Ruling out possible phenomena

First, we would like to stress again that these new conductance oscillations cannot be explained by interference effects in the 2DEG. One argument already given above is that interferences require backscattering with a tip close to the surface, whereas the new rings are observed up to large tip heights (Fig.5.9). A second argument is that interference fringes would have an increasing spacing for short tip distances because the density is reduced close to the QPC and the electron wavelength is larger, but the opposite behavior is observed.

We now discuss a possible single-particle effect inside the QPC that, at first sight, could give similar conductance oscillations. In case of a non-adiabatic transmission, wave functions are scattered by the QPC potential barrier and transmission resonances appear when the barrier length is equal to an integer number of half the longitudinal wavelength. If the effect of the tip is to change the channel length, such resonances could give conductance oscillations versus tip distance. However, this single-particle mechanism cannot explain the repetitive splittings of the ZBA, which are simultaneous with the observed conductance oscillations, and we therefore need another explanation. As explained in the beginning of this chapter, the ZBA in QPCs has been shown to scale with temperature and magnetic field similar to the Kondo effect in quantum dots[37], and the splittings of the ZBA have been shown to scale as odd and even Kondo effects [9]. We then propose that the repetitive splittings we observe as a function of tip position are similar to the ones observed in Ref.[9], and originate from odd and even Kondo effects. As discussed before,

## 5.2. WIGNER CRYSTALLIZATION REVEALED BY SCANNING GATE MICROSCOPY

---

this possibility requires that a definite odd or even number of electrons are localized in the channel, which is not obvious regarding the open nature of a QPC.

We now consider different scenarios to explain the presence of such localized states in our system. In a recent work on QPCs made out of a 2D hole gas, a spontaneous splitting of the ZBA as the QPC opens has been reported[106]. This effect was attributed to a charge impurity forming a potential well close to the channel, containing one or two charges, leading to different types of Kondo screening. In our case, the spontaneous splitting of the ZBA as the QPC opens (Fig.5.7c) could be explained by this effect. However, the fact that approaching the tip towards the QPC results in four successive splittings of the ZBA indicates that this impurity should contain at least eight charges, which is unlikely for a single impurity. Nevertheless, one could imagine that a shallow quantum dot has formed in the QPC due to potential fluctuations induced by residual disorder[108] and giving Coulomb blockade oscillations as often observed in long 1D wires[109]. The major argument to exclude this scenario is that the split gates have a larger capacitive coupling to the channel than the tip has (that is, a larger lever-arm parameter), so the gates should induce more charging events than the tip, but we observe the opposite: approaching the tip by 600 nm produces four successive splittings of the ZBA and sweeping the gate voltage produces only one splitting. It can therefore not be Coulomb blockade in a disorder-induced quantum dot.

### 5.2.5.2 Wigner crystallization

The only remaining possibility to explain the presence of localized states in the channel is a spontaneous electron localization, which is not induced by potential barriers but instead by electron–electron interactions. Indeed, a large number of theoretical and numerical investigations show that interactions can localize a finite number of electrons in the channel[46, 45, 53, 52]. On the first conductance plateau and below, transport can be considered as 1D, and the electron density is so low that the Coulomb repulsion overcomes the kinetic energy. When the 1D density  $n_{1D}$  fulfills the criterion  $n_{1D} \times a_B \ll 1$ , where  $a_B$  is the effective Bohr radius (10 nm in GaAs), electrons are expected to spontaneously order in a crystal, with an interparticle distance minimizing Coulomb repulsion[51]. This many-body state, known as a Wigner crystal[49, 110], has been suggested to be responsible for the 0.7 anomaly in QPCs[46]. When the electron density in the channel is decreased below the critical value, the density modulations evolve continuously from the  $\lambda_f/2$  periodicity of Friedel oscillations to the  $\lambda_f/4$  periodicity of the Wigner crystal[54]. Quantum Monte Carlo simulations have also shown that electrons in the crystallized region can be relatively decoupled from the high-density reservoirs and present an antiferromagnetic coupling  $J$  between adjacent spins[52]. In contrast to the case of quantum dots with real tunnel barriers, electron localization in a QPC is not straightforward and results from emergent barriers in the self-consistent potential. On the other hand, the Kondo effect requires a relatively open system with a good coupling to the reservoirs, and this makes the QPC a suitable platform to observe Kondo phenomena on an interaction-induced localized state, as shown recently in length-tunable QPCs[9].

This last scenario being the most realistic one in our case, we therefore interpret the four observed oscillations as a signature of eight successive states of a small non-uniform 1D Wigner crystal with an alternating odd and even number of localized charges.

Situations with an odd number of electrons in a spin  $S = 1/2$  ground state show a ZBA due to Kondo screening of non-zero spin states. Situations with an even number of electrons in a spin singlet  $S = 0$  ground state show a splitting of the ZBA due to non-equilibrium Kondo screening[111, 102] of the spin triplet  $S = 1$  excited state with peaks at a finite bias  $eV = J$  (Fig.5.11c). The four oscillations, suggestive of eight successive states, reveal that a large number of electrons can spontaneously localize in the channel of a QPC, as shown in Fig.5.11d. Observing Kondo screening on a system with many localized charges is not so surprising if we compare with quantum dots where the Kondo effect is observed up to large numbers of electrons[93]. Nevertheless, the particular case of a 1D chain of localized charges in the Kondo regime still requires theoretical investigations.

This analysis is consistent with the interpretation given in ref.[9] extensively discussed in section 5.1.4. Our SGM experiment brings additional information on this effect, as scanning the tip around the QPC, laterally or vertically, changes the shape, extension and symmetry of the channel potential. The circular and almost isotropic rings in Fig.5.9 show that the localized states survive to all these potential deformations. The regularity of the successive rings also suggests that this localization occurs rather independently of disorder, although possible crystal pinning effects should be investigated in the future. In ref.[9], the parameter controlling the number of localized states is the effective length of the channel, defined in ref. [105] and computed using an analytical approach assuming a fixed zero potential at the surface[16]. This method is not suitable to model our SGM experiment, as the tip is situated above the surface. In the following, we analyze our experiment with different approaches.

### 5.2.5.3 Evaluation of the 1D density

To evaluate the one-dimensional electronic density in the QPC channel, a first order analytic calculation can be done using the Büttiker's saddle-point model[10]. The potential in the constriction created by the gate can be approximated by  $V(x, y) = V_0 + 1/2m^*\omega_y^2y^2 - 1/2m^*\omega_x^2x^2$ , where  $\omega_x$  and  $\omega_y$  can be evaluated from the linear and non-linear transport curves (see Fig.5.7d). The first subbands are spaced by about  $\Delta E = 4meV$ , and so  $\omega_y = \Delta E/\hbar$ , and the shape of the conductance steps indicates a longitudinal curvature of  $\omega_x \sim 0.5 \times \omega_y$  (since  $T = 20 mK \ll \hbar\omega$ , there is no thermal broadening). The 2D electronic density then writes in the classical limit (or Thomas-Fermi approximation) :

$$n_{2D}(x, y) = \frac{m^*}{\pi\hbar}(E_F - V(x, y)) \quad (5.1)$$

To evaluate the 1D electronic density at an abscissa  $x$ , the 2D electronic density can be integrated over the transverse axis, up to the width  $W(x)$  accessible for electrons coming from infinity with energy  $E_f$  (see Fig.5.13a).

$$n_{1D}(x) = \int_{-W(x)}^{W(x)} n_{2D}(x, y)dy = \frac{4\sqrt{2m^*}}{3\pi\hbar\omega_y}(E_f - V_0 + 1/2m^*\omega_x^2x^2)^{3/2} \quad (5.2)$$

This approach has the advantage to be analytically solvable though it can be criticized for its simplicity (classical and not self-consistent). To evaluate the size of the region over which the kinetic energy drops below the repulsive Coulomb energy, we have to choose a

## 5.2. WIGNER CRYSTALLIZATION REVEALED BY SCANNING GATE MICROSCOPY

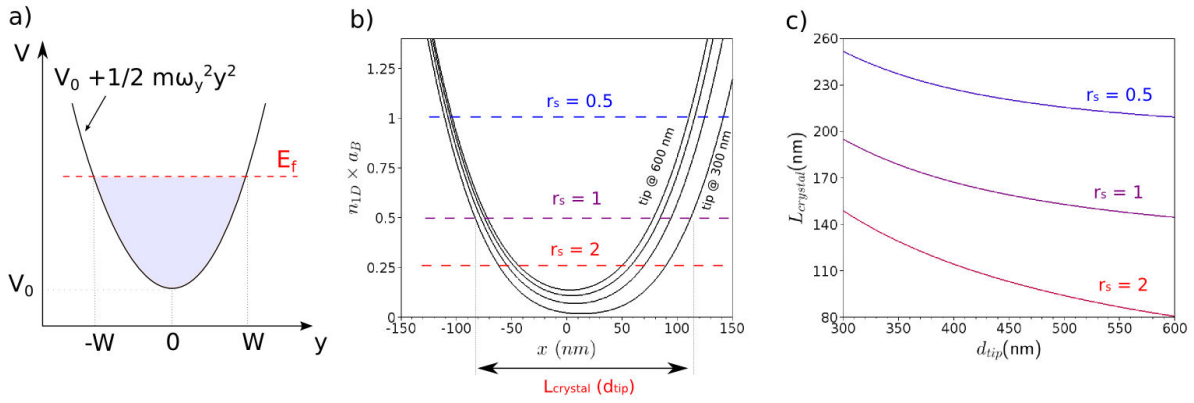


**Figure 5.13** *Analytical estimation of the 1D density based on Buttiker saddle-point model* a) Schematics of the transverse confinement and the accessible energetic range, at given longitudinal position  $x$ . b) 1D density times the Bohr radius  $a_B$  along the transport axis for different tip positions, and  $E_f - V_0 = 0.8\hbar\omega_y$ : just above half transmission. Different possible Wigner crystallization thresholds are plotted as horizontal lines. c) Size of the crystallization region for different crystallization thresholds, as a function of tip-to-QPC distance.

critical density. This criterion required to reach Wigner crystallization is highly debated, but a recent numerical study has given interesting insights[51]. This criterion is often discussed in terms of the Wigner-Seitz radius  $r_s = 1/(2n_{1D}a_B)$ , representing the ratio of the Coulomb repulsion to the kinetic energy. In Ref.[51], the critical  $r_s^c$  parameter was found to be in the range 0.5 to 2, depending on the transverse confinement potential. This typical values combined with equation (5.2) show that below the first plateau, the length  $L_{crystal}$  of the region in which the density is critically low ranges from 100 to 300 nm depending on  $r_s^c$  value, the QPC opening and its geometry (see Fig.5.13b). Finally, integrating this 1D density over the critically low density region gives a total charge of a few electrons, justifying that a finite number of charges should localize, though this very simple estimation does definitely not hold to calculate the number of crystallized electrons.

The tip can then be added to the saddle potential landscape. As explained in Chapter 3, the tip-induced potential is modeled by a lorentzian potential, which is characterized experimentally thanks to the tip lever-arm parameter. The same integration as in equation (5.2) is then done numerically including the tip-induced potential to evaluate how is the length of the critically low density region modified by the tip. The results are sketched Fig.5.13b and c. Essentially, approaching the tip by 300 nm toward the QPC can enlarge the crystallization region by about one hundred nanometers depending on  $r_s^c$ . Considering at the very first order that charges are spaced in this small Wigner crystal by a distance  $1/n_{1D}^c$  shows that approaching the tip could substantially change the number of crystallized charges. However, the calculations show that the main effect of the tip is to close the QPC by a direct gating effect. Then the number of localized charges should change almost by the same amount when the tip is approached and when the gate voltage is changed, which is not the case in the experiment (approaching the tip by 500 nm creates 4 successive splittings of the ZBA whereas opening the first mode generates only one splitting). An essential ingredient missing to this model is the electrostatic screening.

## CHAPTER 5. WIGNER AND KONDO PHYSICS IN QUANTUM POINT CONTACTS

As sketched Fig.5.14b, the screening by the metallic gate tends to reduce the effect of the tip at the very center of the QPC (and hence the cross-talk), but does not prevent the tip to affect the side of the channel.

A more accurate way to evaluate the electronic density in this complex problem is to perform self-consistent numerical simulations with COMSOL as explained in section 3.4.3.

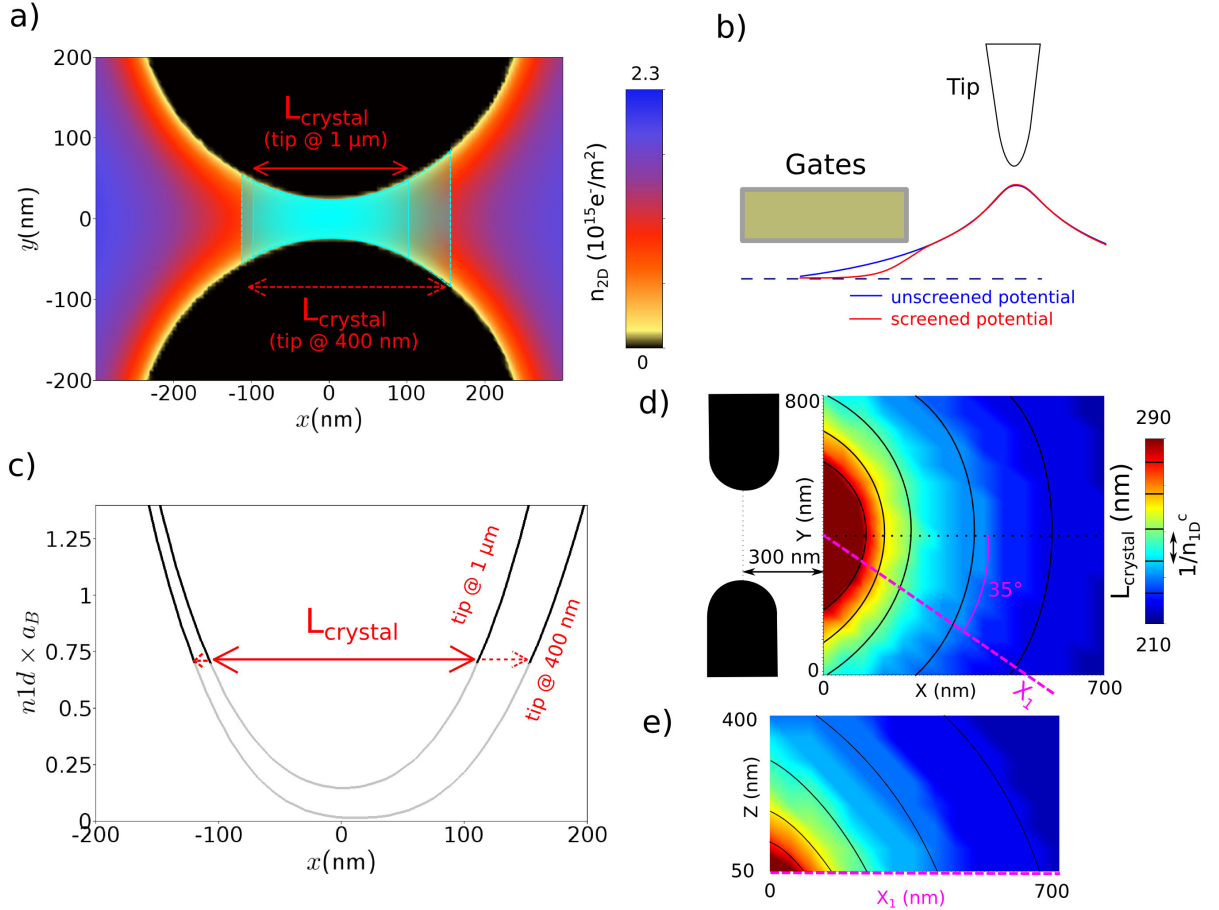


**Figure 5.14** *Calculation of the electron density and estimation of the Wigner crystal size.* (a) Map of the two-dimensional electron density  $n_{2D}$  in the 2DEG computed classically but self-consistently with the potential, when the tip is at 1  $\mu\text{m}$  from the QPC. (b) Scheme of the screening effect from the metallic gates on the tip induced potential. (c) One-dimensional electron density  $n_{1D}$  obtained by integration of  $n_{2D}$  along the  $y$ -axis, when the tip is at 1  $\mu\text{m}$  and 400 nm from the QPC. Choosing a critical density  $n_{1D}^c = 0.7/a_B$  determines the expected size  $L_{\text{crystal}}$  of the 1D Wigner crystal. (d) Computed size of the Wigner crystal as a function of tip position in an horizontal plane 30 nm above the surface ( $V_{\text{gate}} = -1$  V). The region in red corresponds to a closed contact (the electron density is zero at the QPC center for these tip positions). Black lines indicate tip positions for which  $L_{\text{crystal}}$  is enlarged by  $1/n_{1D}^c$ , corresponding at first order to the addition of one charge to the crystal. (e) Computed size of the Wigner crystal for tip positions in a vertical plane (above line  $X_1$  at 35° from QPC axis).

To evaluate the size of the region where  $r_s$  is larger than a given threshold, we calculate

## 5.2. WIGNER CRYSTALLIZATION REVEALED BY SCANNING GATE MICROSCOPY

---

the 1D electron density by integration of the 2D electron density in the transverse direction (Fig.5.14a and c). As an example, we choose a critical value  $r_s^c = 0.71$  corresponding to a critical density  $n_{1D}^c = 0.7/a_B$ , and evaluate the size  $L_{\text{crystal}}$  where the density is lower than  $n_{1D}^c$ . This size is found to vary from 210 to 290 nm when the tip is approached by 600 nm towards the QPC, which shows that the tip can strongly affect the size of the low density region, and hence the number of localized charges. The tip positions leading to the same  $L_{\text{crystal}}$  form rings centred on the QPC, both for horizontal and vertical scanning planes (Fig.5.14d and e), in the same way as the conductance oscillations observed in the SGM experiment (Fig.5.8).

Our classical simulation holds only for an estimate of the size  $L_{\text{crystal}}$ , but cannot be used to calculate the number of localized charges, since quantum mechanics dominates at such a low density. Note that charges in this crystal are not expected to be uniformly spaced, because the potential of a QPC shows a strong curvature. This non-uniform situation would require an extension of the concept of Wigner crystal which is usually studied in a flat potential landscape. A rather crude approach to evaluate how many charges can be added by approaching the tip is to suppose that one charge is added to the crystal each time the region is enlarged by  $1/n_{1D}^c$  (about 14 nm for  $r_s^c = 0.71$ ). With this assumption, about 5 charges can be added to the crystal when the tip is approached close to the QPC (Fig.5.14d). This value is qualitatively consistent with the 4 oscillations observed in the experiment, and interpreted as the addition of 8 charges. Simulations also show that the number of charges can be modified simply by changing the split-gate voltage. This could explain the ZBA splitting observed above  $0.7 G_0$  in absence of the tip (Fig.5.7c).

Our assumption that electrons form a 1D system in the low density region is justified *a posteriori* by the fact that only the first and second transverse modes are occupied over the length  $L_{\text{crystal}}$ . The presence of the second mode at the extremities of this region indicates that the system is not strictly 1D, but theory still predicts the formation of a Wigner crystal in the second subband of quasi-1D wires, forming a zigzag chain [112], as possibly observed in experiments [113, 56]. Interestingly, the simulations show that a small crystallized region survives when the second mode reaches the central part of the channel, which could explain the 0.7 analogues often observed between the first and second conductance plateaus, as discussed in section 5.2.7.

### 5.2.6 Reproducibility in a second sample

As the existence of this spontaneously localized state is supposed to be generic, and proposed to occur in every QPC in the low density limit, these results have to be reproducible. To support our interpretation, we now investigate the reproducibility of our results in a second sample. We performed the same experiment on sample C, with a slightly different geometry. The transport features in this sample are presented Fig.5.15. The linear conductance trace  $G(V_g)$  indicates that disorder may play a role in this specific sample (at least for this cooldown). The plateaus are not flat and well quantized, but present dips, possibly arising because of resonant effects as discussed in the first chapter of this thesis. Nevertheless, the non-linear transport features (Fig.5.15c-d) indicate that these resonances are weak features, and the overall non-linear trace looks like a usual QPC characteristic. Note that in this specific sample, no spontaneous splitting of the ZBA is observed as the

QPC opens below the first plateau, but the dip on the first plateau might have a similar origin as the ZBA splitting in terms of change in the number of localized charges, though the investigation has not been pushed far enough to conclude.

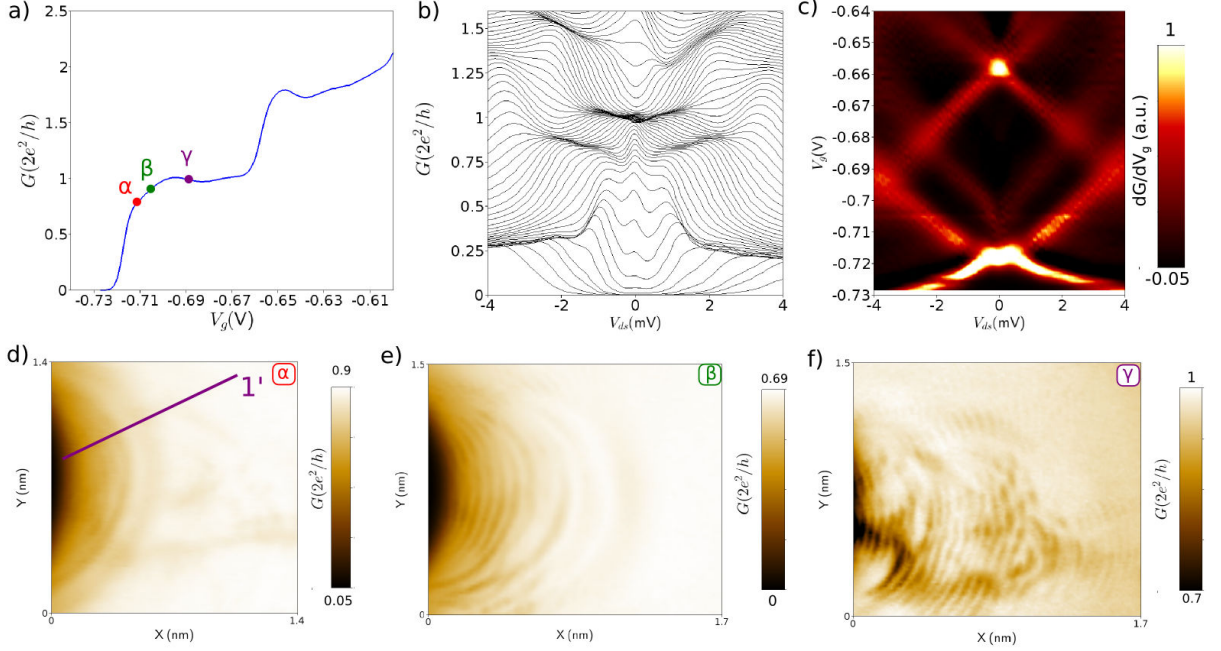


**Figure 5.15 Scanning gate microscopy on a different QPC.** a) Linear conductance trace  $G(V_g)$ . Plateaus present dips indicating a possible residual disorder in the channel. b) Non-linear cascade plot,  $G(V_{sd})$  for different values of  $V_g$ . c) Colorplot of the transconductance  $\partial G/\partial V_g$  as a function of gate voltage and source-drain bias. d) SGM image for a QPC in the 0.7 regime, for a tip height of 60 nm. e) SGM at a gate voltage corresponding to  $\beta$ ,  $z_{tip} = 30$  nm. f) SGM image recorded on the plateau,  $z_{tip} = 30$  nm.

SGM images below and on the first plateau are presented in Fig.5.15d-f. For the image Fig.5.15d, the tip is scanned 60 nm above the sample surface for the interferences to be less pronounced. This highlights the ring structure. Images in Fig.5.15e-f the tip scanned 30 nm above the sample surface, with a tip voltage of -6 V. The conductance is recorded by a 4-points measurement, using an AC excitation of  $\sim 10\mu V$ , at a base temperature of 20 mK. On the plateau, we see branches and interferences as observed in previous experiments and extensively discussed in Chapter 3. Below the first plateau, an additional structure can be guessed, looking like the ring structure presented above, but less pronounced.

Nonetheless, to evaluate what do these rings correspond to, the same experiment as presented before can be realized. For this purpose, we choose a line where the interference are less pronounced (purple line 1'), lift the tip 60 nm above the surface to avoid the creation of a depletion spot, and scan the tip along this line while a transport parameter is varied.

Fig.5.16 presents the main results concerning the dependence in gate voltage and source-drain bias of these oscillations. Concerning gate voltage, traces  $G(V_g)$  for different

## 5.2. WIGNER CRYSTALLIZATION REVEALED BY SCANNING GATE MICROSCOPY

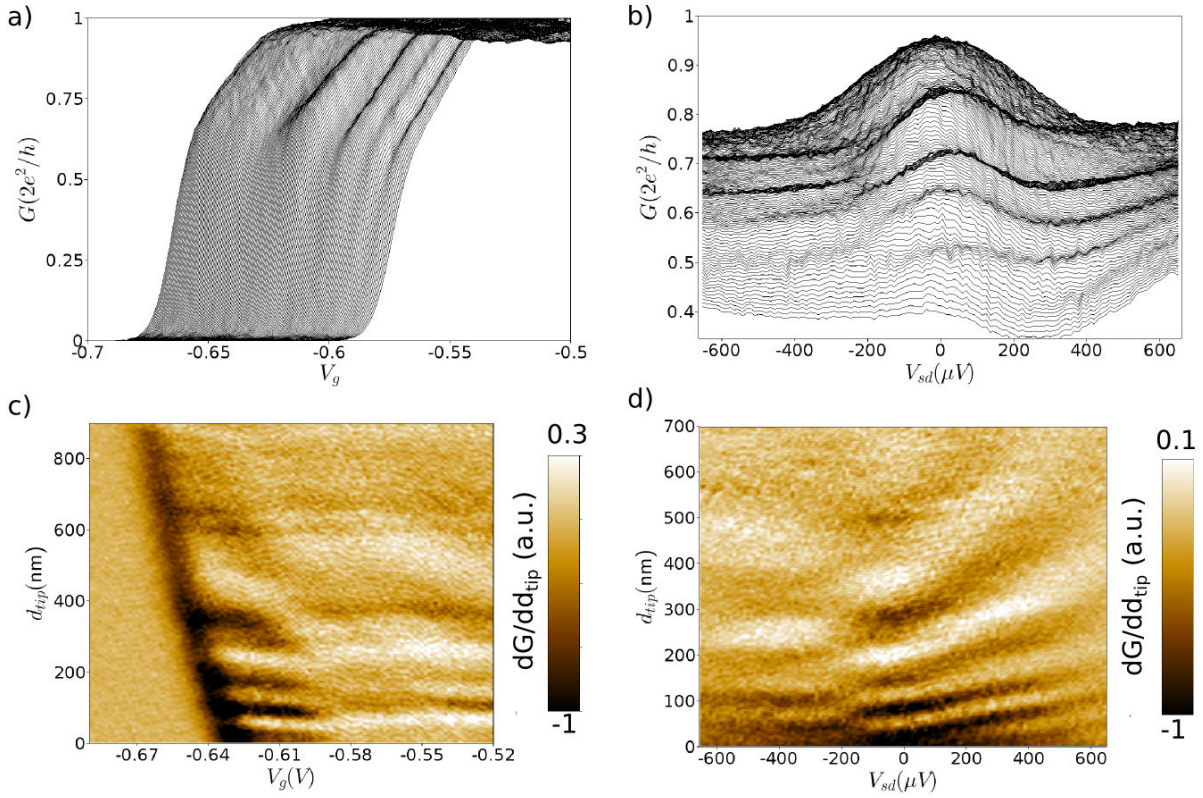


**Figure 5.16** *Modulations of the 0.7 an zero bias anomalies* a) Linear conductance traces  $G(V_g)$  for different tip positions along purple line 1'. Curves are shifted in  $V_g$  for clarity b) Non-linear conductance traces  $G(V_{sd})$  for different tip positions along 1', when the QPC is below the first plateau. Curves are not shifted, the average conductance decreases because of cross-talk effect. c) Derivative  $\partial G/\partial d_{tip}$  as a function of tip position along line 1' and gate voltage, up to the first plateau. Same data as a). d) Derivative  $\partial G/\partial d_{tip}$  as a function of tip position along line 1' and source-drain bias. Same data as b).

tip positions along line 1' are presented Fig.5.16a and the derivative with respect to tip position is plotted Fig.5.16c. It appears clearly that approaching the tip results in an alternating modulation of the 0.7 anomaly, that is alternatively pronounced or almost invisible depending on tip position. This is really similar to the data presented in the previous section, and those obtained in Ref.[9]. However, a noticeable difference is that these oscillations seem to re-appear for gate voltage corresponding to the dip on the first “plateau“. Though this is not understood at the moment, it could be related to the pinning of the small Wigner crystal by residual potential fluctuations in the channel. It also suggests that this localized state survives even when the first mode of the QPC is fully open. We usually do not have signatures of this localized state in the channel when plateaus are well-quantized (as in the previous section), but if disorder induces non-perfect transmission, the modification of this Wigner crystal by approaching the tip could possibly lead to the conductance modulations observed in this sample.

Fig.5.16b and d present the modulations of the ZBA induced by approaching the tip. The ZBA is alternatively modulated depending on tip position, its width changes and side peaks alternatively appear and disappear. However, the effect does not lead to clear

split peaks as in the previous measurements. It is not so surprising as for a non-equilibrium Kondo effect, decoherence of the Kondo mechanism is expected and would give weaker split peaks as compared to zero-bias peaks due to an equilibrium Kondo mechanism. However, differentiating these data with respect to tip position (Fig.5.16d) highlights a checkerboard pattern really similar to the one shown Fig.5.11b.

Though these measurements confirm the reproducibility of the conductance anomalies modulation as a function of tip position, the signatures are more complex. Indeed if residual disorder is responsible for the signatures in the linear conductance trace, one should stretch one step further the concept of Wigner crystal, usually studied in clean potential landscapes.

### 5.2.7 Higher conductance analogues

Other features associated with the 0.7 anomaly are its analogues at higher conductance values. They usually appear as weak kinks features, below the second and third plateaus at values around  $1.7 \times 2e^2/h$  and  $2.7 \times 2e^2/h$ , that also evolve down to the spin resolved plateaus under strong parallel magnetic field [114]. Moreover, though it has never been discussed to our knowledge, the zero bias anomaly is visible in a large range of experiments up to the third plateau. For example, Fig.5.17 presents some data extracted from Ref.[36], where we indicate single peak ZBA, split peaks and triple peaks. Note that these rich structures are visible up to the third plateau, suggesting that Wigner and Kondo physics are still at play at least up to the third mode.

The fact that a Kondo resonance appearing alternatively as a single or several peaks, is still present up to the third plateau raises some questions. It has never been discussed to our knowledge probably because it is somehow inconvenient. Indeed, the parallel is made between the Kondo effects observed in QPCs is usually compared to those observed in quantum dots[37, 9], where the Kondo effect cannot be observed for tunnel barriers more open than the conductance quantum, as this forbids Coulomb blockade. Indeed, Coulomb blockade generated by potential barriers cannot occur at conductances higher than  $\sim e^2/h$ . Therefore, the situation in a QPC is more subtle.

If these analogues of the ZBA are due to an exotic kind of Kondo effect, it must come from the same interaction-induced localized state discussed above. This means that Wigner crystallization is still at play at rather high conductance in QPCs. To investigate this possibility, we analyze the ring structure above the first plateau following the same analysis as described above.

On the sample presented Fig.5.15, we scanned the tip along the purple line 1', and opened the QPC up to the third plateau. Results are summarized on Fig.5.18. First, it shall be noticed that the conductance modulations associated with the ring structure and modulations of the ZBA and the 0.7 anomaly below the first plateau are visible up to the third mode. It appears clearly on Fig.5.18c, where we have plotted the derivative of the conductance with respect to the tip position along line 1', as a function of tip position and the QPC opening (horizontal axis). One can see that the rings are contrasted up to the third mode, and not only in the transitions but also on the "plateaus" that don't look like plateaus in this sample. If our interpretation is correct, this means that the small Wigner crystal survives up to wide openings of the QPC. It is not surprising in a sense,

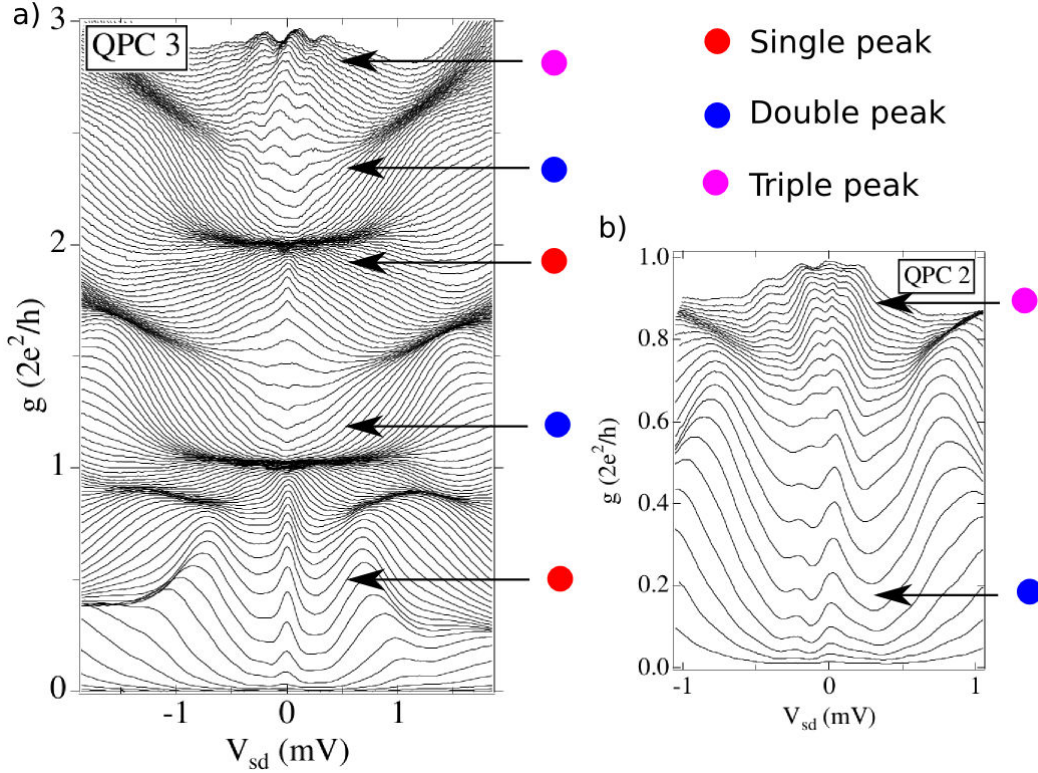


**Figure 5.17** *Split peaks in Cronenwett’s thesis:* a) Spectroscopy of a QPC where alternating single (or triple) and double peaks ZBA are visible up to the third plateau. b) Example of a sample in which a double peak is visible at low conductance, that becomes a triple peak on the first plateau, suggesting rich spin physics. Both figures are extracted from [36].

as for the criterion  $r_s^c = 0.71$  proposed above simulations show that electrons shall be localized up to the second mode.

The results of the simulations of  $L_{crystal}$  for the geometry discussed in the previous section are presented Fig.5.19. The positions of plateaus are estimated based on the experimental values. Indeed, our classical simulations do not allow to evaluate the electronic modes, but as the gate voltage required to close the QPC ( $\sim -1.1V$ ) is well reproduced considering the geometry of sample C, we evaluate that the modes should be spaced in gate voltage by roughly 0.1 V as in the experiment. Under this assumption, it appears that a finite crystallization region (i.e. a region where the density is lower than the crystallization criterion) survives up to the second mode in this geometry.

Still scanning the tip above the line 1’, the non-linear conductance between the first and second mode is investigated and plotted Fig.5.18d. Though the peaks are less pronounced than their low-conductance analogues, it appears clearly that the ZBA forms alternatively one or two peaks depending on tip position. This suggests that the Wigner crystal is still present at this conductance, and that approaching the tip can change the number of charges from odd to even situations leading to different Kondo effects.

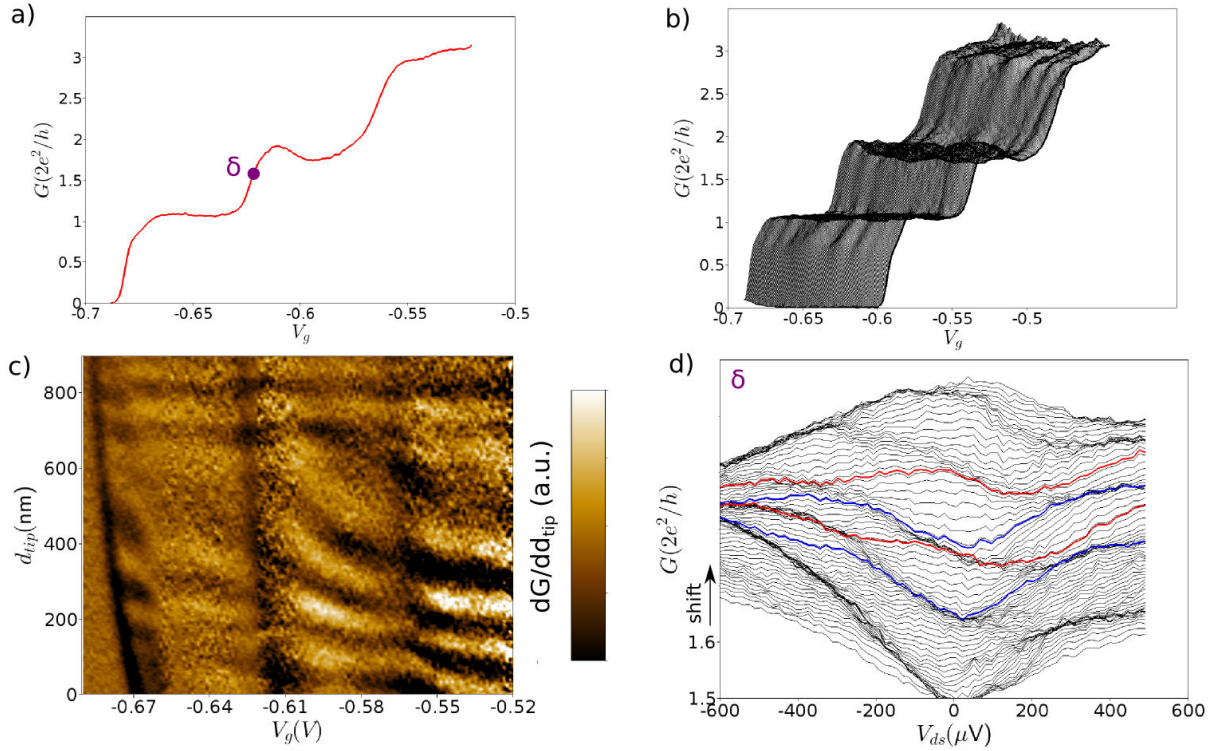


**Figure 5.18** *Signatures of the ring structure up to the third plateau:* a)  $G(V_g)$ , the tip being 900nm away from the QPC, at the end of line 1'. b)  $G(V_g)$  for different tip positions along line 1', up to the third plateau. Curves are shifted in  $V_g$  for clarity. c) Colorplot of  $\partial G/\partial d_{tip}$  as a function of  $V_g$  and  $d_{tip}$ . d)  $G(V_{sd})$  for different tip positions along 1', the QPC being opened between the first and second mode (gate voltage  $\delta$  in a). Curves are shifted in  $G$  for clarity.

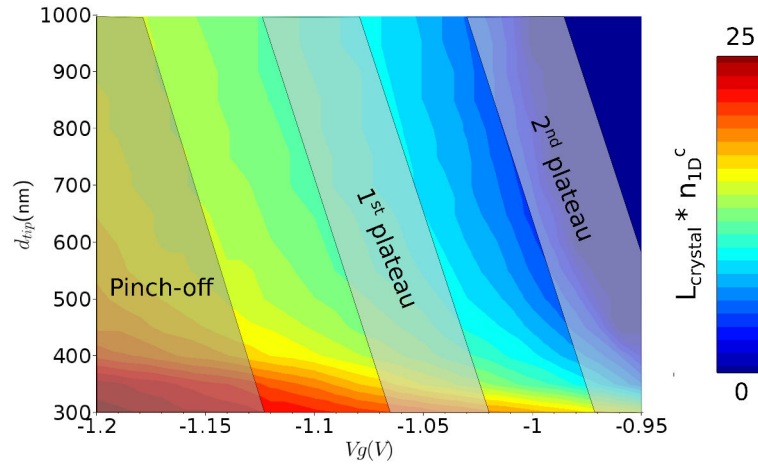


**Figure 5.19** *Simulations of crystal length up to the second plateau:* Simulation of the crystallization region length for the parameters presented in the previous section, as a function of both gate voltage and tip position along the modeled QPC axis. Estimation of the modes positions is made compared to the experiment. This region is non-zero up to the second mode.

## 5.3 Conclusion

In this Chapter, we have shown how the scanning gate technique allowed us to bring a significant contribution to a still unelucidated problem in mesoscopic physics.

It has first been reminded the breakthroughs achieved in the late 90's by observing different types of Kondo effects on controllable localized systems. In these quantum dots, one or a few electrons are localized, leading to different Kondo effects at low temperature depending on their total spin state. Soon after, a similar phenomenon has been proposed to explain the ZBA in QPCs, though no mechanism was proposed to elucidate the fact that some electrons could be localized in QPCs, that are essentially open systems [37].

Then, a really recent result has been discussed, suggesting that rich Kondo physics can occur in QPCs, and demonstrating that a finite number of electrons can spontaneously localize in these systems, whose number can be controlled by the means of several metallic split gates[9].

Our SGM experiments presented in this Chapter confirmed the existence of such localized state, and the resulting Kondo effects at low temperature. We demonstrate that the number of localized spins in the QPC channel can be controlled simply by approaching the polarized tip, which gives concentric rings in the SGM images below the first plateau, corresponding to successive splittings of the zero bias anomaly. We propose that the parameter controlling the number of localized electrons is the size of the critically-low electronic density region, and that electrons form a small Wigner crystal in the channel. Classical electrostatic simulations show that this interpretation is qualitatively consistent with the experimental observations.

Finally, we discussed the 0.7 and zero bias anomalies analogues at higher conductance, and propose that this Wigner crystal survives at least up to the third mode and leads to Kondo effect in this regime.

This study therefore brings strong support to the interpretation proposed in Ref.[9], and discards another recent proposition to explain conductance anomalies in QPCs without invoking localization[57], since this proposition cannot explain peak splittings.

Finally, it shall be stressed that despite revealing the existence of a Wigner crystal in QPCs, this study does not solve at all the whole problem despite what was claimed concerning our work [115], but rather gives a starting point. To really explain these conductance anomalies, some theoretical and experimental investigations are required. On a theoretical point of view, it shall be calculated how does the current flow through such an exotic state, formed by a small 1D Wigner crystal smoothly connected to the leads, in which the interparticle distance probably evolves along the channel. Are spin and charged excitations decoupled in such a system, as proposed in Ref.[46]? Does the Kondo effect restore the spin excitations? In particular, it should be found what gives this shoulder called 0.7 anomaly and why it survives at temperatures much higher than the zero bias anomaly.

On the experimental point of view, it remains to be clarified how many charges does this crystal contain. By performing our scanning gate experiment, we get signatures of the *changes* induced by the tip in the number of localized electrons, but not on their absolute number. One can dream that one day advanced scanning probe techniques will allow to really count these localized electrons, by scanning tunneling microscopy on a

*CHAPTER 5. WIGNER AND KONDO PHYSICS IN QUANTUM POINT CONTACTS*

---

QPC designed out of a surface 2DEG (device that does not exist at the moment), or on a buried QPC by subtle electric force microscopy.

### 5.3. CONCLUSION

---

# Chapter 6

## Kondo phase shift revealed by scanning gate interferometry

### Contents

---

<b>6.1</b>	<b>Introduction</b>	<b>120</b>
<b>6.2</b>	<b>Kondo transmission and Kondo temperature in QPCs</b>	<b>121</b>
6.2.1	Universal scaling of the conductance	121
6.2.2	Analysis of the Kondo peak in our QPCs	123
6.2.3	Discussion	126
<b>6.3</b>	<b>Probing Kondo phase shift with a scanning gate microscope</b>	<b>126</b>
6.3.1	Description of the experiment	126
6.3.2	Avoiding ZBA splittings	129
6.3.3	Temperature dependence of the phase shift	130
6.3.4	The energy window of the phase shift	131
6.3.5	Value of the phase shift	133
6.3.6	Phase shift versus QPC opening	135
6.3.7	Interpretation	135
<b>6.4</b>	<b>Conclusion and perspectives</b>	<b>137</b>

---

## 6.1 Introduction

Although the zero-bias peak observed in QPCs shows very strong similarities with the Kondo effect known in quantum dots, several aspects differ and are not yet understood. In a first part, we discuss the temperature dependence of the ZBA whose scaling with a Kondo temperature has to be different from that in quantum dots, but could not find any theoretical grounds. Note that the magnetic field dependence of the ZBA, showing anomalous  $g$  factors, is also an open question, but this problem will not be investigated here (because we cannot apply a magnetic field parallel to the 2DEG in our experiment). In a second part, we consider another property of the Kondo effect that can be investigated with the SGM technique and that could shine light on the specificity of the Kondo effect in QPCs. This feature is the Kondo phase shift. It corresponds to the phase shift experienced by a conduction electron scattering off a Kondo system, i.e. a spin  $1/2$  screened by surrounding electrons, forming a spin singlet. In the low temperature limit  $T \ll T_K$ , where  $T_K$  is the Kondo temperature associated with the impurity, this universal phase shift is predicted to be  $\pi/2$ [116]. Though this phase shift cannot be probed in bulk systems, it has regained interest with the ability to probe the transmission phase of quantum dots. This type of beautiful experiment was realized by embedding a quantum dot in one of the arms of an Aharonov-Bohm (AB) ring. First developed in Moty Heiblum's team at the Weizmann institute, this type of devices basically consists in an interferometer controlled by a weak perpendicular magnetic field. Electrons entering on one side of the ring go on left and right arms and interfere on the other side. Depending on the magnetic flux in the ring, the two paths accumulate different phases, therefore the total conductance of this type of devices oscillates periodically as a function of magnetic field, depending on the interference state between the two paths.

By smartly embedding a quantum dot in one of the arms, the authors were able to probe the additional transmission phase of conduction electrons flowing through the dot. They first demonstrated that the transport through the dot is coherent (i.e. interferences are still visible in this configuration), and that an additional phase shift of  $\pi$  is observed each time one electron is added to the dot[117, 118].

This experiment has inspired theorists from Karlsruhe, who proposed to use this method to measure the phase shift due to the scattering off a Kondo singlet[119]. They predicted that the expected phase shift of  $\pi/2$  in the ideal case (at zero temperature, in a symmetric dot) should be visible in the interferences. This experiment has immediately been realized, and the authors found a phase shift of  $\pi$  when traversing a Kondo valley instead of the  $\pi/2$  predicted value[120]. Repeating the same experiment in a more open quantum dot, exhibiting fully developed Kondo effect, the authors found that the problem is more complex. They measured a phase shift ranging from 0 to  $1.5\pi$ , and observed that the presence of the Kondo resonance in odd occupied valleys of the dot affects the phase in the even valleys, though no Kondo effect is visible in this even occupation situation[121]. This result has generated a hot theoretical debate in the community, and was presumably attributed to the too large number of electrons, differing from the ideal one channel case. This experiment has recently been revisited in different AB interferometers, containing only a few electrons and a clear phase shift of  $\pi/2$  was reported when entering a Kondo valley at low temperature[122, 123].

As QPCs also exhibits a Kondo effect (presumably due to an interaction-induced localized

state), one can wonder whether the transmission phase through a QPC in the Kondo regime is also  $\pi/2$ . To answer this question, we use the SGM technique to build a Fabry-Perot interferometer and analyze the phase of the interference fringes observed in the SGM images (see Chapter 3).

## 6.2 Kondo transmission and Kondo temperature in QPCs

### 6.2.1 Universal scaling of the conductance

As explained in the introduction, defining the Kondo temperature in QPCs still is an open question.

For quantum dots,  $T_k$  expresses as [124]:

$$T_k = \sqrt{\Gamma U}/2 \exp[\pi\epsilon_0(\epsilon_0 + U)/\Gamma U] \quad (6.1)$$

where  $\epsilon_0$  is the energy of the bound screened spin,  $\epsilon_0 + U$  is the energy of the next available state ( $U$  corresponds to the charging energy to pay to add one more electron to the dot), and  $\Gamma$  is the width of the tunnel barrier. None of these parameters have obvious equivalent in the case of a spontaneously localized state in quantum point contacts, which makes the assert of an unambiguous Kondo temperature a debated subject.

In quantum dots in the Kondo regime, the conductance as a function of temperature takes a universal form that only depends on  $T_K$  [125]:

$$G(T/T_K) = G_0(1 + (2^{1/s} - 1)(T/T_K)^2)^{-s} \quad (6.2)$$

where  $s = 0.22$  for a spin  $1/2$ , such that  $G(T_K) = G_0/2$ .

The low temperature limit  $G_0$  is equal to the conductance quantum  $2e^2/h$  in the ideal symmetric case. In quantum dots, two tunable tunnel barriers allow to explore the perfectly symmetric case, where the two tunnel barriers connecting the electronic island to the leads are equal, and to reach the unitary limit at low enough temperature [121]. However in quantum point contacts, this symmetry is not obvious and requires to deeply investigate how the small Wigner crystal forming in the QPC channel and leading to Kondo effect is connected to the leads.

An empirical modified form of the Kondo effect has initially been proposed in Ref.[37] to scale the QPC conductance as a function of temperature on a universal function. In this paper, a detailed investigation of the ZBA temperature dependence is reported, and the main results are sketched Fig.2.3 in Chapter 2. These results can be summarized as follows:

1) Above the half transmitted plateau, the conductance of a QPC as a function of temperature scales as a modified form of the Kondo effect, depending only on a fitting parameter  $T_K$  that varies with the QPC opening:

$$G(T/T_K) = 2e^2/h[1/2 \times (1 + (2^{1/s} - 1)(T/T_K)^2)^{-s} + 1/2] \quad (6.3)$$

where  $s = 0.22$ . Comparing to the case of quantum dots (equation(6.2)), it corresponds to adding a constant  $e^2/h$  and change the low temperature conductance increase to  $e^2/h$ . The authors justified this empirical form by the fact that a QPC does not show Coulomb blockade, hence the conductance does not go to zero in the high T limit ( $T \gg T_K$ ). This could also be justified if one spin specie is perfectly transmitted and the other is blocked at high temperature, and restored at low temperature due to the Kondo effect.

2) The fitting parameter  $T_K$  is found to vary exponentially with gate voltage, ranging from 200 mK just above half transmission to 12K close to the first plateau. This can be understood from the quantum dots case where the Kondo temperature exponentially depends on the energy of the last occupied state and of the next available state with respect the Fermi energy (see equation 6.1). In analogy with this equation, the authors proposed that  $\epsilon_0$  and  $\epsilon_0 + U$  represent the energy of the two spin channels whose degeneracy is lifted by the interactions [36]. The authors also argued that this exponential behavior could come from the exponential dependence of  $T_k$  on the tunnel barrier height. In QPCs, it is plausible that the more the first mode is open, the better the localized state giving Kondo effect is connected to the leads, hence the higher is  $T_K$ .

3) The full width at half maximum of the zero bias peak is found be equal to  $2k_B T_K/e$  (where  $T_K$  is extracted from the fitting process described above at fixed gate voltage), within a good agreement, which is consistent with a Kondo-like phenomenon.

4) The zero bias peak is found to split under parallel magnetic field, though this splitting is not uniform in the whole range of gate voltages.

Though this analysis is really convincing to explain that the zero bias anomaly is related to Kondo effect, the chosen scaling law does not allow to evaluate the Kondo temperature below half transmission, because the high temperature conductance in this model is limited to  $e^2/h$  (equation 6.3).

A detailed analysis of the dependence of the ZBA on temperature and magnetic field is presented in Ref[41]. The authors reported that the ZBA was visible in many samples down to conductances of  $10^{-4} \times 2e^2/h$ . They aptly stressed that it was difficult to interpret in terms of a single magnetic impurity forming in the QPC, as no electrons are expected in the center of the channel below the half-transmitted first mode. Interestingly, they proposed that this low-conductance ZBA could arise from two separated localized states on both sides of the channel, each of them being smoothly connected to one lead, and separated by a saddle-point like tunnel barrier. This fact could explain why the ZBA is visible down to very low conductances, and why the conductance in this regime does not reach  $2e^2/h$  but rather saturates to a value limited by the central tunnel barrier.

Formally, it can be understood from the physics of asymmetric quantum dots, where a number of localized electrons is asymmetrically connected to the left and right reservoirs by two different tunneling rates  $\Gamma_L$  and  $\Gamma_R$ . In this situation, the low-temperature transmission in the Kondo regime does not reach unity but saturates to  $2\Gamma_L\Gamma_R/(\Gamma_L^2 + \Gamma_R^2)$ [92]. In the case of QPCs, this could explain why (at least in the low conductance regime), the transmission does not reach unity at low temperature but is limited by the central part tunneling rate.

Another detailed investigation of the ZBA in undoped GaAs structures (in which the electronic density is controlled by a top gate to get cleaner 2DEGs) has been performed in the

Cavendish group (Cambridge) [40]. The authors reported the same kind of observations, with a qualitatively different behavior of the ZBA below and above  $0.7 \times 2e^2/h$ .

## 6.2.2 Analysis of the Kondo peak in our QPCs

### 6.2.2.1 The full width at 2/3 of the maximum

Following these investigations, we can try to define a ‘‘Kondo temperature’’ in our QPCs for different openings. Fig.6.1a shows the temperature dependence of the ZBA for different gate voltages (Fig.6.1a). The ZBA is a sharp peak at low conductance values and broadens above the 0.7 anomaly, as reported in Refs.[37, 40, 41]. Data for higher conductances are not presented here because the ZBA splits into two peaks. Indeed, these data are recorded on the same sample presented Fig.6.4, the tip being close to the QPC, leading to a configuration where the ZBA splits above  $\sim 0.9 \times 2e^2/h$ .

In analogy with Kondo effect in quantum dots, the width of the ZBA is expected to be independent of T below  $T_K$ [124], and be only given by  $T_K$  within a prefactor. In the zero temperature limit, the width of this Kondo peak is expected to be given by  $\Delta V = 2k_B T_k/e$ . The early 2000’s experiments found a reasonable agreement with this factor 2 in carbon nanotubes [126], and also 2 in QPCs, using a modified scaling form[37] (equation 6.3). Pioneering experiments in open GaAs quantum dots also found a prefactor of 1.7, close to 2, but nevertheless lower[95].

But this is also a debated subject in quantum dots, as the intermediate regime where the bias is comparable to the Kondo temperature appears to be a really complicated problem. More recent theoretical investigation of the Kondo peak dependence on temperature and bias showed that a better estimate of  $T_k$  is obtained at 2/3 of the conductance maximum instead of 1/2[127], or equivalently by dividing the temperature scale  $e\Delta V/2k_B$  by  $\sqrt{\pi}$ . This is in very good agreement with a detailed experimental investigation of this problem on InAs nanowire-based quantum dots[128]. It has also been carefully checked in spin 3/2 holes quantum dots but a worse agreement was found[129].

Following these recent developments, we performed this analysis of the full width at 2/3 of the conductance peak maximum (FW2/3M) at different openings, labeled A to E (see Fig.6.1a-b). In contrast to what is done for quantum dots and because of the temperature independent conductance background in case of QPCs, we take the FW2/3M between the conductance maximum at zero bias and the average of the local conductance minima at finite biases (as sketched Fig.6.1b). The FW2/3M is found to be roughly independent of the temperature from 25 mK to 230 mK within the represented error bars, and then increase with T for higher temperatures (not shown here). The average value is plotted in Fig. 6.1d for the different gate voltages and converted into a temperature scale on the right axis.

### 6.2.2.2 Scaling of the conductance

In analogy with the Kondo effect in quantum dots, the temperature dependence of the conductance as a function of  $T/T_K$  shall follow a universal scaling form. As discussed above, we cannot use the modified form proposed by Cronenwett [37] (Eq.6.3) because this formula does not describe the low conductance regime (below half transmission). We

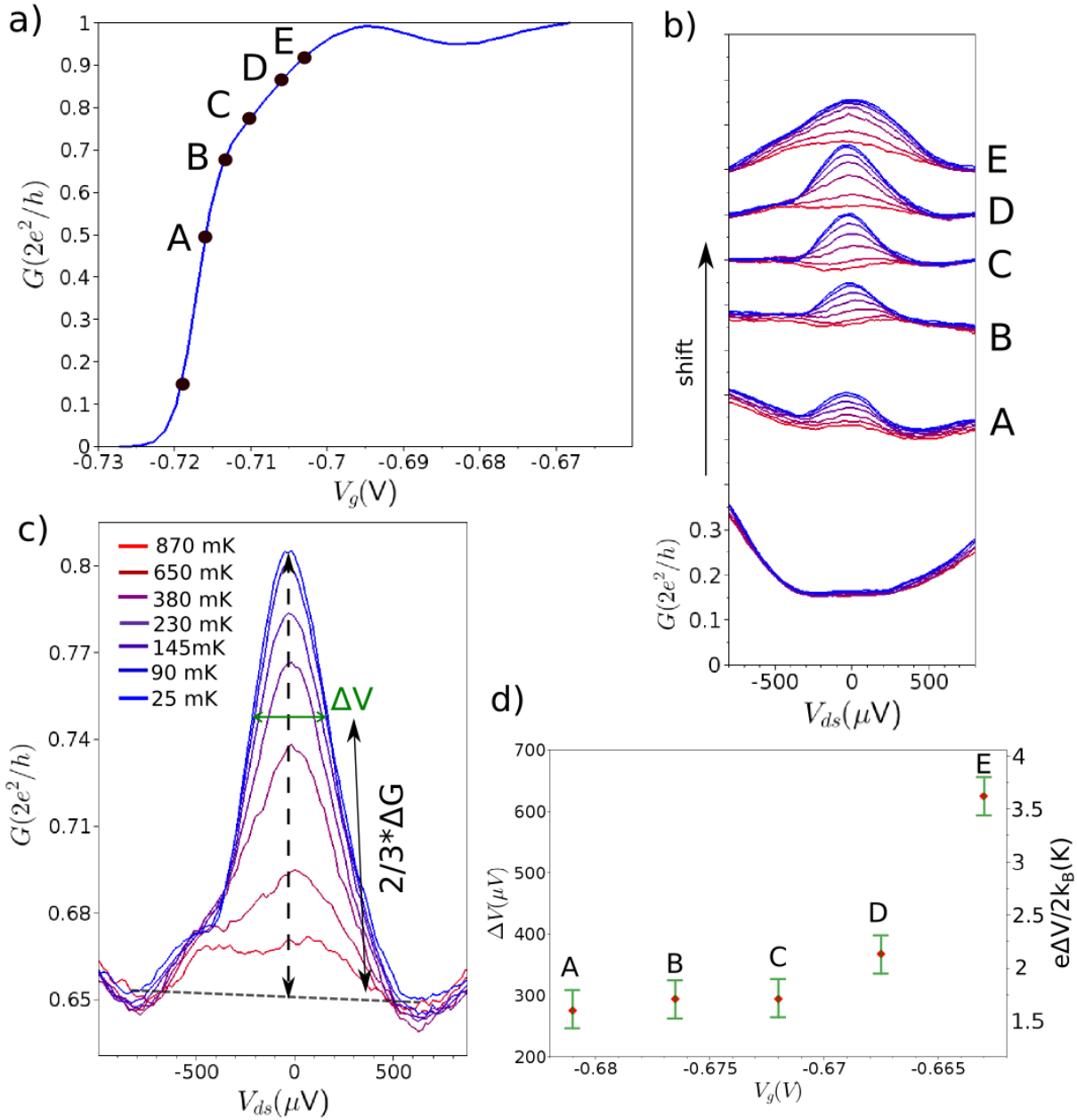


**Figure 6.1** *Temperature dependence of the ZBA* a) Linear conductance  $G(V_g) =$  at  $25\text{ mK}$ , in absence of the tip. Gate voltages A to E are corrected by the tip cross-talk effect to compare with the analysis in b) to d) where the tip is close to the QPC. b) Non-linear conductance for different QPC openings (A to E) and different temperatures. Curves are shifted by  $0.07\ 2e^2/h$ . c) Temperature dependence of the zero bias peak for a specific gate voltage and extraction of the  $FW_{2/3M}$ . d)  $FW_{2/3M}$   $\Delta V$  of the ZBA for different gate voltages (left axis) and corresponding temperature scale  $e\Delta V/2k_B$ . These data are recorded in Louvain-La-Neuve on sample C, in 4 points, using an AC excitation  $\lesssim 10\mu\text{V}$  and taking into account a series resistance of  $1600\Omega$ .

instead take the universal scaling law Eq.6.2 and replace the low temperature limit  $2e^2/h$  by a reduced value  $G_{max} < 2e^2/h$  given by the transmission of an asymmetric quantum

dot as explained in section 6.2.3. The conductance as a function of  $T/T_K$  would then follow the form:

$$G(T/T_K) = G_{max}(T = 0)(1 + (2^{1/s} - 1)(T/T_K)^2)^{-s} \quad (6.4)$$

In practice,  $G_{max}$  will be approximated by the value measured at the lowest possible temperature, and  $T_K$  appears as the only free parameter. By fitting the measured conductance versus temperature according to Eq.6.4 for the different QPC openings, we obtain the values of  $T_k$  plotted as triangles in Fig. 6.2b.

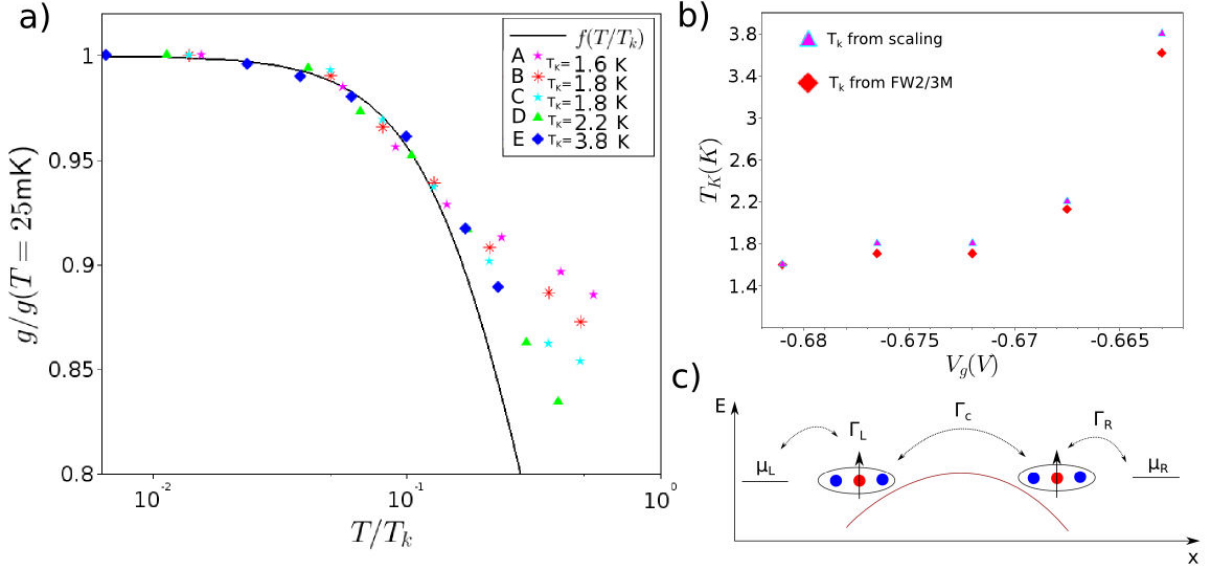


**Figure 6.2** *Scaling of the conductance with the temperature* Conductance at zero bias normalized to the saturation conductance obtained at 25 mK, for the different gate voltages labeled A to E. The horizontal axis represents the temperature in log scale divided by the scaling parameter  $T_K$ . The different  $T_K$  for openings A to E are given in the inset. The black curve shows the scaling law plotted from Eq.6.4. b) Comparison between the temperature corresponding to the FW2/3M extracted from Fig.6.1b (red diamonds) and scaling parameter used in a) (triangles). c) Scheme of a possible configuration of two crystallized regions on both sides of the QPC separated by a saddle-point-like region. At low temperature, the conductance would reach the saddle-point transmission, and not  $2e^2/h$ .

Though this analysis would require more temperatures and gate voltages to be convincing, the temperature deduced from the FW2/3M of the ZBA (red diamonds Fig.6.2b) and  $T_k$  used to scale the conductance as a function of temperature on equation 6.4 (triangles Fig.6.2b) match pretty well. Of course at high temperature the conductance deviates from the proposed scaling law 6.4 inspired from asymmetric quantum dots, because the conductance of a QPC does not reach 0 at high temperature but rather saturates to a high temperature curve  $G(V_g)$ . This curve is itself not understood at the moment and probably deals with the conductance of the Wigner crystal forming in the channel. Note that in quantum dots the conductance also deviates from the scaling law at high temperature because of the broadening of the Coulomb blockade peaks, that can be reproduced by a phenomenological approach[128].

Nevertheless, the correspondence of  $T_k$  extracted from the FW2/3M and from the scaling of the conductance indicates that equation 6.4 could be considered as a possible modified Kondo form to describe the ZBA in QPCs.

### 6.2.3 Discussion

Based on the above analysis, the ZBA in QPCs does not match completely with the Kondo effect in quantum dots. This non-correspondence has been reported[40, 39] and (together with the anomalous magnetic field behavior) has been interpreted as a failure of the Kondo effect to explain the ZBA in QPCs.

On the other hand, our scaling law (Eq. 6.4) could nevertheless be justified if the Kondo effect occurring in the low-conductance regime of QPCs is somehow due to an asymmetric coupling as discussed above and proposed in Ref.[41]. This situation also arises in asymmetric QDs where the linear conductance saturates below  $2e^2/h$  [129]. Theory indeed predicts in this case that the zero temperature conductance saturates to  $2\Gamma_L\Gamma_R/(\Gamma_L^2+\Gamma_R^2)$ [92].

A corresponding situation possibly explaining this behavior in QPCs is sketched Fig.6.2b, where two presumed localized states are present on both sides of the QPC, separated by a central tunneling region. This scenario could explain why the ZBA does not reach  $2e^2/h$  at low temperature below the first half-plateau but rather saturates to a conductance limited by a behavior similar to the Büttiker saddle-point model [10], that depends on gate voltage.

Above half-transmission, if these two localized states exist, they are expected to merge into a single 1D Wigner crystal with non-uniform charges spacing, and it is possible that transport is governed by different effects in this regime. This scenario could explain why both the linear and non-linear conductance seem to present qualitatively different behaviors below and above half transmission. Indeed, the linear conductance seem to present a regular curve from the pinch-off to  $e^2/h$  but exhibits the 0.7 anomaly above, and the ZBA in the non-linear conductance curves leads apparently to different forms of the Kondo effect below and above half transmission [37, 41, 40, 30]).

The possible existence of two separated localized states on both sides of a QPC have indeed been found in a numerical study[45], but never in other studies to our knowledge[130], which makes this scenario only an hypothesis .

## 6.3 Probing Kondo phase shift with a scanning gate microscope

### 6.3.1 Description of the experiment

Though the temperature and magnetic field dependence of the ZBA are the cause of its debated link with Kondo physics, we can wonder if another hallmark of the Kondo effect could be associated with the ZBA observed in QPCs like the famous Kondo transmission phase of  $\pi/2$ . This section presents how an effect like the Kondo phase shift can be detected in scanning gate experiments, that could reconcile the ZBA in QPCs with Kondo physics. The idea is to perform an interferometric measurement, relying on the interferences visible in the SGM images, and to investigate the influence of the ZBA on

these interferences.

In the case of quantum dots embedded in AB rings, the plunger gate voltage is generally used as the control parameter to go from a Kondo valley to a non-Kondo valley, and the interferences are followed while sweeping this control parameter. As crossing a Coulomb peak, which can be modeled by a Breit-Wigner resonance, an additional transmission phase shift of  $\pi$  is experienced by the conduction electrons crossing the dot. The difficulty to observe the expected  $\pi/2$  phase shift in the Kondo valleys is still responsible for the scientific debate on the interpretation of these measurements.

In our study, the interferometer is not an Aharonov-Bohm ring but rather a Fabry-Pérot cavity, formed by the QPC and the tip-induced depletion spot in the leads. When the QPC is below the first plateau, a Kondo resonance develops. We then have an interesting situation of a Fabry-Pérot cavity, in which one of the mirrors contains a Kondo singlet (a small spin 1/2 Wigner crystal screened by the surrounding electrons), as sketched Fig.6.3c. We will demonstrate in this chapter that we indeed observe a phase shift of the interferences at the ZBA, possibly connected to the Kondo phase shift.

In our case, the parameter used to cross the Kondo resonance is the source-drain bias instead of the gate voltage in AB experiments, and the interferences are recorded by sweeping the tip distance instead of the magnetic field.

To do so, we perform the same experiment as presented in Chapter 3 Fig.3.11. We first record an SGM image by scanning the tip in a parallel plane 30 nm above the sample surface, with an applied negative voltage of -6V. We then choose a line along which these interferences are visible, and record the interferences for different DC source-drain bias, at a given QPC opening (for fixed gate voltage). Note that in all the following figures, we choose as a convention the voltage bias to denote the potential of the reservoir opposite to the tip.

A first glance at this type of experiment is given Fig.6.3. This figure presents the spectroscopy of the interferences at different openings for the two samples discussed in Chapters 3 and 5 (sample B and C).

The SGM images obtained on the plateau are presented in a) and b). A specific line is chosen for each sample, where interferences are clearly visible. We then record the spectroscopy of these interferences, i.e. how these interferences evolve with source-drain bias, at different two QPC openings, labeled  $\alpha$  and  $\beta$ .

Fig.6.3f and i present these spectroscopies on the plateaus. In this configuration, the interferences accumulate phase linearly with source-drain bias in a monotonic fashion. As discussed in Chapter 3, we interpret this phase accumulation by a displacement of the QPC saddle-point in real space induced by the source-drain bias that deforms the potential landscape together with an increasing wavelength of the electrons with decreasing energy.

By repeating the same experiment below the first plateau, around  $0.7 \times 2e^2/h$  (Fig.6.3e and h), the behavior of these interferences with source-drain bias dramatically changes. A clear phase shift of the interferences is observed around zero bias, superimposed on a monotonic accumulation of phase with source-drain. As we will see in the following, this phase shift can undoubtedly be attributed to the zero bias anomaly, and may be related to the Kondo phase shift. To show that this phase shift is correlated to the presence of the ZBA, two profiles of  $G(V_{sd})$  below and on the first plateau have been extracted Fig.6.3d

### 6.3. PROBING KONDO PHASE SHIFT WITH A SCANNING GATE MICROSCOPE

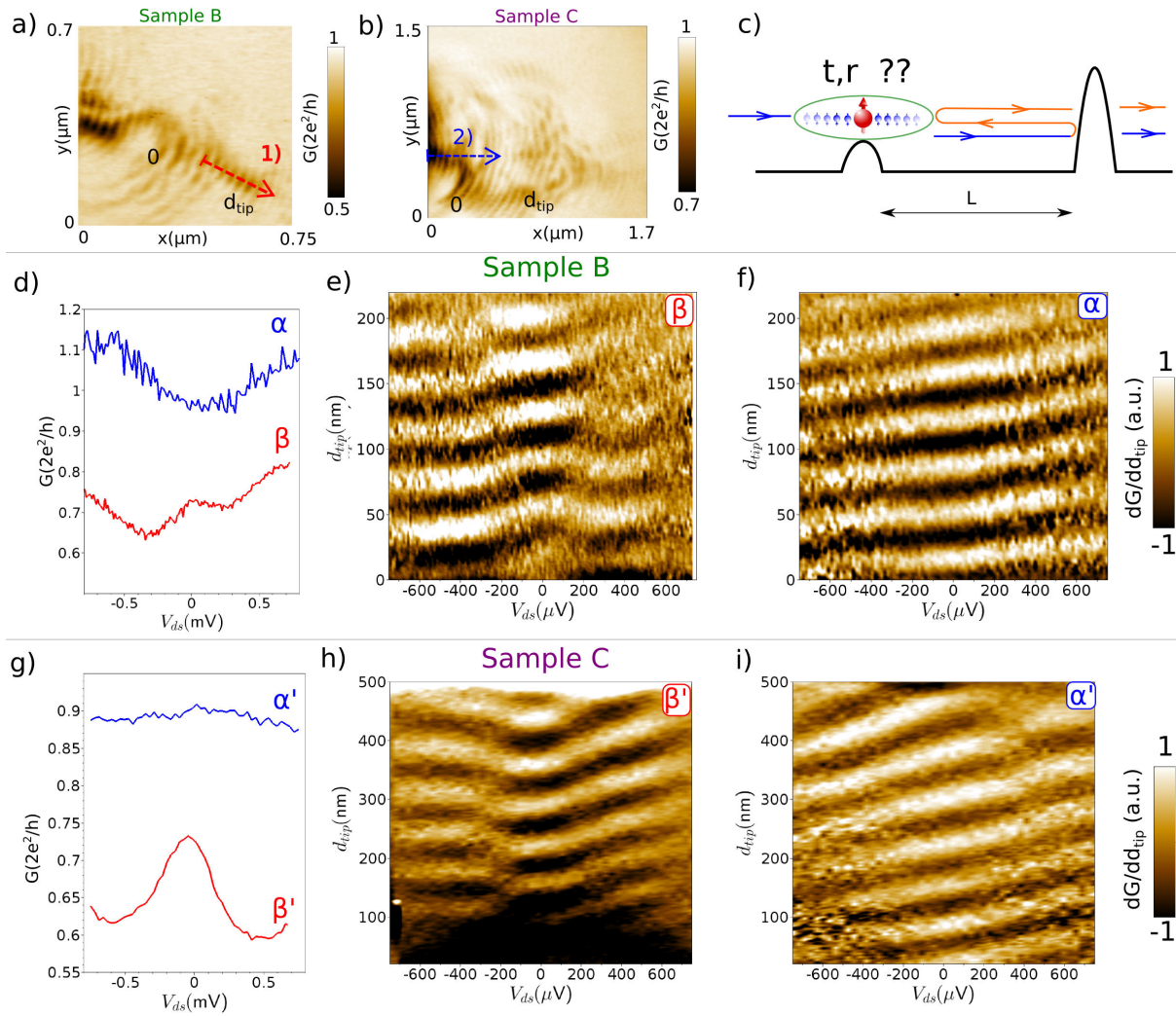


**Figure 6.3 Non-linear dependence of the interferences** a) SGM image recorded on the first plateau for sample B. b) SGM image recorded on the first plateau for sample C. c) Schematics of the interferometric experiment: a Fabry-Pérot cavity with a Kondo singlet as a mirror. d-e) Data recorded on sample B. d) Conductance as a function of source-drain bias on the plateau (blue curve) and below (red curve). e) Spectroscopy of the interferences:  $\partial G/\partial d_{\text{tip}}$  as a function of tip position along red line 1 and source-drain bias, differentiated with respect to tip position to highlight details. The QPC is open below the first plateau, for gate voltage  $\beta$  f) Same data but the first QPC mode is fully open, for gate voltage  $\alpha$ . g-i) Same experiment recorded on sample C. g)  $G(V_{sd})$  for two different gate voltages  $\alpha'$  (on the first plateau) and  $\beta'$  (below). h) Spectroscopy of the interferences at gate voltage  $\beta'$ . i) Spectroscopy of the interferences at gate voltage  $\alpha'$

and g. For sample C, the interferences in Fig.6.3h below the first plateau experience a shift in a voltage range corresponding to the ZBA in Fig.6.3g (red line), whereas on the plateau (blue line), the conductance is monotonic and the interference do not experience any shift except a constant accumulation of phase with source-drain.

### 6.3.2 Avoiding ZBA splittings

In the following, we concentrate only on sample C. As detailed in the previous Chapter, approaching the tip towards the QPC can change the number of localized charges and hence the nature of the ZBA from a single to a double peak. As the situation of our experiment is already complex, and has never been studied theoretically, we will try to avoid the more complicated case where the QPC contains an even number of charges that lead to a split-peak ZBA, though this situation could be really interesting to investigate in the future. The phase shift experienced by electrons crossing two coupled quantum dots in series has to our knowledge never been explored, though recent investigations of two quantum dots embedded in an AB rings have made a step in this direction [131]. Here our case of a two-impurity Kondo system leading to even Kondo effect and constituting one mirror of a Fabry-Pérot cavity is far beyond the scope of this thesis and the actual theoretical knowledge.

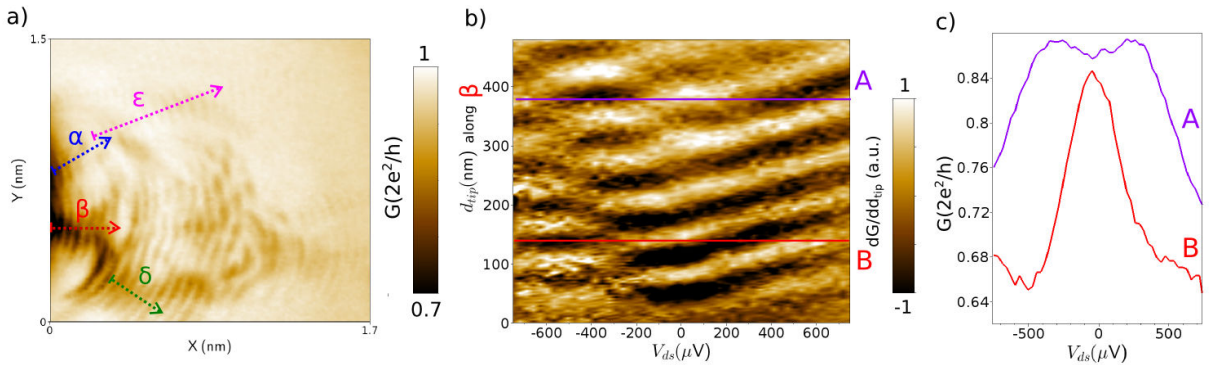


**Figure 6.4** *Effect of the ZBA splittings* a) SGM map recorded on the first plateau for the sample C. Different lines  $\alpha$ ,  $\beta$ ,  $\delta$  and  $\epsilon$  are drawn, that will be used in the following. The origin of the abscissa is taken on the left side. b) Spectroscopy of the interferences recorded along line  $\beta$ , differentiated with respect to the tip abscissa along this line to highlight details. c) Non-linear conductance  $G(V_{sd})$  for two different tip positions A and B, corresponding respectively to a split peaks and a single peak ZBA.

Nevertheless, an interesting experimental result that could be analyzed in the future is presented in Fig.6.4. We place in purpose the system in a situation where moving the tip away from the QPC generates a splitting of the ZBA. Fig.6.4c presents the non-linear conductance traces of the QPC for two different tip positions A and B along red line  $\beta$ . The average conductance of the QPC is about  $0.75 \times 2e^2/h$ . For position A, with the tip away from the QPC, the ZBA appears as two peaks centered at  $\pm 300 \mu V$ , presumably attributed to a situation where the Wigner crystal contains an even number of charges. Approaching the tip to position B leads to a single-peak ZBA, hence an odd number of localized electrons in the channel.

The spectroscopy of the interferences along this line is interesting. The phase shift seems to split in two successive phase shifts as the ZBA is brought from an odd situation (B) to an even situation (A). Though this situation is too complex to be investigated, it is a first demonstration that the phase shift of the interferences is really sensitive to the nature of

the ZBA.

In the following, the tip will be scanned along the different lines  $\alpha$ ,  $\beta$ ,  $\delta$  or  $\epsilon$  depending on the QPC opening, to avoid splittings of the ZBA to occur as a function of tip position.

### 6.3.3 Temperature dependence of the phase shift

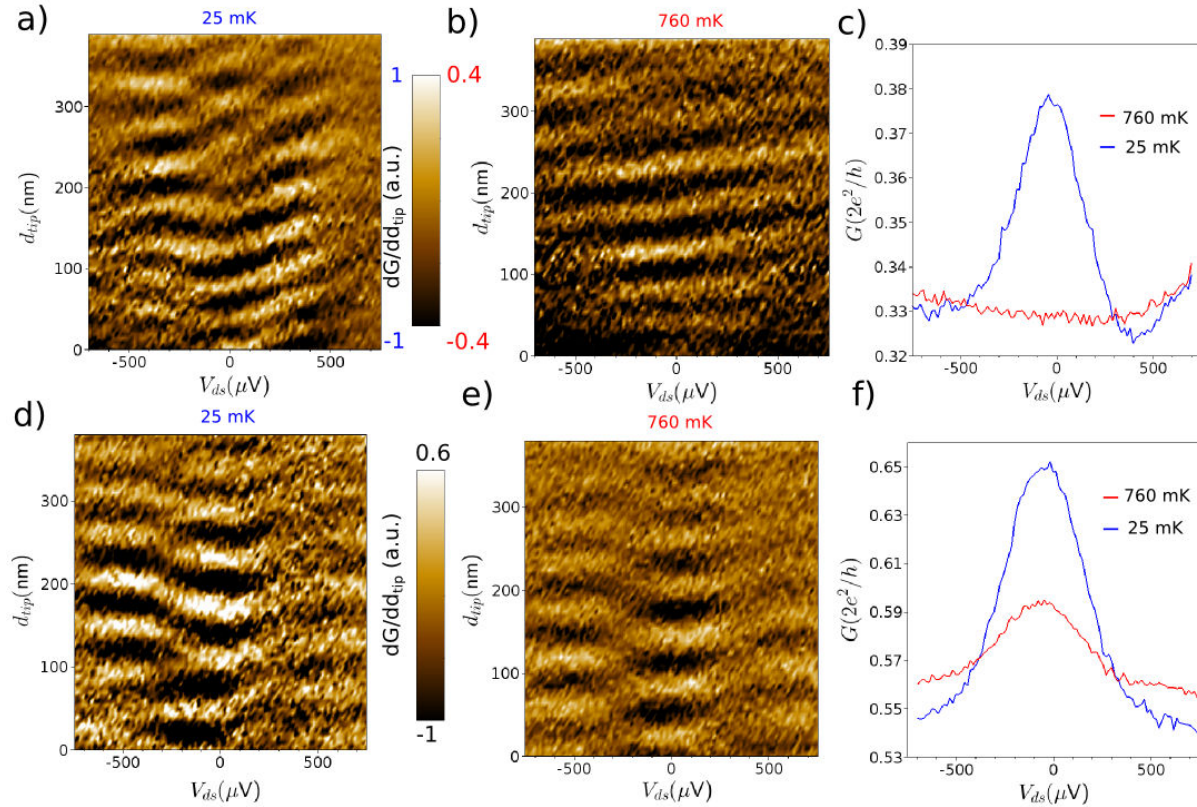


**Figure 6.5** *Disappearance of the Kondo phase shift at high temperature.* a) Spectroscopy of the interferences near pinch-off, at a base temperature of 25 mK. The tip is scanned along green line  $\delta$  Fig.6.4a, the abscissa is oriented away from the QPC. Data are differentiated w.r.t. tip position along this axis to highlight details. b) Same experiment recorded at a base temperature of 760 mK. The phase shift has disappeared. The colorscale has been adapted compared to a) because the interferences are less contrasted due to the higher temperature. c) Two extracted profiles  $G(V_{sd})$  at 25 and 760 mK, the tip being at the line end (far from the QPC). d) Spectroscopy of the interferences at 25 mK, the tip is scanned along blue line  $\alpha$  Fig.6.4a. e) Same data recorded at 760 mK. f) Two profiles of  $G(V_{sd})$  at these two temperatures.

A smoking gun to attribute this phase shift of the interferences to the presence of the ZBA is its temperature dependence. One has to be in a suitable configuration to observe this subtle behavior, which explains why the results presented in this section will not be perfectly systematic but rather give a flavor of what happens.

We shall first consider a gate voltage for which the ZBA disappears rapidly with temperature. One of the subtleties is that  $T_K$  shall be low enough at this QPC opening for the ZBA to disappear *before* the interferences. As explained in Chapter 3, the interferences

in this SGM experiment are blurred by thermal averaging around 1K. Therefore, we shall place ourselves in a situation where:

- The ZBA disappears around 500mK.
- The tip follows a line where the interferences are visible and do not disappear up to 1K.
- The tip does not change the nature of the ZBA along the studied line.

Fig.6.5 shows the results of this experiment for two different QPC openings, hence two different  $T_K$ . Fig.6.5a to c present data obtained near pinch-off, around  $0.35 \times 2e^2/h$ . At this opening, the ZBA presents a clear well-developed peak at 25 mK, that disappears completely at 760 mK (Fig.6.5c). The corresponding interferences are analyzed for tip positions along green line  $\delta$  Fig.6.4a. At 25mK (a), a clear phase shift of the interferences is observed around zero bias. Note that the width of this phase shift is not uniform all along the line, but is clearly present for every tip positions. At 760mK (b), though the interferences are less contrasted due to thermal averaging, the phase shift has disappeared and the interferences accumulate phase monotonically with source-drain bias, as observed on the plateau (see Fig. Fig.6.3f and i).

The same analysis is repeated for a different QPC opening Fig.6.5d to f. At this opening, the average conductance is around  $0.6 \times 2e^2/h$  and the ZBA is still visible at 760 mK, presumably due to a higher Kondo temperature. The corresponding spectroscopy of the interferences is performed by scanning the tip along a different line (blue line  $\alpha$  Fig.6.4a), to avoid ZBA splittings. From Fig.6.5e, it is clear that the phase shift of the interferences around zero bias is still present at this high temperature. Note that the ZBA width is the same at both temperatures and that the phase shift also occurs in the same voltage range at both temperatures.

These data clearly demonstrate that the phase shift of the interferences can undoubtedly be attributed to the presence of the zero bias anomaly. At low temperature, below the first plateau, a clear phase shift is observed in the interferences around zero bias, when the ZBA is visible in the conductance. However, when no ZBA is visible in the non-linear conductance (on the plateau or at high enough temperature below the plateau), the phase shift is not visible and the interferences simply accumulate phase with source-drain, in a monotonic fashion.

### 6.3.4 The energy window of the phase shift

A natural question that arises at this point is the energy width on which this phase shift occurs, and how does it compare to the width of the ZBA. To answer this question, we analyze the interferences along pink line  $\epsilon$ , for a gate voltage around half transmission. Following the discussion of section 6.2.2.1, we will compare the energy on which the phase shift occurs to the full width at 2/3 of the maximum of the ZBA, which seems to give  $T_k$  more accurately than the FWHM. The results are presented Fig.6.6.

It is first important to note that the ZBA width evolves with tip position along this line. Though we do not have a conclusive explanation for this fact, it is possible that the tip-induced potential changes the coupling between the localized state in the QPC and the leads, hence changes the Kondo temperature, as does the gate voltage ( $T_k$  evolves with the QPC opening). We will use this effect to correlate the width of the ZBA and

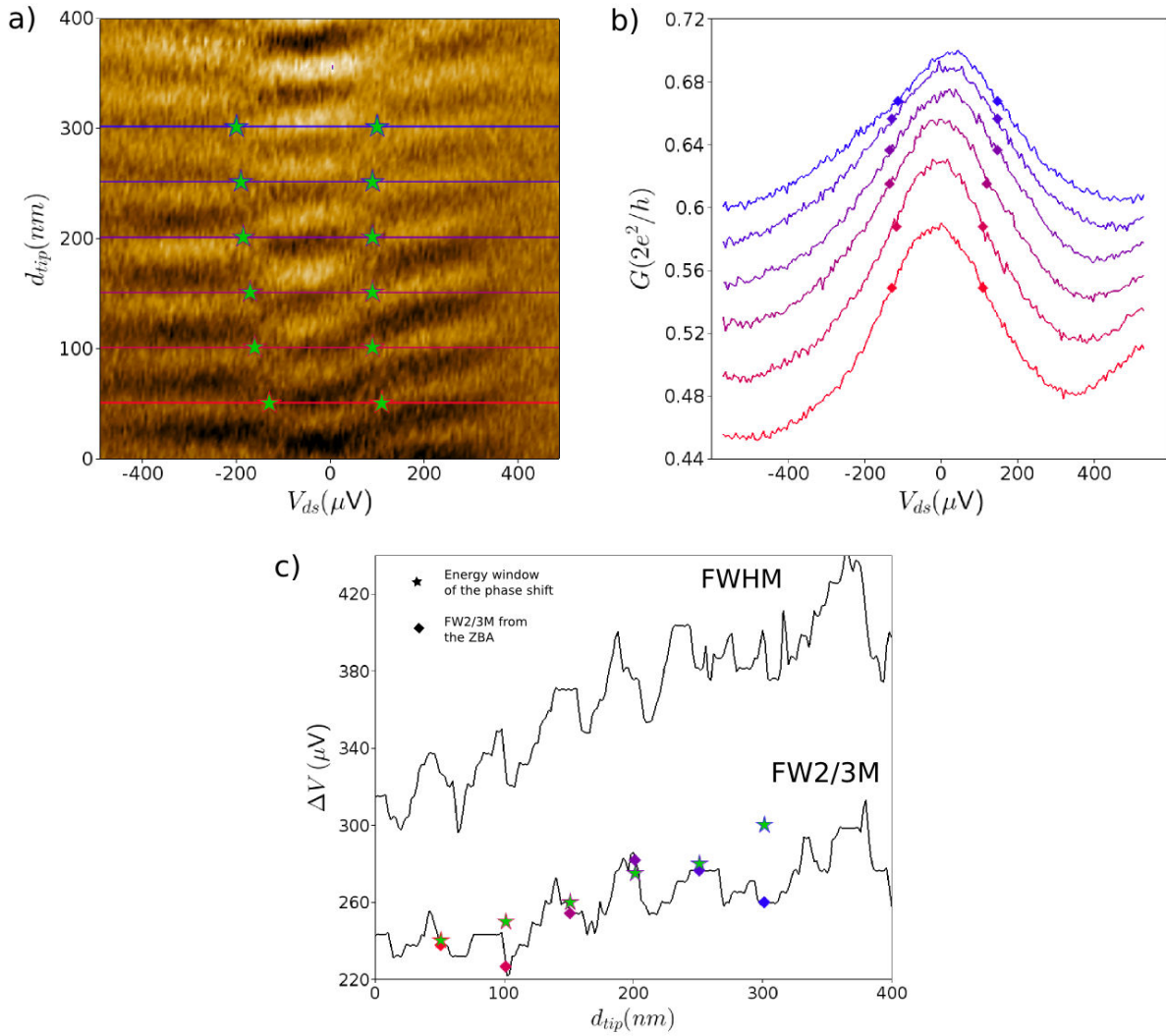


**Figure 6.6 Analysis of the phase shift energy width.** a) Spectroscopy of the interferences recorded at 20 mK by scanning the tip along pink line  $\epsilon$ , the QPC being open below the half transmission. Colored stars represent the evaluated bounds on which the phase shift occurs. b) Extracted profiles  $G(V_{sd})$  for different tip position. The corresponding tip positions are drawn as colored lines in a). c) Extracted FW2/3M (lower curve) and FWHM (higher curve) as a function of tip position. The energy window of the phase shift for specific tip positions is reported at color stars. The FW2/3M for the 6 specific tip positions in b) are plotted as colored diamonds.

the energy window on which the phase shift occurs.

Some profiles of  $G(V_{sd})$  are extracted for specific tip positions and plotted Fig.6.6b. On this figure, one can already guess that the width of the ZBA changes between these tip positions. To quantify this effect, we numerically extract the FW2/3M and the FWHM of the ZBA for all tip positions along a part of line  $\epsilon$  at this opening, following the method exposed in section6.3.1, and plot both results Fig.6.6c. An interesting observation is that both FWHM and FW2/3M seem to oscillate as a function of tip position, with the same periodicity as the conductance, though the signal is noisy.

This fact is interesting by itself because it means that the interference state in the Fabry-

Pérot cavity formed between the tip-depleted region and the QPC can affect the Kondo temperature. This type of "back-action" of the cavity on the Kondo system could be interesting to investigate in the future, and a recent theoretical work has made a step in this direction [132].

Letting aside this oscillating effect, we can concentrate on the fact that the width increases in average as the tip is brought away from the QPC. Six specific tip positions are chosen, colored from red to blue. For these positions, the energy window on which the phase shift of the interferences occurs can be evaluated. As this phase shift changes from one conductance oscillation to another no clean signal treatment allows to extract this width. We therefore evaluate it by hands, and as this phase shift is quite abrupt, we evaluate the uncertainty of this method to  $\pm 30\mu V$ . This estimation is reported Fig.6.6c as colored stars. For comparison, we reported the FWHM and the FW2/3M on the same graph. The bias range on which the phase shift occurs seems clearly given by the FW2/3M of the ZBA rather than the FWHM. Note that the FW2/3M and the bias range of the phase shift follow the same tendency: as the tip is approached towards the QPC, the FW2/3M of the ZBA decreases, and so does the energy window of the phase shift, with a similar average slope.

Two main conclusions shall be emphasized from this analysis. First the phase shift does not evolve following the zero bias peak continuously, but is rather abrupt and seems to jump to another value. The bias range on which this phase shift takes place seems to really match the FW2/3M of the ZBA, and follows the same average variations.

### 6.3.5 Value of the phase shift

#### 6.3.5.1 Signal analysis

To analyze how much the interferences shift, we use a numerical Fourier analysis. To have a better resolution, we choose to scan the tip along the longest line where interferences are visible: pink line  $\epsilon$ .

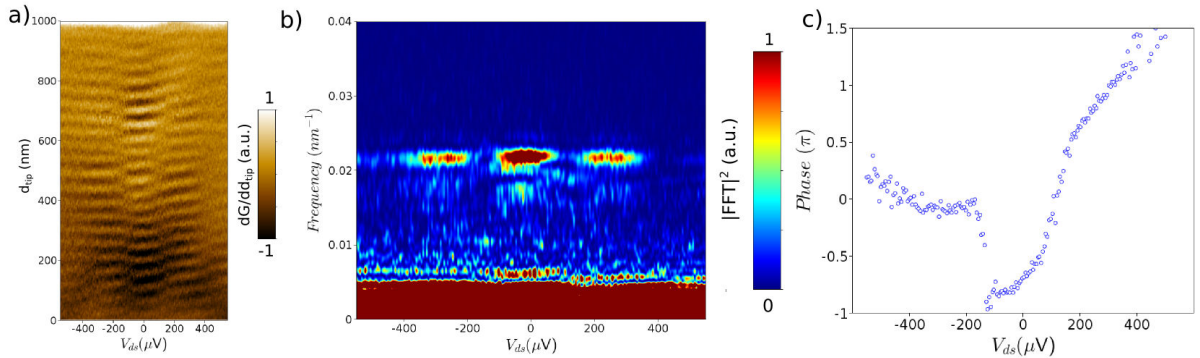


**Figure 6.7** *Fourier analysis along line  $\epsilon$ . a) Interferences along line  $\epsilon$  as a function of source-drain bias and tip position. The signal is differentiated w.r.t. position along this line. b) Square modulus of the Fourier transform modulus, as a function of spatial frequency and source-drain bias. The dominant frequency appear as bright spots at  $0.022\text{ nm}^{-1}$ . c) Phase of the interferences normalized to  $\pi$  as a function of DC source-drain bias.*

The results of this analysis are presented Fig.6.7. Fig.6.7a presents the spectroscopy of the interferences along this line. The data have been differentiated w.r.t. the tip position to highlight details (note that raw data are used for Fourier analysis). We then perform the Fast Fourier transform (FFT) and plot the square modulus of the FFT as a function of the spatial frequency and source-drain bias (see Fig.6.7b). The colorscale is adapted to saturate the low-frequency component, that dominates due to the average conductance of the signal (leading to a zero-frequency maximum in the FFT modulus). The dominant frequency clearly appears around  $0.022 \text{ nm}^{-1}$ , which corresponds to the spatial period of  $45 \pm 5 \text{ nm}$ . The phase of the interferences is then calculated as the argument of the complex Fourier transform at this dominant frequency, with an arbitrary reference. The result of the phase of the interferences as a function of source-drain bias is plotted Fig.6.7c. It results that the phase shift of the interferences in the ZBA region is slightly less than  $\pi$ , a first sharp shift occurring around  $-150 \mu\text{V}$ , and a second around  $+150 \mu\text{V}$ . Note that these voltages are average values because the energy width of the phase shift constantly evolves depending on tip position as discussed above. The FFT computed all along the scan line can therefore not resolve the position of this phase shift in source-drain bias.

### 6.3.5.2 Another example

This analysis can be repeated along a different line and for another QPC opening. As an example, we choose the red line  $\beta$  to perform the same analysis. The results are presented Fig.6.8.

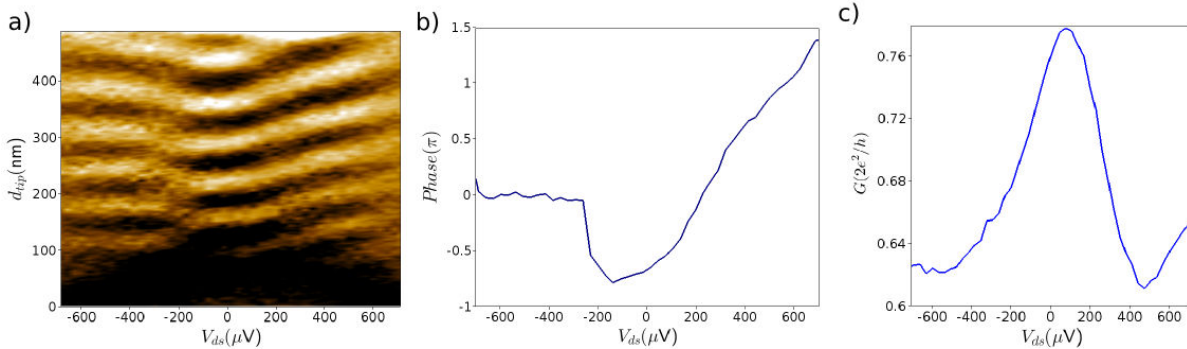


**Figure 6.8** *Fourier analysis along line  $\beta$  at 25 mK.* a) Interferences along line  $\beta$  as a function of source-drain bias and tip position. The signal is differentiated w.r.t. tip position along this line. b) Phase of the FFT at the dominant frequency, normalized to  $\pi$ , as a function of source-drain bias. c) Profile of  $G(V_{sd})$  when the tip is at the end of line  $\beta$  ( $d_{tip} = 500 \text{ nm}$ ).

Fig.6.8a shows the spectroscopy of the interferences along line  $\beta$ , when the QPC is open around  $0.65 \times 2e^2/h$ . The ZBA is well developed and forms a single peak in this configuration, as shown Fig.6.8c where a profile of  $G(V_{sd})$  is extracted, the tip being at the end of line  $\beta$ .

We compute the FFT of the raw conductance signal and extract the dominant frequency. Note that in this configuration, the spatial period of the interferences is larger than along line  $\epsilon$ , presumably due to the reduced density. Indeed, this analysis is performed very close to the QPC, and the Fabry-Pérot cavity between the QPC and the tip fully-depleted

region may experience in average a reduced density because of the tip and gates voltages. As explained above, we then extract the phase of the FFT at this dominant frequency and plot this phase as a function of the source-drain bias. We can note that on one side of the ZBA (for negative source-drain biases), the phase of the interferences is almost insensitive to the source-drain bias. It then exhibit a sharp shift of about  $0.8\pi$ , and a second less sharp and less important shift. On the other side of the ZBA, for positive source-drain biases, the interferences continuously accumulate phase with increasing source-drain bias, as do the interferences on the plateau.

### 6.3.6 Phase shift versus QPC opening

This section establishes a connection between this phase shift and the one observed in the three-gate interferometers as a function of the split gate voltage (see Chapter 3, section 4.2.1). To show that the phase shift observed as a function of source-drain bias in SGM experiments and the one observed as a function of split gate voltage in the three gate interferometers at the 0.7 anomaly are linked, we proceed as follows. We scan the tip along red dashed line  $\beta$  Fig.6.4a, and vary the QPC opening from the pinch-off to the middle of the first plateau. We first perform this experiment at zero DC bias voltage (i.e. at the top of the ZBA), and plot the result in Fig.6.9a. A phase shift is observed before the opening of the first plateau, as observed in the interferometers (see Fig.4.4). We then repeat this experiment, but applying a DC voltage of  $-350\mu V$  to be out of the ZBA, and plot the result in Fig.6.9b. Interestingly, the abrupt phase shift as the first mode opens has disappeared in these conditions, which indicates that the observed phase shift in source-drain bias and the one observed as a function of  $V_g$  are intimately linked, and are the signature of the same phenomenon.

Note that this phase shift at the first mode opening can be guessed in the same kind of data recorded with a SGM on a QPC presented in Ref.[133] (Fig.4.5), though it has not been analyzed, as this thesis focused on quantum Hall physics.

### 6.3.7 Interpretation

Though at this time a clear interpretation of these results is still lacking (but ongoing work), some hand-waving interpretation can already be drawn. In the experiment described above, we are in a configuration of a Fabry-Pérot cavity, which contains a Kondo singlet on one side. It clearly appears that the interferences developing in the cavity are phase-sensitive to the Kondo resonance. The question is to understand where does this phase shift takes place and how it is connected to the universal phase shift by  $\pi/2$  experienced by an electron scattering off a Kondo system.

Before taking a look at different possible scenarios, some assumptions shall be made. We will first make the hypothesis that the problem can be reduced to a single-mode Fabry-Pérot cavity forming between the QPC and the tip-depleted region, and that the main contribution to the interferences comes from trajectories crossing once the cavity, and trajectories making two turns in it, hence reflected once on the QPC. As discussed in Chapter 4, this is oversimplified because disorder in the leads is responsible for inter-mode scattering in the cavity, which itself may be responsible for non-vanishing contrast of the

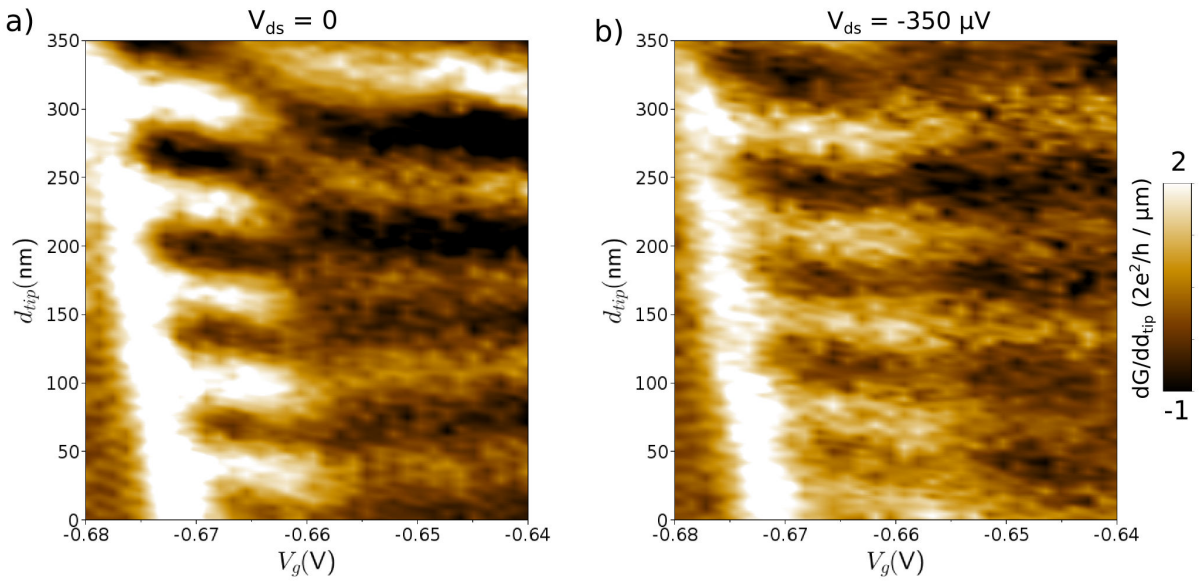


**Figure 6.9** *Phase shift as a function of the opening.* a) Interferences as a function of gate voltage, from the pinch-off ( $V_g = -0.68\text{V}$ ) to the middle of the first plateau ( $V_g = -0.64\text{V}$ ), the tip is scanned along red line  $\beta$  Fig.6.4a. Data are differentiated w.r.t. the tip abscissa along this line to get rid of the average conductance. No DC voltage is applied to the sample. b) Same data recorded in the exact same conditions, but a DC voltage of  $-350 \mu\text{V}$  is applied to the sample.

interferences on the plateau. We remind at this point that in the perfect single-mode case, the interferences would not be visible on the first plateau, as this would correspond to a Fabry-Pérot cavity with a transparent mirror. Nevertheless, this simple model can already give some clues and allows a hand-waving analysis, but is not aimed to catch all the physics of the problem.

That being said, it shall be emphasized that the transmission phase experienced by the electrons crossing the saddle-point cannot be probed in this experiment, since all trajectories contributing to the conductance cross the QPC. Indeed, the path differences leading to interferences in this model come from the coherent superposition of the blue and orange trajectories sketched Fig.6.10. The total path difference includes the phase accumulated by crossing twice the cavity (the orange trajectory crosses twice more the cavity than the blue one), and eventually an additional phase experienced at the *reflexion* on the QPC. In the case of localized states forming in the channel and leading to a Kondo resonance (scenario b), the orange path experiences once an additional phase due to the reflexion on this Kondo system. The phase shift would then be of  $\pi/2$  at the Kondo resonance.

If an entire Kondo system, including the localized spin and the surrounding screening electrons was contained in this Fabry-Pérot cavity, we should expect a dephasing of  $\pi$  at the Kondo resonance, because one path (the orange one) would cross three times the Kondo singlet and the blue one only once, experiencing each time a dephasing of  $\pi/2$ . In this situation, represented for example in scenario c) Fig.6.10, the interferences would shift by  $3\pi/2 - \pi/2 = \pi$  at the Kondo resonance.

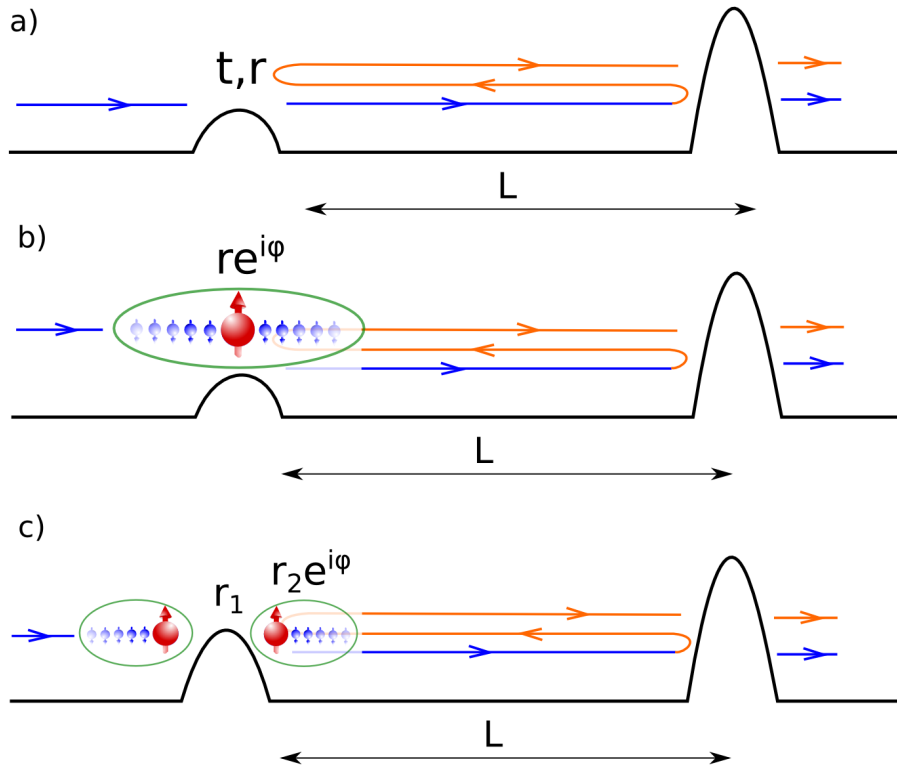


**Figure 6.10** *Different scenarios to understand this phase shift.* a) Simple non-interacting case. A Fabry-Pérot cavity forms between the QPC and the tip-depleted region. b) Case of a single Kondo resonance in the center of the QPC, forming one of the mirrors of the Fabry-Pérot cavity. c) Situation of two separate impurities, on both sides of the channel, and their respective screening clouds.

Let's now compare with the experimental results presented in the previous section. As far as our investigation can tell, the additional phase shift observed at the Kondo resonance is more than  $\pi/2$ , but seems less than  $\pi$ . As this signature is superimposed to a background phase shift with source-drain, this renders the analysis difficult, and we cannot unambiguously distinguish between  $\pi$  and  $\pi/2$ . Finally, a complete treatment and theoretical investigation of the problem is needed, that we do not have at the moment, but which is on the way with the grateful help of Pascal Simon, expert in this field.

## 6.4 Conclusion and perspectives

In conclusion, we studied in this chapter the features of the zero bias anomaly in QPCs that can be related to the Kondo effect. We first studied the temperature dependence of the ZBA and correlated it with its FW2/3M. We showed that the temperature corresponding to the FW2/3M of the ZBA allows to scale the temperature evolution of the ZBA on a universal scaling function similar to the expected one for the Kondo effect in an asymmetric quantum dot.

Pushing one step further the similarities with the Kondo effect, we have presented in

this chapter an interferometric study of the zero bias anomaly. By forming a Fabry-Pérot cavity between the QPC and the tip-depleted region, we can analyze the dependence of the interferences with DC source-drain bias. When the QPC is open to the first plateau, we observe that interferences monotonically accumulate phase with source-drain bias, that might be attributed to the displacement of the QPC in real space and the changes in  $\lambda_F$  with energy.

Below the first plateau, where the zero bias anomaly is present in the differential conductance, an additional phase shift of the interferences is observed in the bias range of the ZBA. In addition, the interferences are insensitive to source-drain bias on one side of the ZBA, and monotonically accumulate phase with source-drain on the other side. Around zero bias, an additional phase shift is observed, sharp on one side and smoother on the other, of more than  $\pi/2$  but less than  $\pi$ . The energy width on which this phase shift is observed appears intimately correlated to the full width at 2/3 of the maximum of the zero bias peak, which itself seems to match the Kondo temperature.

This phase shift disappears at high temperature when the ZBA is no longer present, depending on the QPC opening and the tip position. Finally, this phase shift exhibits even more confusing signatures when the ZBA appears as a double peak, showing that it is intimately connected to the ZBA.

Though we do not have an exact explanation for this phase shift, we propose that it is somehow connected to the universal Kondo phase shift. Indeed, simple considerations show that the studied system is likely to be sensitive to this phase if a Kondo resonance develops around the interaction-induced state forming in the QPC. Though this statement still requires some theoretical work to be fully convincing, it could be the smoking gun to rule out the possible non-Kondo scenario proposed to explain the zero-bias peak in quantum point contacts [57]. Indeed, the additional phase shift accumulated in reflection in the ZBA regime as well as the splittings of the zero-bias anomaly observed in SGM and in length-tunable QPCs [9] put some strong experimental bounds on the possible scenarios to explain the ZBA, and the Kondo effect appears as a promising phenomenon to explain both of these facts.

I would like to mention a last perspective that this work opens. Though it is well-known that when scattering off a Kondo singlet the conduction electrons experience a phase shift of  $\pi/2$ , it is still a hotly debated subject to know *where* this phase shift occurs. In particular, the spatial structure of a Kondo singlet remains nowadays a purely theoretical debate. It is usually accepted that the spin correlations around a magnetic impurity present a large spatial extend [134]. If  $T_k$  is the Kondo temperature, this length scale is given by  $\xi_k = \hbar v_f / k_B T_K$ . Simple orders of magnitude show that for the usual Kondo systems in 2DEGs, this spatial extend ranges from 100 nm to  $1\mu m$ . Therefore, the electrons dynamically screening the spin of the magnetic impurity are expected to extend on a huge length scale, forming what is usually called the Kondo screening cloud [135]. Despite the very large length scale on which these correlations are expected and the large amount of theoretical proposals to detect the Kondo cloud (a few examples can be found in Refs.[136, 137, 132]), it has never been observed experimentally.

The experiment presented in this chapter offers a new promising technique to investigate this phenomenon. We are in a situation of a distant scatterer to a magnetic impurity forming in the QPC. The interferometric measurements on the Fabry-Pérot cavity formed

by this system shows signatures of the Kondo phase shift at the Kondo resonance. If the size of the cavity was reduced below the size of the Kondo cloud, and if the Kondo phase shift is accumulated by crossing the Kondo cloud as expected theoretically, then this effect could be detectable in this type of experiment. This offers a promising proposal to detect the existence of the Kondo cloud with a scanning gate microscope and even one day measure its spatial extend.



# Chapter 7

## Imaging a coherent electron flow driven by a temperature difference

### Contents

---

<b>7.1</b>	<b>Introduction</b>	<b>142</b>
<b>7.2</b>	<b>The thermopower</b>	<b>142</b>
7.2.1	Definition	142
7.2.2	Thermopower of a QPC	144
7.2.3	The Mott's law	145
7.2.4	First measurements on QPCs	145
<b>7.3</b>	<b>Thermopower measurements</b>	<b>146</b>
7.3.1	Experimental technique	146
7.3.2	Differential conductance	147
7.3.3	Thermopower	147
7.3.4	Evaluating $\Delta T$	149
7.3.5	Influence of the heating current	150
7.3.6	Deviations from the Mott's law	152
<b>7.4</b>	<b>Scanning gate microscopy of the thermopower</b>	<b>152</b>
7.4.1	Imaging thermally-induced coherent flow	152
7.4.2	Validity of the Mott's law	153
<b>7.5</b>	<b>Conclusion</b>	<b>155</b>

---

## 7.1 Introduction

This last chapter presents measurements of the thermopower in quantum point contacts. The purpose of this study is to probe the electron interactions by measuring a quantity different from the conductance. In particular, deviations of the thermopower from the Mott's law is an indication of interaction effects, as has been used for example in the case of the fractional quantum Hall effect[138], in quantum dots in the Kondo regime[139] and in QPCs to study the 0.7 anomaly[33]. In addition, in thermopower measurements, the system has almost the same chemical potential on both sides. There is no intentional potential drop across the QPC and the thermovoltage is only about  $1 \mu V$ . One can thus probe the localized states in the QPC in an unperturbed potential profile. Finally, from a measurement point of view, the thermovoltage shows a signal only when the transmission is energy dependent. This is therefore a sensitive probe of small transmission changes.

A first part briefly describes the thermopower in QPCs, and presents the first measurements of this interesting quantity. A second part is dedicated to the measurement technique we use to measure the thermopower, and the method to evaluate the temperature difference that we apply to the QPC. We also discuss the deviations observed from the signal expected from the Mott's law.

Finally, we describe how the SGM technique can be successfully combined to thermopower measurement to image a coherent electron flow driven by a temperature difference from a QPC.

As these measurements were obtained at the very end of this thesis, the analysis is incomplete and ongoing work. I would like at this point to thank Frederico Martins that continued this experiment after my departure from Louvain and analyzed part of the data with Vincent Bayot and Benoit Hackens.

## 7.2 The thermopower

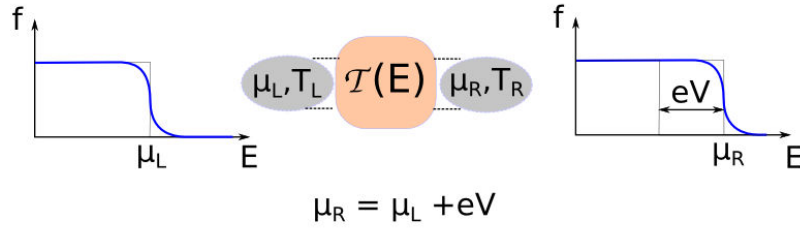
### 7.2.1 Definition

Up to this chapter, we considered only the differential conductance of our devices which consists in probing the current flowing in response to a voltage difference applied between two reservoirs, namely  $G = \partial I / \partial V|_{V_{ds}=0}$ , and traduces the transmission of electrons.

However, there are other measurable quantities in condensed matter physics, corresponding to "cross" thermodynamical effects. These are out of equilibrium effects relating thermal and electrical forces and flows. The first discovered and most famous one is the so-called Seebeck coefficient or thermopower  $S$ , which traduces the fact that a voltage difference appears between two parts of a conductor submitted to different temperatures. Formally, it expresses as  $S = \partial V / \partial T|_{\Delta T=0}$ .

To understand this effect and how it is connected to the transmission of a device, we consider a mesoscopic device connected to large reservoirs which are characterized by thermodynamical quantities. If for example a chemical potential difference is applied between the two reservoirs, a current flows through the device. The quantity that traduces this effect is the differential conductance  $G$ . As seen in Chapter 1, the conductance is simply connected to the transmission of the device by the Landauer-Buttiker formula. If

a) Differential conductance:  $G = dI/dV$



b) Thermopower:  $S = dV/dT$

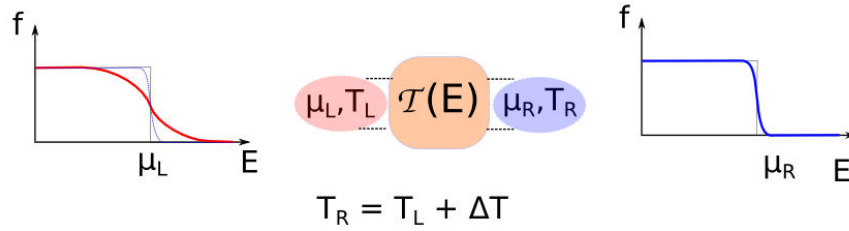


**Figure 7.1** *Conductance and Seebeck coefficients.* a) Differential conductance scheme: a scattering region connects two reservoirs at different chemical potentials. b) Thermopower scheme: a scattering region connects two reservoirs at different temperatures. c) Transmission of a QPC as a function of energy.

the two reservoirs are placed at different chemical potentials  $\mu_R$  and  $\mu_L$ , and different temperatures  $T_R$  and  $T_L$ , they have different Fermi distributions  $f_L(E)$  and  $f_R(E)$ , as schemed Fig.7.1b. This corresponds on the hot side to some occupied states above the Fermi energy and some room below the Fermi energy. Electrons with higher energy can eventually cross the device more easily, if its transmission depends on energy. As a consequence, fluxes from the hot to the cold side and opposite are inequivalent (sketched Fig.7.2). To restore the equilibrium where no current flows, a voltage difference develops across the device.

Formally, the current from one side to the other is given by the Landauer formula:

$$I = 2e/h \int_0^\infty \tau(E)(f_L(E) - f_R(E))dE \quad (7.1)$$

where  $\tau(E)$  is the transmission of the device that depends on energy. If the reservoirs are placed at a chemical difference  $e\Delta V \ll \mu$  and a temperature difference  $\Delta T \ll T$ , where  $T$  and  $\mu$  are the equilibrium chemical potential and temperature, the two Fermi functions can be expanded with respect to  $\Delta T$  and  $\Delta V$ . If the total current is zero (for an open circuit for example), then the quantity  $S = \Delta V/\Delta T$  writes:

$$S(\mu, T) = \frac{1}{eT} \frac{\int_0^\infty \tau(E)(E - \mu)(\partial f/\partial E)dE}{\int_0^\infty \tau(E)(\partial f/\partial E)dE} \quad (7.2)$$

where  $f$  denotes here the equilibrium Fermi distribution at temperature  $T$  and chemical potential  $\mu$ . This is the single-particle integral formula for the thermopower.

### 7.2.2 Thermopower of a QPC

As for the conductance, the QPC appears as a good pedagogical object to understand the thermopower. The dependence of the QPC transmission with incident electrons energy is sketched Fig.7.2b. To understand the basics of thermopower in QPCs, we choose two different points: 1 and 2, corresponding to different dependence of the transmission with energy.

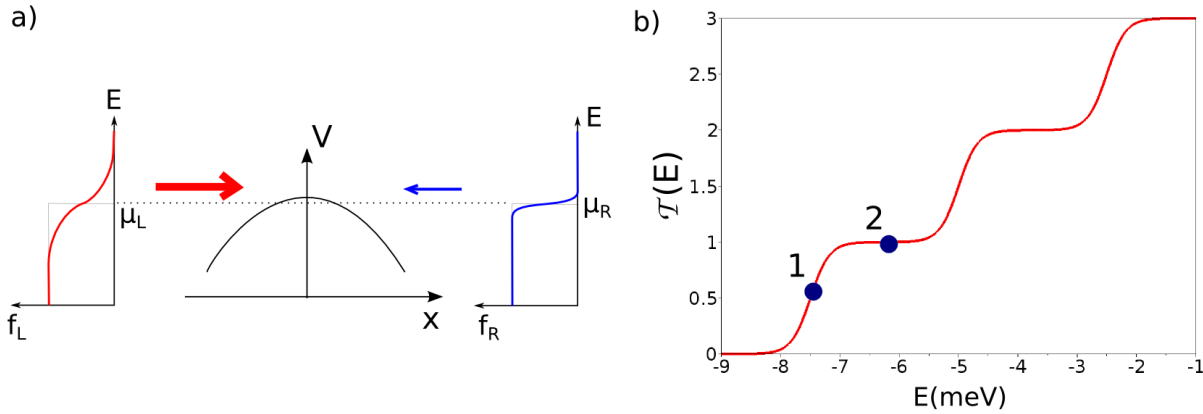


**Figure 7.2 Conductance and Seebeck coefficients.** a) Schematics of different thermally induced transmission across a potential barrier. More electrons go from the hot to the cold side because they experience higher transmission as they have higher energy. b) Transmission of a QPC as a function of energy.

At point 1, the transmission of the QPC strongly varies with energy. If one of the reservoirs is “hot”, some electrons have a higher energy, due to the finite temperature that spreads the Fermi distribution of the reservoir on a range  $k_B T$ . These electrons will experience a higher transmission through the device, as they have a higher energy. By crossing the device and thermalizing in the other reservoir, they will not be able to come back to the first reservoir because they have less energy, and the transmission is smaller at their lower energy. It results that more electrons go from the hot to the cold side than the opposite flux. At equilibrium, since the total current through the device is zero, charges accumulate on the cold side of the QPC and create a voltage difference called thermovoltage. The potential on the cold side is negative for a QPC (increase of the chemical potential to restore equilibrium) such that  $S = dV/dT \geq 0$  where  $dV$  and  $dT$  are measured on the same side.

At point 2 however, the transmission does not vary with energy, as we are on a plateau. Therefore hotter electrons do not experience higher transmission, hence the fluxes from the hot to the cold side and from the cold to the hot side equilibrate without requiring an additional voltage to develop: the thermovoltage is zero. This holds of course as soon as the transmission is flat over the energy range  $k_B T$ .

### 7.2.3 The Mott's law

The thermopower can be derived from the transmission of the device, using the Cutler-Mott's formula 7.3. This formula is obtained by developing the exact single-particle thermopower formula with respect to the temperature (called the Sommerfeld expansion), to keep only the linear term. The thermopower can then simply be expressed as a function of the conductance at zero temperature  $G(\mu, T = 0)$ . The Mott's approximation is then to consider in this expression the finite temperature conductance  $G(\mu, T)$  instead of the zero temperature value. In this approximation, the thermopower writes:

$$S^M(\mu, T) = \frac{\pi^2 k_B^2}{3e} T \frac{1}{G(\mu, T)} \frac{\partial G(\mu, T)}{\partial \mu} \quad (7.3)$$

Since this expression results from a linear expansion of the thermovoltage, the temperature has to be lower than all the others energy scales involved, in particular the curvatures of the potential in the case of a saddle-point like QPC ( $\hbar\omega_x$  and  $\hbar\omega_y$ ). A detailed theoretical investigation of the validity of the Mott's approximation for QPCs is done in Ref.[140], and a very good agreement between the exact formula and the Mott's law is found as long as the temperature is lower than the subbands spacing. In practice, it means that the temperature should be kept lower than typically 1 K. A detailed experimental study also points in this direction[141].

Therefore, any observed breakdown of the Mott's law can be a signature of the electron-electron interactions, which have not been taken into account in this single-particle derivation of the thermopower. For example, the Mott approximation has first been shown to fail for QPCs in the regime of the 0.7 anomaly, a fact attributed to the interactions dominant in this regime [33].

### 7.2.4 First measurements on QPCs

The first measurements of QPCs' thermopower were realized in 1990 by Laurens Molenkamp et al.[142]. They adapted this technique known for bulk materials to mesoscopic devices, and first discovered quantum oscillations in the thermopower of QPCs [142]. This work was done after a calculation that predicted this effect [143], assuming a parabolic transverse confinement. Soon after, a calculation based on Buttiker's saddle-point model [10] was proposed to explain the experimental observations, and to show the role of perpendicular magnetic field and base temperature on these thermopower oscillations [144].

The smart device configuration and the first measurement results are presented in Fig.7.3. The method chosen to heat one side of the QPC is Joule heating. The central channel is brought to a higher electronic temperature than the bulk by making a DC current of some  $\mu A$  flow through it. The studied QPC is one of the two constrictions visible on both sides of the heating channel. The principle of measuring thermopower is to measure the voltage developing across the QPC when both sides are at different temperatures. As the voltage drops all along the heating channel, the authors measured this thermoelectric voltage thanks to an additional QPC facing the measured one on the opposite side of the heating channel. This second QPC acts as a local voltage probe, serving as a reference, its gate voltage being kept constant during the measurement. The measured quantity is the DC voltage difference  $V_2 - V_1$  as a function of the first QPC gate voltage.

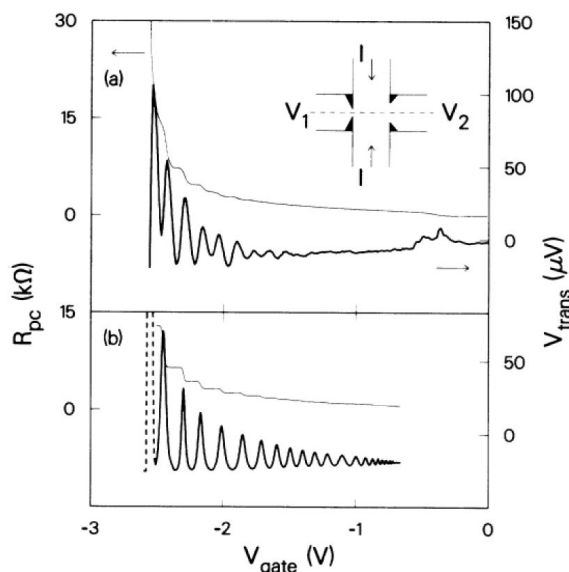


**Figure 7.3** *First experimental measurements of a QPC thermopower* Up: Transverse voltage between both sides of the channel as a function of gate voltage (thick curve, right axis) and resistance of the QPC (thin curve, left axis) Inset: scheme of the device. Down: Calculations of these two quantities assuming a square well potential. The broadening of the steps is explained by thermal averaging.

Clear oscillations are observed in this transverse voltage, corresponding to the plateaus in the device conductance (see Fig.7.3). As explained above, these oscillations correspond to alternating situations where the transmission does not vary with energy (plateaus), leading to zero thermopower, and transitions, producing a finite thermopower. An undesired background is superimposed to these oscillations, that the authors attributed to a device asymmetry.

## 7.3 Thermopower measurements

### 7.3.1 Experimental technique

Though our devices are not as specifically designed for thermoelectric measurements, we tried to measure the thermopower of our QPCs. We use the two ohmic contacts on one side of the QPC to heat the reservoir on this side by Joule effect, and measure the transverse voltage arising across the QPC. The heating current  $I_h$  induces an undesired voltage drop inside the left reservoir, i.e. between the left QPC entrance and the left voltage probe (see Fig.7.4), To evaluate the voltage difference only due to thermoelectric effects, we first have to get rid of the additional voltage difference. Since the Joule power is proportional to  $I_h^2$ , we use an AC current at frequency  $f_h$  to heat one side of the contact, and the additional temperature  $\Delta T$  caused by the Joule effect will oscillate at twice this frequency:  $2 \times f_h$ . Consequently, the voltage  $V_{th}$  measured at frequency  $2f_h$  only contains informations related to  $\Delta T$ . The current used to heat the reservoir is measured thanks to a current amplifier connected to a lock-in operating at frequency  $f_h$ , as schemed Fig.7.4.

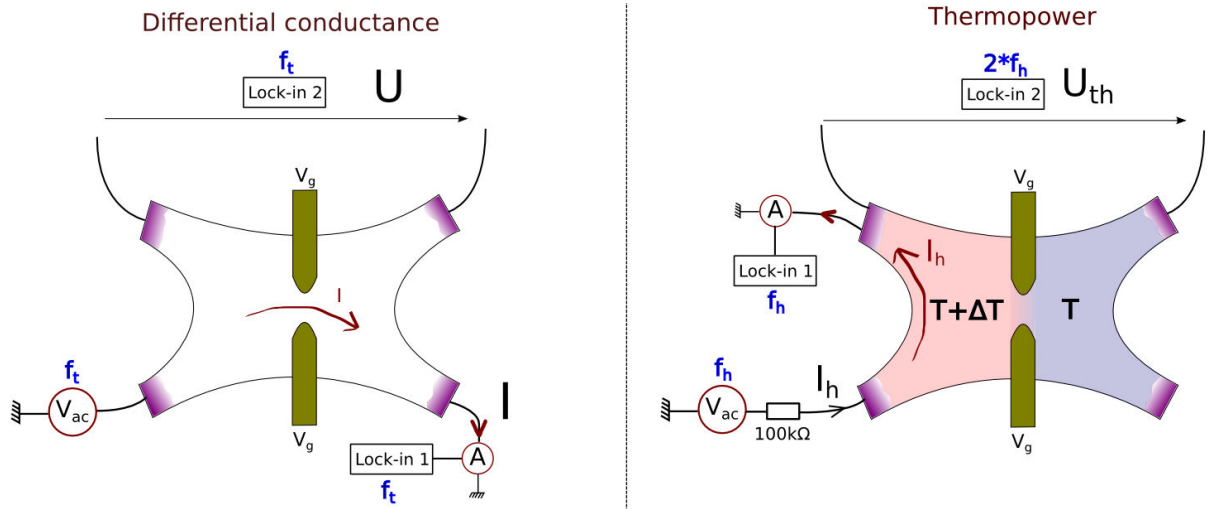


**Figure 7.4** *Principle of our thermopower measurements.* Left: Setup used to measure the differential conductance. An AC current at frequency  $f_t$  flows through the device, measured with lock-in at the same frequency. A second lock-in is used to read the voltage in a 4-point configuration, at the same frequency  $f_t$ . Right: setup used to measure the thermopower. A heating current flows through one side of the device, at frequency  $f_h$ , measured with a lock-in at the same frequency. The transverse voltage across the QPC is measured by a lock-in operating at a frequency  $2 \times f_h$ .

### 7.3.2 Differential conductance

The sample measured in this section is sample D (same lithographic dimensions as sample C). To know the energy scales involved in this QPC, we first measure its conductance, in linear and non-linear regimes. This characterization is summarized Fig.7.5.

In this sample, the ZBA splits as the first mode opens (see Fig.7.5b), an effect which we attribute to a change in the number of localized charges in the channel, as detailed in Chapter 5. This fact explains why the 0.7 anomaly is still visible as a deformation of the first plateau Fig.7.5a, despite the base temperature of 20 mK during this experiment. The lever-arm parameter of the gates will be of importance in this chapter and can be deduced from Fig.7.5c and d. The colorplot of the spectroscopy indicates that the subbands are spaced by  $\Delta V_{ds} = 4meV$ , and on the conductance  $G(V_g)$  one can see that about  $\Delta V_g = 70mV$  is required to go from a transition to the next one. Therefore the lever-arm is given by  $\alpha = \Delta V_{ds}/\Delta V_g = 0.057 \pm 0.005$ .

### 7.3.3 Thermopower

We then measure the thermoelectric voltage developing across the QPC in response to a Joule heating on one side, as explained section 7.3.1. The typical heating currents range from 10 to 200 nA. An example of the measured thermoelectric voltage as a function of gate voltage is plotted Fig.7.6.

Clear oscillations are seen in the thermoelectric voltage as a function of gate voltage. Fig.7.6a allows a direct comparison between these oscillations and the steps in the conductance curve. The thermoelectric voltage  $V_{th}$  oscillations are of the order of a  $\mu V$ . The

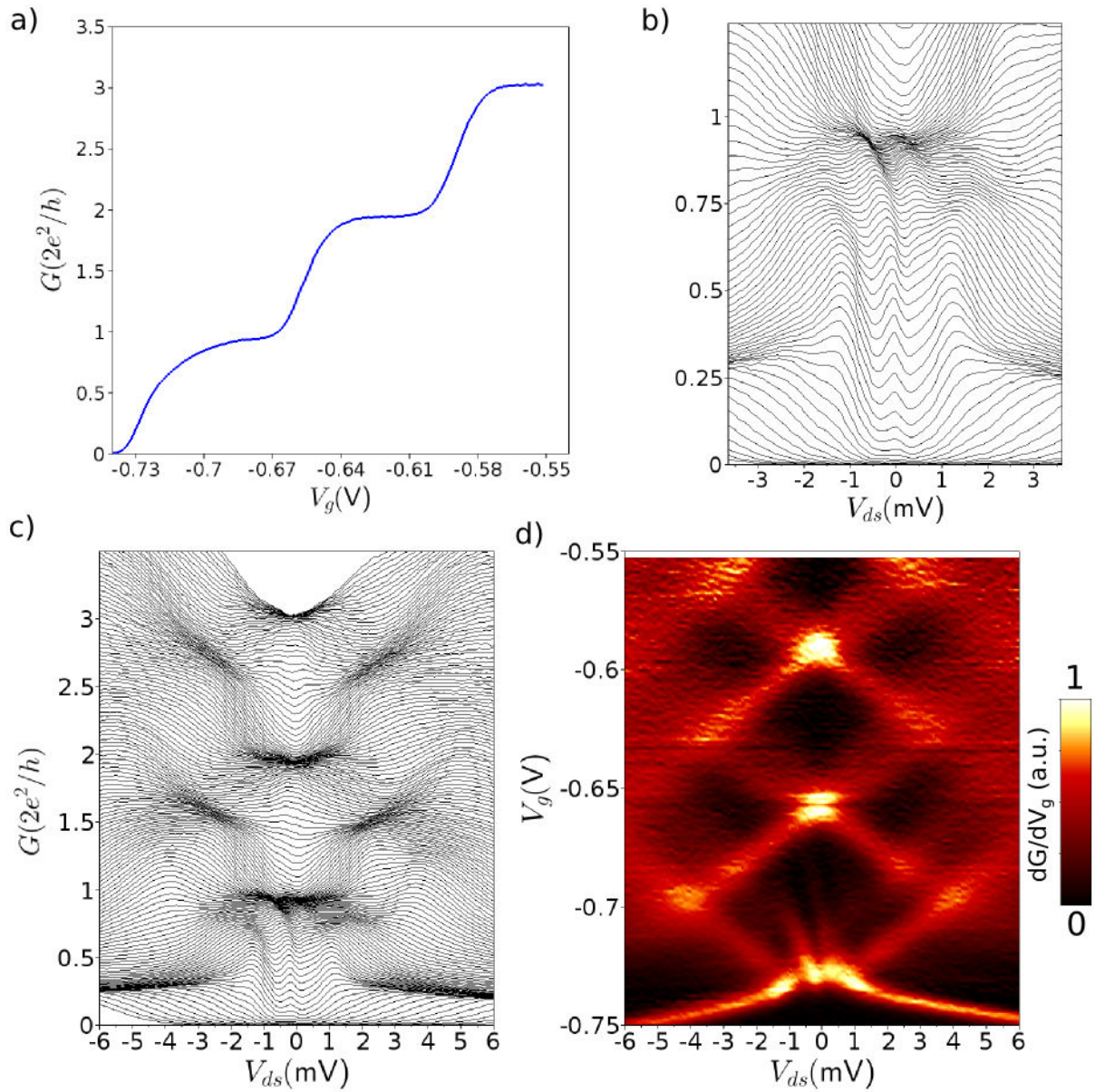


**Figure 7.5** *Conductance measurements at 20 mK.* a) Linear conductance as a function of gate voltage, in units of the conductance quantum. b) Traces of  $G(V_{sd})$  for different gate voltages  $V_g$ , zoomed on the ZBA. c) Traces of  $G(V_{sd})$  for different gate voltages  $V_g$ , up to the third plateau. d) Differentiate of c) vs. gate voltage, plotted as a function of  $V_{sd}$  and  $V_g$ .

oscillations of  $V_{th}$  are intimately correlated to the steps in the conductance curve. Indeed,  $V_{th}$  reaches maximum values in the transitions between plateaus, and minima on plateaus. Note that the signal is superimposed to a flat background of  $1\mu V$  that should be subtracted to obtain the thermopower. The origin of this background will be discussed later.

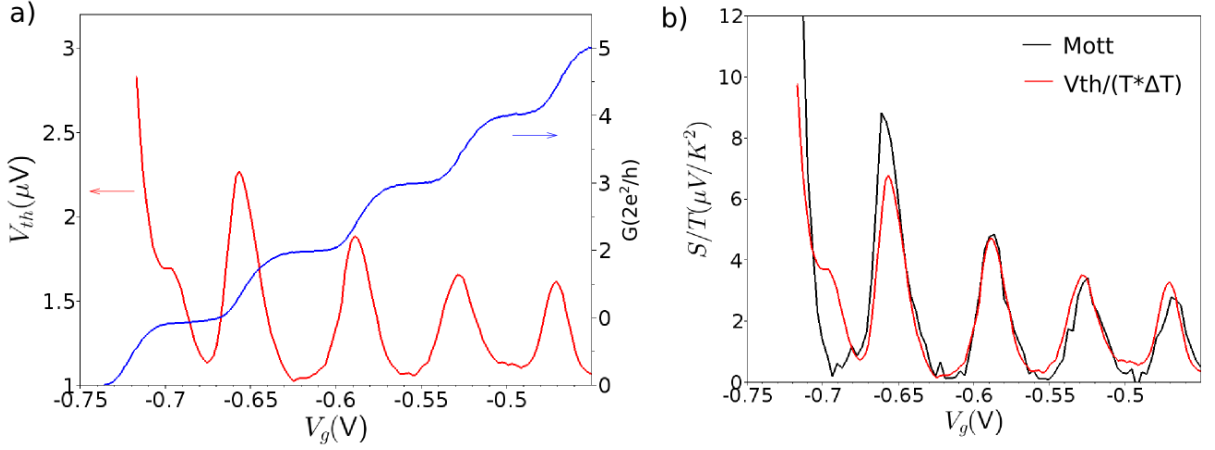


**Figure 7.6 Thermopower measurements.** a) Measured thermoelectric voltage as a function of gate voltage (red curve, left axis) for a 145 nA heating current, at 7 Hz, together with the device conductance measured at 20 mK (blue curve, right axis). b) Comparison between the thermopower ( $-S/T$ ) obtained by the Mott's law from the measured conductance (black curve), and by dividing the thermoelectric voltage by the temperature difference and the mean temperature (red curve).

### 7.3.4 Evaluating $\Delta T$

To evaluate the temperature difference generated by the heating current, we assume the validity of the Mott's law, at least above the second mode. Knowing the lever-arm parameter, we can extract the expected thermopower from the  $G(V_g)$  curve. We use the Mott's law (Eq.7.3) and replace  $\mu$  by  $-\alpha e V_g$  to obtain the thermopower from the experimentally measured conductance::

$$S^M = \frac{\pi^2 k_B^2}{3e^2 \alpha} T \frac{1}{G} \frac{\partial G}{\partial V_g} \quad (7.4)$$

This is the experimental version of the Mott's law. To get rid of the fact that the thermopower depends on the average temperature  $T$ , we plot the expected thermopower divided by the average temperature  $S^M/T$  (black curve Fig.7.6b).

Then we have to compare this expected thermopower value to the thermopower extracted from the measured  $V_{th}$  (corrected from the background) according to  $S/T = V_{th}/(\Delta T \times T) = V_{th}/2(T_L^2 - T_R^2)$  with  $T_R$  being the known temperature of the cold and  $T_L$  the unknown temperature of the hot reservoir.

We evaluate the base electronic temperature (on the cold side) to be about 100 mK in the following, but we have no precise evaluation of it during this experiment. Note that assuming 50 mK or 150 mK does not substantially change the following results, justifying this crude estimation.

Red curve on Fig.7.6c presents the result of this adjustment procedure for a heating current of 145 nA, that gives a temperature of 480 mK on the hot side, and therefore a temperature difference of 380 mK. The two curves match pretty well for the three peaks on the right (modes 3, 4, 5) but show significant differences for the transitions to the first and second modes, as will be discussed afterwards. Note that a hot temperature

of 480 mK corresponds to an energy of  $\sim 50\mu\text{eV}$ , which is much lower than the 1 meV energy scales of the QPC transmission curve, such that the linear regime of the Mott's law is valid.

### 7.3.5 Influence of the heating current

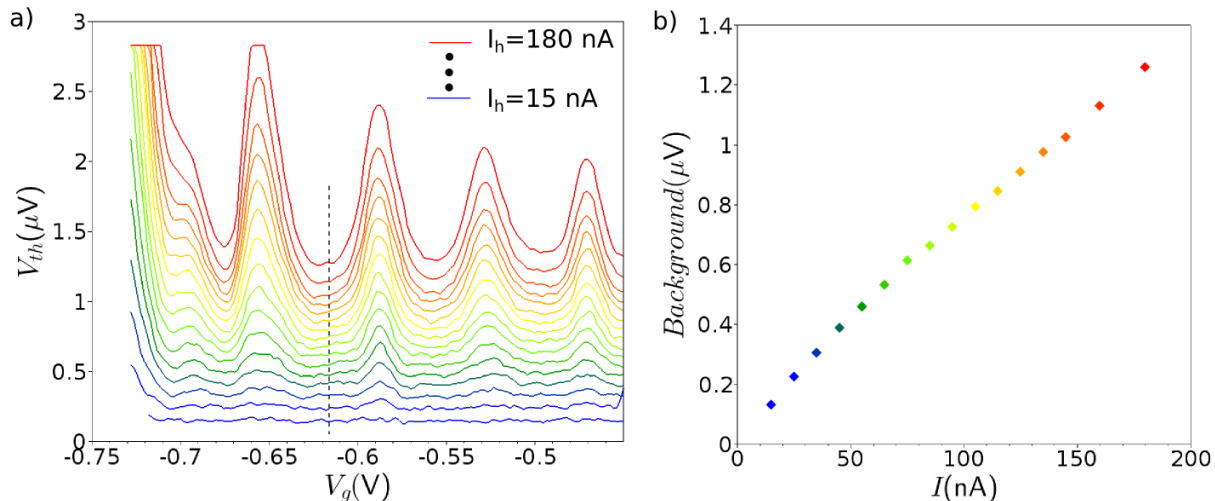


**Figure 7.7 Influence of the heating current.** a) Thermoelectric voltage as a function of gate voltage for different heating current values, ranging from 15 nA (blue curve) to 180 nA (red curve). b) Background signal evaluated from the minimum value at the second mode (along dashed line in a) as a function of the heating current.

Fig.7.7a shows the different traces of  $V_{th}(V_g)$  obtained for different heating currents. Since the thermovoltage is at first order proportional to the temperature difference, the signal  $V_{th}$  strongly increases with the heating current. In addition to the increasing oscillations, the flat background also increases with increasing power. We determine the value of this background as the minimum of  $V_{th}$  when the QPC is open to the second mode. As seen in Fig.7.7b, this background increases almost linearly with the heating current. Since the signal is measured at  $2f_h$ , it could have been simply proportional to  $I_h^2$ , but however seems to have a more complex dependence on  $I_h$ . We do not know the origin of this background signal, but it could be due to the non-linear resistance or to the thermopower of the ohmic contacts or the 2DEG. The thermopower of the 2DEG can be separated in two main contributions: the thermopower due to the phonons, usually called the phonon drag, and the diffusion thermopower, that is connected to the electrical conductivity through the Mott's formula (7.3). This diffusion part can be expressed as:

$$S^d = \frac{\pi^2 k_B^2 T}{3eE_f} (p + 1) \quad (7.5)$$

where  $p$  traduces the dependence of the electrons scattering rate with energy, that depends of the scattering mechanism but is close to unity [145]. This gives a contribution to the thermopower of about  $0.6\mu\text{V}/\text{K}$ . Using the evaluated temperature differences as a function of the heating current (as explained afterwards), we can *a posteriori* calculate the

thermopower corresponding to the observed background. It appears that this background corresponds to  $2.7 \pm 0.2 \mu\text{V}/\text{K}$ , and is independent of the average temperature. This is much larger than the expected thermopower of the 2DEG (7.5) and does not depend on the temperature. The 2DEG diffusion thermopower can therefore not account for this background.

The contribution of phonons could be invoked, but it is likely that the phonon drag does not contribute to the thermopower in our case, due to the sub-Kelvin temperature, regarding other works[145, 146, 147].

The thermopower due to the ohmic contacts is not well characterized, and might be responsible for this background signal.

We then evaluate the temperature difference obtained for each value of the heating current, repeating the procedure explained above. We first subtract the background signal and then rescale the measured thermopower to the one obtained by the Mott formula, the fitting parameter being the hot reservoir temperature, assuming a temperature of 100 mK on the cold side. We did not precisely evaluate the base electronic temperature during the experiment, but assuming 50 mK or 150 mK does not substantially change the following results.

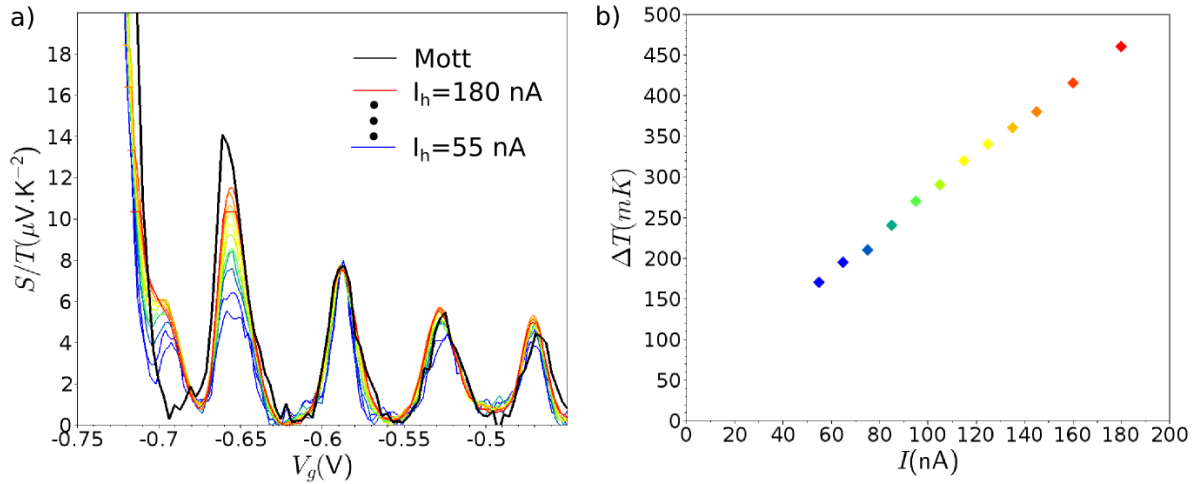


**Figure 7.8** *Evaluating  $\Delta T$  as a function the heating current* a) Thermopower evaluated from the measured thermoelectric voltage for different heating currents (colored curves), with temperature differences chosen to match Mott’s law. Black curve represent the thermopower divided by the average temperature extracted from the conductance thanks to the Mott’s formula. b) Fitting parameter  $\Delta T$  used to scale the different thermopower curves on Mott’s law.

We adjust the hot temperature to make the thermopower match the Mott’s law above the second plateau. Indeed, we cannot find an appropriate hot temperature that suits well for the two first transitions and the three following ones. Therefore, we favor the three last transitions, as the Mott’s law is more likely to be valid at high opening than in the low-density regime, where electron interactions are more important.

The estimated temperature differences range from 170 mK for a heating current of 55 nA to almost 460 mK for heating currents of 180 nA. Note that in any case we are far from the linear regime of small temperature differences compared to the base temperature. For lower heating current values, the signal was too noisy to precisely operate the fitting

procedure. However these temperature differences are smaller than the energy scales of the QPC, including the Kondo temperature which is about 1K. This therefore allows us to investigate the conductance anomalies in the thermopower signal.

### 7.3.6 Deviations from the Mott's law

In the first and second transitions, the measured thermopower seems to be really different from what is expected from the Mott's relation (see Fig.7.8a), as already reported in Ref.[33]. This breakdown of the Mott's relation appears at sufficiently low heating currents, hence low temperature differences, close to the linear regime. These differences are the strongest in the transition from the pinch-off to the first plateau, but surprisingly are also present in the transition from the first to the second plateau. This is in contrast with the study reported in Ref.[33], where the breakdown of the Mott's law was observed only below the first plateau. If the deviations from the Mott's law that we observe are due to electron-electron interactions, it suggests that they dominate thermoelectric transport not only in the 0.7 regime but also in the second transition.

Indeed, the anomalous thermopower observed in the first transition is probably related to the 0.7 anomaly visible as a shoulder in the conductance curve (see 7.5a). Note that a flat sub-plateau at  $0.7 G_0$  would give a zero in the thermopower, as it is observed at low heating currents.

The reduced thermopower in the second transition might also be related to an 0.7 analogue at  $1.7 G_0$  (see Fig.5.7 and discussion in section 5.2.7). A smoother transition would indeed give a smaller thermopower, as it is also observed. The absence of the corresponding features in the signal calculated using the Mott's law shows that our thermopower measurements are more sensitive than our conductance measurements regarding the interaction effects.

Note that for small heating currents, the thermovoltage in the region of the 0.7 anomaly is as low as  $0.5 \mu\text{V}$ , which is much less than AC bias typically used in conductance measurements, about 5 to  $10 \mu\text{V}$ . This difference could explain the higher capability of thermopower measurements, carried out very close to equilibrium, to detect interaction effects like spontaneously localized states and the Kondo effect.

## 7.4 Scanning gate microscopy of the thermopower

### 7.4.1 Imaging thermally-induced coherent flow

Now that we have analyzed the thermopower signal and determined the temperature difference related to the heating current, we can perform SGM measurement of the thermopower, as we did for the conductance in the previous chapters. This original idea was suggested in the thesis of Adel Abbout[148], Chapter 5, in which a theoretical investigation of what would be observed by applying scanning gate microscopy to the thermopower is presented.

To perform SGM of the thermopower, we proceed exactly as for SGM of the conductance, except that the thermoelectric voltage is recorded instead of the conductance. A typical image obtained using this technique is shown Fig.7.9b. This image is recorded for

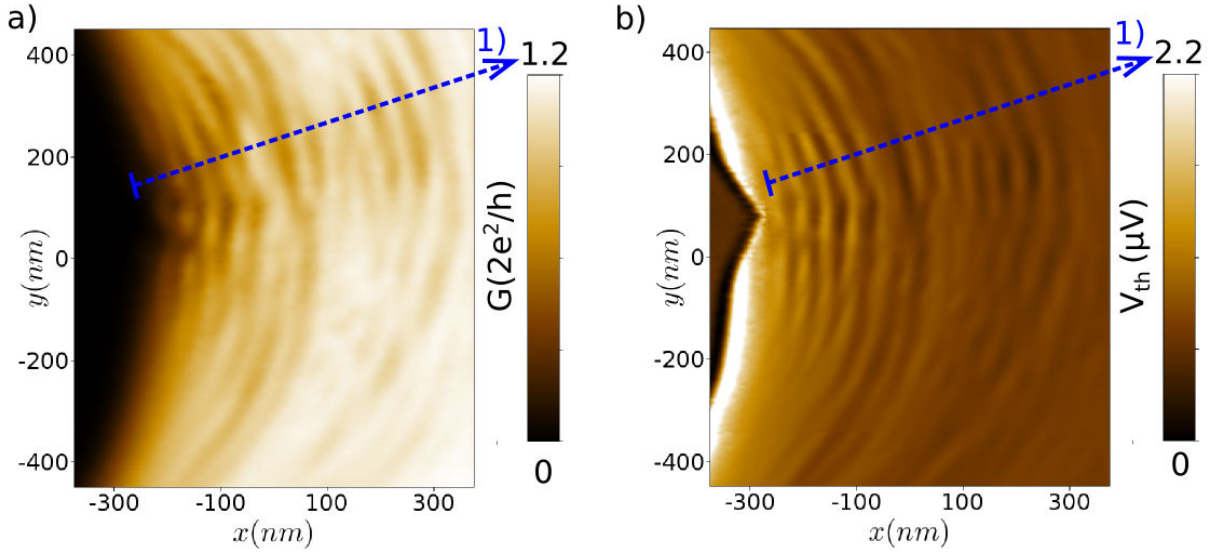


**Figure 7.9 Scanning gate imaging of the thermopower** a) SGM image of the conductance recorded for a QPC open just above the first plateau ( $V_g = -0.66V$ ). b) Thermoelectric voltage as a function of tip position, for the same gate voltage  $V_g = -0.66V$ .

a gate voltage of  $-0.66V$ , when the QPC is open to first plateau, i.e. the thermopower is at the bottom of the first dip. A heating current of  $200\text{ nA}$  is used leading to a temperature difference  $\Delta T \sim 500\text{ mK}$  and an average temperature  $T = 300\text{ mK}$ . For comparison, a SGM image of the conductance at the same gate voltage is given Fig.7.9a. The two signals exhibit the same main features. In particular, similar interferences are observed in both signals, revealing that the electron flow is coherent in both experiments. Though it is not surprising to find the same main features in the thermopower and in the conductance as they are intimately connected, it is amazing to see that we can directly observe in real space the coherence of an electron flow driven by a temperature difference since temperature is usually synonym of decoherence.

The reason is that thermalization of the hot electrons is done by electron-electron and electron-phonon interactions at a distance from the QPC larger than the coherence length and given by the scattering lengths  $L_{e-e}$  and  $L_{e-ph}$ . Hot electrons are therefore fully coherent in the region scanned by the SGM tip and can interfere to produce the observed fringes.

On the other hand, the interference fringes will disappear at distances larger than the thermal length  $L_T$  of the hot reservoir due to the blurring of the interferences over the thermal energy window  $k_B T_{hot}$ .

## 7.4.2 Validity of the Mott's law

One can wonder if the Mott's law is still valid in this situation where a micron-size Fabry-Pérot cavity is formed between the QPC and the tip-depleted region. To verify the validity of the Mott's law in the SGM images, we should in principle differentiate the conductance with respect to chemical potential of the entire scattering region, including the QPC and

#### 7.4. SCANNING GATE MICROSCOPY OF THE THERMOPOWER

the depleted region below the tip. Since the transmission is dominated by the QPC, an approximation will be to differentiate the conductance with respect to the gate voltage of the QPC, as done previously in absence of the tip. Note however that the cavity formed by the tip is also part of the coherent scattering region and should in principle not be separated from the QPC. Because we could not find a way to take this into account, we decide to evaluate the thermopower by differentiating the conductance with respect to gate voltage only.

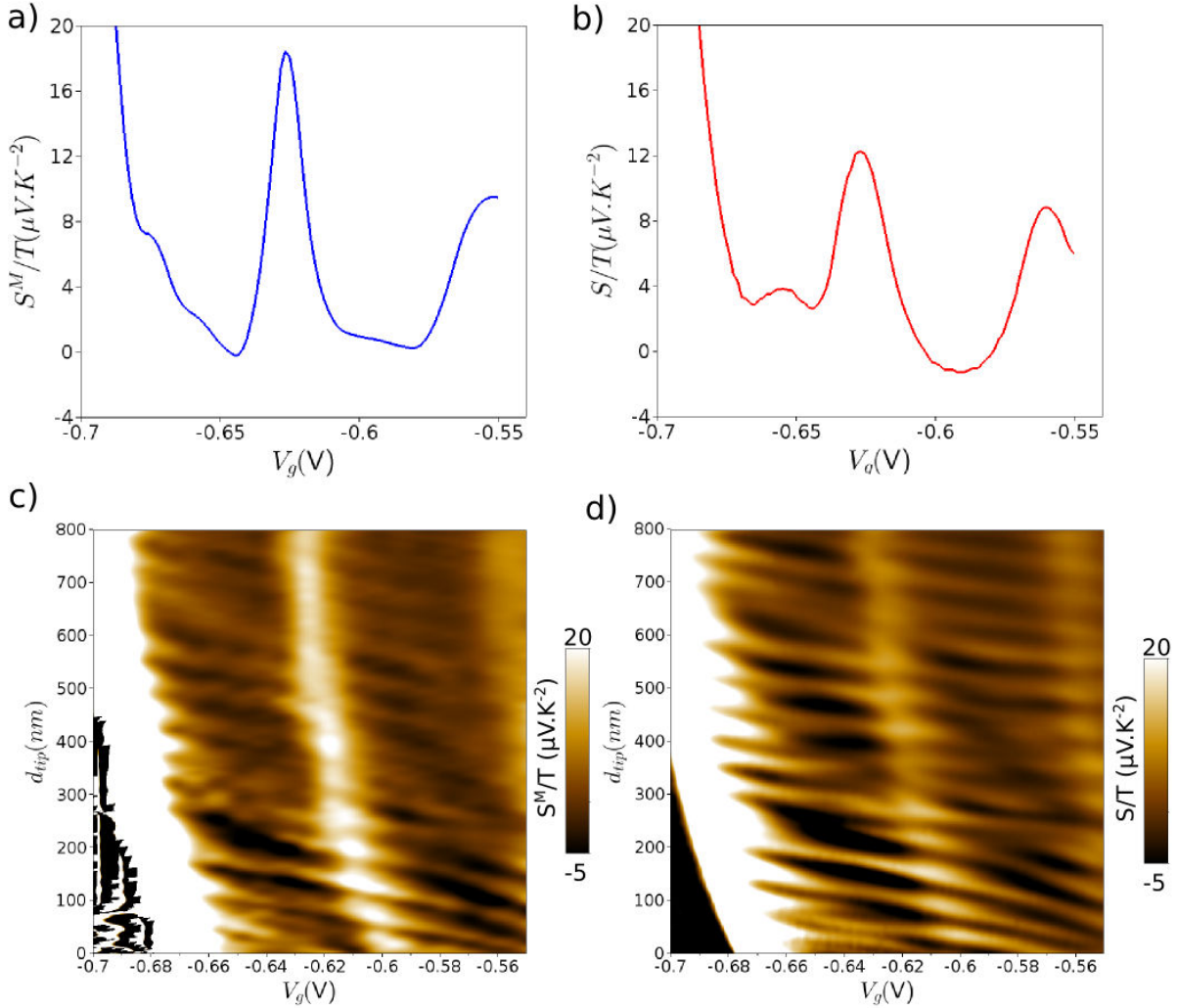


**Figure 7.10** *Validity of the Mott's law in SGM experiments* a) Profile of the expected thermopower from the Mott's law, calculated from the conductance, considering  $\Delta T \sim 500\text{mK}$  and  $T \sim 300\text{mK}$ , the tip being at 640 nm from line 1 origin. b) Measured thermopower for the same tip position. c) Thermopower deduced from the Mott's law as a function of gate voltage and tip position along line 1  $d_{\text{tip}}$ , the origin being taken on the QPC side. d) Measured thermopower for the same range of parameters.

Since the SGM image in Fig.7.9a is recorded for a single gate voltage, we can let aside one dimension of space and scan a single line while sweeping the gate voltage. We choose

to scan the tip along blue line 1 Fig.7.9 and vary the gate voltage between two successive lines. We first measure the thermovoltage, and then start again the same sweep to measure the conductance. By doing so, we can numerically differentiate the conductance with respect to the gate voltage, and check the validity of the Mott's law at different QPC openings and tip positions.

Fig.7.10a presents a profile of the measured thermopower deduced from the thermoelectric voltage as a function of the gate voltage, the tip being at 640 nm from the origin of line 1. The signal is divided by the average temperature. In this experiment, the heating current is about 200 nA, hence the temperature difference is estimated to be about 500 mK. For comparison, the thermopower deduced from the measured conductance using the Mott's law is plotted Fig.7.10b for the same tip position. Both signals present the same overall features though different peaks and dips are visible. Note that the differences between these two signals are strongly dependent on the chosen tip position.

Colorplots of the thermopower obtained from these two methods are plotted Fig.7.10c and d as a function of gate voltage and tip position. These two plots show that the interferences obtained in both signals evolve in the same way with gate voltage. Note that the signals can become negative in some configurations, because of the tip-induced interferences lead to dips in the conductance curve  $G(V_g)$ . Hence the thermopower that is proportional to  $\partial G/\partial V_g$  can change sign in some configurations.

These results are the starting point of a deeper analysis with smaller heating currents, hunting for breakdowns of the Mott's law in the interferences. Indeed, interesting deviations can be seen in both signals near pinch-off, that are not shown here and still under investigation at the time this manuscript is written..

## 7.5 Conclusion

We studied in this chapter the thermopower of quantum point contacts. Though the devices are not designed for this purpose, we can measure a thermoelectric voltage developing across the QPC when we heat one side by Joule effect. The Mott's law allows us to evaluate the applied temperature difference, at least if we consider the law to be valid when more than two modes are transmitted.

Important differences are seen between the measured thermopower and the one evaluated from the Mott's formula at the opening of the first mode and between the first and the second modes. These differences are greater in the linear regime for small temperature differences, and tend to blur for important temperature differences, which is counter-intuitive, and indicates that electron interactions might be responsible for this breakdown of the Mott's law.

We then applied the scanning gate microscopy technique, and obtained images of the thermopower as a function of tip position that exhibit electronic interferences, just as for the conductance. Data analysis is still ongoing work, especially near pinch-off where the interferences obtained in the measured thermopower and the one obtained by the Mott's law show qualitative differences.



# Conclusion and perspectives

During this thesis, we studied by different means the conductance anomalies of quantum point contacts. We have seen that the polarized tip of a scanning gate microscope can be used in two different ways, that bring distinct informations on the system.

We used the long-range potential of the tip to finely tune in situ the potential of the QPC channel. By approaching the negatively polarized tip, we can enlarge the low-density region. Consequently, we have seen that approaching the tip can change the nature of the ZBA, forming alternatively a single or a split peak, that we interpret as arising from odd and even Kondo effects, depending on the parity of the localized electrons number. We have seen that a Wigner-like mechanism, in which electrons would spontaneously form an ordered 1D chain due to the Coulomb repulsion below a given density threshold is consistent with our observations. This result arrives at a time where the 0.7 anomaly has regained interest in the community, and its debated origin has once again been put in the forefront of the scene by a publication of two different studies in the same journal, proposing different origins for these anomalies[9, 57]. It also received interest from other journals, that commented this debate[149]. Indeed, the debate on the origin of the anomalies has turned in recent years to a simple question: does localization occur in QPCs? The Wigner-like mechanism that we propose offers a new way of looking at this problem, fits a large range of numerical and experimental investigations, and is completely compatible with the experiment and interpretation of Ref.[9].

This is a great ingredient on the way to understanding this problem, but does not solve the whole matter. In particular, our work does not explain the 0.7 anomaly, on the contrary to what was written in Ref.[115]. Indeed, our work shows that localization can explain the zero bias anomaly in terms of the Kondo effect, arising at low temperature and restoring the shoulder created above half transmission (the 0.7 anomaly), if the number of charges is odd at this opening. We have also seen that if an even number of charges is localized above the half plateau, the zero bias anomaly is split, hence the 0.7 shoulder is still visible even at very low temperature. This demonstrates that the Kondo effect can in particular cases really restore the conductance at low temperature, but lets the origin of the 0.7 “plateau“ unexplained. In particular, it should be understood in the future why it is the only feature that remains at high temperature (above 4.2K) when all the other plateaus have disappeared and why it becomes a strong plateau around  $0.85 \times 2e^2/h$  under DC source drain bias.

Though our work does not solve this question, it shall guide future theoretical and experimental investigations. In particular, the possible existence of a Wigner crystal in QPCs has been proposed to explain the 0.7 anomaly[46], but this study relied on an infinite 1D Wigner crystal, in which spin and charge excitations are independent. It could be

interesting to investigate the finite length case that occurs in QPCs, to see if this effect still occurs. Transport through a chain of non-uniformly spaced charges could also be interesting to investigate.

Some ingredients are still missing to perform such investigations in a sane way. In particular, the exact number of localized charges and their spatial repartition shall be investigated first, both numerically by completely solving the Poisson-Schrödinger equation in a realistic environment, and experimentally with advanced scanning probe techniques. Then it could be conceivable to investigate theoretically the transport through this state and really understand what happens in the 0.7 regime.

We have also used the scanning gate microscope to create in situ interferometers and perform phase-sensitive measurements. We used the depletion region created below the tip as a movable scatterer to generate interferences between this depletion spot and the QPC. By studying the temperature dependence of these interferences, we have shown that they possibly arise from the Fabry-Pérot cavity forming directly between the tip and the QPC. To confirm this eventuality, that differs from the interferences seen at higher temperatures in lower mobility samples[60, 71], we developed and studied a new type of interferometers by designing a sharp gate in front of QPCs. The results obtained on these interferometers are also compatible with interferences forming between the QPC and the scatterer, as revealed by perpendicular magnetic field and temperature dependence. This scenario is also supported by our numerical simulations, that indicate that disorder plays a non-trivial role in the formation of these interferences, and may be responsible for the observed contrast on plateaus.

By studying the non-linear behavior of these interferences below the first plateau, we have discovered that they experience a sharp phase shift in the bias range of the zero bias anomaly. Though we could not clearly conclude on the exact origin of this phase shift, simple considerations suggest that it is linked to the universal Kondo phase shift. If it is confirmed, this would be a final proof for the Kondo nature of the zero bias anomaly. Moreover, it would open the way to a novel type of interferometric study of the Kondo phase shift, and allow at last to investigate experimentally the predicted existence of the Kondo screening cloud.

Finally, we successfully adapted the scanning gate microscopy technique to the study of thermoelectric transport. Using this technique, we imaged the coherent flow of electrons driven by a temperature difference, coming out of a QPC. This experiment opens the way to subtle investigations of the interaction effects, as the potential landscape of the QPC is almost unchanged using this technique compared to conductance measurements.

# Appendices



# Appendix A

## Kwant code example

Here is a Kwant code including different possibilities that I used during my thesis. It defines a QPC, possibly including a disordered potential landscape that has to be stored in a .dat file. Two typical loops are presented: a first one to calculate the total transmission of the QPC as function of gate voltage and a second one used to simulate SGM maps by calculating the total transmission for different tip positions, modeled by a Lorentzian potential.

It is a starting point for every type of simulations, and one can vary magnetic field, disorder amplitude, tip position, gate voltage, etc...

```
from __future__ import division
import math
from math import atan2, pi, sqrt, cos, sin
from cmath import exp
import numpy as np
from numpy import prod
import kwant
import random
import matplotlib.pyplot as plt

#Define potential created by rectangular gates using the "Davies" method:
class RectangleGate(object):
def __init__(self, voltage, depth, left, right, bottom, top):
self.voltage = voltage
self.depth = depth
self.left = left
self.right = right
self.bottom = bottom
self.top = top
def __call__(self, pos):
x, y = pos
voltage, d, l, r, b, t = (self.voltage, self.depth, self.left, self.right, self.bottom, self.top)
def g(u, v): return atan2(u * v, d * sqrt(u**2 + v**2 + d**2)) / (2 * pi)
return voltage * (g(x-l, y-b) + g(x-l, t-y) + g(r-x, y-b) + g(r-x, t-y))
```

---

```

#Define a Lorentzian potential for the tip:
class Lorentzian(object):
def __init__(self, voltage, xcenter, ycenter, radius):
self.voltage = voltage #maximum potential value
self.xcenter = xcenter #Tip center abscissa
self.ycenter = ycenter #Tip center ordinate
self.radius = radius #Decay length
def __call__(self, pos):
x, y = pos
voltage, xc, yc, R= (self.voltage, self.xcenter, self.ycenter, self.radius)
voltage = voltage* R**3/(R**2+abs(x-xc)**2+ abs(y-yc)**2)**(3/2)
return voltage

```

```

# Define disordered landscape using a normalized matrix contained in a text file generated in Scilab:

```

```

class Disorder(object):
def __init__(self,volt, voltage, amp, x1, x2, y1, y2, Ltot):
self.volt = volt #Matrix extracted from text file
self.voltage = voltage #local potential
self.amp = amp #energy spreading around Ef
self.x1 = x1 #lower abscissa of the disordered region
self.x2 = x2 #uper abscissa of the disordered region
self.y1 = y1 #lower ordinate of the disordered region
self.y2 = y2 #uper ordinate of the disordered region
self.Ltot = Ltot #disordered region size (nm)
def __call__(self, pos):
x, y = pos
volt, voltage, amp, x1, x2, y1, y2, Ltot = (self.volt, self.voltage, self.amp, self.x1, self.x2,
self.y1, self.y2, self.Ltot)
for i in range (0,Ltot//2):
if x1 + (2*i-2)*(x2-x1)/Ltot < x <= x1 + (2*i)*(x2-x1)/Ltot:
for j in range(0,Ltot//2):
if y1 + (2*j-2)*(y2-y1)/Ltot < y <= y1 + (2*j)*(y2-y1)/Ltot:
voltage = (volt[i,j])*amp
return voltage

```

```

# Define the system:

```

```

class My2DEG(object):
"""A rectangular system with two leads.
The following attributes may be modified:
a : the lattice constant
pot : a function defining the potential
phi : the strength of the magnetic field
"""
def __init__(self, L, W, a=5):

```

---

```

self.L = L
self.W = W
assert W % 2 == 1, 'Width has to be odd.'
assert L % 2 == 1, 'Length has to be odd.'

    self.a = a
self.pot = lambda pos: 0
self.phi = 0 # phase per plaquette

    # Make a square lattice whose origin lies at (0., 0.).
self.lat = lat = kwant.lattice.Monatomic([(a, 0), (0, a)],(0., 0.))
# Build scattering region.
b = kwant.Builder()
b[(lat(x, y) for x in xrange(-L//2, L//2)
for y in xrange(-W//2, W//2))] = self._onsite
b[lat.neighbors()] = self.phase_y

    # Build and attach leads:
for direction, lead_onsite in [(-1, self._left_lead_onsite),(1, self._right_lead_onsite)]:
sym = kwant.TranslationalSymmetry(lat.vec((direction, 0)))
lead = kwant.Builder(sym)
lead[(lat(0, y) for y in xrange(-W//2, W//2))] = lead_onsite
lead[lat.neighbors()] = self.phase_x
b.attach_lead(lead)

    for lead_onsite, direction in [(self._down_lead_onsite, -1),(self._up_lead_onsite, 1)]:
sym1 = kwant.TranslationalSymmetry(lat.vec((0, direction)))
lead1 = kwant.Builder(sym1)
lead1[(lat(x, 0) for x in xrange(-100, L//2))] = lead_onsite
lead1[lat.neighbors()] = self.phase_y
b.attach_lead(lead1)

    kwant.plot(b) #Check the system and leads
self.sys = b.finalized()

    def _left_lead_onsite(self, site):
y = site.pos[1]
return self.pot((-self.L//2 * self.a, y)) + 4.

    def _right_lead_onsite(self, site):
y = site.pos[1]
return self.pot((self.L//2 * self.a, y)) + 4.

    def _up_lead_onsite(self, site):
x = site.pos[0]
return self.pot((x,-self.W//2) * self.a) + 4.

```

---

```

    def _down_lead_onsite(self, site):
x = site.pos[0]
return self.pot((x,self.W//2 * self.a)) + 4.

    def _onsite(self, site): return self.pot(site.pos) + 4.

    def phase_x(self,a, b):
# """Return hopping integral including the phase from magnetic field for vertical leads."""

ap = a.pos
bp = b.pos
phase = -self.phi * (0.5 * (ap[1] + bp[1]) * (bp[0] - ap[0]))
return -complex(cos(phase), sin(phase))

    # def gauge_x_to_y(s):
# return np.prod(s.pos)

    def phase_y(self, a, b):
# """Return hopping integral including the phase from magnetic field for horizontal
leads."""
ap = a.pos
bp = b.pos
phase = -self.phi * (0.5 * (ap[1] + bp[1]) * (bp[0] - ap[0]) + np.prod(ap) - np.prod(bp))
return -complex(cos(phase), sin(phase))

    def plot_potential(self):
pot, lat = self.pot, self.lat
L, W, = self.L, self.W
arr = np.empty((L, W))
for x in xrange(L):
for y in xrange(W):
arr[x, y] = pot(lat(x - L//2, y - W//2).pos)
# Plot transposed array so that the x axis points to the right.
plt.imshow(arr.T, origin='lower')
plt.colorbar()
plt.show()

    # Calling the system:
def main():
myfile='test.dat'
fich=open(myfile,'w')

    # Define potential.
def potential(pos): return sum(gate(pos) for gate in gates)

```

---

```

d = 100 # depth
L=401 #system length (sites)
W=301 #system width (sites)
V=4.2 #Potentiel split gates
Ef=0.47 #correspond a density  $n_s = 3.10^{15}m^{-2}$  (depends on a!)
V2=1 #Third gate potential
Vg3=10 #potentiel rugosites
l=700 #Third gate distance
xc=0 #decallage troisieme grille lateralement
wi=120 #Distance between split gates

#Define QPC split gates:
bottom_gate = RectangleGate(V, d, -650, -450, -1000, -20-wi)
top_gate = RectangleGate(V, d, -650,-450, 20+wi, 1000)

#Define sharp scattering gate for interferometers simulations:
right_gate = RectangleGate(Vg3, d,l, l+375, -40+xc, 40+xc)
tri1 = RectangleGate(Vg3, d,l-2,l,-30+xc, 30+xc)
tri2 = RectangleGate(Vg3, d,l-4,l-2,-17+xc, 17+xc)
tri3 = RectangleGate(Vg3, d,l-6,l-4, -12+xc, 12+xc)
tri4 = RectangleGate(Vg3, d,l-9,l-6, -4+xc, 4+xc)

#Define tip for SGM simulmations:
tip = Lorentzian (V2,400, 0, 40)

#Define disordered potential stored in 'potential.dat' for example
Ltot = 2001
fluc = np.loadtxt('potential.dat')
desordre = Disorder(fluc,0,0.47*10/100,-1000,1000,-1000,1000,Ltot)

#Define items used in the potential
gates = [bottom_gate, top_gate, tip, desordre]

#####

#Let's go!
qpc = My2DEG(L, W)
qpc.pot = potential
sys = qpc.sys
qpc.plot_potential() #Plot the potential landscape
qpc.phi=0 #Zero magnetic field (can be changed in loops)

#Calculate wavefunction
wf_func = kwant.solvers.default.wave_function(qpc.sys, Ef)
wfs = wf_func(0) #Wavefunction coming out of the left lead
ma=len(wfs)

```

---

```

modes=range(1, ma)
dens = abs(wfs[0])**2
for mode in modes:
dens += abs(wfs[mode])**2 #sum the different modes' contribution

    #Print wafunc in a file:
for n in range(len(dens)):
site=qpc.sys.site(n)
i = site.pos[0]
j = site.pos[1]
fich.write("%.7f %.7f %.7f \n" % (i,j,dens[n]))

    #Plot computed wavefunction:
kwant.plotter.map(qpc.sys, dens)

    #Calculate for example G(Vg) curve:
volts = np.linspace(4.3,3,num=10)
for volt in volts:
bottom_gate.voltage = volt
top_gate.voltage = volt
smat = kwant.smatrix(qpc.sys, Ef)
G = smat.transmission(0, 1) + smat.transmission(0, 2) +smat.transmission(0, 3)
print volt, G
#Print gate voltage and total transmission in file:
fich.write("%.7f %.7f \n" % (volt, G))

    #Calculate SGM map:
bottom_gate.voltage = 4
top_gate.voltage = 4
xcenters=np.linspace(0,400,num=30)
ycenters=np.linspace(-300,300,num=30)
for yc in ycenters:
tip.ycenter=yc
for vc in xcenters: tip.xcenter=xc
smat = kwant.smatrix(qpc.sys, Ef) #Calculate Smatrix
G = smat.transmission(0, 1) + smat.transmission(0, 2) +smat.transmission(0, 3) #Trans-
missions
print yc, xc, G
#Print tip position and total transmission in file:
fich.write("%.7f %.7f %.7f \n" % (yc, xc, G))

    if __name__ == '__main__':
main()

```

# Appendix B

## Publication related to Chapter 5

# Wigner and Kondo physics in quantum point contacts revealed by scanning gate microscopy

B. Brun<sup>1,2</sup>, F. Martins<sup>3</sup>, S. Faniel<sup>3</sup>, B. Hackens<sup>3</sup>, G. Bachelier<sup>1,2</sup>, A. Cavanna<sup>4</sup>, C. Ulysse<sup>4</sup>, A. Ouerghi<sup>4</sup>, U. Gennser<sup>4</sup>, D. Mailly<sup>4</sup>, S. Huant<sup>1,2</sup>, V. Bayot<sup>1,3</sup>, M. Sanquer<sup>1,5</sup> & H. Sellier<sup>1,2\*</sup>

<sup>1</sup>*Univ. Grenoble Alpes, F-38000 Grenoble, France*

<sup>2</sup>*CNRS, Inst. NEEL, F-38042 Grenoble, France*

<sup>3</sup>*IMCN/NAPS, Université catholique de Louvain, B-1348 Louvain-la-Neuve, Belgium*

<sup>4</sup>*CNRS, Laboratoire de Photonique et de Nanostructures, UPR20, F-91460 Marcoussis, France*

<sup>5</sup>*CEA, INAC-SPSMS, F-38054 Grenoble, France*

\*Correspondence should be addressed to H.S. (*hermann.sellier@neel.cnrs.fr*).

Quantum point contacts exhibit mysterious conductance anomalies in addition to well known conductance plateaus at multiples of  $2e^2/h$ . These 0.7 and zero-bias anomalies have been intensively studied, but their microscopic origin in terms of many-body effects is still highly debated. Here we use the charged tip of a scanning gate microscope to tune *in situ* the electrostatic potential of the point contact. While sweeping the tip distance, we observe repetitive splittings of the zero-bias anomaly, correlated with simultaneous appearances of the 0.7 anomaly. We interpret this behaviour in terms of alternating equilibrium and non-equilibrium Kondo screenings of different spin states localized in the channel. These alternating Kondo effects point towards the presence of a Wigner crystal containing several charges with different parities. Indeed, simulations show that the electron density in the channel is low enough to reach one-dimensional Wigner crystallization over a size controlled by the tip position.

## I. INTRODUCTION

Quantum point contacts<sup>1</sup> (QPCs) are among the simplest quantum devices made out of a two-dimensional electron gas (2DEG). Applying a negative voltage on a split-gate creates a quasi-one-dimensional (1D) channel connected to large 2D reservoirs. This narrow channel behaves as an electron wave-guide and transmits a finite number of modes, each of them carrying one quantum of conductance  $G_0 = 2e^2/h$  ( $e$  is the electron charge and  $h$  the Planck constant). As a result, the conductance versus gate voltage curve shows a series of quantized plateaus with transitions which are well reproduced by a single-particle model<sup>2</sup>.

However, since the early days of QPCs, a shoulder-like feature is commonly observed<sup>3</sup> at a conductance around  $0.7 G_0$ , which cannot be explained by single-particle theories. With lowering temperature, this “0.7 anomaly” rises to reach the first plateau, and a zero-bias peak called “zero-bias anomaly” (ZBA) emerges in the non-linear differential conductance<sup>4</sup>. These anomalies have been extensively studied through transport experiments<sup>3-7</sup>, revealing the complexity of the underlying phenomena. Different theoretical models have been proposed<sup>8-13</sup>, but no consensus could be reached so far on their interpretation<sup>14</sup>.

Recently, an experiment using several gates to vary the channel length<sup>15</sup> revealed the possible existence of several emergent localized states responsible for the conductance anomalies. At the same time, a different theoretical model was proposed<sup>16</sup>, explaining the anomalies without invoking localized states in the channel. As stressed in Ref.<sup>17</sup>, investigating these anomalies using scanning probe techniques could make it possible to check the existence of spontaneously localized states and discriminate between these two proposals: this is the aim of the present letter.

Here we perform scanning gate microscopy<sup>18</sup> (SGM), in which a negatively charged tip is scanned above the sample surface and modifies the electrostatic potential in the 2DEG. This local potential change induces electron back-scattering towards the QPC, which can be used to image single-particle phenomena such as wave-function quantization in the channel<sup>19</sup>, branched flow in the disorder potential<sup>20</sup>, interference patterns induced by the tip<sup>21-23</sup>, or to investigate electron-electron interactions inside<sup>24</sup> or outside<sup>25</sup> the QPC. This movable gate can also be used to tune *in situ* the saddle potential of the QPC, in a more flexible and less invasive way than fixed surface gates, and probe intrinsic properties of the QPC such as the 0.7 anomaly<sup>26,27</sup>.

Here we show that approaching the tip towards the QPC produces an oscillatory splitting of the ZBA, correlated with simultaneous appearances of the 0.7 anomaly, thereby confirming that both features share a common origin<sup>4,15</sup>. We interpret these observations as the signature of a small one-dimensional Wigner crystal<sup>28-30</sup> forming in the channel<sup>31</sup> (a quantum chain of charges localized by Coulomb interactions in absence of disorder). The number of charges in this many-body correlated state is tuned by changing the tip position, leading alternatively to a single- or a two-impurity Kondo effect (screening of a localized spin by conducting electrons), with a conductance peak either at zero, or at finite bias, depending on the charge parity.

Our observations therefore strongly support the existence of emergent localized states, as suggested in Ref.<sup>15</sup> where the number of localized charges is controlled by changing the effective channel length. Here we show that a similar effect is observed when changing the distance of an additional gate placed around the QPC. To understand this new

result, we perform classical electrostatic simulations and evaluate the size of the region where electrons should form a 1D Wigner crystal thanks to the critically low electron density. We show that the calculated size of this small crystal is in good agreement with the observed change in the number of localized charges, thereby revealing that Wigner crystallization is, to our opinion, the correct way to understand this spontaneous localization.

## II. RESULTS

### Transport measurements

The QPC (see Methods and Fig. 1a) is cooled down to a temperature of 20 mK in a cryogenic scanning probe microscope<sup>32</sup>. In the absence of the tip (moved several microns away), the linear conductance shows the usual staircase behaviour versus gate voltage (Fig. 1b). The shoulder below the first quantized plateau is the puzzling 0.7 anomaly. The source-drain bias spectroscopy (Fig. 1c) shows that this shoulder evolves to a clear plateau at  $0.85 G_0$  at finite bias<sup>5,33,34</sup>. The narrow peak around zero bias is the ZBA and disappears above 1 K (Supplementary Figure 1). Its width of  $200 \mu\text{eV}$  is much smaller than the 1D subband spacing of  $4.5 \text{ meV}$  (Fig. 1d). Above  $0.7 G_0$ , the ZBA splits into finite-bias peaks<sup>15,35</sup> centred at  $\pm 250 \mu\text{V}$ . We show in the following that the presence of the 0.7 anomaly is related to this splitting of the ZBA.

### Scanning gate microscopy

When the tip is scanned near the QPC and polarized such as to deplete locally the 2DEG (see Methods), we observe two distinct phenomena. On the first conductance plateau (Fig. 2b), SGM images reveal the electron flow coming out of the QPC, with fringes spaced by half the Fermi wavelength, as already observed by several groups<sup>20,22,23</sup>. The fringes result from interferences of electrons backscattered by the depleted region below the tip and reflected by impurities<sup>20,22</sup> in the 2DEG or directly by the gates<sup>21,36</sup>.

Below the first plateau (Fig. 2a), SGM maps reveal a novel set of concentric rings centred on the QPC, with a spacing increasing with tip distance (see also Supplementary Figure 2). As opposed to the previous one-particle interference fringes, these new rings are not linked to the electron flow (black region in Fig. 2b) but extend rather isotropically around the QPC, not only in the horizontal plane but in all three directions of space. This is revealed by scanning the tip in a vertical plane (Fig. 2c), unveiling half spheres centred on the QPC (purple line 1). This behaviour contrasts with that of interference fringes (green line 2) that quickly disappear when the tip is scanned more than 50 nm above the surface (see also Supplementary Figure 3). Interferences indeed require electrons at the Fermi level to be backscattered by a depleted region below the tip, a situation which is only obtained for the tip close

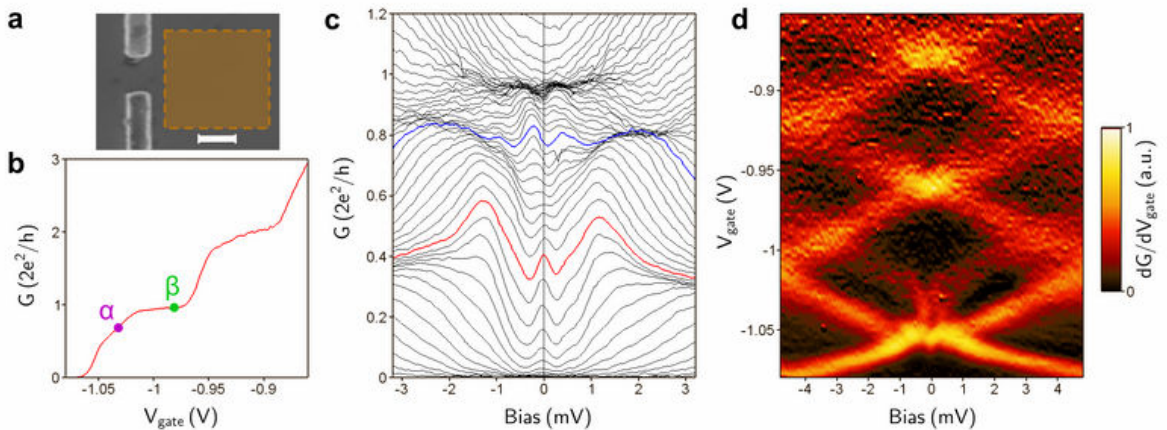


FIG. 1: **Transport measurements.** Base temperature is 20 mK. (a) Electron micrograph of the QPC gates. The scale bar is 300 nm. The dashed box indicates the position of the scanning area used in Fig. 2. (b) Differential conductance  $G$  at zero bias versus split-gate voltage  $V_{\text{gate}}$ . The 0.7 anomaly is visible below the first plateau. Positions  $\alpha$  and  $\beta$  are used in Fig. 2a,b. (c) Differential conductance  $G$  versus source-drain bias for different gate voltage  $V_{\text{gate}}$  from  $-1.08 \text{ V}$  to  $-0.96 \text{ V}$ . The zero-bias peak in the red curve splits into finite-bias peaks in the blue curve. (d) Numerical derivative of the differential conductance  $dG/dV_{\text{gate}}$  versus bias and gate voltage. Yellow lines highlight transitions between conductance plateaus.

enough to the 2DEG (and at low enough temperature to avoid thermal averaging of the interferences). We therefore conclude that the new rings are not interferences but result from a direct tuning of the electrostatic potential in the QPC. The larger ring spacing at larger distances results from the smaller potential changes induced by the tip.

### Conductance anomalies

To demonstrate that these rings correspond to modulations of the conductance anomalies, the tip is scanned along a single line in a region with almost no interference (line 3 in Fig. 3a) and the QPC parameters (gate and bias voltages) are varied. Fig. 3b shows that the ring-related conductance oscillations are only visible for gate voltages in the transition below the first plateau, just where the ZBA and 0.7 anomaly are observed. Fig. 3c shows how the conductance oscillations evolve when the average conductance goes from 0 to  $G_0$  while changing the gate voltage. The oscillations are clearly visible between 0.4 and 0.8  $G_0$ . They are blurred when approaching  $G_0$  because some interference fringes come into play. The increasing distance between conductance extrema (labeled A to D for maxima and A' to D' for minima) is consistent with an oscillatory phenomenon in the QPC, controlled by the decreasing

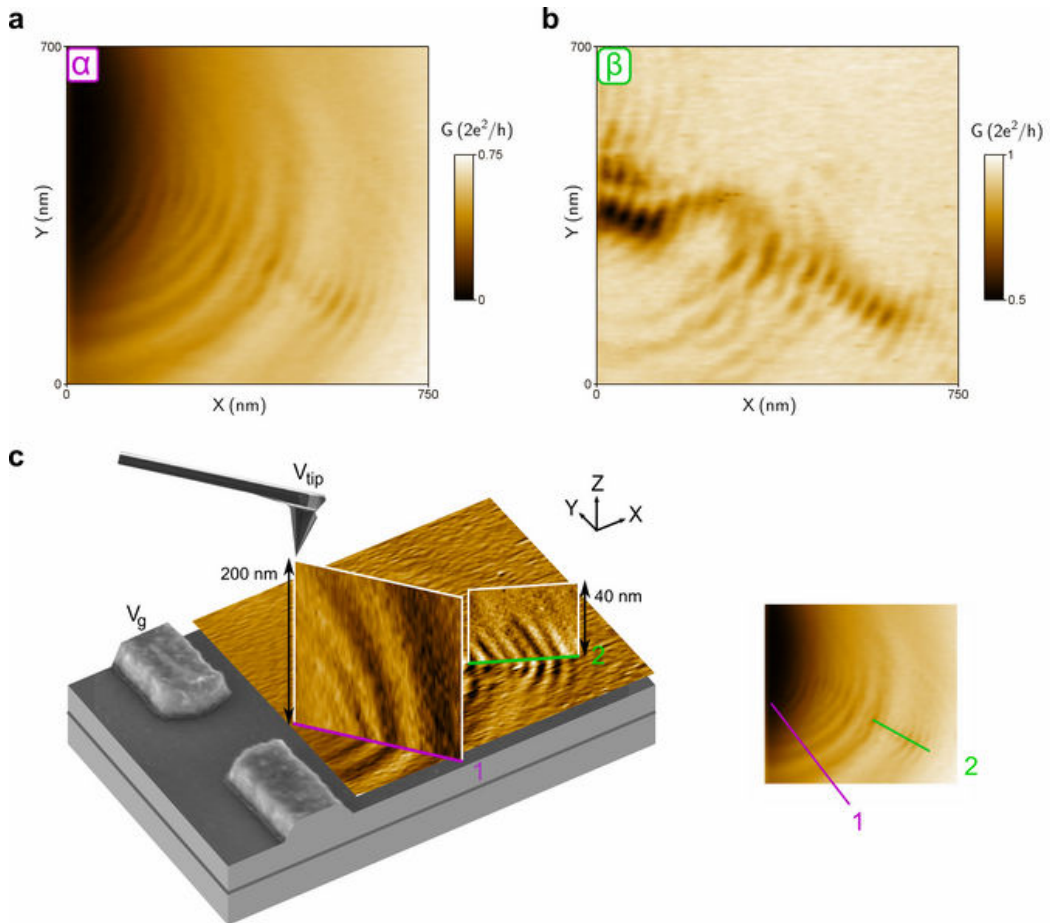
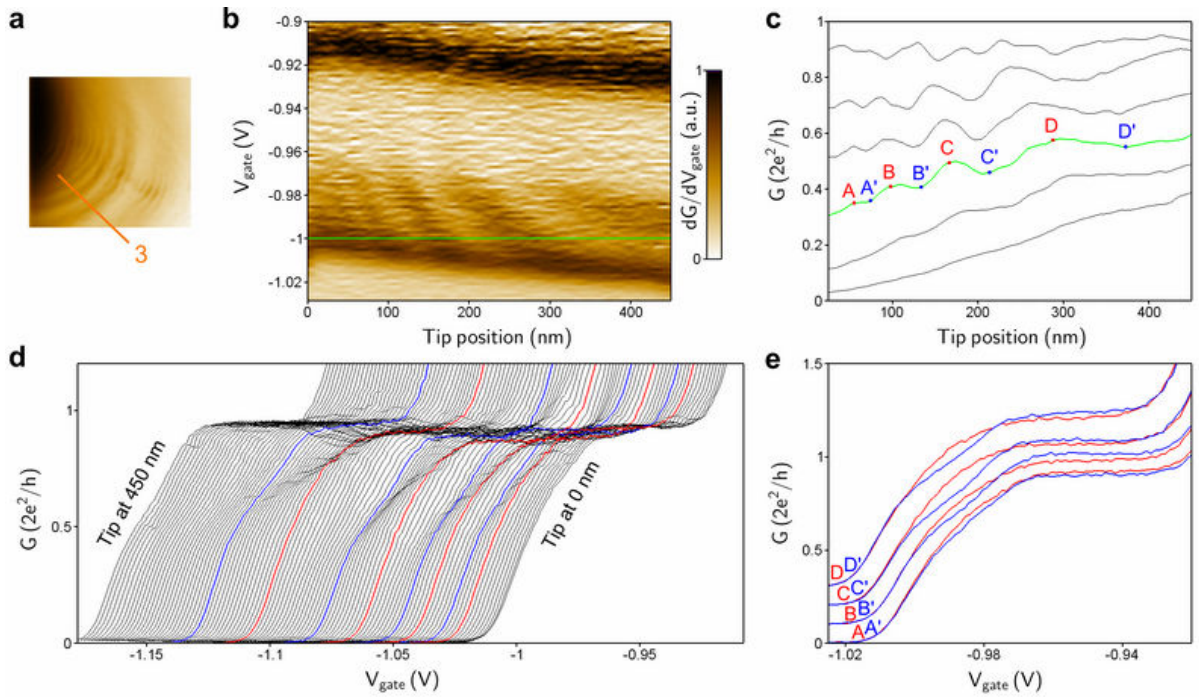


FIG. 2: **Scanning gate microscopy.** Base temperature is 20 mK. (a,b) SGM maps of the QPC conductance  $G$  versus tip position in the  $(X, Y)$  horizontal plane for gate voltages  $V_{\text{gate}} = -1$  V (a) and  $-0.95$  V (b) corresponding respectively to points  $\alpha$  and  $\beta$  as defined in Fig. 1b (gate voltages are shifted by 35 mV in presence of the tip). Concentric rings are only visible at  $\alpha$ , and interference fringes are more contrasted at  $\beta$ . Additional data are presented in Supplementary Figure 2. (c) Schematic view of the SGM experiment showing the tip scanning above the 2DEG near the QPC gates and three SGM maps. The horizontal map is the same as in (a), but the data have been differentiated with respect to the  $Y$ -coordinate to highlight details. The two vertical maps are recorded in planes perpendicular to the surface along the purple line 1 (size  $500 \times 200$  nm, gate voltage  $\alpha$ ) and the green line 2 (size  $250 \times 40$  nm, gate voltage  $\beta$ ) as indicated on the right image (identical to (a)). The two vertical maps have been differentiated with respect to their horizontal coordinate to highlight details (raw data are shown in Supplementary Figure 3). The vertical map along line 1 reveals that the concentric rings visible in (a) form also rings in the vertical plane, whereas the vertical map along line 2 shows that interference fringes disappear rapidly with the tip-to-surface distance.

electrostatic coupling to the tip. Plotting the conductance versus gate voltage (Fig. 3d) reveals the oscillatory behaviour of the 0.7 anomaly. The amplitude of this modulation can be read from Fig. 3e, where curves at positions X and X' are compared two-by-two (curves are shifted horizontally to compensate for the drift of the pinch-off voltage while approaching the tip). Curves at positions A to D are smooth with no shoulder, i.e. no anomaly, whereas curves at positions A' to D' present a reduced conductance above  $0.5 G_0$ , i.e. the 0.7 anomaly. The concentric rings observed in SGM images (Fig. 2a) therefore correspond to an alternating modulation of the 0.7 anomaly when the tip approaches the QPC.

We now analyse the behaviour of the ZBA when the 0.7 anomaly repeatedly appears and disappears, and show that both anomalies are linked. Fig. 4a shows the differential conductance versus source-drain bias for different tip positions (same scan line as in Fig. 3a). Curves at positions A to D have a peak centred at zero bias (ZBA), whereas curves at positions A' to D' have a dip at zero bias and local maxima at  $\pm 250 \mu\text{V}$  bias (splitting of the ZBA), on top of the same V-shaped background. Scanning the SGM tip therefore produces a repetitive splitting of the ZBA, that draws a checkerboard pattern in a color-plot of the spectroscopy versus tip position (Fig. 4b). Note that the spontaneous splitting of the ZBA observed without the tip (Fig. 1c) also shows peaks at  $\pm 250 \mu\text{V}$  and probably has the same origin.

Considering the regularity of the concentric rings in Fig. 2a, this oscillatory behaviour of the 0.7 and zero-bias anomalies would be observed for any scanning line in a large range of angles (see Supplementary Figure 4 and Supplementary Note 1). As a consequence, rings with conductance maxima correspond to a simple staircase in the linear conductance and a ZBA in the non-linear spectroscopy, whereas rings with conductance minima correspond to a 0.7 anomaly and a splitting of the ZBA. This result shows that the ZBA suppresses the 0.7 anomaly at low temperature<sup>4</sup> only if the ZBA is not split into finite-bias peaks.



**FIG. 3: Modulation of the 0.7 anomaly.** The figure analyses the zero-bias conductance oscillations when the tip is scanned along the orange line 3 indicated in (a) with the origin of positions in the QPC direction. (b) Trans-conductance  $dG/dV_{\text{gate}}$  versus tip position and gate voltage. Black regions correspond to transitions between plateaus. The conductance oscillations are only visible below the first plateau. (c) Conductance  $G$  versus tip position for gate voltages  $V_{\text{gate}} = -0.964 \text{ V}$ ,  $-0.983 \text{ V}$ ,  $-0.992 \text{ V}$ ,  $-1.000 \text{ V}$ ,  $-1.006 \text{ V}$ ,  $-1.012 \text{ V}$  (from top to bottom). Conductance extrema at  $V_{\text{gate}} = -1 \text{ V}$  (green curve) are labelled A to D (maxima) and A' to D' (minima). The global slope corresponds to the rise of the saddle-point potential when the tip approaches the QPC. (d) Conductance  $G$  versus gate voltage for different tip positions from 0 to 450 nm (successive curves are shifted to the left). (e) Same data as in (d) but for tip positions A to D (red curves, shifted vertically) and A' to D' (blue curves, shifted also horizontally to be compared with red curves). Red curves show no shoulder, whereas blue curves show the 0.7 anomaly. Small differences between plateau values come from residual interference fringes.

### III. DISCUSSION

First, we would like to stress again that these new conductance oscillations cannot be explained by interference effects in the 2DEG. One argument already given above is that interferences require backscattering with a tip close to the surface, whereas the new rings are observed up to large tip heights (Fig. 2c). A second argument is that interference fringes would have an increasing spacing for short tip distances because the density is reduced close to the QPC and the electron wavelength is larger, but the opposite behaviour is observed.

We now discuss a possible single-particle effect inside the QPC that, at first sight, could give similar conductance oscillations. In case of a non-adiabatic transmission, wave-functions are scattered by the QPC potential barrier and transmission resonances appear when the barrier length is equal to an integer number of half the longitudinal wavelength. If the effect of the tip is to change the channel length, such resonances could give conductance oscillations versus tip distance. However, this single-particle mechanism cannot explain the repetitive splittings of the ZBA which are simultaneous with the observed conductance oscillations and we therefore need another explanation.

The ZBA in QPCs has been shown to scale with temperature and magnetic field like the Kondo effect in quantum dots<sup>4</sup>. This effect corresponds to the screening of a single degenerate level by a continuum of states, and therefore indicates the presence of a localized spin in the QPC channel<sup>11</sup>. Splittings of the ZBA have been observed recently

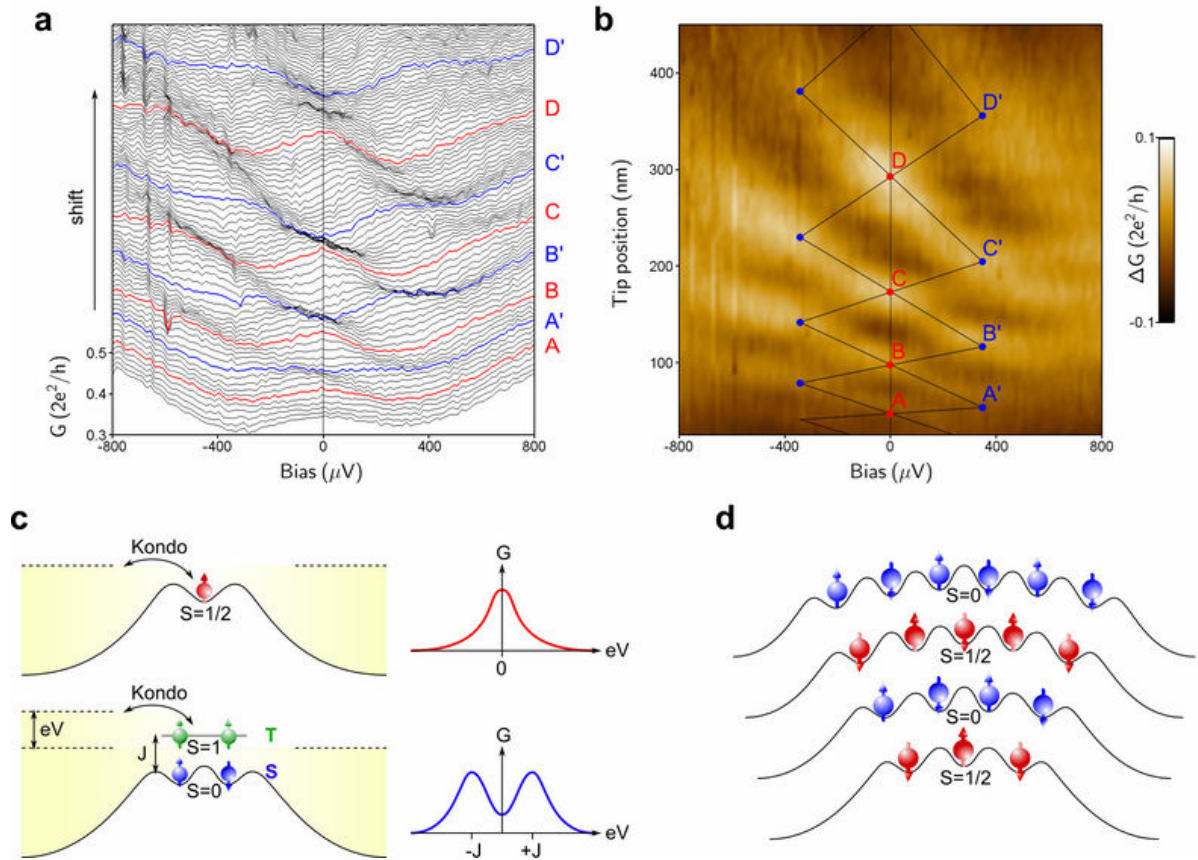


FIG. 4: **Successive splittings of the ZBA.** The figure analyses the low bias source-drain spectroscopy when the tip is scanned along the orange line 3 indicated in Fig. 3a. (a) Differential conductance  $G$  versus source-drain bias at a fixed gate voltage  $V_{\text{gate}} = -1$  V for different tip positions from 0 to 450 nm. Successive curves are shifted upwards by  $0.0075 \times 2e^2/h$ . Conductance peaks are visible at zero and finite bias on red and blue curves, respectively. (b) Color plot of the same data as in (a) after subtraction of a smooth background to suppress the main gating effect of the tip. Peak positions are indicated by dots. The successive ZBA splittings give a checkerboard pattern. The asymmetry results from the bias-induced change of the QPC position. (c) Schematic of the QPC potential with one (top) and two (bottom) localized electrons, corresponding respectively to a  $S = 1/2$  ground state with a zero-bias Kondo peak and to a  $S = 0$  ground state with finite-bias Kondo peaks involving the excited state  $S = 1$  with singlet-triplet energy splitting  $J$ . The expected conductance  $G$  versus bias  $V$  is shown on the right for each state. (d) Schematic of the QPC potential with an increasing number of electrons localized by Coulomb interactions. The antiferromagnetic spin coupling in this small 1D Wigner crystal gives either a  $S = 1/2$  ground state (ZBA) or a  $S = 0$  ground state (splitting of the ZBA), depending on the parity (respectively odd or even).

in length-tunable QPCs<sup>15</sup> and interpreted as a two-impurity Kondo effect<sup>37,38</sup>, involving non-equilibrium Kondo screening<sup>39,40</sup>, as commonly observed in quantum dots with even numbers of electrons<sup>42</sup>, coupled quantum dots<sup>43</sup>, and molecular junctions<sup>44</sup>.

We now consider different scenarios to explain the presence of such localized states in our system. In a recent work on QPCs made out of a two dimensional hole gas, a spontaneous splitting of the ZBA as the QPC opens has been reported<sup>35</sup>. This effect was attributed to a charge impurity forming a potential well close to the channel, containing one or two charges, leading to different types of Kondo screening. In our case, the spontaneous splitting of the ZBA as the QPC opens (Fig. 1c) could be explained by this effect. However, the fact that approaching the tip towards the QPC results in 4 successive splittings of the ZBA indicates that this impurity should contain at least 8 charges, which is unlikely for a single impurity. Nevertheless, one could imagine that a shallow quantum dot has formed in the QPC due to potential fluctuations induced by residual disorder<sup>45</sup> and giving Coulomb blockade oscillations as often observed in long 1D wires<sup>46</sup>. The major argument to exclude this scenario is that the split-gate has a larger capacitive coupling to the channel than the tip has (i.e. a larger lever-arm parameter), so the split-gate should induce more charging events than the tip, but we observe the opposite: approaching the tip by 600 nm produces four successive splittings of the ZBA and sweeping the gate voltage produces only one splitting. It can therefore not be Coulomb blockade in a disorder-induced quantum dot.

The only remaining possibility to explain the presence of localized states in the channel is a spontaneous electron localization which is not induced by potential barriers but instead by electron-electron interactions. Indeed, a large number of theoretical and numerical investigations show that interactions can localize a finite number of electrons in the channel<sup>12,13,47,48</sup>. On the first conductance plateau and below, transport can be considered as 1D, and the electron density is so low that the Coulomb repulsion overcomes the kinetic energy. When the 1D density  $n_{1D}$  fulfills the criterion  $n_{1D} \times a_B < 1$ , where  $a_B$  is the effective Bohr radius (10 nm in GaAs), electrons are expected to spontaneously order in a crystal, with an inter-particle distance minimizing Coulomb repulsion<sup>49</sup>. This many-body state, known as a Wigner crystal<sup>28,29</sup>, has been suggested to be responsible for the 0.7 anomaly in QPCs<sup>12</sup>. When the electron density in the channel is decreased below the critical value, the density modulations evolve continuously from the  $\lambda_F/2$  periodicity of Friedel oscillations to the  $\lambda_F/4$  periodicity of the Wigner crystal<sup>50</sup>. Quantum Monte Carlo simulations have also shown that electrons in the crystallized region can be relatively decoupled from the high density reservoirs and present an antiferromagnetic coupling  $J$  between adjacent spins<sup>48</sup>. In contrast to the case of quantum dots with real tunnel barriers, electron localization in a QPC is not straightforward, and results from emergent barriers in the self-consistent potential. On the other hand, the Kondo effect requires a relatively open system with a good coupling to the reservoirs, and this makes the QPC a suitable platform to observe Kondo phenomena on an interaction-induced localized state, as shown recently in length-tunable QPCs<sup>15</sup>.

This last scenario being the most realistic one in our case, we therefore interpret the four observed oscillations as a signature of eight successive states of a small non-uniform 1D Wigner crystal with an alternating odd and even number of localized charges. Situations with an odd number of electrons in a spin  $S = 1/2$  ground state show a ZBA due to Kondo screening of non-zero spin states. Situations with an even number of electrons in a spin singlet  $S = 0$  ground state show a splitting of the ZBA due to non-equilibrium Kondo screening<sup>39,40</sup> of the spin triplet  $S = 1$  excited state with peaks at a finite bias  $eV = J$  (Fig. 4c). The four oscillations, suggestive of eight successive states, reveal that a large number of electrons can spontaneously localize in the channel of a QPC, as shown in Fig. 4d. Observing Kondo screening on a system with many localized charges is not so surprising if we compare to quantum dots where the Kondo effect is observed up to large numbers of electrons<sup>41</sup>. Nevertheless, the particular case of a 1D chain of localized charges in the Kondo regime still requires theoretical investigations.

This analysis is consistent with the interpretation given in Ref.<sup>15</sup> for similar observations using a QPC with six surface gates to tune the channel length. Our SGM experiment brings additional information on this effect, since scanning the tip around the QPC, laterally or vertically, changes the shape, extension, and symmetry of the channel potential. The circular and almost isotropic rings in Fig. 2c show that the localized states survive to all these potential deformations. The regularity of the successive rings also suggests that this localization occurs rather independently of disorder, though possible crystal pinning effects should be investigated in the future.

In Ref.<sup>15</sup>, the parameter controlling the number of localized states is the effective length of the channel, defined in Ref.<sup>51</sup> and computed using an analytical approach assuming a fixed zero potential at the surface<sup>52</sup>. This method is not suitable to model our SGM experiment, as the tip is situated above the surface. To evaluate the potential landscape in presence of the tip, we perform 3D classical electrostatic simulations in the Thomas-Fermi approximation (see Methods and Supplementary Note 2) and compute self-consistently the local potential  $V(x, y)$  in the 2DEG and the local 2D electronic density  $n_{2D}(x, y)$  (Fig. 5a). In this way, the tip-induced potential is correctly calculated, with the screening effects from the 2DEG and the metallic gates taken into account. We obtain a good agreement between calculated and experimental values regarding the gate voltage required to close the QPC, the tip voltage to reach depletion in the 2DEG, and the cross-talk between the tip position and the QPC opening. The effective channel length used in Ref.<sup>15</sup> was calculated in Ref.<sup>51</sup>, using the unscreened gate potential. This length cannot be calculated here from our self-consistent potential, because screening effects induce non-parabolic transverse confinement potentials.

We propose instead that the parameter controlling the number of localized charges is the size of the region where the 1D Wigner crystallization should occur. This interaction-induced spontaneous ordering is often discussed in terms of the Wigner-Seitz radius  $r_s = 1/(2n_{1D}a_B)$ , representing the ratio of the Coulomb repulsion to the kinetic energy. A recent numerical investigation of the 1D Wigner crystallization shows that the critical parameter  $r_s^c$  varies between 0.5 and 2, depending on the strength of the transverse confinement potential<sup>49</sup>. To evaluate the size of the region where  $r_s$  is larger than a given threshold, we calculate the 1D electron density by integration of the 2D electron density in the transverse direction (Fig. 5b and 5c). As an example, we choose a critical value  $r_s^c = 0.71$  corresponding to a critical density  $n_{1D}^c = 0.7/a_B$ , and evaluate the size  $L_{\text{crystal}}$  where the density is lower than  $n_{1D}^c$ . This size is found to vary from 210 to 290 nm when the tip is approached by 600 nm towards the QPC, which shows that the tip can strongly affect the size of the low density region, and hence the number of localized charges. The tip positions leading to the same  $L_{\text{crystal}}$  form rings centred on the QPC, both for horizontal and vertical scanning planes (Fig. 5d and 5e), in the same way as the conductance oscillations observed in the SGM experiment (Fig. 2c).

Our classical simulation holds only for an estimate of the size  $L_{\text{crystal}}$ , but cannot be used to calculate the number of localized charges, since quantum mechanics dominates at such a low density. Note that charges in this crystal are not expected to be uniformly spaced, because the potential of a QPC shows a strong curvature. This non-uniform

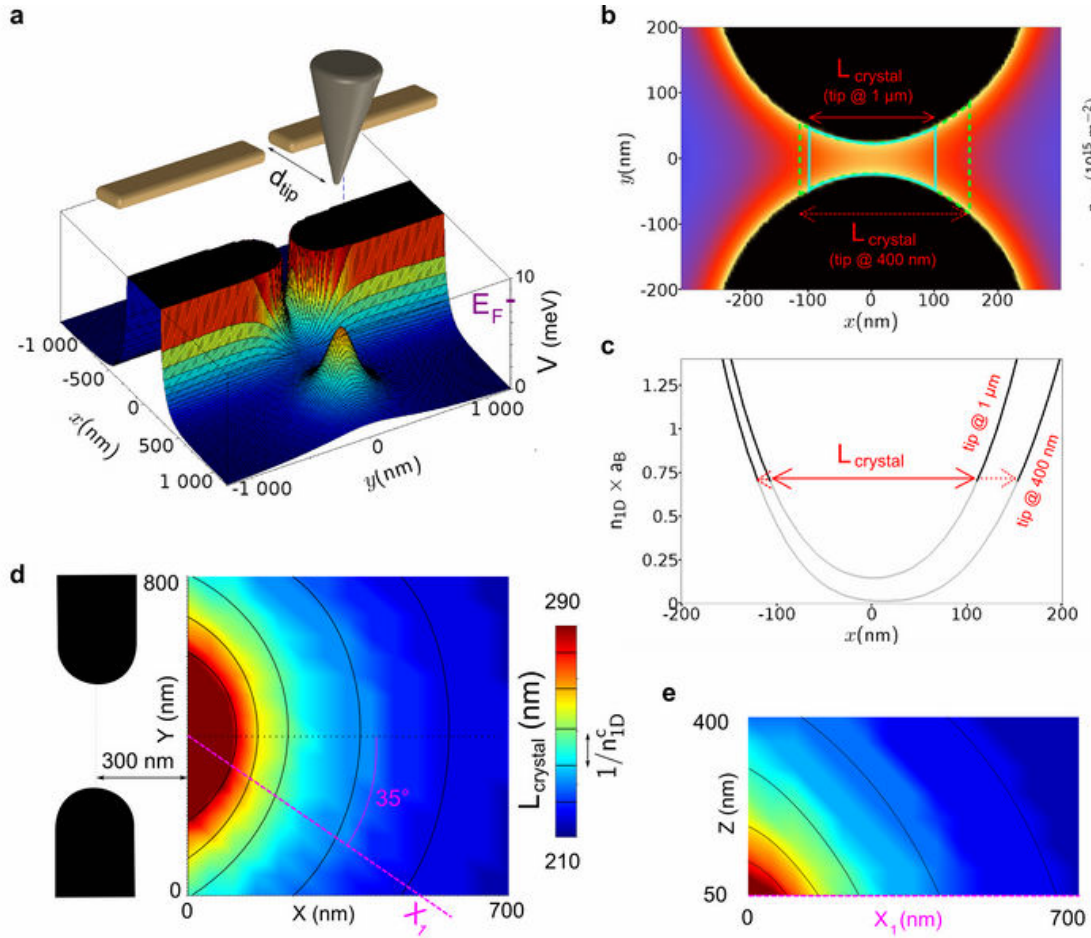


FIG. 5: **Calculation of the electron density and estimation of the Wigner crystal size.** (a) Geometry of the metallic gates and SGM tip defined in the Comsol simulation software and example of electrostatic potential map computed for a given gate voltage and tip position. The Fermi energy  $E_F$  is 8 meV in the 2DEG. (b) Map of the two-dimensional electron density  $n_{2D}$  in the 2DEG computed classically but self-consistently with the potential, when the tip is at 1  $\mu\text{m}$  from the QPC. (c) One-dimensional electron density  $n_{1D}$  obtained by integration of  $n_{2D}$  along the  $y$ -axis, when the tip is at 1  $\mu\text{m}$  and 400 nm from the QPC. Choosing a critical density  $n_{1D}^c = 0.7/a_B$  determines the expected size  $L_{\text{crystal}}$  of the 1D Wigner crystal. (d) Computed size of the Wigner crystal as a function of tip position in an horizontal plane 30 nm above the surface ( $V_{\text{gate}} = -1$  V). The region in red corresponds to a closed contact (the electron density is zero at the QPC center for these tip positions). Black lines indicate tip positions for which  $L_{\text{crystal}}$  is enlarged by  $1/n_{1D}^c$ , corresponding at first order to the addition of one charge to the crystal. (e) Computed size of the Wigner crystal for tip positions in a vertical plane (above line  $X_1$  at  $35^\circ$  from QPC axis).

situation would require an extension of the concept of Wigner crystal which is usually studied in a flat potential landscape. A rather crude approach to evaluate how many charges can be added by approaching the tip is to suppose that one charge is added to the crystal each time the region is enlarged by  $1/n_{1D}^c$  (about 14 nm for  $r_s^c = 0.71$ ). With this assumption, about 5 charges can be added to the crystal when the tip is approached close to the QPC (Fig. 5d). This value is qualitatively consistent with the 4 oscillations observed in the experiment, and interpreted as the addition of 8 charges. Simulations also show that the number of charges can be modified simply by changing the split-gate voltage (see Supplementary Figure 5). This could explain the ZBA splitting observed above  $0.7 G_0$  in absence of the tip (Fig. 1c).

Our assumption that electrons form a 1D system in the low density region is justified *a posteriori* by the fact that only the first and second transverse modes are occupied over the length  $L_{\text{crystal}}$ . The presence of the second mode at the extremities of this region indicates that the system is not strictly 1D, but theory still predicts the formation of a Wigner crystal in the second subband of quasi-1D wires, forming a zigzag chain<sup>53</sup>, as possibly observed in experiments<sup>31,54</sup>. Interestingly, the simulations show that a small crystallized region survives when the second mode reaches the central part the channel, which could explain the 0.7 analogues often observed between the first and second conductance plateaus.

In summary, we observe a periodic modulation of the conductance anomalies in a QPC at very low temperature while tuning continuously the potential with the polarized tip of a scanning gate microscope. We explain this experimental observation by the formation of an interaction-induced localized state in the QPC channel, which gives rise to a single- or two-impurity Kondo effect depending on the odd or even number of localized charges, respectively. Indeed, electrostatic simulations show that the electron density in the channel is low enough to result in a spontaneous 1D Wigner crystallization. Our study gives new information on QPC conductance anomalies, which should guide future theoretical works, and will open the way to further experimental investigations involving fine tuning of the QPC potential using various methods.

## IV. METHODS

### Sample and measurement

The QPC is designed on a GaAs/AlGaAs heterostructure hosting a 2DEG 105 nm below the surface with  $2.5 \times 10^{11} \text{ cm}^{-2}$  electron density and  $1.0 \times 10^6 \text{ cm}^2 \text{ V}^{-1} \text{ s}^{-1}$  electron mobility. A Ti/Au split-gate is defined by e-beam lithography on a mesa with four ohmic contacts and forms a 270 nm long and 300 nm wide opening. The device is fixed to the mixing chamber of a dilution fridge, in front of a cryogenic scanning probe microscope<sup>32,55,56</sup>. The QPC is cooled down to a base temperature of 20 mK at zero gate voltage. The four-probe differential conductance  $G = dI/dV_{\text{bias}}$  is measured by a standard lock-in technique, using a  $10 \mu\text{V}$  AC excitation at a frequency of 123 Hz. A series resistance of  $600 \Omega$  is subtracted from all data, in order to have the conductance of the first plateau at  $2e^2/h$ . Since the temperature evolution of the zero-bias peak does not saturate below 90 mK, the temperature of electrons in the QPC is probably below this value.

### Scanning gate microscopy

The tip of a commercial platinum-coated cantilever is fixed on a quartz tuning fork, which is mounted on the microscope actuators. The position of the QPC is determined by SGM, as the tip position corresponding to the maximum change in conductance while scanning at large tip-surface distance. Then, the tip is lowered to a few tens of nanometres above the surface and scanned at fixed height on a single side of the 200 nm thick split-gate in the scanning area shown in Fig. 1a. All the SGM results reported here are obtained for a tip voltage of  $-6 \text{ V}$  and a tip-to-surface height of 40 nm (except for vertical scans in Fig. 2c starting at 30 nm). Note that the dilution fridge stays at its base temperature of 20 mK during tip scanning.

### Electrostatic simulations

Classical electrostatic simulations are performed with the Comsol software. We model the system in three dimensions as follows. The 2DEG plane is located 105 nm below the surface according to our heterostructure. The region between the 2DEG and the surface is filled with the GaAs dielectric constant  $\epsilon_r = 12.9$ . The initial electron density in the 2DEG is set at  $2.5 \times 10^{11} \text{ e}^- \text{ cm}^{-2}$  by the addition of a uniform plane of positive charges modelling ionized dopants (in the same plane as the 2DEG for better computation stability). The metallic gates are 120 nm thick and define a 270 nm wide and 300 nm long constriction, corresponding to our sample geometry. The tip is modelled by a cone

---

# Appendix C

## French summary

---

## Introduction

En réduisant la taille des conducteurs et en abaissant la température, on entre dans un régime où les effets quantiques se font sentir dans le transport électronique. La longueur de cohérence des électrons devient de l'ordre de la taille du système, et on voit apparaître leur nature ondulatoire dans les propriétés de transport. Par exemple, à cette échelle dite mésoscopique, des interférences entre électrons ont pu être mises en évidence dans les années 80 par des fluctuations universelles de conductance dans des fils très fins[25] et par des oscillations de conductance dans des anneaux Aharonov-Bohm métalliques[27]. La physique mésoscopique a pris une nouvelle tournure en abaissant la dimension des conducteurs, en particulier grâce aux gaz d'électrons bidimensionnels (gaz 2D). Ces gaz 2D, tout d'abord réalisés dans la couche d'inversion de transistors de Silicium, ont permis la découverte de l'effet Hall quantique entier, qui a valu le prix Nobel de physique à Klaus Von Klitzing en 1985[11]. Cette découverte a démontré que les gaz 2D ouvrent une nouvelle voie pour l'investigation des effets quantiques en matière condensée. En modifiant localement le potentiel des gaz 2D à l'aide de grilles métalliques, le transport électronique a pu être étudié au travers de petits îlots d'électrons (les quantum dot) et de canaux quasi-unidimensionnels, les contacts ponctuels quantiques (QPC)[26, 28], où les effets quantiques dominent le transport. Peu après la découverte de l'effet Hall quantique entier, dans des gaz 2D très propres fabriqués à base de GaAs, la découverte de l'effet Hall quantique fractionnaire[24] et son explication en termes d'interactions entre électrons[13] a également valu le prix Nobel à Tsui, St Ormer and Laughlin (1998). Ces découvertes ont démontré que les gaz 2D offrent non seulement la possibilité d'étudier les effets quantiques en matière condensée, mais permettent d'étudier les effets d'interactions, ouvrant un nouveau champ d'investigations de phénomènes passionnants en mécanique quantique.

Dans cette thèse, nous étudions les effets d'interactions entre électrons dans les systèmes unidimensionnels. Nous nous intéressons en particulier aux effets d'interactions dans les contacts ponctuels quantiques. Les QPCs sont de petits canaux quasi-1D, créés dans les gaz 2D à l'aide de grilles métalliques situées au dessus de la surface, et que l'on peut ouvrir ou fermer à volonté en appliquant une tension négative sur ces grilles. La conductance de ces dispositifs est quantifiée, et cela peut se comprendre simplement par les effets de confinement. En effet, seuls certains modes électroniques transverses sont autorisés dans ces canaux, et ces modes ne peuvent contribuer à la conductance que si les électrons ont suffisamment d'énergie pour les occuper. En ouvrant un QPC, de plus en plus de modes sont accessibles pour les électrons, et comme chaque mode contribue pour un quantum de conductance ( $2e^2/h$ ), la conductance totale ne peut prendre que des valeurs entières du quantum de conductance, et évolue par pas séparés de  $2e^2/h$ . Mais depuis que ces dispositifs ont été inventés, des anomalies contredisant cette explication simple basée sur la mécanique quantique à une particule sont systématiquement observées. Ces anomalies sont attribuées aux interactions entre électrons, qui compliquent largement le problème. L'anomalie la plus connue est un petit épaulement observé sous le premier plateau de conductance, autour de  $0.7 \times 2e^2/h$ , appelé l'anomalie 0.7. Une autre anomalie est également visible dans la conductance différentielle à basse température: un pic de conductance autour de la polarisation nulle: l'anomalie à zéro polarisation (ZBA). Ces deux anomalies ont concentré les efforts de beaucoup de groupes reconnus dans le

---

monde, et sont toujours très débattues aujourd’hui après plus de 15 ans de recherches intensives, aucune explication n’ayant intégralement convaincu la communauté pour le moment. Elles traduisent le fait que même dans un système aussi simple qu’un QPC, une description complète ne peut être obtenue sans prendre en compte les effets d’interactions, qui sont souvent à l’origine des problèmes les plus riches et les plus complexes en mécanique quantique.

L’objet utilisé dans cette thèse pour étudier ces effets d’interactions est un microscope à effet de grille local (ou SGM, pour scanning gate microscopy). Cette technique, dérivée de la microscopie à force atomique, consiste à modifier localement le potentiel des gaz 2D à l’aide d’une pointe métallique chargée. L’effet de ces modifications de potentiel se traduit par des changements de la conductance du dispositif, qui est enregistrée tandis que la pointe se déplace au dessus de la surface. Si on cartographie la conductance en fonction de la position de la pointe, on obtient alors des images du transport électronique quantique dans les gaz 2D. Mais un SGM permet bien plus que l’obtention d’images, et la pointe peut être utilisée comme un paramètre de transport additionnel, permettant une investigation subtile des phénomènes de transport dans les gaz 2D.

Nous verrons dans cette thèse deux façons d’utiliser la pointe pour révéler des informations cruciales sur les anomalies de conductance des QPCs. Nous décrirons comment le potentiel de pointe peut être utilisé pour modifier in situ le potentiel du QPC par un effet électrostatique à longue portée, et permet de modifier les anomalies de conductance, révélant ainsi les mécanismes sous-jacents à ces anomalies. Nous verrons également comment la pointe permet de créer in situ des interféromètres incluant le QPC, ouvrant la voie des expériences interférométriques, et donc sensibles à la phase des électrons, qui joue un rôle fondamental en mécanique quantique.

Ce manuscrit est organisé comme suit:

Le chapitre 1 présente le transport électronique dans les QPCs, dans les régimes linéaire et non linéaire, et se base sur des considérations à une particule. Nous présentons également un outil numérique: Kwant[8], qui est utilisé au cours de cette thèse pour étudier les phénomènes de transport dans les gaz 2D. Nous discutons le désordre dans les gaz 2D, et ses effets sur la conductance des QPCs.

Dans le chapitre 2, nous présentons les effets d’interactions dans les QPCs, et passons rapidement en revue les observations expérimentales et les propositions théoriques les plus pertinentes réalisées sur ce sujet.

Le chapitre 3 présente l’outil utilisé dans cette thèse: le microscope SGM. Nous proposons différentes méthodes pour évaluer le potentiel créé par la pointe au niveau du gaz 2D, principalement la taille de la zone de déplétion créée sous la pointe, et le potentiel à longue portée. Nous étudions également les interférences électroniques obtenues dans les images SGM et discutons des différents mécanismes pouvant leur donner naissance. Nous présentons enfin des simulations numériques permettant de mieux comprendre le signal observé en SGM.

Le chapitre 4 présente des interféromètres créés à l’aide d’une troisième grille située en face des QPC. Nous discutons le transport dans ces interféromètres, et présentons l’effet de la température et du champ magnétique sur les interférences obtenues. Un parallèle est fait avec les interférences obtenues en SGM, et nous verrons qu’elles partagent la même origine. Des simulations numériques permettent également de mieux comprendre le rôle

---

complexe du désordre dans la formation de ces interférences.

Dans le chapitre 5, nous présentons le principal résultat obtenu au cours de cette thèse. Nous verrons comment la pointe permet de modifier les anomalies de conductance des QPCs, et conforte une expérience récente proposant que les électrons se localisent spontanément dans les QPCs[9]. A la lumière de nos résultats, nous proposons un mécanisme de type “cristallisation de Wigner” pour expliquer cette localisation. Nous présentons également des simulations électrostatiques classiques pour étayer ce scénario.

Le chapitre 6 présente une expérience interférométrique sur les QPCs. Nous utilisons la pointe pour créer des interféromètres de type Fabry-Pérot entre le QPC et la zone déplétée sous la pointe. Nous mettons en évidence un déphasage des interférences intimement relié à l’anomalie à zéro polarisation, et proposons une ébauche d’explication basée sur la physique Kondo.

Enfin, nous présentons une nouvelle piste d’exploration expérimentale dans le chapitre 7. Nous montrons comment nous avons su adapter la technique SGM à l’étude du transport thermoélectrique des QPCs, et présentons les premières images du transport thermoélectrique cohérent des électrons dans le gaz 2D. Nous proposons des pistes d’explorations que cette nouvelle technique offre pour étudier les effets d’interactions dans les QPCs.

## 1. Transport dans les contacts ponctuels quantiques

Ce premier chapitre vise à présenter le transport dans les QPCs, sous un angle faisant abstraction des interactions entre électrons. Une première partie présente les gaz bidimensionnels de haute mobilité obtenus dans les hétérostructures de GaAs/AlGaAs. Nous présentons les premières réalisations expérimentales de QPCs de la fin des années 80[26, 28]. Le transport électronique à une dimension et la quantification de la conductance en résultant sont ensuite discutés. Le modèle de Buttiker pour expliquer que les marches de conductance d’un QPC sont séparées par des transitions douces et non abruptes[4] est brièvement présenté. Ce modèle se base sur l’hypothèse d’un potentiel de confinement parabolique dans les directions transverses et longitudinales, et permet de comprendre la forme des courbes de conductance à basse température.

Nous discutons la conductance non-linéaire, et le fait qu’une quantification demi-entière est obtenue quand une tension DC de l’ordre de la séparation entre les sous-bandes 1D du QPC est appliquée. Cette propriété est utile pour faire la spectroscopie des QPC et connaître l’espacement énergétique entre sous-bandes.

Différents échantillons mesurés au cours de cette thèse sont ensuite présentés ainsi que les techniques de mesure en deux ou 4 fils pour s’affranchir des résistances de contact.

Nous introduisons l’outil numérique Kwant[8] développé par Xavier Waintal et Christophe Groth au CEA Grenoble. Je tiens au passage à les remercier pour leur implication et leur aide indispensable pour modéliser le transport dans nos QPCs et nos interféromètres. Enfin, nous discutons le rôle du désordre dans les QPCs et illustrons comment le désordre peut affecter le transport à l’aide de simulations Kwant.

---

## 2. Interactions dans les contacts ponctuels quantiques

Nous discutons dans ce chapitre les anomalies de conductance observées dans les QPCs. Les deux anomalies systématiques sont l'anomalie 0.7, un épaulement à l'ouverture du premier mode des QPCs, et l'anomalie à zéro polarisation (ZBA), un pic dans la conductance différentielle autour du source-drain nul.

L'anomalie 0.7 en particulier, était déjà visible dès les premières expériences sur ces dispositifs. Comme elle peut se confondre avec des signatures du désordre, il a fallu attendre 1996 pour que sa dépendance en température et en champ magnétique soit systématiquement étudiée par le groupe du laboratoire Cavendish (Cambridge)[22]. Nous présentons dans ce chapitre les premiers résultats, montrant que le 0.7 devient un plateau à  $e^2/h$  sous fort champ magnétique parallèle, et s'estompe quand on abaisse la température sous  $\sim 500$  mK. Les auteurs ont dès cette première étude révélé que l'anomalie 0.7 est due aux interactions et au spin des électrons, en proposant qu'une polarisation spontanée de spin près du pinch-off (à basse densité) pourrait être la cause de cette anomalie. La dépendance en source-drain et en température a ensuite été détaillée, et révèle un mécanisme d'activation thermique qui suit la loi d'Arrhenius, avec une certaine température d'activation[12]. Les auteurs proposent un modèle phénoménologique considérant différentes sous-bandes pour les deux espèces de spins, séparés par un gap qui dépend de la tension source-drain, détaillé en Ref.[3].

Cette dépendance en température et en bias a ensuite été revisitée pendant la thèse de S. Cronenwett[5], à Harvard, sous la direction de Charles Marcus et David Goldhaber-Gordon. La disparition de l'anomalie 0.7 correspond à l'apparition d'un pic de conductance autour de la polarisation nulle qui apparaît à basse température: la ZBA[6]. Les auteurs attribuent ce pic à l'effet Kondo, qui apparaît lorsque les électrons de conduction écrantent le spin d'un électron localisé.

Différentes études ont été menées depuis[31, 20, 18, 17], qui font état de différences notables entre la ZBA et l'effet Kondo tel qu'il est connu dans les quantum dots. De plus, l'effet Kondo nécessite un état localisé et la localisation des électrons dans un système ouvert comme un QPC n'est pas du tout évidente.

Nous discutons à la fin de ce chapitre les modèles (souvent numériques) proposant une localisation spontanée des électrons dans les QPCs à cause de l'interaction Coulombienne. Nous discutons des différents mécanismes proposés pour expliquer les anomalies de conductance en supposant une localisation dans le QPC. Enfin, nous présentons brièvement le débat qui a animé la communauté au cours de cette thèse, par la publication de deux articles contradictoires publiés face à face dans le journal *Nature* proposant deux origines très différentes pour expliquer ces anomalies[9, 2]. Alors que Ref.[9] propose qu'un nombre fini d'électrons se localisent spontanément dans les QPCs, donnant naissance à deux types distincts d'effets Kondo selon leur parité, Ref.[2] propose une explication des anomalies sans faire appel à la localisation des électrons. Leur argument est basé sur le fait que la densité d'état à une dimension présente une singularité (dite de Van-Hove), et que combinées à cette singularité, les interactions pourraient expliquer les anomalies de transport. Cependant, les interactions dans ce modèle sont traitées de façon perturbative et ne permettent pas d'obtenir des anomalies de conductance telles qu'observées expérimentalement. Nous discutons au chapitre 5 comment les résultats obtenus au cours de cette thèse permettent de trancher entre ces deux propositions et apportent une contribution

---

significative au débat sur l'existence d'états localisés dans les QPCs.

### 3. Microscopie à effet de grille local

no L'outil principal utilisé au cours de cette thèse est un microscope à effet de grille local (SGM). Cette technique est dérivée de la microscopie à force atomique (AFM). A l'aide d'une pointe métallique chargée, on vient modifier à basse température le potentiel local d'un dispositif, et on enregistre les changements de conductance induits par ces modifications de potentiel. En enregistrant la conductance en fonction de la position de la pointe, on peut obtenir des images qui apportent des informations sur le transport dans le dispositif. Cette technique est particulièrement utile pour l'étude des systèmes à base d'hétérostructures semi-conductrices, car l'utilisation d'un microscope à effet tunnel est impossible à cause de la couche isolante qui sépare le gaz 2D de la surface.

Après une rapide revue de l'invention et du développement de cette technique dans les différents groupes l'ayant adoptée, nous discutons dans ce chapitre les interférences observées lorsqu'on réalise cette étude sur des QPCs. En effet, les premières images haute résolution obtenues en scannant la pointe chargée négativement au dessus de la surface en face d'un QPC ont permis d'observer des chemins ramifiés suivis préférentiellement par les électrons, décorés par des franges d'interférences électroniques[23], séparées par  $\lambda_F/2$ . Nous discutons de l'influence de la mobilité des échantillons sur le type d'interférences observées. En effet, deux types de franges semblent observées selon la mobilité, qui n'ont pas la même dépendance en température. Dans les échantillons de mobilité  $\sim 2.10^5 cm^2/V.s$ , des interférences sont observées jusqu'à des températures de 4K, alors qu'elles ne sont pas présentes dans les échantillons de mobilité  $10^6 cm^2/V.s$  ou supérieures[10]. Cependant, des interférences réapparaissent dans ces échantillons pour des températures plus basses que 1K. Nous discutons les différences entre ces types d'interférences et les mécanismes pouvant leur donner naissance.

Nous présentons le microscope SGM principalement utilisé au cours de cette thèse, situé à Louvain-La-Neuve, et développé dans l'équipe de Vincent Bayot et Benoit Hackens, avec l'expertise de Frederico Martins et Sébastien Faniel. Nous discutons les interférences observées sur nos échantillons, et discutons les différents scénarios possibles pour leur formation, permettant d'expliquer leur dépendance avec l'ouverture du QPC, leur dépendance en température, et en source-drain.

Nous présentons ensuite des méthodes expérimentales et numériques permettant d'évaluer le potentiel électrostatique créé par la pointe, en s'appuyant sur les interférences et le "cross-talk": l'effet direct de la pointe sur l'ouverture du QPC.

Enfin, nous présentons des simulations numériques du transport électronique et montrons comment Kwant apparaît comme un outil très efficace pour simuler et comprendre le signal obtenu en SGM.

### 4. Interféromètres balistiques

Ce quatrième chapitre présente des interféromètres développés au cours de cette thèse. Ceux-ci sont réalisés par une troisième grille lithographiée à environ un micron des QPCs.

---

En appliquant une tension négative sur cette grille, on crée une zone de déplétion au niveau du gaz 2D qui rétro-diffuse les électrons vers le QPC et crée une cavité Fabry-Pérot entre cette zone déplétée et le QPC. En appliquant des tensions plus négatives sur cette grille, la zone de déplétion s’approche du QPC et des interférences apparaissent dans la conductance totale comme des oscillations en fonction de la tension appliquée.

L’étude en température et en champ magnétique semble supporter l’idée que ces interférences se produisent dans la cavité formée par la troisième grille et le QPC. Des simulations numériques incluant le champ magnétique confirment cette proposition. Cependant, cette hypothèse simple ne coïncide pas parfaitement avec le fait que des interférences soient visibles lorsque le premier mode du QPC est parfaitement transmis. Par des simulations numériques, nous montrons que le désordre résiduel du gaz 2D pourrait être responsable de ce contraste.

## 5. Cristallisation de Wigner et effets Kondo dans les contacts ponctuels quantiques

Dans ce chapitre, nous présentons les résultats les plus importants obtenus au cours de cette thèse. Nous commençons par détailler l’effet Kondo dans les métaux puis dans les quantum dots, tout d’abord pour une impureté magnétique portant un spin  $1/2$ . Lorsqu’un nombre impair d’électrons est contenu dans un quantum dot, le spin total du dot est  $1/2$  et l’écrantage de ce spin par les électrons de conduction des réservoirs donne lieu à une forte augmentation de la conductance différentielle autour du source-drain nul. Ceci peut être vu comme une augmentation de densité d’état dans le dot à l’énergie de Fermi des réservoirs à suffisamment basse température. Quand les deux réservoirs sont alignés, ces deux pics se superposent et donnent lieu à une augmentation de conductance à travers le dot, on a donc un pic de conductance différentielle à l’équilibre. Sous l’influence d’un champ magnétique extérieur, ce pic se sépare en deux pics à tensions de polarisation finies. Ces doubles pics peuvent aussi être observés sans champ magnétique via ce qu’on appelle “l’effet Kondo pair”. Cette situation peut être obtenue par exemple dans le cas d’un dot contenant un nombre pair d’électrons. Le niveau fondamental contient alors un spin total nul, et l’effet Kondo à l’équilibre n’est pas possible, aucune augmentation de conductance n’est visible. En revanche, l’état triplet excité correspondant à un spin total 1 peut mener à une augmentation de conductance lorsque les deux niveaux de Fermi des réservoirs sont espacés en énergie, d’une différence correspondant à l’écart entre le niveau fondamental et le niveau excité. On a donc un double pic dans la conductance différentielle.

Une alternance entre ces deux types d’effet Kondo a été récemment reportée dans des QPCs[9]. En étudiant des QPCs dont la longueur peut être changée à l’aide de plusieurs grilles métalliques, les auteurs ont montré qu’au fur et à mesure que le QPC s’allonge, la ZBA passe alternativement d’un simple pic à un double pic, que les auteurs interprètent comme des effets Kondo successivement impairs et pairs. Ils attribuent ce comportement à la localisation d’un nombre bien défini d’électrons dans le canal, dont le nombre dépend de la longueur du QPC, et donnant lieu à l’un des deux types d’effet Kondo selon leur parité.

---

Nous montrons ensuite comment nous pouvons faire une observation similaire avec un SGM. Lorsque le QPC est placé sous le premier plateau, nous observons en plus des interférences habituelles une série d’anneaux concentriques, centrés sur le QPC. En analysant comment ces modulations de conductance dépendent de l’ouverture du QPC, nous avons pu montrer qu’elles correspondent à des apparitions successives de l’anomalie 0.7. En enregistrant la spectroscopie de ces anneaux sous le premier plateau, nous avons également pu montrer que ces modulations correspondent à des splittings successifs de la ZBA. En approchant la pointe du QPC, la ZBA forme alternativement un pic ou deux pics, exactement comme l’observent Iqbal et al.[9] en allongeant le QPC. Nous interprétons également cet effet comme une alternance entre un effet Kondo pair et impair, dû à une alternance de la parité du nombre de charges localisées spontanément dans le QPC. Le fait que nous puissions changer ce nombre de charges simplement en approchant la pointe apporte une information intéressante sur la façon dont ces électrons se localisent. A l’aide de considérations simples et de simulations électrostatiques classiques, nous aboutissons à la conclusion que le paramètre gouvernant le nombre de charges localisées est la taille de la zone où la densité électronique est inférieure à un certain seuil. En effet, si on réduit la densité électronique, il arrive un moment où la répulsion coulombienne devient supérieure à l’énergie cinétique. On ne s’attend plus alors à avoir un liquide de Fermi usuel mais les électrons doivent former un cristal de Wigner[29]. A une dimension, cela se traduit par une chaîne de charges ordonnées, configuration qui minimise l’énergie d’un tel système. La valeur de la densité critique requise pour atteindre cet état est un problème débattu, mais des estimations simples correspondant à notre expérience donnent une valeur comparable à celles déduites d’études théoriques sur le sujet comme par exemple celle présentée Ref.[21].

Nous avons ensuite réalisé cette expérience sur un autre échantillon, et observé globalement les mêmes résultats, traduisant le fait que ce phénomène de cristallisation de Wigner est bien intrinsèque, et qu’un nombre pair ou impair d’électrons peut se localiser dans les QPCs donnant lieu à deux différents types d’effet Kondo.

Ce résultat apparaît comme un résultat important dans le domaine des anomalies de conductance des QPCs, et a été récemment présenté comme résolvant ce problème[7]. Contrairement à ce qui est brièvement proposé dans ce commentaire, nous pensons que notre travail ne résout pas le problème, mais offre un point de départ à de nouvelles investigations. En effet, nous avons pu montrer qu’un nombre déterminé de charges se localise dans les QPCs, et donnent lieu à différents effets Kondo. Lorsque le nombre de charges est impair, et la ZBA forme un simple pic, nous avons vu que cet effet restaure l’anomalie 0.7 à basse température. Mais ceci laisse inexplicée l’anomalie 0.7, et pourquoi la conductance semble bloquée dans ce régime. Pour comprendre d’où vient cet effet, il pourrait être intéressant d’étudier théoriquement la conductance à travers une chaîne finie de charges cristallisées, dont l’espacement évolue probablement le long du canal, avec un espacement maximum au centre. En effet, l’existence d’un cristal de Wigner a été proposé comme une explication possible pour l’anomalie 0.7[14], mais cette explication est basée sur un cristal infiniment long, où les excitations de spins et de charges sont découplées, et n’ont pas la même dépendance en température. Il serait intéressant de voir si cet effet

---

de séparation des excitations se produit dans une chaîne finie.

En parallèle, il serait indispensable de savoir combien de charges composent ce cristal de Wigner. Dans notre expérience, nous avons des signatures des *changements* du nombre de charges, mais n'avons pas accès à leur nombre absolu. Cette investigation pourra se faire numériquement, en résolvant complètement l'équation de Schrödinger-Poisson dans un environnement réaliste, en parallèle d'une investigation expérimentale, à l'aide de techniques de sondes locales avancées. Par exemple, en utilisant un STM sur QPC défini sur un gaz 2D de surface (qui n'existe pas encore pour le moment), ou à l'aide de microscopie à force électrique subtile sur un gaz 2D enterré dans une hétérostructure.

## 6. Mesurer le déphasage Kondo par interférométrie

Dans ce chapitre, nous nous intéressons à la ZBA, et étudions son effet sur les interférences. Dans une première partie, nous présentons une étude de la dépendance en température de la ZBA, et de sa largeur, en fonction de l'ouverture du QPC. Comme déjà reporté par différents groupes (par exemple Ref.[6]), la largeur de la ZBA et sa dépendance en température évoluent en fonction de la tension de grille. Par analogie avec l'effet Kondo, ces deux quantités doivent être déterminées entièrement par un paramètre unique: la température Kondo  $T_K$ . Dans les QPCs, attribuer une température Kondo non ambiguë à la ZBA n'est pas évident. Il faut considérer une forme différente pour le scaling en température, par rapport à ce qu'il se fait dans les quantum dots. Nous proposons une définition pour la température Kondo basée sur une analogie avec des dots asymétriques (dont les couplages aux deux réservoirs sont différents), offrant une potentielle explication au fait qu'à très basse température, la ZBA n'atteint pas  $2e^2/h$ , mais semble saturer à une valeur limite qui dépend de l'ouverture du QPC. En effet, dans un dot asymétrique, on s'attend à ce que la conductance sature à une valeur inférieure à  $2e^2/h$  qui dépend des deux barrières.

La dépendance de la ZBA avec la température peut suivre ce scaling pour certaines valeurs de  $T_K$ , et nous montrons que la largeur aux 2/3 du maximum de la ZBA coïncide avec  $T_K$  extrait de cette façon. Bien que n'étant pas une preuve, ceci montre que modéliser un QPC comme un dot asymétrique mériterait d'être exploré plus en détails.

Pour aller plus loin dans l'analogie avec l'effet Kondo, nous regardons ensuite si l'on peut observer une caractéristique de l'effet Kondo: le déphasage. En effet, les électrons qui diffusent sur (ou traversent) un singulet Kondo (une impureté magnétique et son nuage d'électrons l'écrantant) acquièrent une phase de  $\pi/2$ [16]. Cet effet a été vérifié expérimentalement en plaçant un quantum dot dans le régime Kondo dans l'un des bras d'un anneau Aharonov-Bohm[30, 19].

Ici, nous proposons d'étudier cet effet dans un interféromètre dont un des miroirs est un QPC et l'autre est la zone déplétée sous la pointe du SGM. Nous voyons des interférences comme discuté au chapitre 5, et regardons comment la ZBA influe sur ces interférences. Nous reportons un déphasage du système d'interférence dans le régime de la ZBA lorsque le QPC est sous le plateau et que celle-ci est visible. Nous montrons que ce déphasage apparaît intimement lié à la ZBA. Il est composé de deux changements de phase abruptes, qui apparaissent sur une fenêtre en énergie qui semble donnée par les largeur aux 2/3 de

---

la hauteur de la ZBA. En élevant la température, dans un régime où la ZBA disparaît mais pas les interférences, nous observons que le déphasage disparaît également. Enfin, le déphasage est composé de 3 déphasages successifs lorsque la ZBA forme deux pics.

Des considérations simples montrent que le déphasage observé pourrait être relié au déphasage Kondo, et nous développons en ce moment de petits modèles avec l'aide précieuse de Pascal Simon, expert dans ce domaine, pour investiguer cette interprétation. Si ce scénario était confirmé, ceci apparaîtrait comme une preuve irréfutable de la nature Kondo de la ZBA, et apporterait une contribution significative à ce domaine. De plus, cela permettrait de comprendre comment se fait le transport au travers du cristal de Wigner qui se forme dans les QPCs.

## 7. Imager un flot d'électrons cohérent induit par une différence de température

Ce dernier chapitre présente un travail en cours à l'heure où cette thèse s'achève, qui concerne la thermoélectricité. Lorsqu'un dispositif est soumis à un gradient de température, il apparaît dans certaines conditions une différence de potentiel en réponse à cette différence de température, ce phénomène est appelé effet Seebeck. Ceci est dû à un déséquilibre de flux d'électrons d'un côté à l'autre sous l'effet de l'agitation thermique. Nous commençons par un bref rappel de la thermoélectricité en physique mésoscopique, et une description des premières mesures faites sur les QPCs[15]. Nous discutons le lien entre la conductance et le pouvoir thermoélectrique, reliés par la loi de Mott. Nous discutons comment des déviations de la loi Mott peuvent être interprétées comme des signatures des interactions entre électrons.

Nous présentons ensuite la technique utilisée pour mesurer le pouvoir thermoélectrique et nos observations expérimentales. A l'aide de la loi de Mott, nous pouvons évaluer la différence de température que nous appliquons en chauffant un des réservoirs par effet Joule. Nous observons des déviations à la loi de Mott sous le premier plateau dans la transition entre le premier et le deuxième plateau, qui pourraient être dues aux interactions, comme révélé dans la Ref.[1].

Enfin, nous présentons comment adapter la technique SGM à l'étude du pouvoir thermoélectrique, et enregistrons la tension thermoélectrique en fonction de la position de la pointe. Nous obtenons des images d'interférences qui ressemblent beaucoup aux images de conductance, démontrant la cohérence des électrons dont le déplacement est gouverné non pas par une différence de potentiel, mais par une différence de température. Cette technique pourrait permettre à l'avenir une investigation plus fine des effets d'interactions par la SGM, car les tensions thermoélectriques impliquées par ces effets sont inférieures au microvolt. Le potentiel du QPC est donc très peu déformé par cette tension, contrairement aux mesures de conductance.

---

## 8. Conclusion et perspectives

Au cours de cette thèse, nous avons étudié les effets d'interactions dans les contacts ponctuels quantiques. Nous avons utilisé un microscope à effet de grille local afin de modifier la conductance des QPCs à très basse température. Nous avons distingué deux façons différentes d'utiliser le SGM qui apportent toutes deux des informations très intéressantes sur les anomalies conductance.

Premièrement, nous avons utilisé le potentiel électrostatique longue portée de la pointe polarisée pour modifier *in situ* le potentiel des QPCs. Nous avons observé dans les images SGM un nouveau phénomène lorsque le QPC est placé sous le premier plateau, où les interactions sont les plus importantes à cause de la faible densité électronique: une série d'anneaux concentriques, centrés sur le QPC. Nous avons montré que ces anneaux correspondent à des modulations des anomalies de conductance. Ils correspondent à des apparitions successives de l'anomalie 0.7, et à une ZBA formant alternativement un simple pic ou un double pic. Nous interprétons ces signatures comme la conséquence d'un cristal de Wigner se formant à basse densité dans le QPC, et dont le nombre de charges peut être changé en approchant la pointe. Un nombre pair ou impair de charges donne naissance à deux types distincts d'effets Kondo. Ce mécanisme de type cristallisation de Wigner est compatible avec une récente étude montrant qu'un nombre défini de charges peut se localiser dans les QPCs, et dont le nombre peut être contrôlé à l'aide de plusieurs grilles déposées sur la surface[9]. Ces résultats écartent une proposition théorique récente proposant d'expliquer les anomalies de conductance sans faire appel à la localisation d'électrons dans les QPCs[2]. Mais ceci ne résout pas le problème de l'anomalie 0.7 vieux de maintenant 15 ans. Nous avons pu montrer que l'effet Kondo peut restaurer l'anomalie 0.7 à basse température si un nombre impair de charges est localisé dans le canal, mais ceci n'explique pas l'origine de l'anomalie. Pour comprendre ce problème, l'investigation théorique du transport à travers un petit cristal de Wigner contenant des charges non uniformément réparties est nécessaire. Il faudra aussi comprendre combien de charges contient ce cristal, et comment elles sont réparties, à l'aide de microscopies à sonde locale avancées, et en résolvant numériquement le problème électrostatique associé à un QPC en prenant pleinement en compte les interactions et les effets quantiques.

Nous avons également utilisé la pointe du microscope pour créer *in situ* des interféromètres entre le QPC et la zone déplétée par la pointe. La dépendance en température, des modèles simples et des simulations numériques du problème grâce à Kwant[8] suggèrent que les interférences visibles dans les images SGM se produisent entre la pointe et le QPC. Pour confirmer cette éventualité, nous avons créé des interféromètres à l'aide d'une troisième grille lithographiée en face des QPCs. Appliquer une tension négative sur cette grille génère des interférences. Leur dépendance en température et en champ magnétique montrent que ces interférences se produisent dans la cavité formée par le QPC et la zone de déplétion sous la pointe, et sont donc de même nature que celles observées en SGM.

A l'aide de la pointe SGM, nous avons étudié comment ces interférences dépendent de la tension source-drain. Nous observons un déphasage abrupte dans le régime de la ZBA, que nous attribuons au déphasage dû à l'effet Kondo. Ce scénario, en cours d'investigation,

---

pourrait être la preuve que l'effet Kondo est bien le phénomène responsable de la ZBA dans les QPCs, qui est un sujet encore vivement débattu aujourd'hui.

Enfin, nous avons adapté la technique SGM à l'étude des effets thermoélectriques dans les QPCs, et observé pour la première fois un flot cohérent d'électrons induit par une différence de température.

# Bibliography

- [1] C. P. Umbach, S. Washburn, R. B. Laibowitz, and R. A. Webb. Magnetoresistance of small, quasi-one-dimensional, normal-metal rings and lines. *Phys. Rev. B*, 30:4048–4051, Oct 1984. →.
- [2] R. A. Webb, S. Washburn, C. P. Umbach, and R. B. Laibowitz. Observation of  $\frac{h}{e}$  aharonov-bohm oscillations in normal-metal rings. *Phys. Rev. Lett.*, 54:2696–2699, Jun 1985. →.
- [3] K. v. Klitzing, G. Dorda, and M. Pepper. New method for high-accuracy determination of the fine-structure constant based on quantized hall resistance. *Phys. Rev. Lett.*, 45:494–497, Aug 1980. →.
- [4] B. J. van Wees, H. van Houten, C. W. J. Beenakker, J. G. Williamson, L. P. Kouwenhoven, D. van der Marel, and C. T. Foxon. Quantized conductance of point contacts in a two-dimensional electron gas. *Phys. Rev. Lett.*, 60:848–850, Feb 1988. →.
- [5] D A Wharam, T J Thornton, R Newbury, M Pepper, H Ahmed, J E F Frost, D G Hasko, D C Peacock, D A Ritchie, and G A C Jones. One-dimensional transport and the quantisation of the ballistic resistance. *Journal of Physics C: Solid State Physics*, 21(8):L209, 1988. →.
- [6] D. C. Tsui, H. L. Stormer, and A. C. Gossard. Two-dimensional magnetotransport in the extreme quantum limit. *Phys. Rev. Lett.*, 48:1559–1562, May 1982. →.
- [7] R. B. Laughlin. Anomalous quantum hall effect: An incompressible quantum fluid with fractionally charged excitations. *Phys. Rev. Lett.*, 50:1395–1398, May 1983. →.
- [8] Christoph W Groth, Michael Wimmer, Anton R Akhmerov, and Xavier Waintal. Kwant: a software package for quantum transport. *New Journal of Physics*, 16(6):063065, 2014. →.
- [9] M. J. Iqbal, Roi Levy, E. J. Koop, J. B. Dekker, J. P. de Jong, J. H. M. van der Velde, D. Reuter, A. D. Wieck, Ramon Aguado, Yigal Meir, and C. H. van der Wal. Odd and even Kondo effects from emergent localization in quantum point contacts. *Nature*, 501(7465):79–83, Sep 2013. →.
- [10] M. Büttiker. Quantized transmission of a saddle-point constriction. *Phys. Rev. B*, 41:7906–7909, Apr 1990. →.

- 
- [11] L. P. Kouwenhoven, B. J. van Wees, C. J. P. M. Harmans, J. G. Williamson, H. van Houten, C. W. J. Beenakker, C. T. Foxon, and J. J. Harris. Nonlinear conductance of quantum point contacts. *Phys. Rev. B*, 39:8040–8043, Apr 1989. →.
- [12] N K Patel, L Martin-Moreno, M Pepper, R Newbury, J E F Frost, D A Ritchie, G A C Jones, J T M B Janssen, J Singleton, and J A A J Perenboom. Ballistic transport in one dimension: additional quantisation produced by an electric field. *Journal of Physics: Condensed Matter*, 2(34):7247, 1990. →.
- [13] L Martin-Moreno, J T Nicholls, N K Patel, and M Pepper. Non-linear conductance of a saddle-point constriction. *Journal of Physics: Condensed Matter*, 4(5):1323, 1992. →.
- [14] L. I. Glazman and A. V. Khaetskii. Nonlinear quantum conductance of a lateral microconstraint in a heterostructure. *EPL (Europhysics Letters)*, 9(3):263, 1989. →.
- [15] S. Baer, C. Rössler, E. C. de Wiljes, P.-L. Ardel, T. Ihn, K. Ensslin, C. Reichl, and W. Wegscheider. Interplay of fractional quantum hall states and localization in quantum point contacts. *Phys. Rev. B*, 89:085424, Feb 2014. →.
- [16] John H. Davies, Ivan A. Larkin, and E. V. Sukhorukov. Modeling the patterned two-dimensional electron gas: Electrostatics. *Journal of Applied Physics*, 77(9):4504–4512, 1995. →.
- [17] John A. Nixon and John H. Davies. Potential fluctuations in heterostructure devices. *Phys. Rev. B*, 41:7929–7932, Apr 1990. →.
- [18] Michael J. Laughton, John R. Barker, John A. Nixon, and John H. Davies. Modal analysis of transport through quantum point contacts using realistic potentials. *Phys. Rev. B*, 44:1150–1153, Jul 1991. →.
- [19] E. Tekman and S. Ciraci. Ballistic transport through a quantum point contact: Elastic scattering by impurities. *Phys. Rev. B*, 42:9098–9103, Nov 1990. →.
- [20] E. Tekman and S. Ciraci. Theoretical study of transport through a quantum point contact. *Phys. Rev. B*, 43:7145–7169, Mar 1991. →.
- [21] Y. Takagaki and D. K. Ferry. Conductance of quantum point contacts in the presence of disorder. *Phys. Rev. B*, 46:15218–15224, Dec 1992. →.
- [22] C. S. Chu and Ming-Hui Chou. Effects of an impurity on the conductance and thermopower of a saddle-point-potential quantum point contact. *Phys. Rev. B*, 50:14212–14222, Nov 1994. →.
- [23] B. J. van Wees, L. P. Kouwenhoven, E. M. M. Willems, C. J. P. M. Harmans, J. E. Mooij, H. van Houten, C. W. J. Beenakker, J. G. Williamson, and C. T. Foxon. Quantum ballistic and adiabatic electron transport studied with quantum point contacts. *Phys. Rev. B*, 43:12431–12453, May 1991. →.

- 
- [24] N. K. Patel, J. T. Nicholls, L. Martn-Moreno, M. Pepper, J. E. F. Frost, D. A. Ritchie, and G. A. C. Jones. Evolution of half plateaus as a function of electric field in a ballistic quasi-one-dimensional constriction. *Phys. Rev. B*, 44:13549–13555, Dec 1991. →.
- [25] K. J. Thomas, J. T. Nicholls, M. Y. Simmons, M. Pepper, D. R. Mace, and D. A. Ritchie. Possible spin polarization in a one-dimensional electron gas. *Phys. Rev. Lett.*, 77:135–138, Jul 1996. →.
- [26] Chuan-Kui Wang and K.-F. Berggren. Spin splitting of subbands in quasi-one-dimensional electron quantum channels. *Phys. Rev. B*, 54:R14257–R14260, Nov 1996. →.
- [27] K. J. Thomas, J. T. Nicholls, N. J. Appleyard, M. Y. Simmons, M. Pepper, D. R. Mace, W. R. Tribe, and D. A. Ritchie. Interaction effects in a one-dimensional constriction. *Phys. Rev. B*, 58:4846–4852, Aug 1998. →.
- [28] A. Kristensen, H. Bruus, A. E. Hansen, J. B. Jensen, P. E. Lindelof, C. J. Marckmann, J. Nygård, C. B. Sørensen, F. Beuscher, A. Forchel, and M. Michel. Bias and temperature dependence of the 0.7 conductance anomaly in quantum point contacts. *Phys. Rev. B*, 62:10950–10957, Oct 2000. →.
- [29] Henrik Bruus, Vadim V Cheianov, and Karsten Flensberg. The anomalous 0.5 and 0.7 conductance plateaus in quantum point contacts. *Physica E: Low-dimensional Systems and Nanostructures*, 10(1–3):97 – 102, 2001. →.
- [30] A P Micolich. What lurks below the last plateau: experimental studies of the  $0.7 \times 2e^2/h$  conductance anomaly in one-dimensional systems. *Journal of Physics: Condensed Matter*, 23(44):443201, 2011. →.
- [31] P. Roche, J. Ségala, D. C. Glatthli, J. T. Nicholls, M. Pepper, A. C. Graham, K. J. Thomas, M. Y. Simmons, and D. A. Ritchie. Fano factor reduction on the 0.7 conductance structure of a ballistic one-dimensional wire. *Phys. Rev. Lett.*, 93:116602, Sep 2004. →.
- [32] L. DiCarlo, Y. Zhang, D. T. McClure, D. J. Reilly, C. M. Marcus, L. N. Pfeiffer, and K. W. West. Shot-noise signatures of 0.7 structure and spin in a quantum point contact. *Phys. Rev. Lett.*, 97:036810, Jul 2006. →.
- [33] N. J. Appleyard, J. T. Nicholls, M. Pepper, W. R. Tribe, M. Y. Simmons, and D. A. Ritchie. Direction-resolved transport and possible many-body effects in one-dimensional thermopower. *Phys. Rev. B*, 62:R16275–R16278, Dec 2000. →.
- [34] R Crook, J Prance, KJ Thomas, SJ Chorley, I Farrer, DA Ritchie, M Pepper, and CG Smith. Conductance quantization at a half-integer plateau in a symmetric gaas quantum wire. *Science*, 312(5778):1359–1362, 2006.
- [35] Stefano Roddaro Christian Reichl Werner Wegscheider Giorgio Biasiol Lucia Sorba Fabio Beltram Andrea Iagallo, Nicola Paradiso and Stefan Heun. Scanning gate

- 
- imaging of quantum point contacts and the origin of the 0.7 anomaly. *arXiv*, 1311.6303, 2013. [→](#).
- [36] S. M. Cronenwett. *Coherence, charging and spin effects in quantum dots and quantum point contacts*. PhD thesis, Harvard University, 2001. [→](#).
- [37] S. M. Cronenwett, H. J. Lynch, D. Goldhaber-Gordon, L. P. Kouwenhoven, C. M. Marcus, K. Hirose, N. S. Wingreen, and V. Umansky. Low-temperature fate of the 0.7 structure in a point contact: A Kondo-like correlated state in an open system. *Phys. Rev. Lett.*, 88:226805, May 2002. [→](#).
- [38] Y. Yoon, L. Mourokh, T. Morimoto, N. Aoki, Y. Ochiai, J. L. Reno, and J. P. Bird. Probing the microscopic structure of bound states in quantum point contacts. *Phys. Rev. Lett.*, 99:136805, Sep 2007. [→](#).
- [39] F. Sfigakis, C. J. B. Ford, M. Pepper, M. Kataoka, D. A. Ritchie, and M. Y. Simmons. Kondo effect from a tunable bound state within a quantum wire. *Phys. Rev. Lett.*, 100:026807, Jan 2008. [→](#).
- [40] S. Sarkozy, F. Sfigakis, K. Das Gupta, I. Farrer, D. A. Ritchie, G. A. C. Jones, and M. Pepper. Zero-bias anomaly in quantum wires. *Phys. Rev. B*, 79:161307, Apr 2009. [→](#).
- [41] Y. Ren, W. W. Yu, S. M. Frolov, J. A. Folk, and W. Wegscheider. Zero-bias anomaly of quantum point contacts in the low-conductance limit. *Phys. Rev. B*, 82:045313, Jul 2010. [→](#).
- [42] Georg Seelig and K. A. Matveev. Electron-phonon scattering in quantum point contacts. *Phys. Rev. Lett.*, 90:176804, May 2003. [→](#).
- [43] A. Kristensen, P.E. Lindelof, J. Bo Jensen, M. Zaffalon, J. Hollingbery, S.W. Pederesen, J. Nygard, H. Bruus, S.M. Reimann, C.B. Sorensen, M. Michel, and A. Forchel. Temperature dependence of the “0.7”  $2e^2/h$  quasi-plateau in strongly confined quantum point contacts. *Physica B: Condensed Matter*, 249–251:180 – 184, 1998. [→](#).
- [44] Yigal Meir, Kenji Hirose, and Ned S. Wingreen. Kondo model for the “0.7 anomaly” in transport through a quantum point contact. *Phys. Rev. Lett.*, 89:196802, Oct 2002. [→](#).
- [45] Tomaz Rejec and Yigal Meir. Magnetic impurity formation in quantum point contacts. *Nature*, 442(7105):900–903, Aug 2006. [→](#).
- [46] K. A. Matveev. Conductance of a quantum wire in the wigner-crystal regime. *Phys. Rev. Lett.*, 92:106801, Mar 2004. [→](#).
- [47] O. P. Sushkov. Conductance anomalies in a one-dimensional quantum contact. *Phys. Rev. B*, 64:155319, Sep 2001. [→](#).
- [48] Boris Spivak and Fei Zhou. Ferromagnetic correlations in quasi-one-dimensional conducting channels. *Phys. Rev. B*, 61:16730–16735, Jun 2000. [→](#).

- 
- [49] E. Wigner. On the interaction of electrons in metals. *Phys. Rev.*, 46:1002–1011, Dec 1934. →.
- [50] K. A. Konstantin Matveev. Private communication, May 2013.
- [51] Luke Shulenburger, Michele Casula, Gaetano Senatore, and Richard M. Martin. Correlation effects in quasi-one-dimensional quantum wires. *Phys. Rev. B*, 78:165303, Oct 2008. →.
- [52] A. D. Güçlü, C. J. Umrigar, Hong Jiang, and Harold U. Baranger. Localization in an inhomogeneous quantum wire. *Phys. Rev. B*, 80:201302, Nov 2009. →.
- [53] O. P. Sushkov. Restricted and unrestricted hartree-fock calculations of conductance for a quantum point contact. *Phys. Rev. B*, 67:195318, May 2003. →.
- [54] Stefan A. Söffing, Michael Bortz, Imke Schneider, Alexander Struck, Michael Fleischhauer, and Sebastian Eggert. Wigner crystal versus friedel oscillations in the one-dimensional hubbard model. *Phys. Rev. B*, 79:195114, May 2009. →.
- [55] A. D. Klironomos, J. S. Meyer, T. Hikihara, and K. A. Matveev. Spin coupling in zigzag wigner crystals. *Phys. Rev. B*, 76:075302, Aug 2007. →.
- [56] L. W. Smith, W. K. Hew, K. J. Thomas, M. Pepper, I. Farrer, D. Anderson, G. A. C. Jones, and D. A. Ritchie. Row coupling in an interacting quasi-one-dimensional quantum wire investigated using transport measurements. *Phys. Rev. B*, 80:041306, Jul 2009. →.
- [57] Florian Bauer, Jan Heyder, Enrico Schubert, David Borowsky, Daniela Taubert, Benedikt Bruognolo, Dieter Schuh, Werner Wegscheider, Jan von Delft, and Stefan Ludwig. Microscopic origin of the ‘0.7-anomaly’ in quantum point contacts. *Nature*, 501(7465):73–78, Sep 2013. Letter.
- [58] M. A. Eriksson, R. G. Beck, M. Topinka, J. A. Katine, R. M. Westervelt, K. L. Campman, and A. C. Gossard. Cryogenic scanning probe characterization of semiconductor nanostructures. *Applied Physics Letters*, 69(5):671–673, 1996. →.
- [59] M. A. Topinka, B. J. LeRoy, S. E. J. Shaw, E. J. Heller, R. M. Westervelt, K. D. Maranowski, and A. C. Gossard. Imaging coherent electron flow from a quantum point contact. *Science*, 289(5488):2323–2326, 2000. →.
- [60] M. A. Topinka, B. J. LeRoy, R. M. Westervelt, S. E. J. Shaw, R. Fleischmann, E. J. Heller, K. D. Maranowski, and A. C. Gossard. Coherent branched flow in a two-dimensional electron gas. *Nature*, 410(6825):183–186, Mar 2001. →.
- [61] A A Kozikov, C Rössler, T Ihn, K Ensslin, C Reichl, and W Wegscheider. Interference of electrons in backscattering through a quantum point contact. *New Journal of Physics*, 15(1):013056, 2013. →.
- [62] Katherine E. Aidala, Robert E. Parrott, Tobias Kramer, E. J. Heller, R. M. Westervelt, M. P. Hanson, and A. C. Gossard. Imaging magnetic focusing of coherent electron waves. *Nat Phys*, 3(7):464–468, Jul 2007. →.

- 
- [63] Nicola Paradiso, Stefan Heun, Stefano Roddaro, Lucia Sorba, Fabio Beltram, Giorgio Biasiol, L. N. Pfeiffer, and K. W. West. Imaging fractional incompressible stripes in integer quantum hall systems. *Phys. Rev. Lett.*, 108:246801, Jun 2012. [→](#).
- [64] M. Huefner, C. May, S. Kičín, K. Ensslin, T. Ihn, M. Hilke, K. Suter, N. F. de Rooij, and U. Staufer. Scanning gate microscopy measurements on a superconducting single-electron transistor. *Phys. Rev. B*, 79:134530, Apr 2009. [→](#).
- [65] Ania C. Bleszynski, Floris A. Zwanenburg, R. M. Westervelt, Aarnoud L. Roest, Erik P. A. M. Bakkers, and Leo P. Kouwenhoven. Scanned probe imaging of quantum dots inside inas nanowires. *Nano Letters*, 7(9):2559–2562, 2007. [→](#).
- [66] Parisa Fallahi, Ania C. Bleszynski, Robert M. Westervelt, Jian Huang, Jamie D. Walls, Eric J. Heller, Micah Hanson, and Arthur C. Gossard. Imaging a single-electron quantum dot. *Nano Letters*, 5(2):223–226, 2005. [→](#).
- [67] B. Hackens, F. Martins, T. Ouisse, H. Sellier, S. Bollaert, X. Wallart, A. Cappy, J. Chevrier, V. Bayot, and S. Huant. Imaging and controlling electron transport inside a quantum ring. *Nat Phys*, 2(12):826–830, Dec 2006. [→](#).
- [68] F. Martins, B. Hackens, M. G. Pala, T. Ouisse, H. Sellier, X. Wallart, S. Bollaert, A. Cappy, J. Chevrier, V. Bayot, and S. Huant. Imaging electron wave functions inside open quantum rings. *Phys. Rev. Lett.*, 99:136807, Sep 2007. [→](#).
- [69] B. Hackens, F. Martins, S. Faniel, C. A. Dutu, H. Sellier, S. Huant, M. Pala, L. Desplanque, X. Wallart, and V. Bayot. Imaging coulomb islands in a quantum hall interferometer. *Nat Commun*, 1:39, Jul 2010. [→](#).
- [70] B. J. LeRoy, A. C. Bleszynski, K. E. Aidala, R. M. Westervelt, A. Kalben, E. J. Heller, S. E. J. Shaw, K. D. Maranowski, and A. C. Gossard. Imaging electron interferometer. *Phys. Rev. Lett.*, 94:126801, Apr 2005. [→](#).
- [71] M. P. Jura, M. A. Topinka, L. Urban, A. Yazdani, H. Shtrikman, L. N. Pfeiffer, K. W. West, and D. Goldhaber-Gordon. Unexpected features of branched flow through high-mobility two-dimensional electron gases. *Nat Phys*, 3(12):841–845, Dec 2007. [→](#).
- [72] Rodolfo A. Jalabert, Wojciech Szewc, Steven Tomsovic, and Dietmar Weinmann. What is measured in the scanning gate microscopy of a quantum point contact? *Phys. Rev. Lett.*, 105:166802, Oct 2010. [→](#).
- [73] Cosimo Gorini, Rodolfo A. Jalabert, Wojciech Szewc, Steven Tomsovic, and Dietmar Weinmann. Theory of scanning gate microscopy. *Phys. Rev. B*, 88:035406, Jul 2013. [→](#).
- [74] Adel Abbout, Gabriel Lemarié, and Jean-Louis Pichard. Thermal enhancement of interference effects in quantum point contacts. *Phys. Rev. Lett.*, 106:156810, Apr 2011. [→](#).

- 
- [75] Bo Liu and Eric J. Heller. Stability of branched flow from a quantum point contact. *Phys. Rev. Lett.*, 111:236804, Dec 2013. [→](#).
- [76] Cosimo Gorini, Dietmar Weinmann, and Rodolfo A. Jalabert. Scanning-gate-induced effects in nonlinear transport through nanostructures. *Phys. Rev. B*, 89:115414, Mar 2014. [→](#).
- [77] M. P. Jura, M. Grobis, M. A. Topinka, L. N. Pfeiffer, K. W. West, and D. Goldhaber-Gordon. Spatially probed electron-electron scattering in a two-dimensional electron gas. *Phys. Rev. B*, 82:155328, Oct 2010. [→](#).
- [78] Axel Freyn, Ioannis Klefogiannis, and Jean-Louis Pichard. Scanning gate microscopy of a nanostructure where electrons interact. *Phys. Rev. Lett.*, 100:226802, Jun 2008. [→](#).
- [79] D. Weinmann, R. A. Jalabert, A. Freyn, G.-L. Ingold, and J.-L. Pichard. Detection of interaction-induced nonlocal effects using perfectly transmitting nanostructures. *The European Physical Journal B*, 66(2):239–244, 2008. [→](#).
- [80] M. Topinka. *Imaging Coherent Electron Wave Flow Through 2-D Electron Gas Nanostructures*. PhD thesis, Harvard, 2002. [→](#).
- [81] B. J. LeRoy. *Imaging Coherent Electron Flow Through Semiconductor Nanostructures*. PhD thesis, Harvard, 2003. .
- [82] S. E. J. Shaw. *Propagation in Smooth Random Potentials*. PhD thesis, Harvard, 2002. .
- [83] M. P. Jura, M. A. Topinka, M. Grobis, L. N. Pfeiffer, K. W. West, and D. Goldhaber-Gordon. Electron interferometer formed with a scanning probe tip and quantum point contact. *Phys. Rev. B*, 80:041303, Jul 2009. [→](#).
- [84] Rolf Crook, Abi C. Graham, Charles G. Smith, Ian Farrer, Harvey E. Beere, and David A. Ritchie. Erasable electrostatic lithography for quantum components. *Nature*, 424(6950):751–754, Aug 2003. [→](#).
- [85] K. Gloos, P. Utko, M. Aagesen, C. B. Sørensen, J. Bindslev Hansen, and P. E. Lindelof. Current-voltage characteristics of quantum-point contacts in the closed-channel regime: Transforming the bias voltage into an energy scale. *Phys. Rev. B*, 73:125326, Mar 2006. [→](#).
- [86] T. Ouchterlony and K.-F. Berggren. Analytic modeling of the conductance in quantum point contacts with large bias. *Phys. Rev. B*, 52:16329–16332, Dec 1995. [→](#).
- [87] Axel Freyn and Jean-Louis Pichard. Effect of measurement probes upon the conductance of an interacting nanosystem: Detection of an attached ring by nonlocal many body effects. *Phys. Rev. Lett.*, 98:186401, Apr 2007. [→](#).
- [88] M. J. Iqbal. *Electron many-body effects in quantum point contacts*. PhD thesis, Groningen University, 2014. [→](#).

- 
- [89] W.J. de Haas, J. de Boer, and G.J. van den Berg. The electrical resistance of gold, copper and lead at low temperatures. *Physica*, 1(7–12):1115 – 1124, 1934. →.
- [90] B. Knook and G.J. Van Den Berg. The electrical resistance of pure au and ag at low temperatures. *Physica*, 26(7):505 – 512, 1960. .
- [91] Jun Kondo. Resistance minimum in dilute magnetic alloys. *Progress of Theoretical Physics*, 32(1):37–49, 1964. →.
- [92] Tai Kai Ng and Patrick A. Lee. On-site coulomb repulsion and resonant tunneling. *Phys. Rev. Lett.*, 61:1768–1771, Oct 1988. →.
- [93] D. Goldhaber-Gordon, Hadas Shtrikman, D. Mahalu, David Abusch-Magder, U. Meirav, and M. A. Kastner. Kondo effect in a single-electron transistor. *Nature*, 391(6663):156–159, Jan 1998. →.
- [94] Sara M. Cronenwett, Tjerk H. Oosterkamp, and Leo P. Kouwenhoven. A tunable Kondo effect in quantum dots. *Science*, 281(5376):540–544, 1998. →.
- [95] W. G. van der Wiel, S. De Franceschi, T. Fujisawa, J. M. Elzerman, S. Tarucha, and L. P. Kouwenhoven. The Kondo effect in the unitary limit. *Science*, 289(5487):2105–2108, 2000. →.
- [96] R. Leturcq, L. Schmid, K. Ensslin, Y. Meir, D. C. Driscoll, and A. C. Gossard. Probing the Kondo density of states in a three-terminal quantum ring. *Phys. Rev. Lett.*, 95:126603, Sep 2005. →.
- [97] Ned S. Wingreen and Yigal Meir. Anderson model out of equilibrium: Noncrossing-approximation approach to transport through a quantum dot. *Phys. Rev. B*, 49:11040–11052, Apr 1994. →.
- [98] Yigal Meir, Ned S. Wingreen, and Patrick A. Lee. Low-temperature transport through a quantum dot: The anderson model out of equilibrium. *Phys. Rev. Lett.*, 70:2601–2604, Apr 1993. →.
- [99] Antoine Georges and Yigal Meir. Electronic correlations in transport through coupled quantum dots. *Phys. Rev. Lett.*, 82:3508–3511, Apr 1999. →.
- [100] Ramón Aguado and David C. Langreth. Out-of-equilibrium Kondo effect in double quantum dots. *Phys. Rev. Lett.*, 85:1946–1949, Aug 2000. →.
- [101] H. Jeong, A. M. Chang, and M. R. Melloch. The Kondo effect in an artificial quantum dot molecule. *Science*, 293(5538):2221–2223, 2001. →.
- [102] S. Sasaki, S. De Franceschi, J. M. Elzerman, W. G. van der Wiel, M. Eto, S. Tarucha, and L. P. Kouwenhoven. Kondo effect in an integer-spin quantum dot. *Nature*, 405(6788):764–767, Jun 2000. →.
- [103] Nicolas Roch, Serge Florens, Vincent Bouchiat, Wolfgang Wernsdorfer, and Franck Balestro. Quantum phase transition in a single-molecule quantum dot. *Nature*, 453(7195):633–637, May 2008. →.

- 
- [104] C. H. L. Quay, John Cumings, S. J. Gamble, R. de Picciotto, H. Kataura, and D. Goldhaber-Gordon. Magnetic field dependence of the spin- $\frac{1}{2}$  and spin-1 Kondo effects in a quantum dot. *Phys. Rev. B*, 76:245311, Dec 2007.  $\rightarrow$ .
- [105] M. J. Iqbal, J. P. de Jong, D. Reuter, A. D. Wieck, and C. H. van der Wal. Split-gate quantum point contacts with tunable channel length. *Journal of Applied Physics*, 113(2):024507–024507–7, Jan 2013.
- [106] Y. Komijani, M. Csontos, T. Ihn, K. Ensslin, Y. Meir, D. Reuter, and A. D. Wieck. Origins of conductance anomalies in a p-type gaas quantum point contact. *Phys. Rev. B*, 87:245406, Jun 2013.  $\rightarrow$ .
- [107] A. E. Gildemeister, T. Ihn, R. Schleser, K. Ensslin, D. C. Driscoll, and A. C. Gossard. Imaging a coupled quantum dot-quantum point contact system. *Journal of Applied Physics*, 102(8):–, 2007.  $\rightarrow$ .
- [108] John A. Nixon, John H. Davies, and Harold U. Baranger. Breakdown of quantized conductance in point contacts calculated using realistic potentials. *Phys. Rev. B*, 43:12638–12641, May 1991.  $\rightarrow$ .
- [109] A. A. M. Staring, H. van Houten, C. W. J. Beenakker, and C. T. Foxon. Coulomb-blockade oscillations in disordered quantum wires. *Phys. Rev. B*, 45:9222–9236, Apr 1992.  $\rightarrow$ .
- [110] H. J. Schulz. Wigner crystal in one dimension. *Phys. Rev. Lett.*, 71:1864–1867, Sep 1993.  $\rightarrow$ .
- [111] Rosa López, Ramón Aguado, and Gloria Platero. Nonequilibrium transport through double quantum dots: Kondo effect versus antiferromagnetic coupling. *Phys. Rev. Lett.*, 89:136802, Sep 2002.  $\rightarrow$ .
- [112] Julia S. Meyer, K. A. Matveev, and A. I. Larkin. Transition from a one-dimensional to a quasi-one-dimensional state in interacting quantum wires. *Phys. Rev. Lett.*, 98:126404, Mar 2007.  $\rightarrow$ .
- [113] W. K. Hew, K. J. Thomas, M. Pepper, I. Farrer, D. Anderson, G. A. C. Jones, and D. A. Ritchie. Incipient formation of an electron lattice in a weakly confined quantum wire. *Phys. Rev. Lett.*, 102:056804, Feb 2009.  $\rightarrow$ .
- [114] A. C. Graham, K. J. Thomas, M. Pepper, N. R. Cooper, M. Y. Simmons, and D. A. Ritchie. Interaction effects at crossings of spin-polarized one-dimensional subbands. *Phys. Rev. Lett.*, 91:136404, Sep 2003.  $\rightarrow$ .
- [115] Elisa De Ranieri. Quantum devices: Anomalies explained. *Nat Nano*, Aug 2014. Research Highlights,  $\rightarrow$ .
- [116] P. Nozières. A “fermi-liquid” description of the Kondo problem at low temperatures. *Journal of Low Temperature Physics*, 17(1-2):31–42, 1974.

- 
- [117] A. Yacoby, M. Heiblum, D. Mahalu, and Hadas Shtrikman. Coherence and phase sensitive measurements in a quantum dot. *Phys. Rev. Lett.*, 74:4047–4050, May 1995. [→](#).
- [118] R. Schuster, E. Buks, M. Heiblum, D. Mahalu, V. Umansky, and Hadas Shtrikman. Phase measurement in a quantum dot via a double-slit interference experiment. *Nature*, 385(6615):417–420, Jan 1997. [→](#).
- [119] Ulrich Gerland, Jan von Delft, T. A. Costi, and Yuval Oreg. Transmission phase shift of a quantum dot with Kondo correlations. *Phys. Rev. Lett.*, 84:3710–3713, Apr 2000. [→](#).
- [120] Yang Ji, M. Heiblum, D. Sprinzak, D. Mahalu, and Hadas Shtrikman. Phase evolution in a Kondo-correlated system. *Science*, 290(5492):779–783, 2000. [→](#).
- [121] Yang Ji, M. Heiblum, and Hadas Shtrikman. Transmission phase of a quantum dot with Kondo correlation near the unitary limit. *Phys. Rev. Lett.*, 88:076601, Jan 2002. [→](#).
- [122] M. Zaffalon, Aveek Bid, M. Heiblum, D. Mahalu, and V. Umansky. Transmission phase of a singly occupied quantum dot in the Kondo regime. *Phys. Rev. Lett.*, 100:226601, Jun 2008. [→](#).
- [123] M. Yamamoto S. Hermelin T. Meunier A. Alex A. Weichselbaum J. von Delft A. D. Wieck S. Tarucha S. Takada, C. Bäuerle. Transmission phase in the Kondo regime revealed in a two-path interferometer. *ArXiv*, 2013. [→](#).
- [124] F. D. M. Haldane. Scaling theory of the asymmetric anderson model. *Phys. Rev. Lett.*, 40:416–419, Feb 1978. [→](#).
- [125] D. Goldhaber-Gordon, J. Göres, M. A. Kastner, Hadas Shtrikman, D. Mahalu, and U. Meirav. From the Kondo regime to the mixed-valence regime in a single-electron transistor. *Phys. Rev. Lett.*, 81:5225–5228, Dec 1998. [→](#).
- [126] Jesper Nygard, David Henry Cobden, and Poul Erik Lindelof. Kondo physics in carbon nanotubes. *Nature*, 408(6810):342–346, Nov 2000. [→](#).
- [127] Frank Reininghaus, Mikhail Pletyukhov, and Herbert Schoeller. Kondo model in nonequilibrium: Interplay between voltage, temperature, and crossover from weak to strong coupling. *Phys. Rev. B*, 90:085121, Aug 2014. [→](#).
- [128] Andrey V. Kretinin, Hadas Shtrikman, and Diana Mahalu. Universal line shape of the Kondo zero-bias anomaly in a quantum dot. *Phys. Rev. B*, 85:201301, May 2012. [→](#).
- [129] O. Klochan, A. P. Micolich, A. R. Hamilton, D. Reuter, A. D. Wieck, F. Reininghaus, M. Pletyukhov, and H. Schoeller. Scaling of the Kondo zero-bias peak in a hole quantum dot at finite temperatures. *Phys. Rev. B*, 87:201104, May 2013. [→](#).
- [130] H. Baranger. Private communication. July 2014.

- 
- [131] Luis G. G. V. Dias da Silva, Nancy Sandler, Pascal Simon, Kevin Ingersent, and Sergio E. Ulloa. Tunable pseudogap Kondo effect and quantum phase transitions in aharonov-bohm interferometers. *Phys. Rev. Lett.*, 102:166806, Apr 2009. [→](#).
- [132] Jinhong Park, S.-S. B. Lee, Yuval Oreg, and H.-S. Sim. How to directly measure a Kondo cloud's length. *Phys. Rev. Lett.*, 110:246603, Jun 2013. [→](#).
- [133] Nikola Pascher. *Local Imaging of Graphene and Quantum Hall Systems*. PhD thesis, ETH, Zurich, 2014. [→](#).
- [134] J. E. Gubernatis, J. E. Hirsch, and D. J. Scalapino. Spin and charge correlations around an anderson magnetic impurity. *Phys. Rev. B*, 35:8478–8485, Jun 1987. [→](#).
- [135] Ian Affleck. The Kondo screening cloud: what it is and how to observe it. *arXiv:0911.2209*, 2009. [→](#).
- [136] Pascal Simon and Ian Affleck. Finite-size effects in conductance measurements on quantum dots. *Phys. Rev. Lett.*, 89:206602, Oct 2002. [→](#).
- [137] Thomas Hand, Johann Kroha, and Hartmut Monien. Spin correlations and finite-size effects in the one-dimensional Kondo box. *Phys. Rev. Lett.*, 97:136604, Sep 2006. [→](#).
- [138] Kun Yang and Bertrand I. Halperin. Thermopower as a possible probe of non-abelian quasiparticle statistics in fractional quantum hall liquids. *Phys. Rev. B*, 79:115317, Mar 2009. [→](#).
- [139] R. Scheibner, H. Buhmann, D. Reuter, M. N. Kiselev, and L. W. Molenkamp. Thermopower of a Kondo spin-correlated quantum dot. *Phys. Rev. Lett.*, 95:176602, Oct 2005. [→](#).
- [140] Anders Mathias Lunde and Karsten Flensberg. On the mott formula for the thermopower of non-interacting electrons in quantum point contacts. *Journal of Physics: Condensed Matter*, 17(25):3879, 2005. [→](#).
- [141] A S Dzurak, C G Smith, L Martin-Moreno, M Pepper, D A Ritchie, G A C Jones, and D G Hasko. Thermopower of a one-dimensional ballistic constriction in the non-linear regime. *Journal of Physics: Condensed Matter*, 5(43):8055, 1993. [→](#).
- [142] L. W. Molenkamp, H. van Houten, C. W. J. Beenakker, R. Eppenga, and C. T. Foxon. Quantum oscillations in the transverse voltage of a channel in the nonlinear transport regime. *Phys. Rev. Lett.*, 65:1052–1055, Aug 1990. [→](#).
- [143] P Streda. Quantised thermopower of a channel in the ballistic regime. *Journal of Physics: Condensed Matter*, 1(5):1025, 1989. [→](#).
- [144] C. R. Proetto. Thermopower oscillations of a quantum-point contact. *Phys. Rev. B*, 44:9096–9099, Oct 1991. [→](#).
- [145] V C Karavolas and P N Butcher. Diffusion thermopower of a 2deg. *Journal of Physics: Condensed Matter*, 3(15):2597, 1991. [→](#).

- 
- [146] R. Fletcher, P. T. Coleridge, and Y. Feng. Oscillations in the diffusion thermopower of a two-dimensional electron gas. *Phys. Rev. B*, 52:2823–2830, Jul 1995. →.
- [147] M. Schmidt, G. Schneider, Ch. Heyn, A. Stemann, and W. Hansen. Thermopower of a 2d electron gas in suspended algaas/gaas heterostructures. *Journal of Electronic Materials*, 41(6):1286–1289, 2012. →.
- [148] Adel About. *Transport thermoélectrique dans des contacts quantiques ponctuels et de cavités chaotiques: effets thermiques et fluctuations*. These, Université Pierre et Marie Curie - Paris VI, December 2011. →.
- [149] Adam Micolich. Quantum point contacts: Double or nothing? *Nat Phys*, 9(9):530–531, Sep 2013. News and Views, →.